DTIC FILE COPY

②

MATERIALS

AD-A223 274

TIC
ECTE
18 1990
D
D

FINAL REPORT

to the

DEFENSE ADVANCED RESEARCH PROJECTS AGENCY

and the

OFFICE OF NAVAL RESEARCH

CONTRACT NO. N00014-86-K-0178

TITLE: High Performance Brittle Matrices and Brittle Matrix Composites

PERFORMING ORGANIZATION: UC Santa Barbara Materials Department

PRINCIPAL INVESTIGATORS: A.G. Evans and R. Mehrabian

CONTRACT PERIOD: March 15, 1986 through September 30, 1989

DISTRIBUTION STATEMENT A
Approved for public release;
Distribution Unlimited

BOOK 2 OF 2

90 06 14 184

SECURITY CLASSIFICATION OF THIS PAGE

REPORT DOCUMENTATION PAGE

Form Approved
OMB No. 0704-0188

1a. REPORT SECURITY CLASSIFICATION
Unclassified

1b. RESTRICTIVE MARKINGS

2a. SECURITY CLASSIFICATION AUTHORITY

2b. DECLASSIFICATION / DOWNGRADING SCHEDULE

3. DISTRIBUTION / AVAILABILITY OF REPORT
See distribution list

4. PERFORMING ORGANIZATION REPORT NUMBER(S)

5. MONITORING ORGANIZATION REPORT NUMBER(S)

6a. NAME OF PERFORMING ORGANIZATION
The University of California
Materials Department

6b. OFFICE SYMBOL *(If applicable)*

7a. NAME OF MONITORING ORGANIZATION
Office of Naval Research

6c. ADDRESS *(City, State, and ZIP Code)*
College of Engineering
University of California
Santa Barbara, CA 93106

7b. ADDRESS *(City, State, and ZIP Code)*
800 North Quincy Street
Arlington, VA 22217

8a. NAME OF FUNDING / SPONSORING ORGANIZATION
DARPA/Office of Naval Research

8b. OFFICE SYMBOL *(If applicable)*

9. PROCUREMENT INSTRUMENT IDENTIFICATION NUMBER
N00014-86-K-0178

8c. ADDRESS *(City, State, and ZIP Code)*
1400 Wilson Blvd.
Arlington, VA 22209

10. SOURCE OF FUNDING NUMBERS

PROGRAM ELEMENT NO.	PROJECT NO.	TASK NO	WORK UNIT ACCESSION NO.

11. TITLE *(Include Security Classification)*
Hihg Performance Brittle Matrices and Brittle Matrix Composites

12. PERSONAL AUTHOR(S)
Anthony G. Evans and Robert Mehrabian

13a. TYPE OF REPORT
Final Report

13b. TIME COVERED
FROM 9/15/86 TO 9/30/89

14. DATE OF REPORT *(Year, Month, Day)*
12/31/89

15. PAGE COUNT
406

16. SUPPLEMENTARY NOTATION

17. COSATI CODES

FIELD	GROUP	SUB-GROUP

18. SUBJECT TERMS *(Continue on reverse if necessary and identify by block number)*
Phase diagrams, solidification, composites,toughening residual stress.

19. ABSTRACT *(Continue on reverse if necessary and identify by block number)*

The primary intent of this research was the development of composites having an acceptable combination of toughness and oxidation resistance. The research was closely coordinated with the DARPA/ONR URI program at UCSB concerned with high temperature, high performance composites The study comprised three tasks. The first task was to study phase equilibria, solidification pathways and toughness properties of intermetallics, such as oxidation resistant Ti-Al-Ta and Nb-Al-Si alloys, and ceramics. These studies were then combined with interface interaction studies between the matrix microstructure and ductilizing/toughening particulates and fibers. The second task was a basic study of interface structure and chemistry as it relates to the mechanical properties of the interface. The third task involved studies on aluminum and copper matrix composites. These studies were concerned with developing an understanding of creep resistance.

DISTRIBUTION / AVAILABILITY OF ABSTRACT
☒ UNCLASSIFIED/UNLIMITED ☐ SAME AS RPT. ☐ DTIC USERS

21. ABSTRACT SECURITY CLASSIFICATION
Unclassified

22a. NAME OF RESPONSIBLE INDIVIDUAL
Robert Mehrabian

22b. TELEPHONE *(Include Area Code)*
(805) 961-3141

22c. OFFICE SYMBOL

DD Form 1473, JUN 86 *Previous editions are obsolete.* SECURITY CLASSIFICATION OF THIS PAGE

TABLE OF CONTENTS

Book 2

9.	The Processing and Mechanical Behavior of an Aluminum Matrix Composite Reinforced with Short Fibers	Y.L. Klipfel M.Y. He R.M. McMeeking A.G. Evans R. Mehrabian
10.	Brittle-to-Ductile Transition in Silicon Carbide	G.H. Campbell B.J. Dalgleish A.G. Evans
11.	Whisker Toughening: A Comparison Between Al_2O_3 and Si_3N_4 Toughened with SiC	G.H. Campbell M. Rühle B.J. Dalgleish A.G. Evans
12.	Finite Cracks in Transformation-Toughened Ceramics	D.M. Stump B. Budiansky
13.	On Toughening by Microcracks	D.K.M. Shum J.W. Hutchinson
14.	Fundamental Solutions for Microcracking Induced by Residual Stress	D.K.M. Shum Y.Y. Huang
15.	Phase Diagram and Solidification Models for the Nb-Al-Si System	D.J. Tilly T. Lu A. Paul R. Mehrabian

STATEMENT "A" per Dr. S. Fishman
ONR/Code 1131
TELECON 6/18/90 VG

Accesion For
NTIS CRA&I ☑
DTIC TAB ☐
Unannounced ☐
Justification
By per call
Distribution /
Availability Codes
Dist | Avail and / or Special
A-1

TABLE OF CONTENTS

Book 1

1.	The High Temperature α Field in the Titanium-Aluminum Phase Diagram	C. McCullough J.J. Valencia H. Mateos C.G. Levi R. Mehrabian
2.	Solidification of Supercooled Intermetallic Powders	C.G. Levi J.J. Valencia R. Mehrabian
3.	Microstructure Evolution in TiAl Alloys with B Additions: Conventional Solidification	M.E. Hyman C. McCullough J.J. Valencia C.G. Levi R. Mehrabian
4.	Microstructural Development and Mechanical Properties of Cu-Al *In Situ* Formed Composites	M.L. Borg J.J. Valencia C.G. Levi
5.	Containerless Processing of Niobium-Based Alloys	K.R. Javed G.J. Abbaschian
6.	Formation and Decomposition of Metastable B2 Phase in Ta-Ti-Al Alloys	Y.S. Kim K.R. Javed G.J. Abbaschian
7.	Effects of Interfaces on the Design and Oxidation Resistance of High Performance Composites: Processing Pathways-Phase Equilibria and Interdiffusion Reactions	J.H. Perepezko J.C. Lin T.J. Jewett Y.A. Chang
8.	Combined Mode I - Mode III Fracture Toughness of Alumina Particulate-Reinforced Aluminum Alloy-Matrix Composites	S.V. Kamat J.P. Hirth R. Mehrabian

SUMMARY

Lightweight intermetallics and ceramics have attractive high temperature properties but are mostly brittle and may be subject to oxidation. The primary intent of this research was the development of such materials having an acceptable combination of toughness and oxidation resistance. The research was closely coordinated with the DARPA/ONR URI program at UCSB concerned with high temperature, high performance composites.

The study comprised three tasks. The first task was to study phase equilibria, solidification pathways and toughness properties of intermetallics, such as oxidation resistant Ti-Al-Ta and Nb-Al-Si alloys, and ceramics. These studies were then combined with interface interaction studies between the matrix microstructure and ductilizing/toughening particulates and fibers. The second task was a basic study of interface structure and chemistry as it relates to the mechanical properties of the interface.

The third task involved studies on aluminum and copper matrix composites. These studies were concerned with the understanding of creep resistance. The aluminum matrix composites were prepared by a new process developed in this contract for direct infiltration of fibers and particulates by liquid aluminum alloys. Uniform fiber/particulate distributions were obtained and related to interface interactions and mechanical properties. The latter involved consideration of the separate and the coupled effects of dispersoids and reinforcements on creep and flow strength.

1. Phase Equilibria and Solidification Pathways in Intermetallics

A major portion of the 1100°C isothermal section of the Ti-Al-Ta phase diagram has been determined based on experimental work on annealed bulk alloys and diffusion couples. Significant inconsistencies were found with previously reported diagrams for the same system. It was established that the η phase field, which terminates at the line compounds $TaAl_3$ and $TiAl_3$ on the binaries, exhibits hyperstoichiometric solubility of Ta and Ti in the ternary system, in agreement with similar findings on the Ti-Al-Nb system. It was also found that the σ and γ phases exhibit substantial ternary solubility. Furthermore, a ternary phase with composition near Ti_2TaAl was reported, but its phase boundaries and relationship with the other fields in the ternary system remains to be clarified.

Diffusion couple studies performed in the course of evaluating the phase diagram were also useful in determining the interdiffusion coefficients of Ta and Al in the β phase. This information has been used for the studies on phase stabilities and interface interactions with reinforcing phases within other DARPA sponsored programs.

Ti-Al-Ta alloys were also subjected to rapid solidification processing using an electromagnetic-levitation/splat-cooling technique. Rapid solidification of Ti-36Al-38Ta, Ti-34Al-39Ta and Ti-44Al-4Cr-29Ta melts resulted in the formation of a metastable ordered B2 phase, which converted to the stable σ and γ phases upon annealing at high temperature. On the other hand, no metastable phase was formed in a Ti-46Al-29Ta alloy.

Work on Nb-Al-Si alloys was motivated by a recent finding that under appropriated processing conditions certain alloys in this ternary system form adherent protective oxides at high temperatures enhancing oxidation resistance. Furthermore, the solidification microstructures affect this oxidation behavior profoundly, especially since low diffusion rates inhibit homogenization of the as-cast structures at temperatures and times of practical utility. A comprehensive program was thus carried out to first evaluate the equilibrium phase diagram of the system and compare same with experimental data in this program. Second, a ternary alloy solidification model was combined with the phase diagram information to predict the solidification "path" of a number of alloys in the Nb_5 (Si, Al)$_3$ composition range. In a corollary experimental study, arc-buttons of the alloys were cast and the as-solidified structures characterized by analytical electron microscopy and high temperature X-ray diffractometry. Microsegregation profiles, volume fraction and distribution of the various phases were determined and compared to the calculations. Good agreement was obtained between theory and experiment.

In a related study the niobium-based alloys Nb-7.2Al-59.7Si, Nb-35Al-27Ti and Nb-20Ti-21.3Si were supercooled and splat quenched using the levitation-splat cooling technique. The Nb-35Al-27Ti alloy formed an ordered B2 phase upon rapid solidification, while the formation of the brittle $(NbTi)_5 Si_3$ phase was suppressed upon supercooling of the Nb-20Ti-21.3Si alloy.

2. Matrix Toughening

Process zone and bridging zone mechanisms of matrix toughening have been studied. In particular, short crack effects that arise with process zone toughening have been calculated. These calculations reveal that interaction effects occur between process zones at the two crack tips leading to a reduction in the magnitude of the fracture resistance. The results also indicate that the strength does not scale simply with the toughness. These solutions thus have important implications for the combined optimization of strength and toughness.

A related investigation of ceramics toughened with whiskers has established both the prevalent contributions to toughness, as well as the realistic toughening potential. The two principal toughening contributions derive from the extra surface energy associated with debonding along the amorphous phase at the interface and energy dissipated as acoustic waves when the whiskers fail in the crack wake. These contributions can lead to toughness of order $K_c \approx 10\ \mathrm{MPa}\sqrt{\mathrm{m}}$. Much larger toughness values could be induced by encouraging frictional dissipation by sliding and pull-out along debonded interfaces.

3. Creep Strengthening

The effects on flow and creep of high aspect ration reinforcements have been explored by conducting experiments on an Al/Mg alloy reinforced with chopped Al_2O_3 fibers (20% by volume). These experiments have been coupled with plane strain calculations of steady-state flow using incremental plasticity. The reinforcements have been shown to lead to an anisotropy of flow strength between tension and compression, caused by damage in the form of multiple cracks in the fibers. The strengthening in compression (no damage) is substantial and apparently consistent with that predicted by plasticity calculations. The important role of high aspect ratio is thus confirmed. This material also has good toughness and ductility (~6%) because of the high ductility of the matrix alloy, but fracture models have yet to be produced.

A related study concerns processing routes for oxide-dispersion strengthened copper alloys. The oxides of Y, Zr and the rare earths offer alternatives to the conventional γ-Al_2O_3 dispersoids used in ODS copper. These oxides have flourite-related structures and exhibit interfacial characteristics that should lead to an improved ability to pin dislocations. However, these dispersions cannot be produced by conventional internal oxidation, since the alloying elements are not soluble in Cu matrix, but instead precipitate as intermetallic compounds. On the other hand, the intermetallics are much less stable than the corresponding oxides and readily react with the inward-diffusing oxygen releasing Cu and precipitating the oxide. The extent of the reaction and the fineness of the oxide dispersion depends on the intial scale and distribution of the intermetallic, which can be optimized by rapid solidification processing. To explore this opportunity, powders of a Cu-2wt%Y alloy were produced by ultrasonic gas atomization at the National Institute for Standards and Technology, giving segregate spacings on the order of 1 to 2μm. Y_2O_3 dispersoids on the order of 20nm and ~3 percent in volume fraction were subsequently produced by internal oxidation.

MATERIALS

THE PROCESSING AND MECHANICAL BEHAVIOR OF AN ALUMINUM MATRIX COMPOSITE REINFORCED WITH SHORT FIBERS

by

Y. L. Klipfel, M. Y. He,
R. M. McMeeking, A. G. Evans and R. Mehrabian
Materials Department
College of Engineering
University of California
Santa Barbara, California 93106

KJM-Evans-3•Tech Art•F-G•TA-Flw Frc Al 12/12/88•10:54 AM•7/6/89

ABSTRACT

An aluminum alloy composite reinforced with chopped Al_2O_3 fibers randomly oriented in a plane has been produced by a modified squeeze casting process and its mechanical behavior compared with the corresponding behavior of the matrix. The specific characteristics of the compositing process have been examined vis-a-vis the characteristics of liquid metal infiltration into the capillaries of the fiber bundle. The flow stresses in the as-cast composite have been correlated with predictions based on continuum plasticity. Fracture of the fibers has also been characterized and interpreted using a weakest link statistical model, in conjunction with trends in the stress in the fibers. Changes in the composite flow stress caused by such fractures have been addressed. Finally, residual stress effects have been analyzed.

1. INTRODUCTION

Potential applications for metal matrix composites range from reciprocal and turbine engines to aerospace and space structures. Yet, significant commercial applications have not been realized due to the high cost of these materials and lack of predictable data-base for the practicing design enginee.. Resurgence of interest in this field has evolved from a number of recent developments. First, a new approach for the design of composites based on micromechanics is emerging, and second, the availability of lower cost reinforcements coupled with simple processing techniques (e.g. squeeze casting) permit production of tailored microstructures based on these design principles. In this paper we review and elucidate current understanding of large scale discontinuous reinforcements on the mechanical behavior of a ductile metal matrix. The predictions are then compared with experimental findings on Al-4%Mg alloy matrix composite reinforced with duPont's FP α-Al_2O_3 discontinuous fibers randomly oriented in a plane. The compositing is done by a modified squeeze casting process that permits three dimensional liquid metal infiltration without significant disturbance of the loosely packed fiber preform.

The mechanical behavior of metal matrix composites involves considerations at two distinct size scales of the reinforcing phase. At one scale, small dispersoids interact with individual dislocations and cause Orowan hardening. Such dispersoids induce strengthening when present as a few volume percent and with spacings of order 10–100nm, in accordance with a uniaxial flow stress,[1]

$$\Sigma \approx A\mu b/\ell + \sigma_s \tag{1}$$

where μ is the shear modulus, b is the Burger's vector, ℓ is the average separation between dispersoids on the slip plane, A is an obstacle strength parameter, usually taken to be ≈ 2 and σ_s is the contribution from other dislocations mechanisms. Dispersoid strengthening can be substantial. Also, appreciable ductility is retained. However, the elastic stiffness is essentially unaffected because the volume fraction of particles, f, is typically small.

At a larger scale, discontinuous elastic reinforcements perturb the flow of the matrix and cause hardening in accordance with continuum plasticity considerations. Significant strengthening occurs, accompanied by a related increase in elastic modulus, when the reinforcements are incorporated in substantial volume fractions. The *fully plastic* uniaxial composite flow stress, Σ, at a macroscopic plastic strain ε_p has the form$^{2-5}$

$$\Sigma = B(f, S, N)\ \sigma_s\left(\varepsilon_p\right) \tag{2}$$

where σ_s is the uniaxial flow stress of the matrix at plastic strain ε_p, and N is the hardening exponent in the flow law,

$$\sigma_s = \sigma_o\left(\varepsilon_p/\varepsilon_o\right)^N \tag{3}$$

with σ_o being the uniaxial yield strength, ε_o the yield strain, N the work hardening exponent; f is the volume fraction of the reinforcement: B is a non-dimensional function that depends strongly on reinforcement shape S, as well as on f and N. The composite flow stress for proportional loading is thus elevated upon the matrix level by a *fixed ratio* when fully plastic conditions exist in the matrix, such that the extra strength of the composite is governed exclusively by that fraction of the load capable of being supported by the reinforcements.*

Trends in B have previously been computed for spherical reinforcements[2] and aligned discontinous rods and plates[4], and in a companion study[5] have been estimated for randomly-oriented plates. Experience with the application of continuum plasticity solutions indicates that Eqn. (2) should describe reinforcement behavior when the reinforcement diameter exceeds the dislocation cell size[6]: that is, when the reinforcements are large. Large reinforcements typically have a detrimental influence on ductility/toughness because they either debond from the matrix or crack at moderate plastic strains, resulting in holes that grow plastically to cause rupture.

An intermediate behavior has also been postulated in which the highly local gradients in *strain* that develop around the reinforcements cannot be relieved by dislocation generation. The associated local deficit of dislocations results in a hardening that exceeds the above plasticity predictions.[6-9] In this region, linear and/or parabolic hardening behavior has been suggested as plausible. For example, the predicted linear hardening relation has the form[7]

$$\Sigma = \sigma_s + c f \mu \varepsilon_p \tag{4}$$

where c is a coefficient that depends on reinforcement shape.

Microstructural characteristics that govern the relative applicability of the above approaches to metal matrix composites have yet to be rigorously specified. The present study is one of several having the express intent of critically examining this issue for Al alloys containing micrometer-sized reinforcements. Consequently, the material system chosen to conduct this study is an Al-4% Mg solid solution matrix reinforced with chopped polycrystalline Al_2O_3 fibers randomly oriented in a plane. This system was selected for a variety of reasons. Firstly, precipitation hardening in the matrix can be avoided. Such hardening can be problematic because the hardening characteristics in the matrix of the composites typically differ from those in matrix-only material[10], resulting in an ill-defined matrix reference stress. Secondly, interface debonding during deformation is minimized by selecting a system, Al/Al_2O_3, that resists debonding even at large plastic strains[11], thereby reducing unpredictable effects of debonding on the flow behavior of the composite. Finally, the use of high aspect ratio chopped fibers, randomly oriented in a plane, provides a rigorous test of the hardening calculations.

---

* At small plastic strains, a transient elastic/plastic response occurs in which Σ is smaller than predicted by Eqn. (2).

It has been broadly appreciated that residual stresses exist in metal matrix composites and that this stress may superpose on the applied stresses, causing tension and compression asymmetry[12]. Both tensile and compressive testing are thus used, and residual stresses are analyzed.

2. COMPOSITE PROCESSING BY INFILTRATION

Liquid metal processing of metal matrix composites containing large-scale discontinuous reinforcements can be divided into two general categories; those in which particles, whiskers and fibers are introduced into a melt or partially-solid slurry, and processes wherein a liquid metal infiltrates particulate assemblies, fiber bundles and/or sintered preforms. There are a number of variations in the latter category, vis-a-vis the use and magnitude of pressurization. The "wetting" characteristic of the ceramic by the liquid alloy is an important parameter since it effects infiltration by capillary action and/or externally applied pressure. The variables influencing "wettability" include surface and interfacial energies, which are in turn influenced by alloy composition, ceramic material, surface treatments, surface geometry, interfacial interactions, atmosphere, temperature and time.

The minimum pressure, ΔP, for metal entry, initiation of infiltration, into the capillaries of a porous fiber preform is given by:

$$\Delta P = -2\gamma_{LV}/r \cos\theta \qquad [5]$$

where γ_{LV} is the liquid-alloy/ceramic preform interfacial energy, θ is the contact angle, and r is an average minimum radius of the capillary - which depends on the preform geometry. For a two-dimensional square fiber array (used to simulate random planar orientation of discontinuous Al_2O_3 fibers) and unidirectional metal flow normal to the plane of the fibers:

$$r = R\ [(\pi/2f)^{1/2} - 1] \qquad [6]$$

where R is fiber radius. The surface energy of pure liquid aluminum as a function of temperature is given by the following relationship[13]:

$$\gamma_{LV} = [0.914 - (T - 933) \times 3.5 \times 10^{-4}]\ \mathrm{Jm}^{-2} \qquad [7]$$

Where T is the temperature in degrees K. At a processing temperature of 1100K, $\gamma_{LV} \simeq 0.85\ \mathrm{J/m^2}$. Sessile drop experiments for aluminum on Al_2O_3 indicate a contact angle θ of about 140° at 1100K[14]. Thus, the calculated pressures to overcome capillary forces at the initiation of infiltration (unidirectional flow) are ~72 and ~100kPa for 10μm radius Al_2O_3 fibers arranged in a two dimensional array when $f = 0.2$ and 0.3, respectively. However, γ_{LV} decreases with the addition of solutes (e.g.

Mg) to the melt. Furthermore, θ values as low as 83 to 93 degrees have been reported for Al-3%Mg on Al_2O_3 , at 1073K[15]. However, these are for contact angles under vacuum or very low partial pressures of oxygen.

Analagous results derived for uni - and multi-directional infiltration of square and hexagonal arrays of parallel fibers[16], suggest that the pressures needed to overcome capillary forces, and initiate unidirectional infiltration, are 153 and 135 kPa for square and hexagonal arrays, respectively, when $f = 0.2$. Lowest pressures of infiltration were predicted for these geometries when flow was three dimensional[16]. Spontaneous infiltration is predicted for contact angles less than 90 degrees.

The pressure drop necessary to overcome viscous flow resistance in the preform can be similarly calculated using the Blake-Kozeny relation[17]. Calculations[18] and measurements[19] for laboratory sized specimens show that these pressures are of the same order as those necessary for infiltration initiation. Infiltration times are proportional to the applied external pressure while the pressure itself is inversly proporational to the square of the dimensions of the interstices in the preform. A further complication arises when the preform is below the melting temperature of the alloy, whereupon concurrent solidification in the interstices has to be taken into account.

3. SOME BASIC MECHANICS

3.1. FLOW STRESS

From continuum plasticity considerations the flow stress of a composite containing discontinuous reinforcements when the matrix is fully plastic is a direct multiple B of the matrix flow stress, Eqn. (2), such that B depends on volume fraction, shape, spatial arrangement and hardening coefficient, but is *independent of reinforcement size.* There are relatively few computations of B, but available solutions indicate general trends. In particular, B is known to be sensitive to aspect ratio[4,5]. It is also known that the effects of reinforcements on flow stress become larger as N increases[2,5]. Specific results have been obtained using two approaches: the self-consistent method[2,5] and finite elements[4]. The self-consistent method takes only approximate account of interaction effects between reinforcements, but has the advantage that averaging over a range of orientations and aspect ratios is relatively straightforward. Currently practical finite element calculations make use of periodic boundary conditions and are limited to reinforcements having regular spatial arrangements. An advantage is that interactions between reinforcements are rigorously incorporated (subject to the periodic nature of the arrangement).

The available solutions for equiaxed reinforcements indicate relatively small effects on the flow stress, even when the volume fraction f and N are large.[2,4] However, plates and rods have much larger effects[4,5] because of the plastic constraint induced around the reinforcements (Fig. 1). General trends with aspect ratio, volume fraction and orientation are summarized in Fig. 2. The flow stress is also strongly influenced by the spatial arrangement[4]. In general, therefore, a material will have hard and soft regions governed by the spatial distribution. The overall flow behavior of the composite will be some average between these regions.

Of particular interest for present purposes are the trends with aspect ratio for reinforcements randomly oriented within a plane (Fig. 3). It is apparent that the trend is non-linear such that very large increases in flow stress can exist at high aspect ratio. The enhanced strength of the composite over that of the matrix reflects large stresses that develop in the fiber, leading to the incidence of fiber cracking[*]. Such cracking diminishes the flow stress below that given by Fig. 3, because of the corresponding reduction in effective aspect ratio. It is of particular interest to examine trends in fiber cracking with fiber orientation. For this purpose, it is noted that the self-consistent method used to evaluate orientation effects on composite flow behavior does not give a direct solution for the stresses, σ_I, that develop in the fiber. However, approximate trends can be deduced from the orientation dependence of σ_I, calculated for an elastic matrix (Fig. 4).[5,20] This result suggests that

---

[*] Note that plain strain calculations are for plate reinforcements while experiments were carried out on preforms composed of planar random array of discontinuous fibers.

$$\sigma_I \approx \sigma_{max}\left[\cos^2\beta - (1/4)\sin^2\beta\right] \tag{8}$$

where σ_{max} is the maximum stress in the fiber at $\beta = 0$ (see Fig. 4).

3.2. RESIDUAL STRESSES

Previous analyses of residual stresses in metal matrix composites reinforced with chopped fibers/whiskers have been strictly elastic and based on the Eshelby method[12,20]. On the other hand, matrix yielding will reduce the residual stresses in the reinforcements below those expected for an elastic matrix. Important insight regarding the magnitude of the residual stresses upon matrix yielding can be gained by calculating bounds, represented by spheres and aligned fibers, for a non-hardening matrix. The residual stresses within elastic inclusions in an elastic/plastic matrix are readily derived by matching the elastic/plastic solutions for holes subject to internal pressure[21] with elastic solutions for inclusions under external pressure.

For the case of *spherical inclusions* (Fig. 5), stresses in the inclusion are uniform and related to the displacement of the outer surface of the inclusion, u_r^I, by;

$$u_r^I = -\frac{(1-2\nu_I)pR}{E_I} \tag{9}$$

where R is the inclusion radius, p* is the pressure in the inclusion, E_I and ν_I are elastic modulus and Poisson's ratio of the inclusion, respectively. In the matrix, the radial displacement of the inner surface and stresses are coupled through the plastic zone radius, C (Fig. 5), such that[21]

$$u_r^m = \frac{\sigma_o R}{E_m}\left[(1-\nu_m)\frac{C^3}{R^3} - \frac{2}{3}(1-2\nu_m)\left(1-\frac{C^3}{R^3}f\right) - 2(1-2\nu_m)\ell n\frac{C}{R}\right] \tag{10}$$

where E_m and ν_m are the elastic modulus and Poisson's ratio of the matrix, f, is the volume fraction of inclusions and σ_o is the uniaxial yield strength. Furthermore, C is related to p and σ_o by[21]

$$p/\sigma_o = 2\ell n\frac{C}{R} + \frac{2}{3}\left(1 - \frac{C^3}{R^3}f\right) \tag{11}$$

Imposing continuity of radial displacement at the interface gives,

$$u_r^m - u_r^I = \Delta\alpha\Delta TR \tag{12}$$

where $\Delta\alpha$ is the mismatch in thermal expansion coefficient and ΔT is the cooling range, e.g. from the processing temperature. Consequently, for systems in which yielding occurs progressively upon cooling, Eqns. (9), (10) and (11) yield the non-dimensional relation

---

* p is compressive stress and negative

$$p / \sigma_o = g_s\left(E_m \Delta T \Delta\alpha / \sigma_o, f\right) = g_s(\Delta\alpha\Delta T / \varepsilon_o, f) \tag{13}$$

where g_s is the function plotted in Fig. 6a. Clearly, p/σ_o reaches a maximum when the plastic zones that emanate from neighboring inclusions overlap: this occurs when the ratio of the thermal strain to the yield strain, $\Delta\alpha\Delta T/\varepsilon_o$, is in the range 2–4. The *maximum* value for p/σ_o is given by

$$\left(\frac{p}{\sigma_o}\right)_{max} = -\frac{2}{3}\ell n\, f \tag{14}$$

The corresponding plane strain solution for the case of a *continuous aligned cylindrical fiber* has also been solved. The displacement of the outer surface of the fiber and the stress are related by[22]

$$u_r^I = -\frac{(1-2\nu_I)(1+\nu_I)pR}{E_I} \tag{15}$$

For the matrix, numerical results by Hill and his collaborators[22] can be expressed as,

$$u_r^m = h\left(\frac{p}{\sigma_o}, \frac{C}{R}\right) \tag{16}$$

and

$$p / \sigma_o = \ell n \frac{C}{R} + \frac{1}{2}\left(1 - \frac{C^2}{R^2} f\right) \tag{17}$$

where h is a function. Consequently, by again imposing continuity of radial displacement at the interface, (Eqn. 12), the following non-dimensional relation ensues,

$$p/\sigma_o = g_c(\Delta T \Delta\alpha/\varepsilon_o, f) \tag{18}$$

where g_c is the function plotted in Fig. 6b. Again, p/σ_o reaches a maximum value given by

$$(p/\sigma_o)_{max} = -\frac{1}{2}\ell n\, f \tag{19}$$

Comparison with Eqn. (14) indicates a relatively small difference between spheres and aligned fibers, suggesting that the above results should also have good applicability to short fibers.

Having knowledge of the compressive stress p in the inclusions, it is now possible to estimate the effects of the residual stress on initial plastic flow. The corresponding *tensile* normal stress in the matrix has an average value

$$\left\langle \sigma_m^R \right\rangle = -fp/(1-f) \tag{20a}$$

A simple upper bound estimate of the effect of this stress on initial flow stress of the composite involves the superposition of $\left\langle \sigma_m^R \right\rangle$ onto the matrix flow stress. The initial *tensile* flow stress of the composite is thus

$$\Sigma_R = \left[\sigma_m - \left\langle \sigma_m^R \right\rangle\right](1-\mathrm{f}) + \mathrm{f}\sigma_\mathrm{f}$$

$$= \sigma_m(1-\mathrm{f}) + \mathrm{f}\sigma_\mathrm{f} + \mathrm{f\,p}$$

$$\equiv \Sigma + \mathrm{f\,p} \qquad (20b)$$

where σ_f is the stress in the fiber in the absence of residual stress.
The corresponding initial compressive flow stress is

$$\Sigma_\mathrm{R} \approx \Sigma - \mathrm{f\,p} \qquad (20c)$$

The upper bound asymmetry in initial flow stress between compression and tension, $\Delta\Sigma_\mathrm{R}$, is thus

$$\Delta\Sigma_\mathrm{R} \approx 2\mathrm{f\,p} \qquad (20d)$$

The effects of plastic strain on p are presently unknown, but it is expected that $\Delta\Sigma_\mathrm{R}$ will diminish with increase in plastic strains and approach zero at strains of order $3\Delta\alpha\Delta T$.

3.3. FIBER CRACKING

The incidence and preponderance of fiber cracking are governed by the net *axial stress on the fiber prior to cracking,* σ_I, and by the weakest link statistics of fiber fracture, as represented by;[23]

$$\Phi = 1 - \exp\left[-\frac{1}{\ell_o S_o^m}\int \sigma_z^m(z)\,dz\right] \qquad . \tag{21}$$

where Φ is the fiber failure probability, ℓ_o is a reference length (lm), S_o is the scale parameter, m is the shape parameter and σ_z is the local axial stress in the fiber. The fiber cracking phenomenon having greatest interest in the composite is *multiple cracking*, which degrades the flow stress and contributes to ductile rupture. To address this behavior, the problem of cracking between two previously formed cracks is analyzed (Fig. 7).

Cracks in the fiber modify the local axial stress distribution over a slip length, ℓ. These stresses are estimated using a shear lag procedure with the shear stress at the interface governed by the shear yield strength of the matrix, $\tau = \sigma_o/\sqrt{3}$. Then, within the slip length $z < \ell$,

$$\sigma_z/\sigma_o \approx \left(2/\sqrt{3}\right)(z/R) \tag{22}$$

Furthermore, by equating σ_z to σ_I, and z to ℓ, the slip length is given by;

$$\ell/R \approx \left(\sqrt{3}/2\right)(\sigma_I/\sigma_o) \tag{23}$$

The statistical problem is solved by applying Eqn. (22) to Eqn. (21) in the range $-\ell < z < \ell$ and imposing a constant stress σ_I elsewhere, such that

$$-\ell n(1-\Phi)=\frac{\sigma_I^m(d-2\ell)}{S_o^m\ell_o}+\frac{2^{m+1}\sigma_o{}^m}{3^{m/2}\ell_o S_o^m R^m}\int_o^{\ell} z^m dz$$

$$=\frac{\sigma_I^m(d-2\ell)}{S_o^m\ell_o}+\frac{2^{m+1}\ell^{m+1}\sigma_o{}^m}{(m+1)\,3^{m/2}\ell_o S_o^m R^m} \tag{24}$$

where d is the crack spacing. Then, inserting ℓ from Eqn. (23), gives:

$$-\ell n\,(1-\Phi)=(\sigma_I/S_o)^m\left[d/\ell_o-\sqrt{3}m(\sigma_I/\sigma_o)(R/\ell_o)/(m+1)\right] \tag{25}$$

Rearranging to give the crack spacing yields

$$d/R=\left[-\ell n(1-\Phi)\right](S_o/\sigma_I)^m(\ell_o/R)+\sqrt{3}m(\sigma_I/\sigma_o)/(m+1) \tag{26}$$

Additional progress requires recognition that, for the present model, there is no further increase in the stress on the fibers when d → 2ℓ and *the crack spacing saturates.* The saturation spacing, d_{ss}, is estimated by equating d to 2ℓ in Eqn. (26), using Eqn. (23) to eliminate σ_I and then setting d to d_{ss}. This procedure gives;

$$d_{ss}/R=\left\{(m+1)\left[-\ell n\,(1-\Phi)\right](\ell_o/R)\left(\sqrt{3}S_o/\sigma_o\right)^m\right\}^{1/(m+1)} \tag{27}$$

The distribution in d_{ss} arises because of the random sequence of cracking events. Combining Eqns. (26)and (27) gives;

$$\frac{d}{R} = \frac{\sqrt{3}m}{m+1}\left(\frac{\sigma_I}{\sigma_o}\right) + \left(\frac{d_{ss}}{R}\right)^{m+1}\left(\frac{\sigma_o}{\sigma_I}\right)^m \frac{1}{(m+1)3^{m/2}} \tag{28}$$

This result is valid in the range $d \geq 2\ell$, i.e., $d/R \geq \sqrt{3}\sigma_I/\sigma_o$ (Eqn. 23). Within this range, the trend in d/R with σ_I/σ_o predicted by Eqn. (28) is plotted on Fig. 8 for several choices of d_{ss}/R, using a typical value of m applicable to fibers (m = 3). To interpret Fig. 8, it is necessary to appreciate that d_{ss}/R is governed primarily by the fiber strength S_o and the matrix yield strength, as expressed by Eqn. (27). It is then apparent from Fig. 8 that d approaches d_{ss} over a relatively narrow range of stress, such that the second term in Eqn. (28) dominates. It is also important to note that the stress σ_I depends strongly on the aspect ratio and on the orientation of the fiber (Eqn. 8); notably,

$$d/R \approx (d_{ss}/R)^{m+1}\left[\frac{1}{(m+1)\,3^{m/2}}\right](\sigma_o/\sigma_{max})^m\left[\cos^2\beta - (1/4)\sin^2\beta\right]^{-m} \tag{29}$$

This solution can be used to correlate experimental trends and gain insight about the properties of the fibers in the composites.

4. EXPERIMENTAL PROCEDURE

Composite processing by pressure infiltration was conducted using a modified squeeze casting technique to permit three dimensional melt infiltration of the preform. The usual melt infiltration processes, utilizing a ram or gas pressure, employ one-dimensional melt flow into a preform. As previously noted, an external pressure of ~70 to 150 kPa is needed to initiate infiltration. Furthermore, additional pressure of the same order is required to overcome the viscous flow resistance within the preform. Consequently, loosely packed fibers experience compression with attendent fiber damage, as well as excessive fiber to fiber contact in some regions and matrix only areas in others. In order to minimize these effects in the present study the preform was surrounded with a relatively rigid porous ceramic filter, (Fig. 9), which serves three functions. Firstly, it enables the melt to enter the preform from its sides as well as the top, reducing the pressure for infiltration initiation[16], and allowing preform deformation to be relatively uniform. Secondly, since the die is not evacuated entrapped air is located in the lower filter. Finally, the ceramic filter removes oxides entrained in the melt.

The Al-4wt%Mg alloy was prepared by conventional melting practice, including degasing, using 99.98% purity Al and Mg. Melting was done with an induction power supply. The alloy was superheated ~125K above its liquidus temperature prior to introduction above the filter/preform assemby in the lower die (Fig.9).

The preforms consisted of duPont's FP α-Al_2O_3 discontinuous fibers randomly oriented in a plane (Fig. 10). The as-received preforms contained some organic binder with a very small fraction of SiO_2. The porous ceramic filter containing the preform was preheated to ~1023K in a resistance furnace, to burn-off the organic portion of the binder, prior to introduction in the lower die half. The dies were also preheated to ~573K.

The ram speed in the hydraulic press is controlled between 5 and 12 mm/sec through a hydraulic bypass especially designed for this purpose. The press is capable of generating ~100 MPa pressure, which was maintained on the composite until complete solidification of the alloy.

5. MECHANICAL TESTING

5.1. PROCEDURES

Tension and compression tests were conducted in a hydraulic machine using standard specimen configurations*. Specimens were prepared by water jet cutting from the original casting and then polishing to eliminate surface damage. Composite and matrix-only specimens were obtained from the same casting by confining the fiber preform to the central portion of the die to permit solidification of matrix-only regions adjacent to the composite. This was done to minimize the effect on properties of variations in the matrix composition between composite and matrix castings. Axial displacements were monitored on the gauge length by attaching an extensometer. Alignment in the case of tension tests was achieved by using hydraulic grips. For compression tests, alignment was provided by a hemispherical loading platen.

5.2. RESULTS

The basic engineering stress/strain curves obtained on the matrix material and the composites are shown on Fig. 11a. As expected, the composite exhibits the greater flow strength and a reduced ductility in tension. The anticipated differences between tension and compression are also in evidence. For purposes of comparison with models, the true stress and the plastic strain are obtained from the data and plotted on Fig. 11b. A comparison of the flow characteristics of the matrix, with and without reinforcements, is made by microhardness measurements. Load levels are used that allow the impression to be fully contained within interstices between the fiber reinforcements. Such measurements confirm that the matrix exhibits a consistent hardness.

---

* ASTM standard B557M

6. CHARACTERIZATION

The characteristics of the Al_2O_3 reinforcements, fiber orientation and microstructural homogeneity, have been investigated by deep etching, ~100μm of the matrix, electro-etching with 20% perchloric acid in methanol, to expose the fibers (Fig. 12). These microstructures verify the orientation of the fibers in the composite and absence of fiber damage from the infiltration process. The majority of fibers are oriented within a plane (> 90 % within ± 5°) and orientations within that plane are essentially random. There is also evidence of remanent binder (SiO_2) on some of the fibers. Specimens removed from different locations of the composite were analyzed for volume fraction of fibers, giving $f = 0.19$ with no detectible spatial variation.

Complete dissolution of the matrix in a solution of 30% hydrochloric acid in water permited extraction of the fibers for aspect ratio determination. A distribution of aspect ratios ascertained by optical microscopy with computer assisted imaging of the extracted fibers is summarized in Fig. 13. Some of the larger fibers tend to crack during this process and this biases the distribution to lower levels than actual.

The damage processes that occur in the material upon mechanical testing have also been characterized by using scanning electron microscopy (SEM). For this purpose, cross sections of the gauge length have been prepared by polishing. Some typical features are depicted in Fig. 14. The most prominent characteristics are the fiber cracks that occur in materials subjected to tensile loading. Blunting of the fiber cracks at the matrix/Al_2O_3 interface is clearly noted, as well as crack correlation between neighboring fibers. The cracks are evident at orientations β with the load axis up to about $\pi/4$. The crack spacing diminishes as the plastic strain increases, but tends to saturate (Fig. 15). Some fiber cracks are also evident in specimens tested in compression, especially in those fibers having axis nearly normal to the stress axis. Also, some axially-oriented fibers exhibit buckling related failures. However, the fraction of failed fibers is relatively small.

After the specimens have been tested, the change in fiber aspect ratio induced by cracking has been ascertained by again completely dissolving the matrix. The modified aspect ratio distribution for the tensile specimens tested to rupture is plotted on Fig. 13.

Observation of fracture surfaces (Fig. 16) provide additional information. The matrix fails by necking to a ridge, confirming the high ductility of the cast Al-4%Mg alloy. Exceptions are noted in isolated areas (arrowed in Fig. 16) where zones of radial cracking are attributed to the presence of remanent SiO_2 binder which locally degrades the matrix ductility. A small fraction of the α-Al + Mg_2Al_3 eutectic (~0.023 is expected in the as-cast structure of the Al-4wt%Mg alloy calculated using Scheil's Eqn[25)] preferentially segregated to the matrix/fiber interface may also be responsible for the radial cracks. Some debonding between the fibers and the matrix is also detectable. Finally the fracture plane in Fig. 16 shows a much greater volume fraction of fibers than on the polished section (c.f. Fig. 14). The cracking process thus appears to preferentially follow the location of the fibers.

Elemental X-ray maps on polished cross-sections showed no sign of Mg enrichment. This lack of interaction is attributed to the limited time that the fibers are in contact with the melt for the present process. This feature is in contrast to that found upon incorporation of fibers into agitated partially-solid or completely-liquid aluminum alloys[14, 24].

7. COMPARISON BETWEEN EXPERIMENT AND THEORY

7.1. FLOW STRESS

The difference between the compressive and tensile flow stresses $\Delta\Sigma$, Fig. 17, is first addressed. There are two possible contributions to this difference: the residual stress and fiber cracking. An upper bound estimate of the contribution of residual stress $\Delta\Sigma_R$ may be obtained from Eqn. (20d). The relevant magnitude of p is assessed by noting that the ratio of the thermal mismatch strain to the matrix yield strain is ~6.6*, indicative of a fully plastic matrix (Fig. 6, f = 0.19). Furthermore, at the plastic strain level induced by thermal mismatch, (~ 10^{-2}), the matrix flow stress is ~ 90MPa. Consequently, by using Eqn. (13) to relate p to this flow stress, the flow stress differential becomes: $\Delta\Sigma_R \approx$ 45MPa (Fig. 17). This stress differential is expected to diminish with increase in plastic strain.

The differential in fiber cracking between tension and compression testing provides a second contribution to $\Delta\Sigma$. An estimate of this contribution, $\Delta\Sigma_C$, is obtained by using the self-consistent results for the composite flow stress (Fig. 3) in conjunction with fiber aspect ratio information (Fig. 13). Specifically, the initial fiber aspect ratio frequency distribution, ϕ (L/R) d (L/R), (Fig. 13) is used with the flow strength derived for reinforcements randomly oriented in a plane, Σ (L/R) (Fig. 3) to evaluate the flow strength without cracking,

$$\Sigma = \int_0^{\infty} \Sigma(L/R)\phi(L/R)d(L/R) \quad . \tag{30}$$

---

* The thermal expansion coefficients of Al_2O_3 and Al alloy are 7.5 x 10^{-6} and ~23 x 10^{-6} C^{-1}, respectively. ΔT ~ 698K, is the difference between the eutectic temperature of the alloy and room temperature, such that the mismatch is ~6.6.10^{-3}. The corresponding yield strain is ~1.10^{-3}.

The reduction in flow stress caused by cracking is evaluated using the same procedure but with ϕ (L/R) d (L/R) replaced by the modified frequency distribution after tensile testing ϕ_χ (L/R) d (L/R). This procedure gives the flow strength differential, $\Delta\Sigma_C \approx$ 40MPa. Superposing the two contributions to $\Delta\Sigma$ onto the experimental results (Fig. 16) indicates acceptable consistency. The compression/tension asymmetry is thus seemingly consistent with contributions from fiber cracking and from residual stresses. However, effects of plastic strain on both $\Delta\Sigma_R$ and $\Delta\Sigma_C$ require further investigation.

Based on the above considerations of the effect of residual stress and fiber cracking, it is recognized that a comparison of the measured flow stress levels with predicted values, may be most effectively achieved by beginning with the compression curve and subtracting the residual stress contribution $\Delta\Sigma_R$ as plotted on Fig. 18. This curve is compared with self-consistent predictions for randomly oriented plates at several median aspect ratios (all having that aspect ratio *distribution* given by experiment). It is apparent (Fig. 18) that the shapes of the measured and predicted curves are similar. However, the best agreement between theory and experiment obtains for a median fiber aspect ratio in excess of the measured value. This discrepancy reflects two effects. Fiber cracking during extraction causes the measured L/R to be less than actual and also, the calculations conducted for plates^5 are not rigorously applicable to fibers. It is also noted that predictions overestimate the composite strength at small plastic strains ($\varepsilon_p \lesssim 0.01$). This is the strain range dominated by transient plastic flow whereupon Eqn (3) does not apply. Other models that simulate transient effects maybe more appropriate in this range.

7.2. FIBER CRACKING

The degree of fiber cracking may be investigated by comparing the weakest link statistics predictions with the measured behavior (Fig. 15), by assuming that saturation conditions are satisfied at $\beta = 0$. Preliminary comparison can be achieved based on trends in crack spacing with orientation, as governed by the shape parameter, m (Eqn. 29). The measured angular dependence is consistent with m ≈ 1.5 (Fig. 15). Direct comparison of this result with strength data for Al_2O_3 fibers is problematic because such fibers typically exhibit a bimodal distribution with m being either 0.5 or 6[26]. Furthermore, those fibers that provide the present angular information are located at the surface of the composite and are likely to be subject to damage induced by cutting and polishing. Nevertheless, the value of m implied by the data lies within the quoted range. Another comparison between theory and experiment can be achieved based on d_{ss}/R, by using Eqn. (27). The comparison is quite sensitive to the choice of m. For present purposes, it is assumed that the internal fibers have the same flaw population as the pristine fibers and furthermore, that the "high" strength population ($m \simeq 6$) dominates. With this choice for m, and noting that $d_{ss}/R \approx 10$ (Fig. 13), Eqn. (27) predicts that $S_o/\sigma_o \sim 2$ for $\ell_o = 0.25$ m*. Consequently, since $\sigma_o \approx 100$MPa, S_o is predicted to be $\approx$ 200MPa, compared with a value of ~ 1GPa obtained on pristine fibers.[26] Independent research on Al-4%Mg alloy composites containing continuous Al_2O_3 fibers prepared using the same squeeze casting approach[27] has indicated that fiber degradation upon processing is minimal. The present discrepancy in S_o appears to reflect uncertainties in the fiber properties and the level of simplification used in the statistical analysis.

---

* A reference length of 0.25m has been used for convenience, as in previous studies.[26]

8. CONCLUDING REMARKS

The modified squeeze casting process, using a porous ceramic filter around fiber preforms, permits three-dimensional melt infiltration resulting in uniform microstructure composites free of observable fiber damage. Limited analysis reveals no detectable interfacial phase formation ($MgAl_2O_4$) due to the short solidification times. Analysis suggests that continuum plasticity predictions are basically consistent with the measured stress-strain curves for Al (Mg) reinforced with chopped α-Al_2O_3 fibers arranged in a random planar array. This result is at variance with recent results obtained for equiaxed reinforcements, which do not accord with continuum predictions and, instead reveal a strong effect of particle size on the flow stress through the particle spacing[28]. This paradox remains to be resolved.

To achieve the present comparison, several essential aspects of composite behavior had to be taken into account. In particular, since the flow curves are predicted to be sensitive to the aspect ratios and orientations of the reinforcements, these features of the composite have required careful characterization. Additionally, residual stress effects caused by thermal expansion mismatch between the matrix and reinforcement are significant. Finally, the incidence of fiber failure, which degrades the tensile flow stress, has required understanding.

A significant limitation of the present study is that the available calculations are restricted to plate reinforcements. Further application of continuum plasticity calculations to predict trends in the flow behavior of metal matrix composites clearly requires that solutions be obtained for rods having a spectrum of aspect ratios.

ACKNOWLEDGEMENTS

The authors are grateful to Dr. Francisco Folger of duPont for donation of the fibers used in this study. The support of the Defense Advanced Research Projects Agency (DARPA) through contract N00014-86-K-0178, supervised by Dr. Ben A. Wilcox and monitored by Dr. Steven G. Fishman of the Office of Naval Research is also gratefully acknowledged.

REFERENCES

[1] U. F. Kocks, A. S. Argon and M. F. Ashby, Progress in Material Science (Ed. Chalmers et al.), Pergamon, Oxford, Vol. 19 (1975) p. 40.

[2] J. M. Duva, Jnl. Engr. Mater. Tech 106 (1984) 317.

[3] A. Needleman, Jnl. Appl. Mech. 109 (1987) 525.

[4] T. Christman, A. Needleman and S. Suresh, to be published.

[5] M. Y. He, to be published.

[6] M. F. Ashby, private communication.

[7] L. M. Brown and D. R. Clarke, Acta Metall. 25 (1977) 562.

[8] L. M. Brown and W. M. Stobbs, Phil. Mag 23 (1971) 1201.

[9] K. Tanaka and T. Mori, Acta Metall 18 (1970) 931.

[10] T. Christman and S. Suresh, Acta Metall. 36 (1988) 1691.

[11] B. J. Dalgleish, K. P. Trumble and A. G. Evans, Acta Metall. 37 (1989) 1923.

[12] R. J. Arsenault and M. Taya, Acta Metall 35 (1987) 651.

[13] Smithells Metals Reference Book, 6th Edition, Edited by Eric A. Brandes, Butterworths, London, (1983).

[14] C.G. Levi, G.J. Abbaschian, and R. Mehrabian, Met. Trans. 9A (1978) 697.

[15] D.A. Weirauch, Jr., J. of Mater. Res. 3 (4) (1988) 729.

[16] S. Nourbakhsh, Fei-Lin Liang, and H. Margolin, to be published.

[17] D.H. Geiger and D.R. Poirier, Transport Phenomena in Metallurgy, Addison Wesley, Reading, Mass., (1973) 93.

[18] T.W. Clyne and J.F. Mason, Met. Trans. 18A (1987) 1519.

[19] J.A. Cornie, A. Mortensen and M.C. Flemings, Proceedings of the Sixth International Conference of Composite Materials, ICCM and ECCM, Editors, F.L. Mathews, N.C.R. Buskell, J.M. Hodgkinson and J. Morton, (1987) 2297.

[20] J.D. Eshelby, Proc. Roy. Soc. London A241 (1957) 376.

[21] R. Hill, The Mathematical Theory of Plasticity, Oxford (1960).

[22] R. Hill, E. H. Lee and S. J. Tupper, Proc. Roy. Soc. London 191 (1947) 278.

[23] M. D. Thouless and A. G. Evans, Acta Metall. 36 (1988) 517.

[24] A. Munitz, M. Metzger and R. Mehrabian, Met. Trans 13A (1982) 93.

[25] E. Scheil, Z. Metallk, 34 (1942) 70.

[26] J. Nunes, "Tensile Property Evaluation of Polycrystalline Al_2O_3 filaments and their composites:, AMMRC TR 82-6)

[27] Y.L. Klipfel, A.G. Evans and R. Mehrabian, to be published.

[28] S.V. Kamat, J. P. Hirth and R. Mehrabian, Met. Trans., to be published.

FIGURE CAPTIONS

Fig. 1. Plastic strain fields calculated around plate reinforcements[5]

Fig. 2. a) Trends in hardening with volume fraction for several aspect ratios for plates randomly oriented in a plane: $1/N = 5$: self-consistent calculation

b) Trends in hardening with volume fraction for aligned plates at different orientations β with respect to the applied stress ($1/N = 5$, aspect ratio $L/R = 10$). Also shown is the result for plates randomly oriented in a plane: self-consistent calculation

Fig. 3. Effect of aspect ratio on flow stress for randomly oriented plates: $1/N = 5$, $f = 0.19$, self-consistent calculation

Fig. 4. Effect of orientation and aspect ratio on the axial stress in the fibers, σ_I, compared with the applied stress Σ: elastic calculation[5,20]

Fig. 5. The plastic zone around a spherical inclusion subject to a mismatch strain

Fig. 6. Trends in the normalized stress p/σ_0 inside the inclusion with the relative mismatch strain for several volume fractions, f, and for $E_m/E_I = 0.19, \nu_m = 0.3, \nu_I = 0.2$.

a) Spherical inclusions

b) Aligned fibers

Fig. 7. Model used to analyze statistical aspects of fiber cracking

Fig. 8. Predicted trends in crack spacing with stress in the fiber for several choices of the saturation spacing d_{ss}/R and for a shape parameter $m = 3$

Fig. 9. Schematic illustration of preform and die arrangement for composite fabrication

Fig. 10. SEM top-view of the FP α-Al_2O_3 preform prior to infiltration

Fig. 11. Stress/strain curves obtained for the matrix and the composite in both tension and compression

a) Engineering stress/strain

b) True stress plotted as a function of true plastic strain

Fig. 12. Scanning electron micrographs showing fiber orientations revealed by deep etching the matrix

Fig. 13. Aspect ratios of fibers in the composite: before and after testing to failure

a) frequency distribution

b) cumulative distribution

Fig. 14. Micrographs showing fiber cracking caused by testing, as well as blunting of the fiber crack at the Al-4%Mg/Al_2O_3 interface

Fig. 15. Trends in crack spacing d/R with fiber orientation, β, measured after composite failure. Also shown is the predicted line for three values of the shape parameter, m.

Fig. 16. Fracture surface of Al-4%Mg/discontinuous α-Al_2O_3 fiber composite at two levels of magnification.

Fig. 17. Differential in tensile and compressive true flow stress obtained from Fig. 11. Also shown are the predictions for residual stress effects and fiber cracking, plotted as if they were strain independent

Fig. 18. The true composite flow stress obtained from the compressive stress (Fig. 11) with the residual stress contribution subtracted. Also shown are curves predicted using self-consistent calculations for several values of the median aspect ratio.

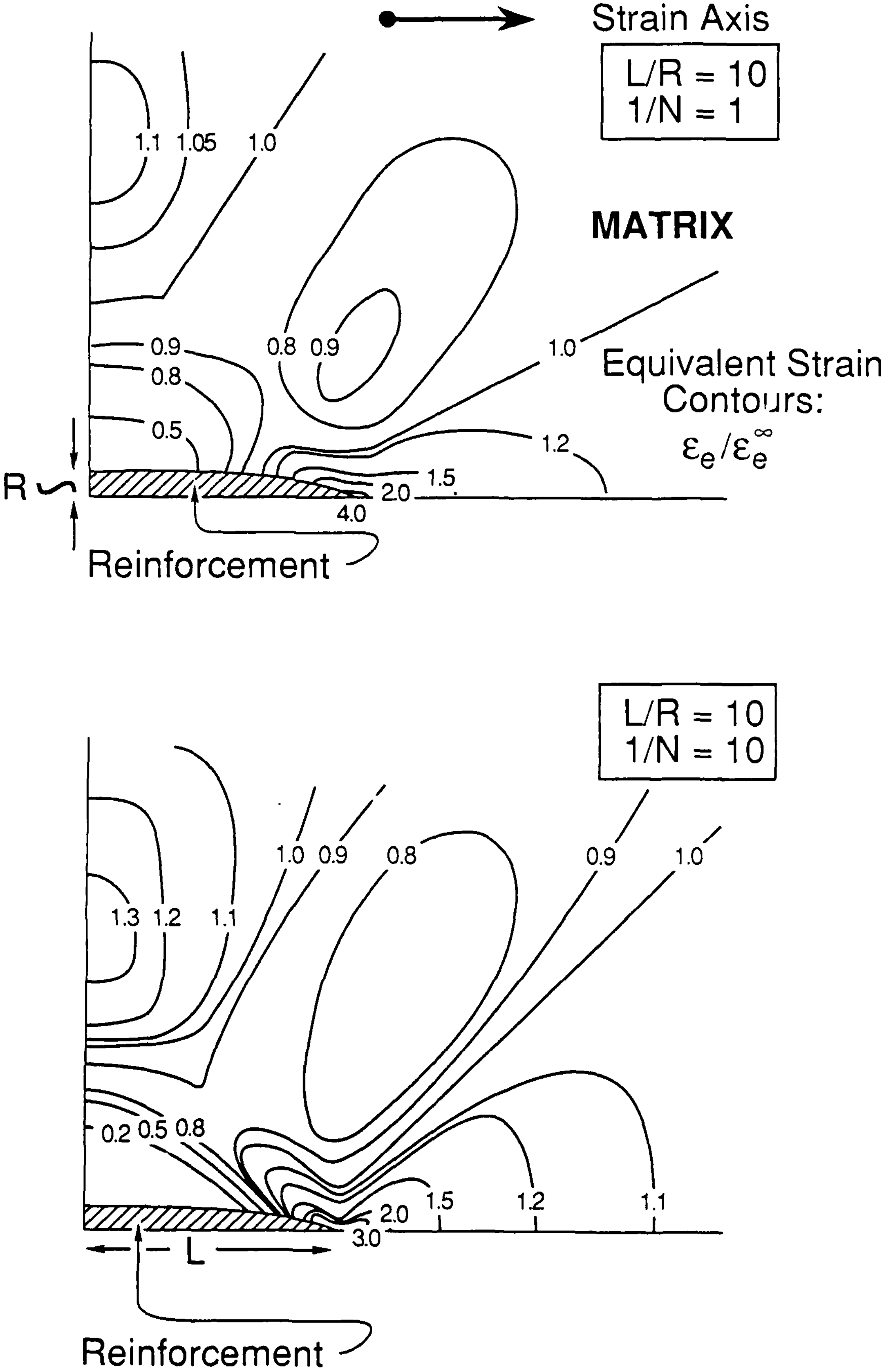

D23 A89-157'9.8

Figure 1

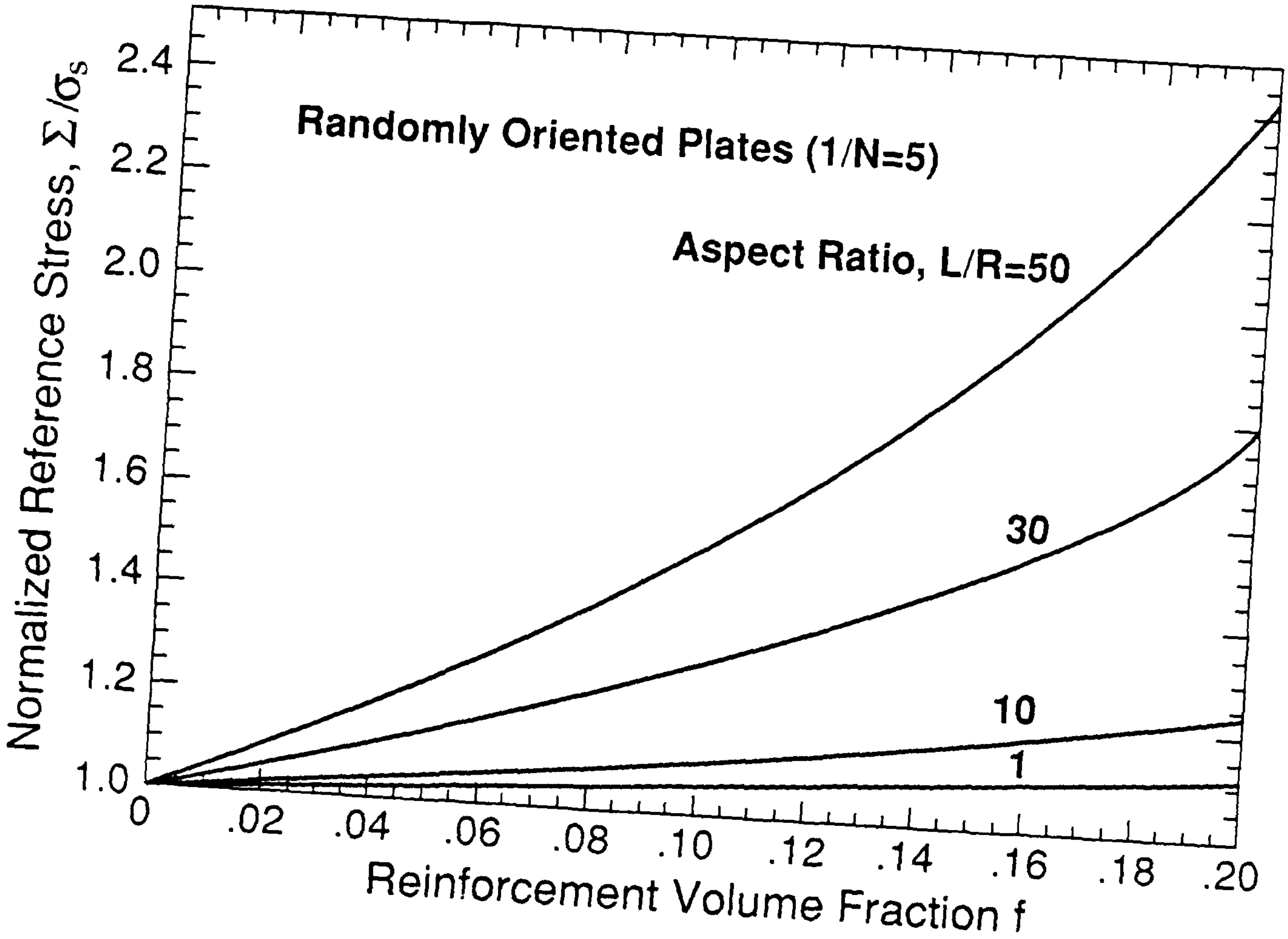

D23 A89-158a*9/15

Figure 2

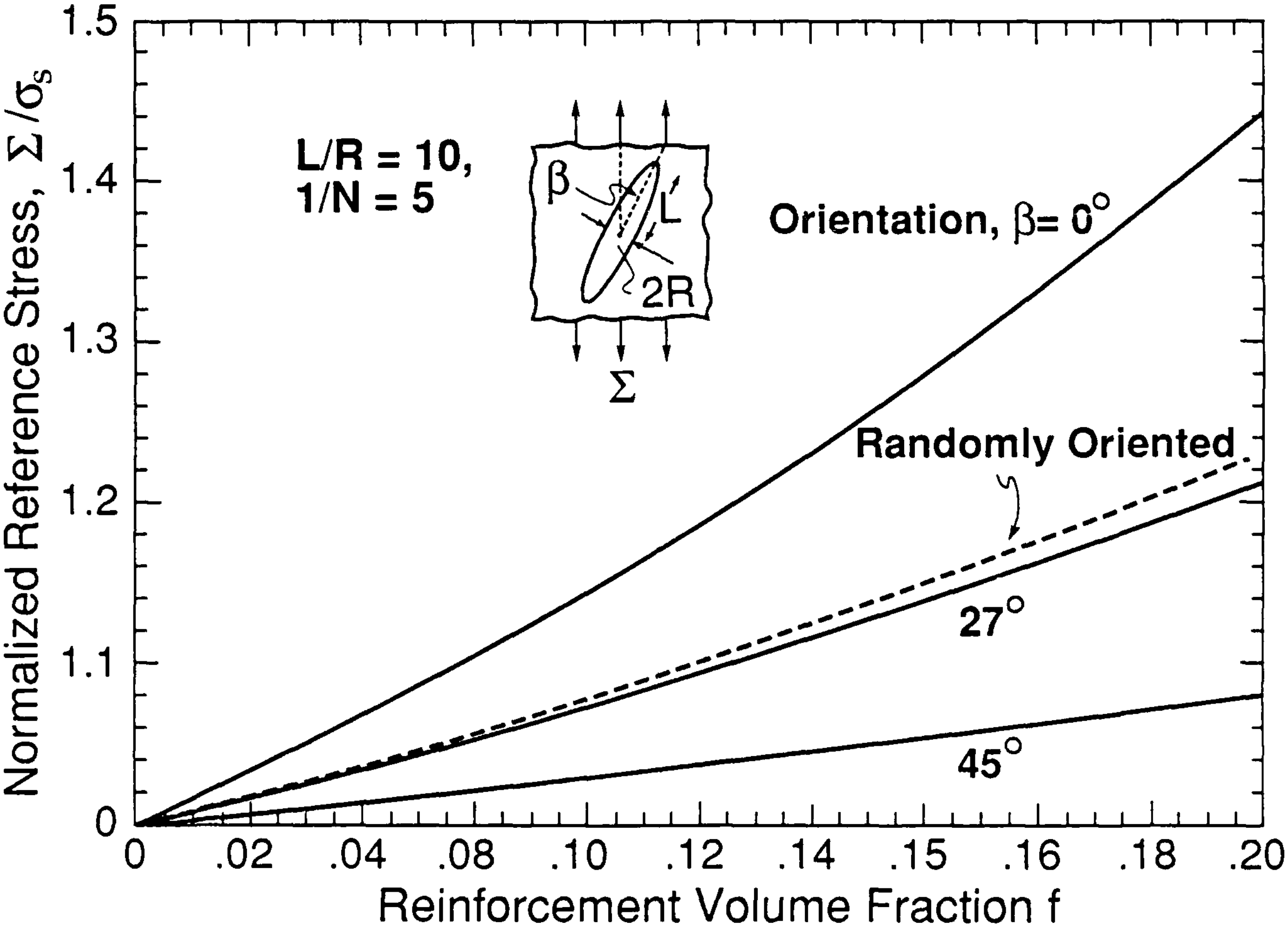

D23 A89-158b'9/15

Figure 2

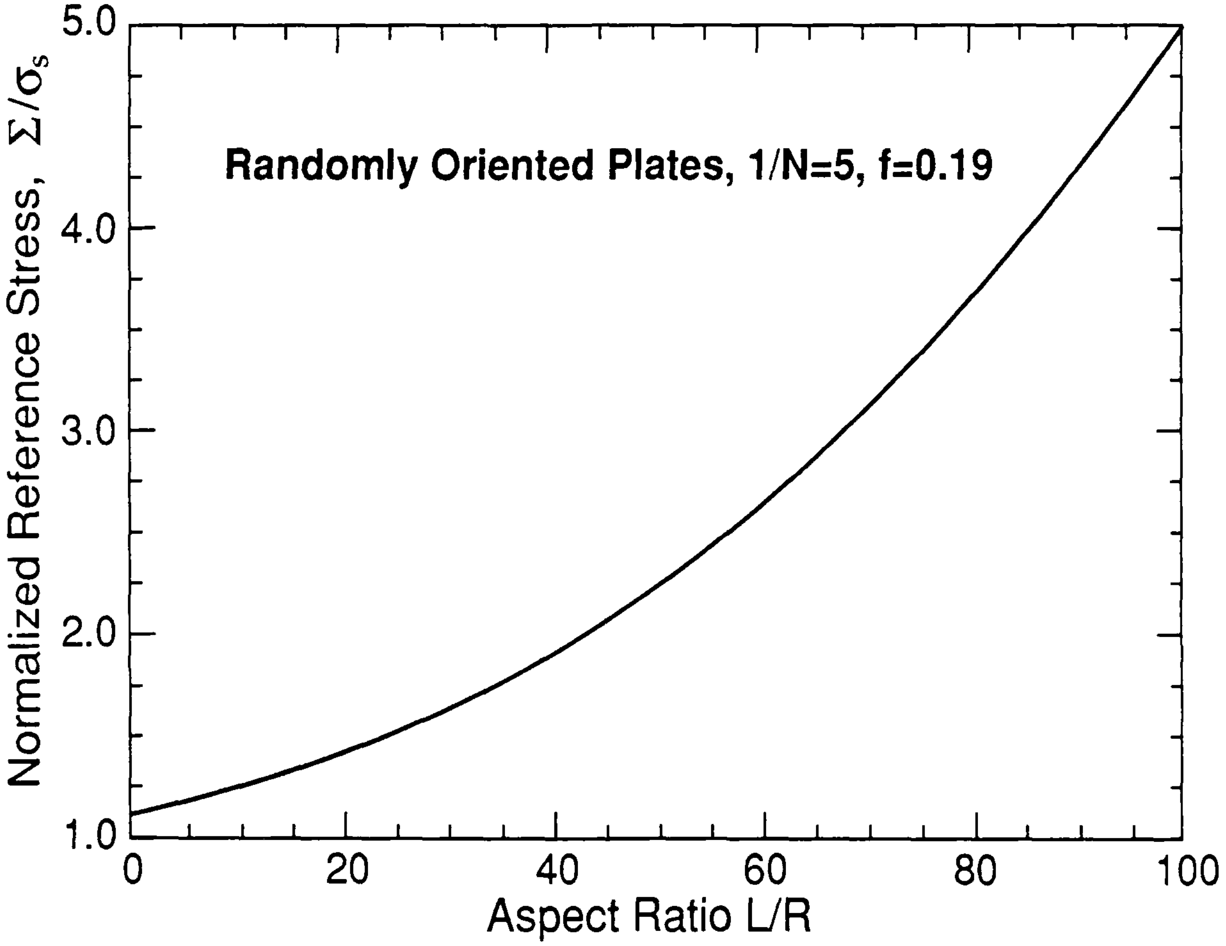

D23 A89-159'9/15

Figure 3

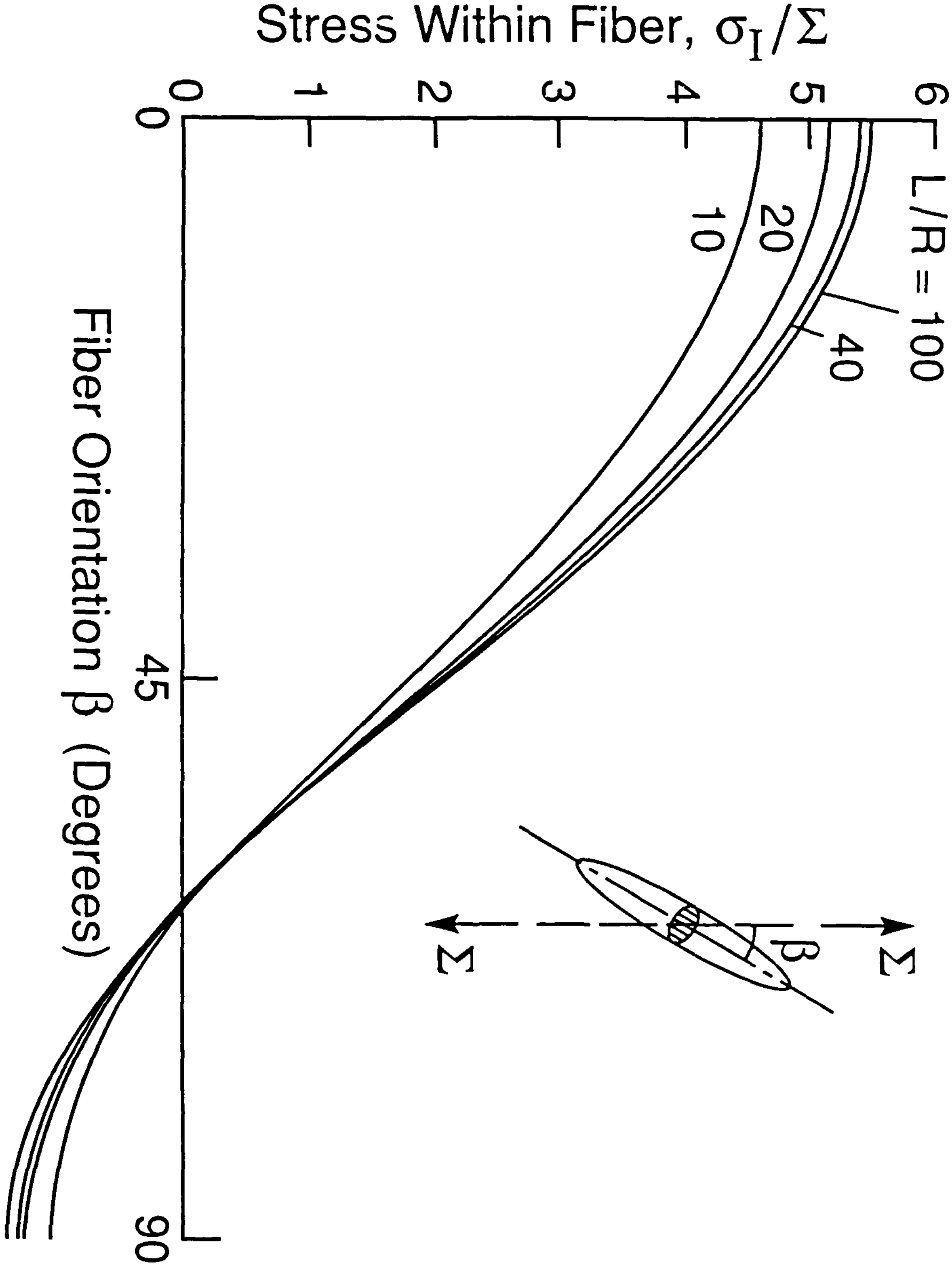
Stress Within Fiber, σ_I/Σ
0
1
2
3
4
5
6
L/R = 100
40
20
10
Fiber Orientation β (Degrees)
0
45
90
Σ
Σ
β

Figure 4

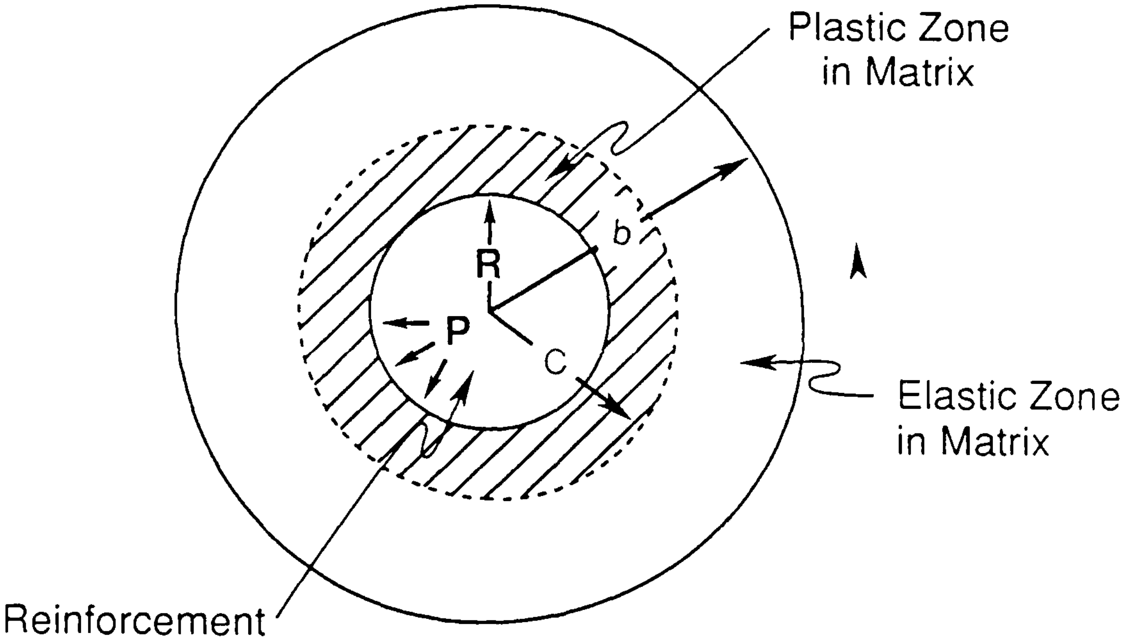
Plastic Zone
in Matrix
b
R
P
C
Elastic Zone
in Matrix
Reinforcement

Figure 5

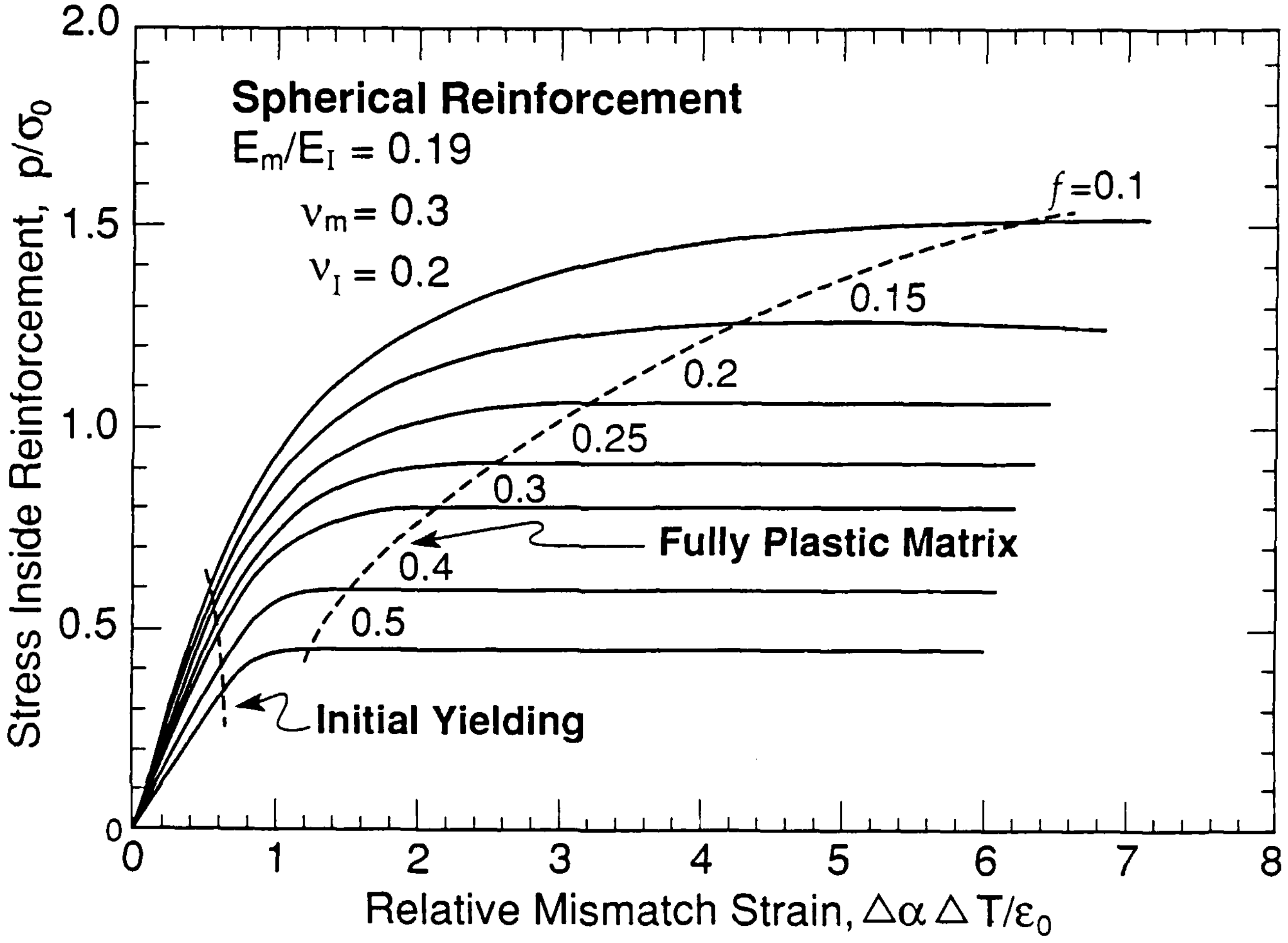

D23 A89-160*9/19

Figure 6a

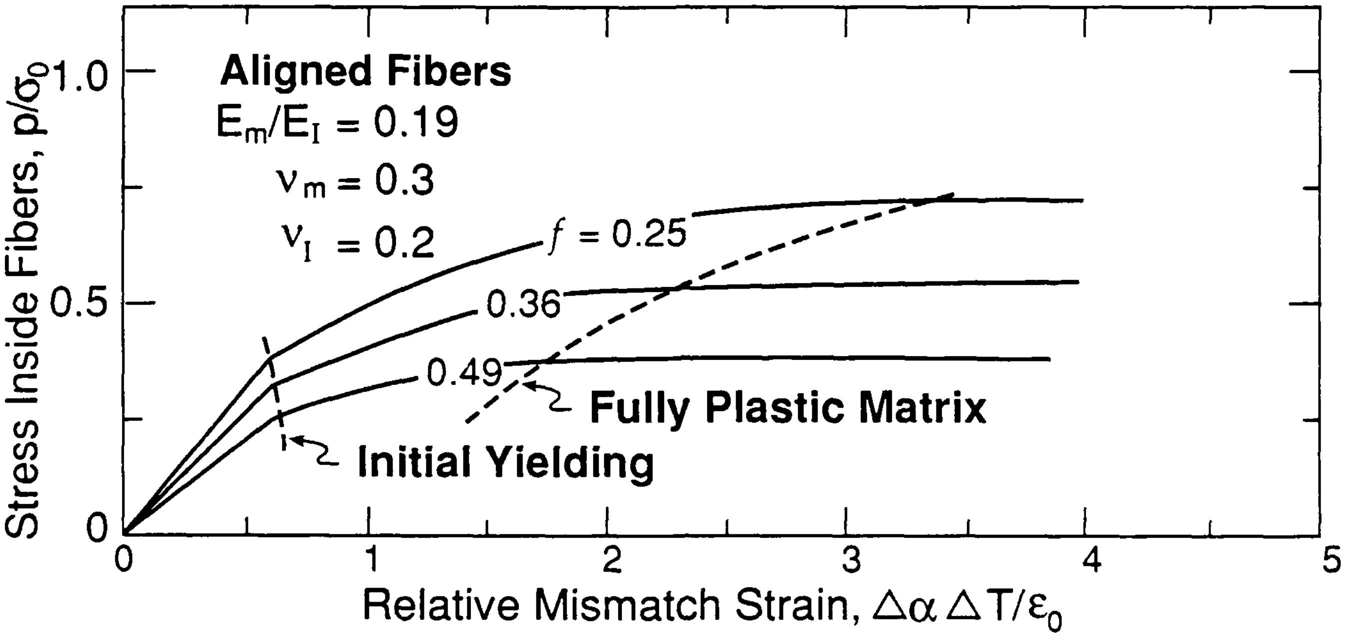
Aligned Fibers
$E_m/E_I = 0.19$
$\nu_m = 0.3$
$\nu_I = 0.2$
$f = 0.25$
0.36
0.49
Fully Plastic Matrix
Initial Yielding
Stress Inside Fibers, p/σ_0
1.0
0.5
0
0
1
2
3
4
5
Relative Mismatch Strain, $\Delta\alpha\Delta T/\varepsilon_0$

Figure 6b

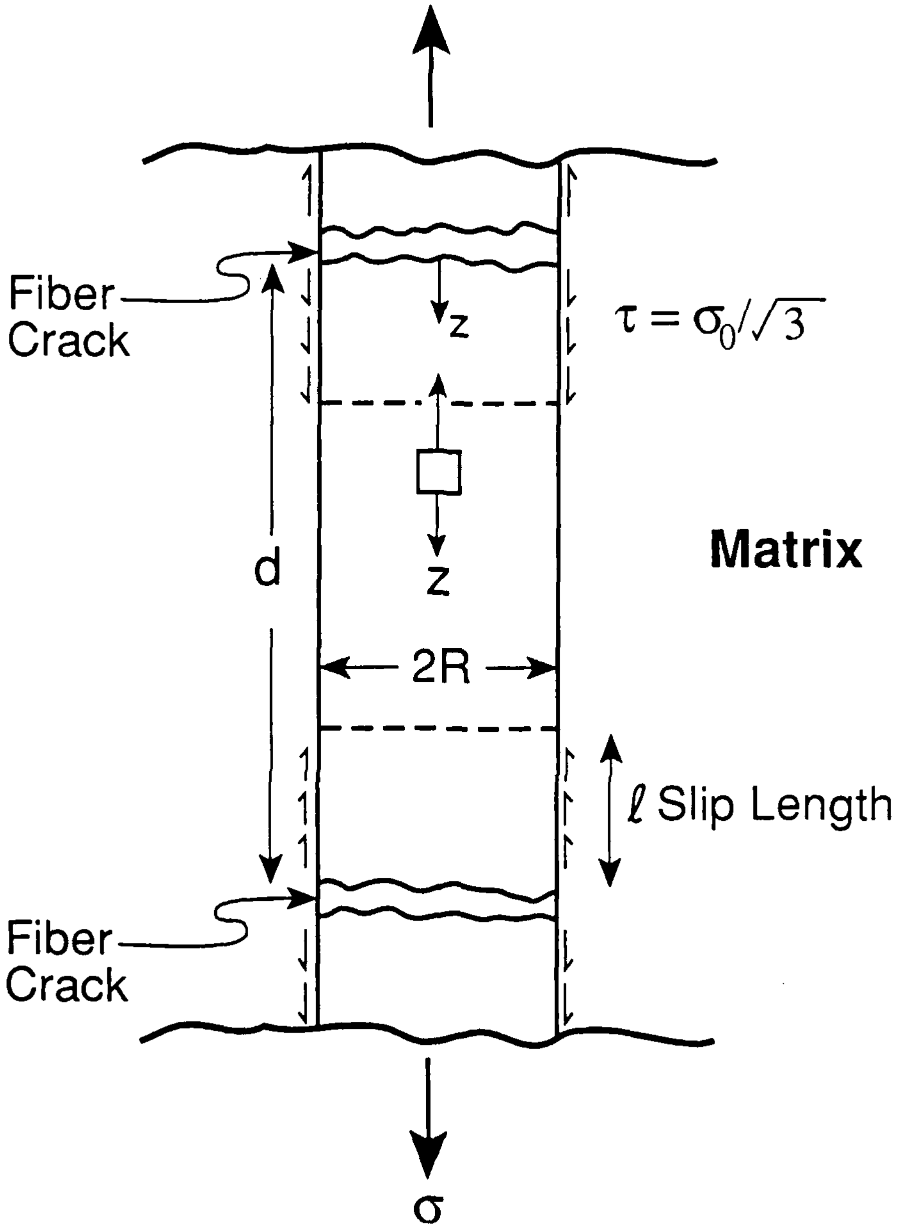

Fiber Crack
z
$\tau = \sigma_0/\sqrt{3}$
Matrix
d
z
2R
ℓ Slip Length
Fiber Crack
σ

D23 A89-162*9/14

Figure 7

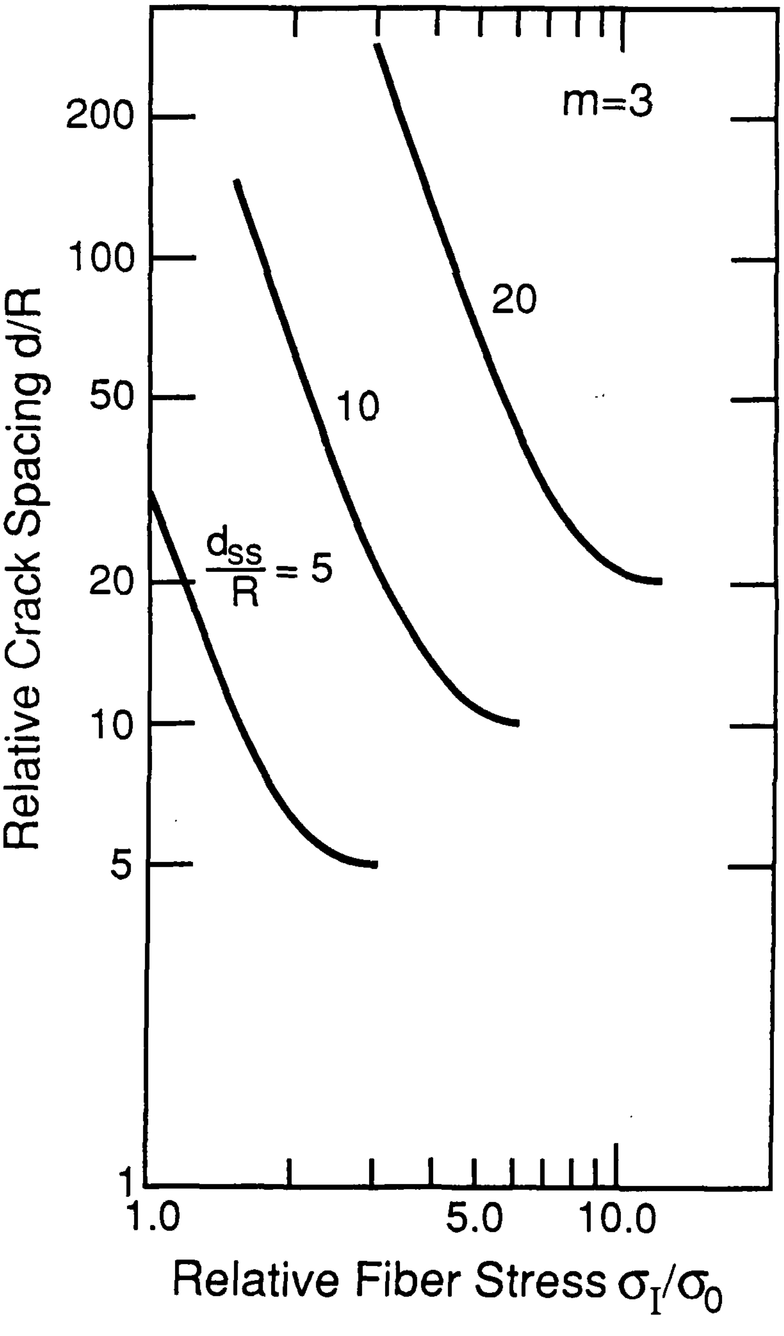

D23 A89-153*9/15

Figure 8

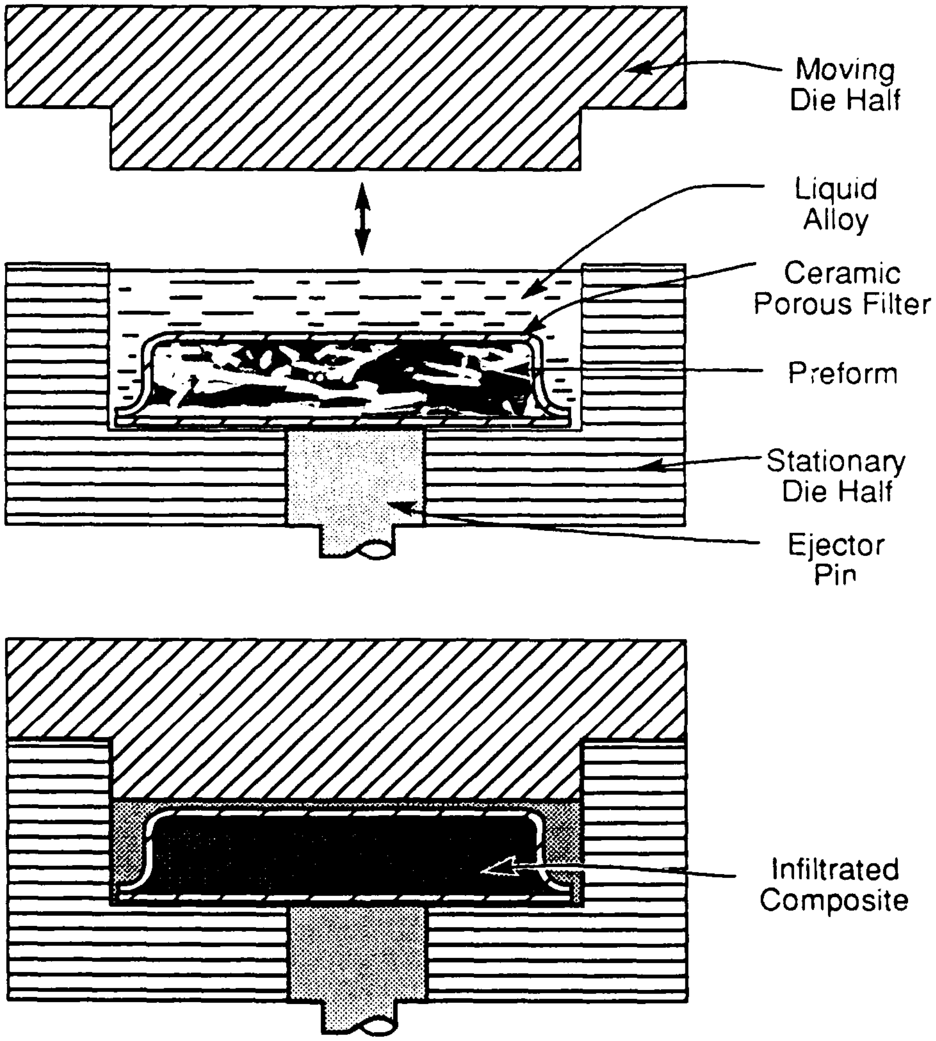
Moving Die Half
Liquid Alloy
Ceramic Porous Filter
Preform
Stationary Die Half
Ejector Pin
Infiltrated Composite

D21 A89-122*6/26

Figure 9

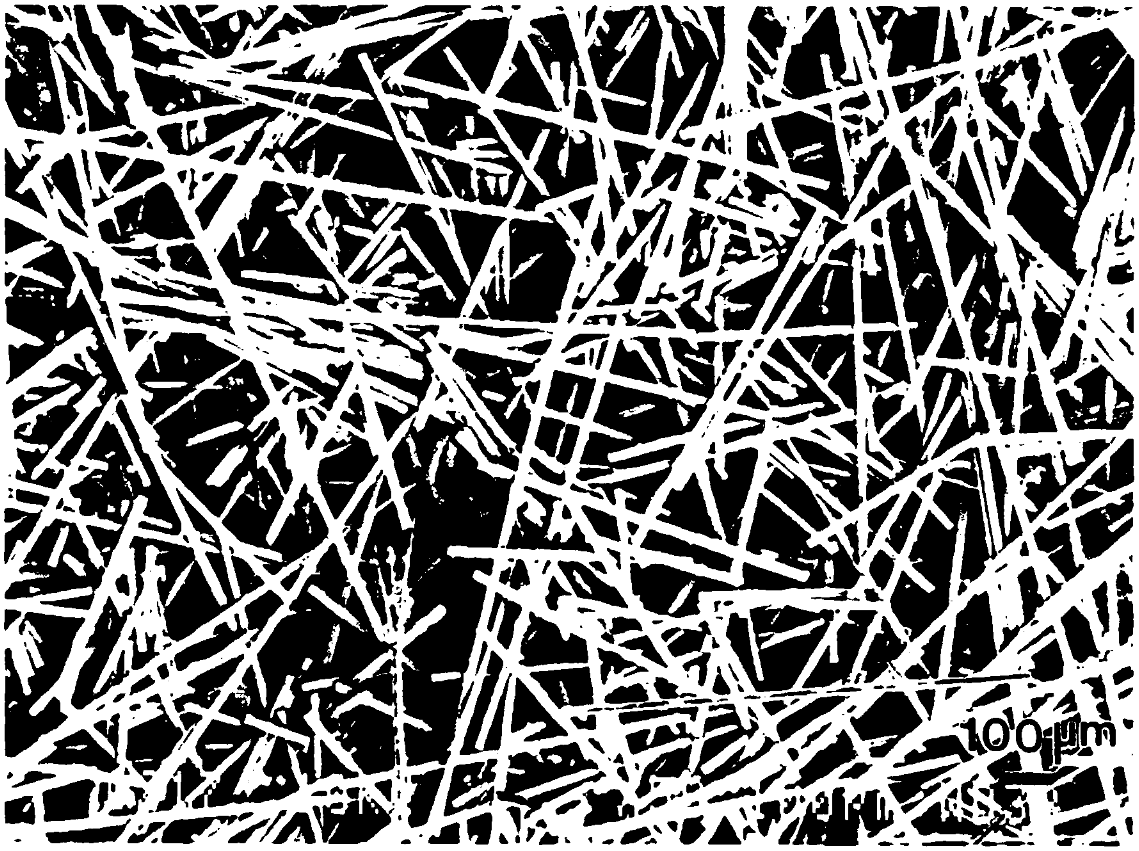

Figure 10

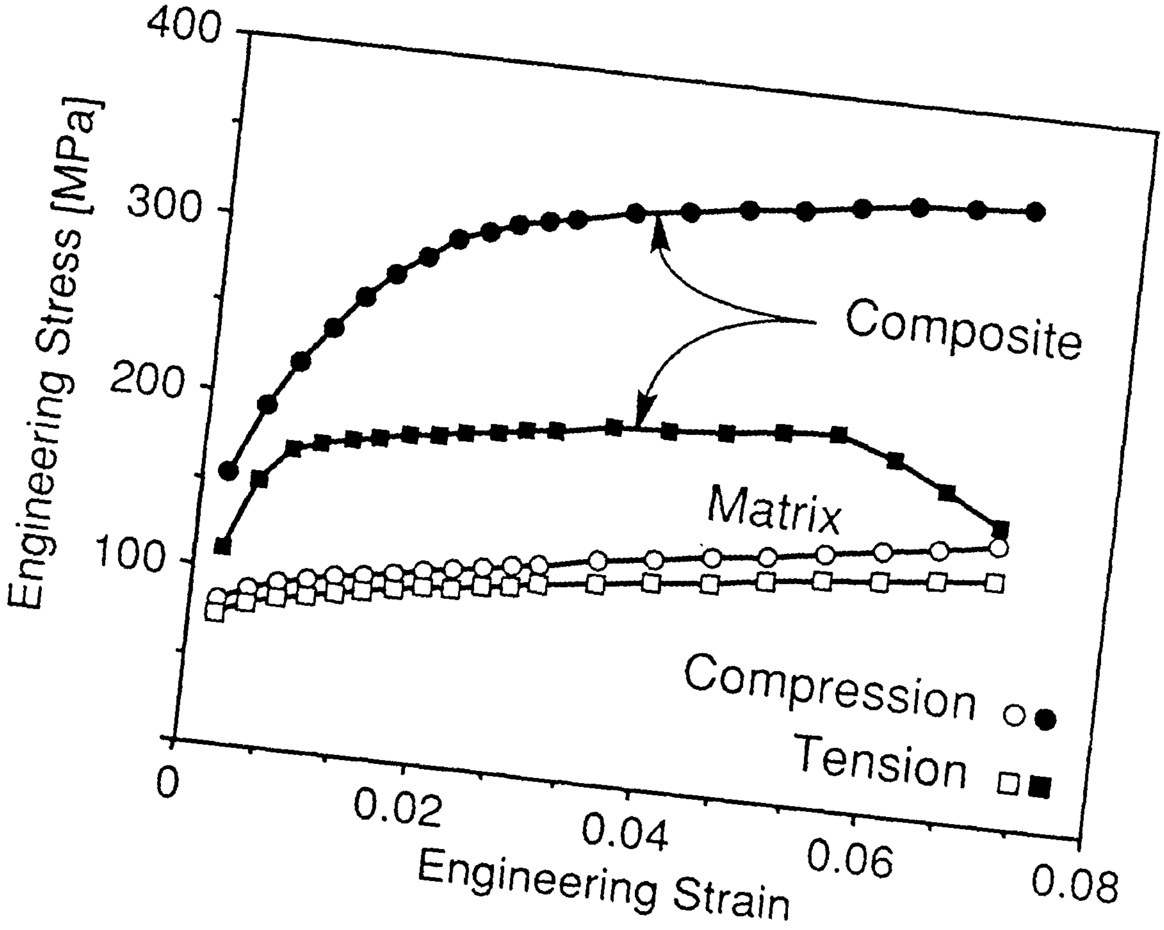
400
300
200
100
0
0.02
0.04
0.06
0.08
Engineering Stress [MPa]
Engineering Strain
Composite
Matrix
Compression ○ ●
Tension □ ■

Figure 11

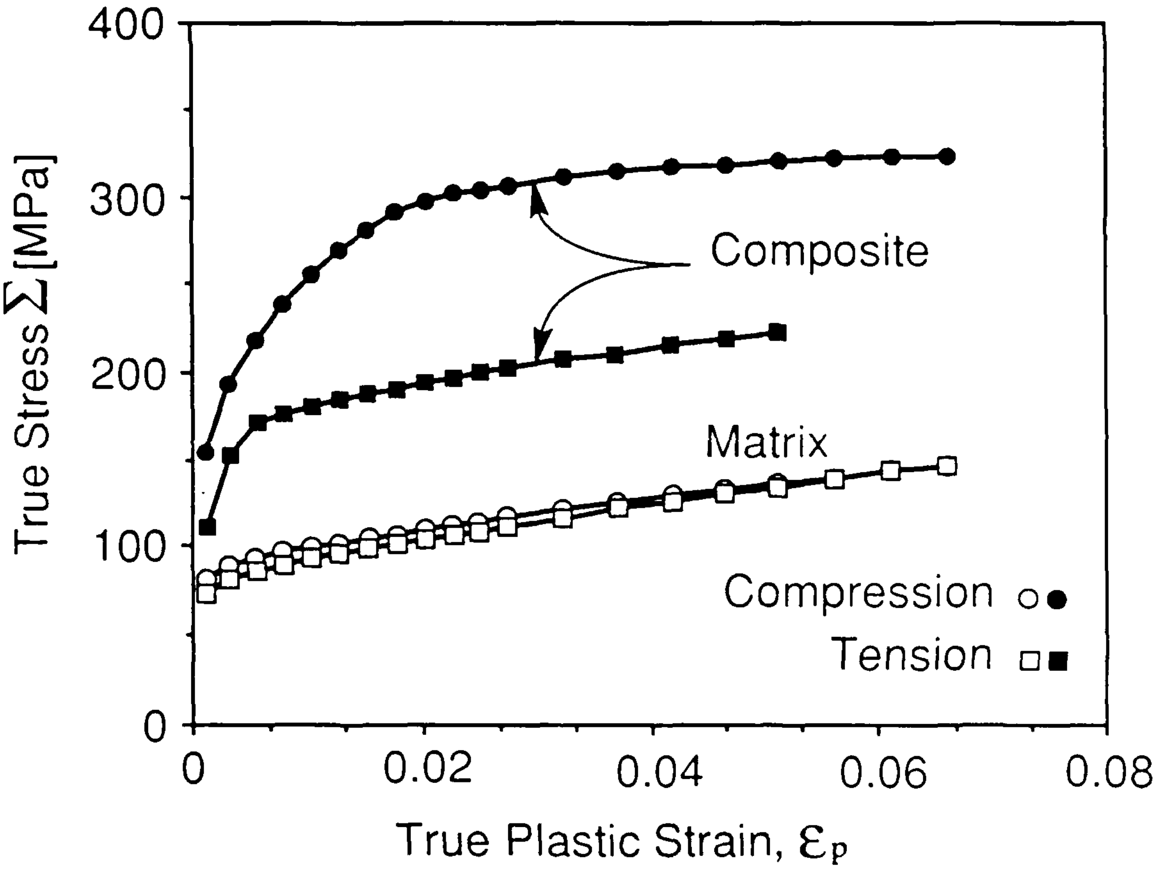

400
300
200
100
0
True Stress Σ [MPa]
0
0.02
0.04
0.06
0.08
True Plastic Strain, ε_p
Composite
Matrix
Compression ○●
Tension □■

Figure 11b

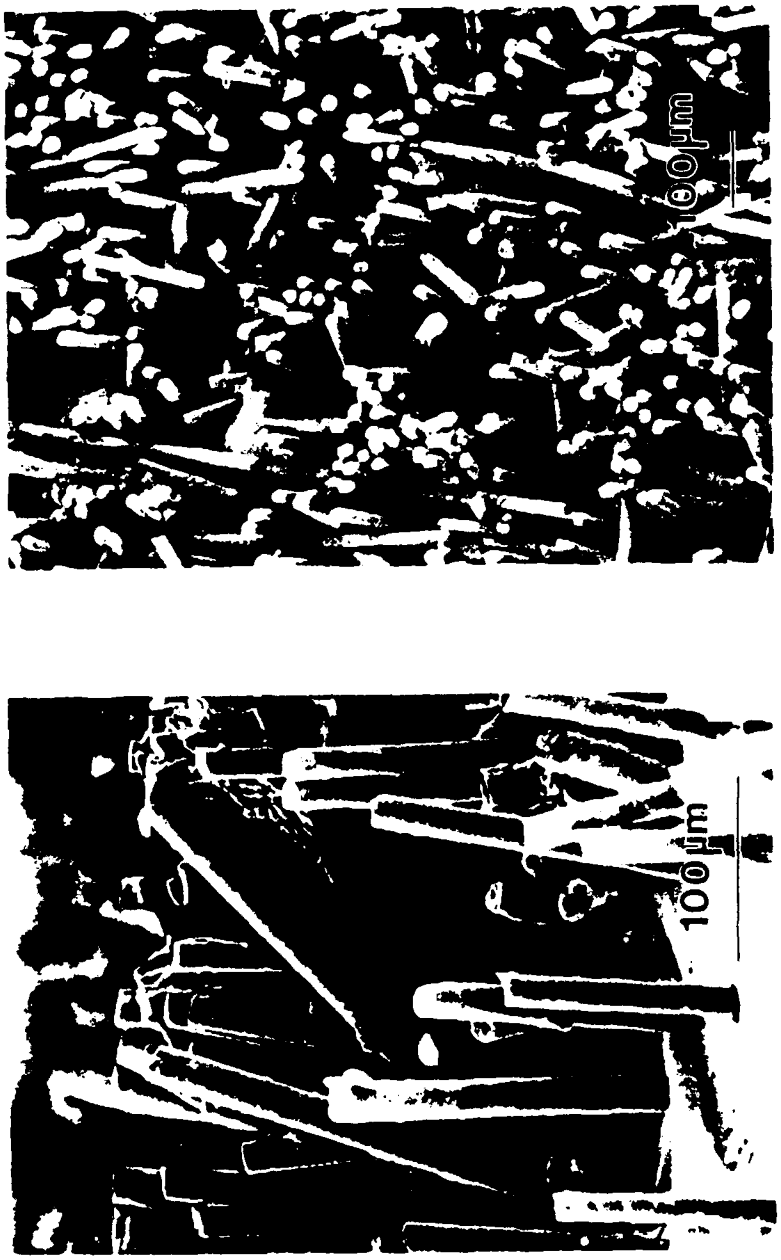
100µm
100µm

Figure 12

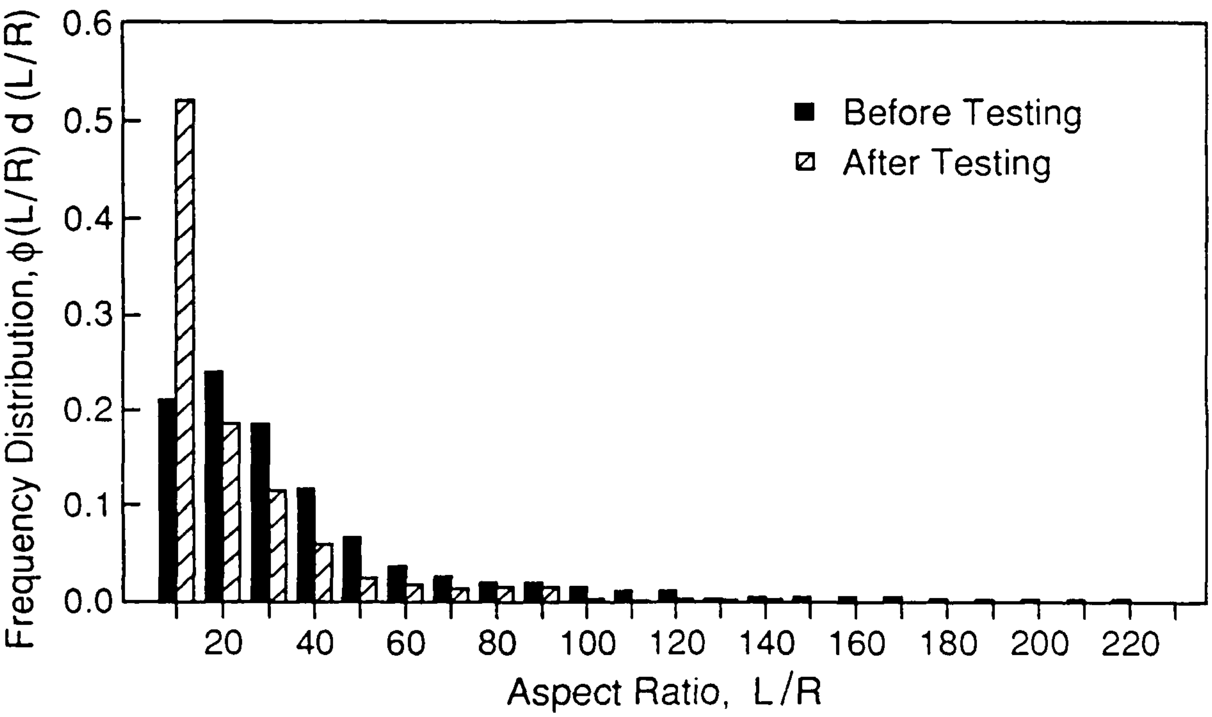
0.6
0.5
0.4
0.3
0.2
0.1
0.0
Frequency Distribution, ϕ(L/R) d (L/R)
■ Before Testing
▨ After Testing
20
40
60
80
100
120
140
160
180
200
220
Aspect Ratio, L/R

Figure 13a

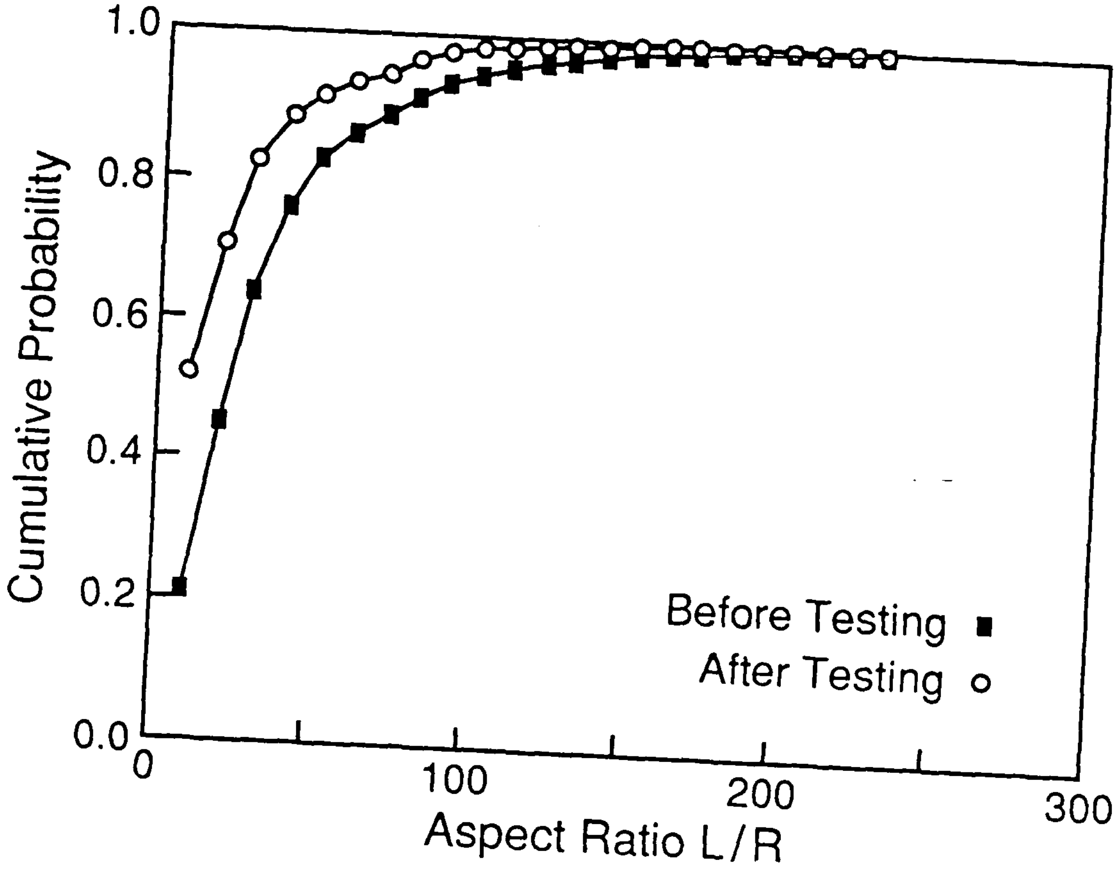
1.0
0.8
0.6
0.4
0.2
0.0
Cumulative Probability
0
100
200
300
Aspect Ratio L/R
Before Testing ■
After Testing ○

Figure 13

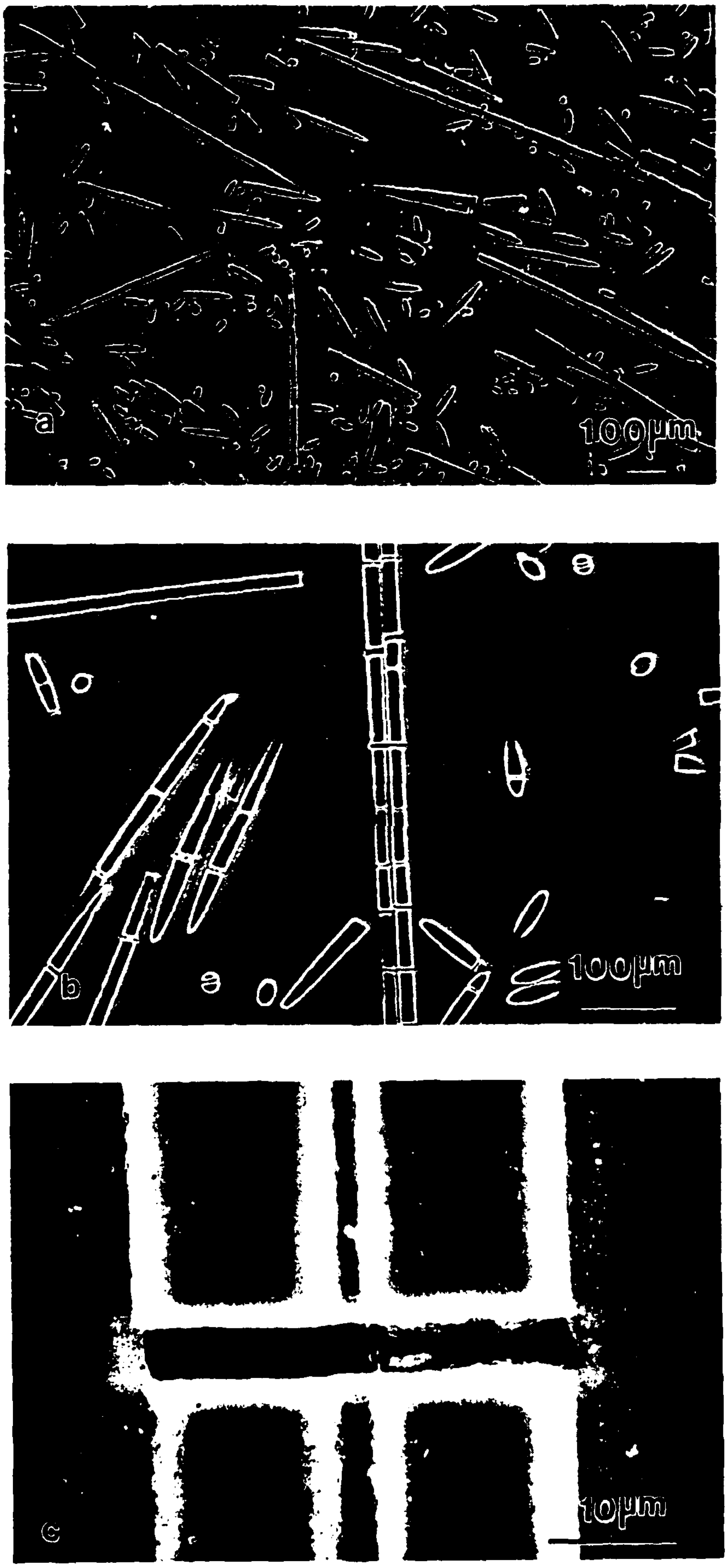
a
100μm
b
100μm
c
10μm

Figure 14

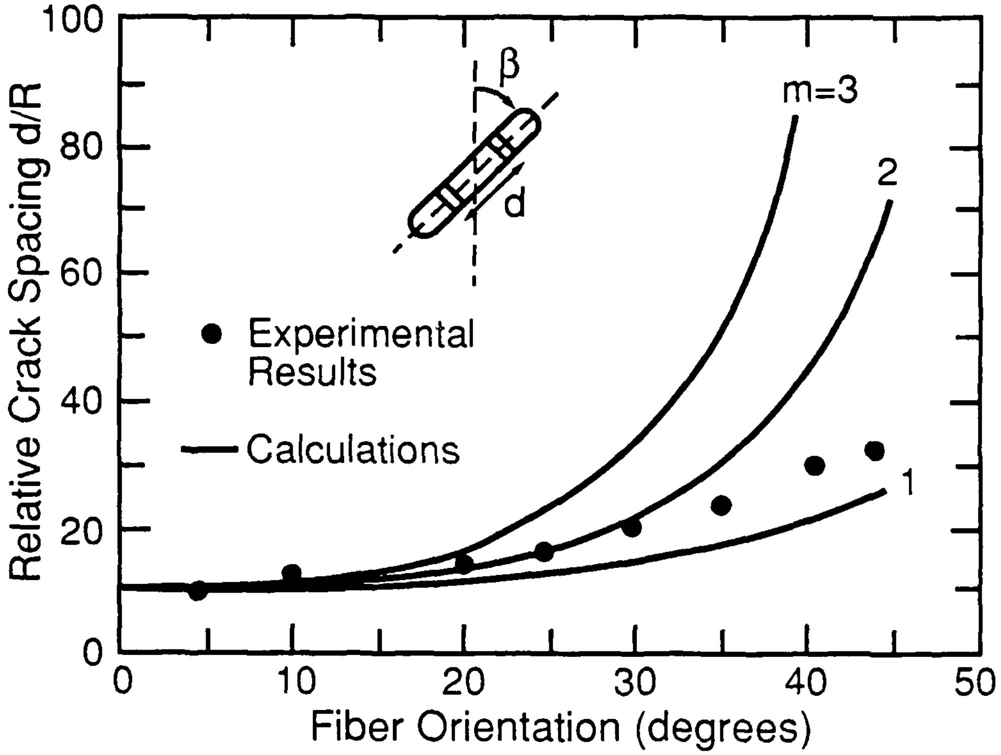

D23 A89-163'89/14

Figure 15

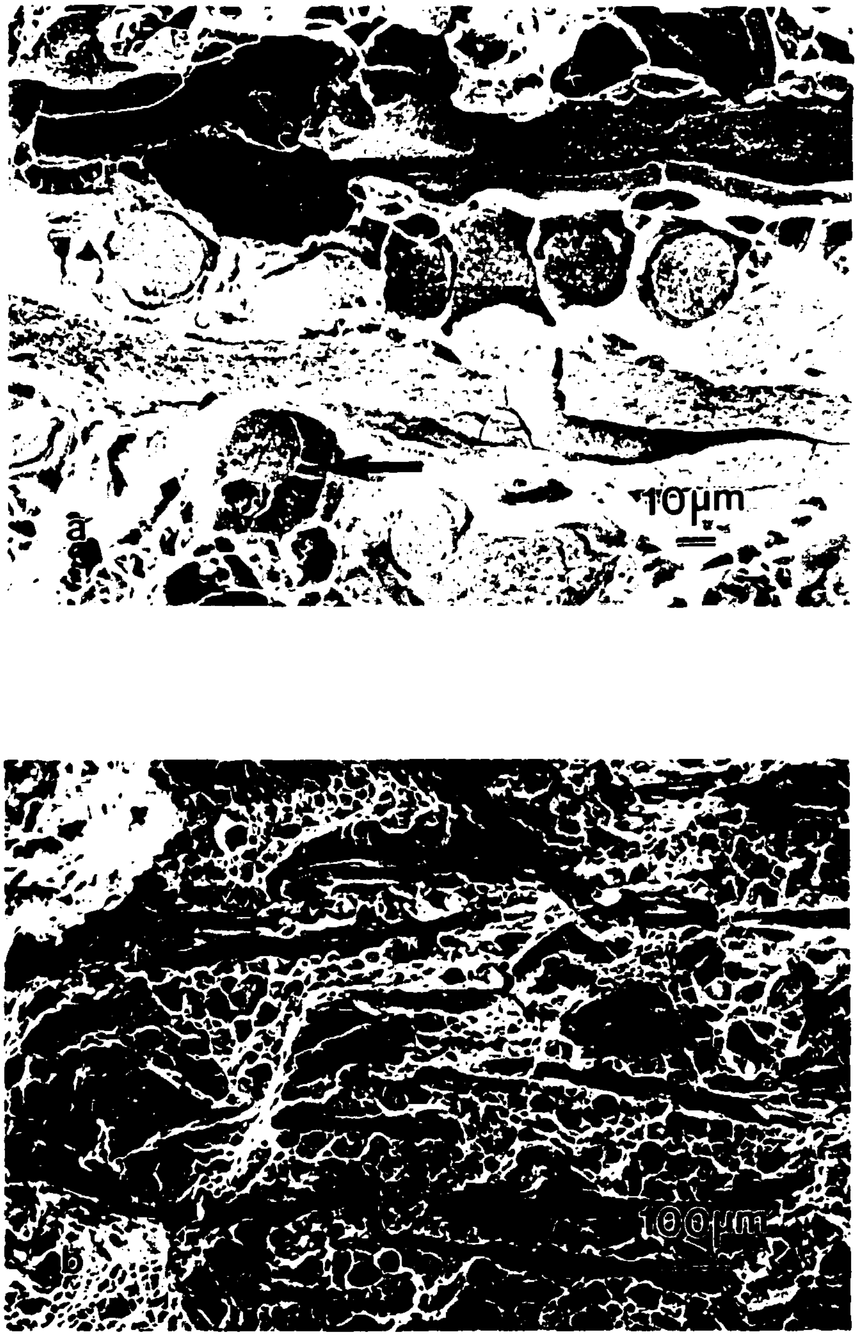
10µm
a
100µm
b

Figure 16

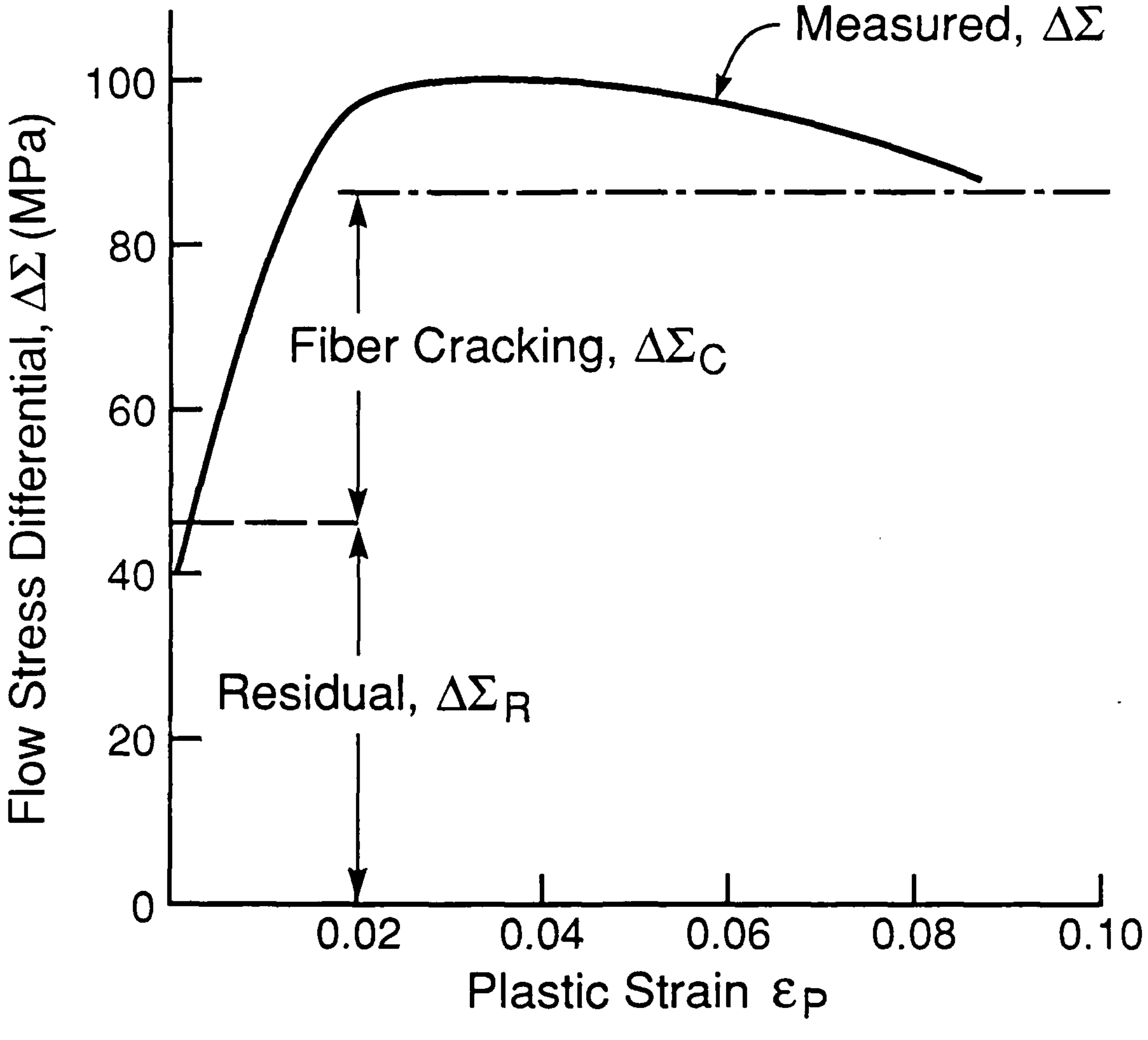

D23 A89-155*3/18

Figure 17

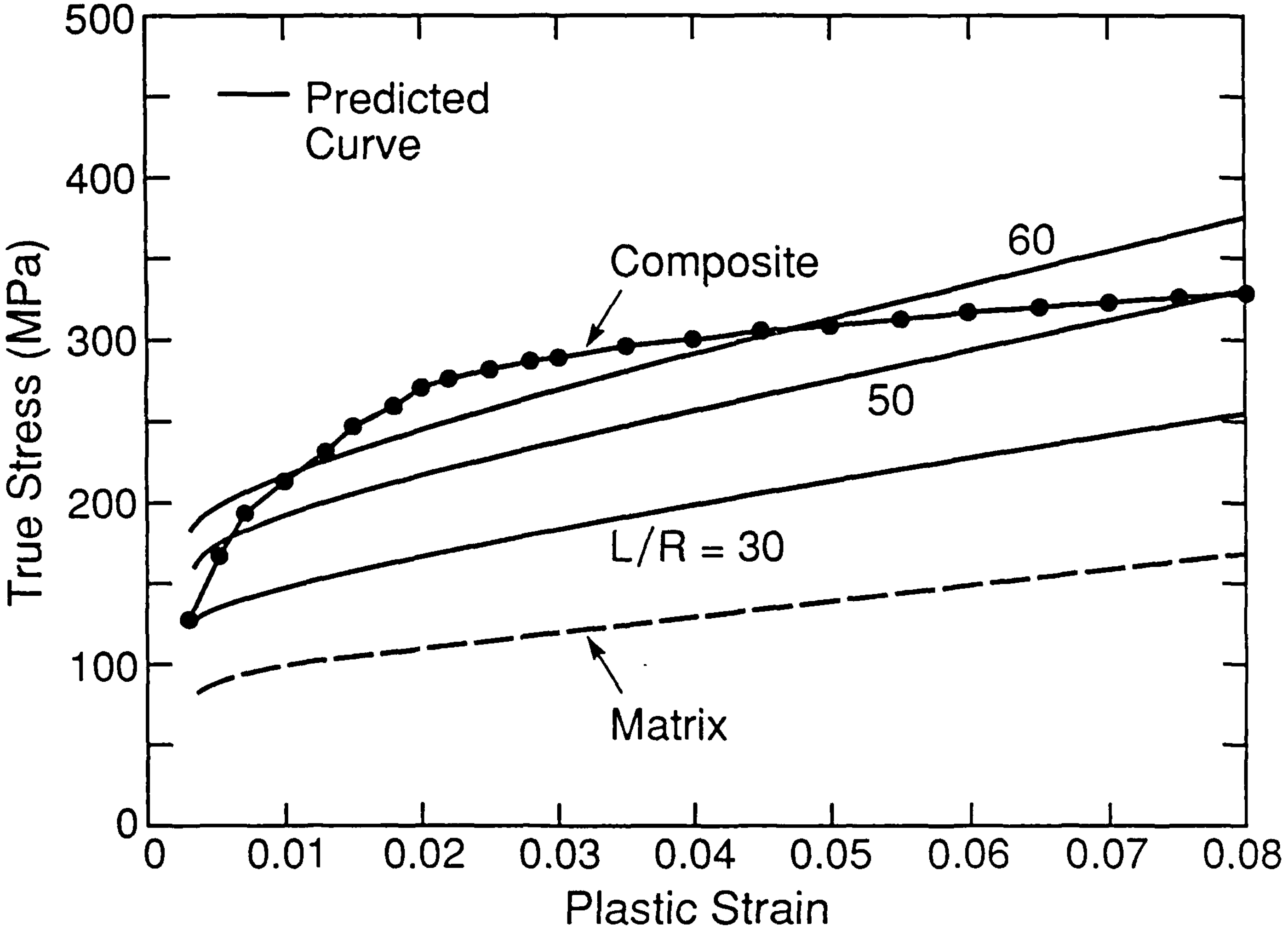

500
400
300
200
100
0
True Stress (MPa)
0
0.01
0.02
0.03
0.04
0.05
0.06
0.07
0.08
Plastic Strain
Predicted Curve
Composite
60
50
L/R = 30
Matrix

Figure 18

journal

J. Am. Ceram. Soc., 72 [8] 1402-408 (1989)

Reprinted from the Journal of the American Ceramic Society, Vol. 72, No. 8, August 1989
Copyright © 1989 by The American Ceramic Society, Inc.

Brittle-to-Ductile Transition in Silicon Carbide

Geoffrey H. Campbell,* Brian J. Dalgleish,* and Anthony G. Evans*

Materials Department, College of Engineering, University of California,
Santa Barbara, California 93106

Observations of the microstructure and creep behavior of two commerical silicon carbides are presented. A combination of techniques has been used to characterize the microstructures. Sequential creep rupture testing has been carried out and scanning electron microscopy used to observe creep-crack propagation and damage development. Basic theory for stress fields and creep rates around a crack tip is related to the observed brittle-to-ductile transition in these materials. Analogy with the brittle-to-ductile transition in steels is made and used to interpret the present observations. [Key words: silicon carbide, mechanical properties, creep, microstructure, cracks.]

I. Introduction

THE high-temperature failure of ceramics has been shown to involve two predominant regimes: rupture at *high stress* occurring by the extension of preexisting cracks and *low-stress* fractures that occur by damage accumulation (Fig. 1). The transition between regimes coincides with a relatively abrupt change in rupture strain (Fig. 1) and is accompanied by the creep blunting of preexisting flaws.[1] Some aspects of the blunting transition have been studied for various Al_2O_3,[1-6] SiC,[7-10] and Si_3N_4[11] materials. However, present understanding of this vitally important aspect of creep rupture is still speculative. The prevalent speculation is that blunting occurs when the stress and displacement field ahead of the crack reduces below a threshold value, at which the nucleation of a crack-tip damage zone (i.e., cavities at grain boundaries and/or in amorphous phases) is suppressed, resulting in a threshold stress intensity, K_{th}.

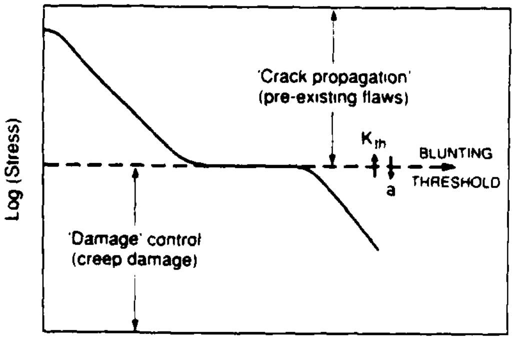

Fig. 1. Schematic of stress versus failure time for alumina at high temperature indicating crack growth and creep-damage-controlled regimes of failure and associated blunting threshold.[1]

At stress intensities below K_{th}, rupture occurs by damage accumulation. For Al_2O_3, failure in this damage-controlled regime has been shown to occur by the growth and coalescence of shear bands that nucleate at large microstructural and chemical heterogeneities within the material.[1-6] However, when such damage mechanisms are suppressed, by having superior microstructural and chemical homogeneity, recent research on ZrO_2[12] (TZP) and Al_2O_3/ZrO_2 composites[13-15] indicates that the material then becomes superplastic.

The abrupt change in rupture behavior around the blunting threshold can be regarded as a transition from creep brittleness to creep ductility. The rupture characteristics thereby exhibit a strain-rate-dependent transition temperature, T_t. Below T_t, the material fails at small strains, by crack growth from preexisting flaws. Above T_t, creep ductility obtains with failure proceeding by damage mechanisms.

The intent of the present research is to examine aspects of the brittle-to-ductile transition for two SiC materials, as needed to further understand this important phenomenon. Some prior research on SiC[7-10] has provided indirect evidence of a blunting threshold that varies with temperature, microstructure, and environment. This research has also suggested that both the threshold and the creep-crack growth rate above the threshold are dominated by the presence and the characteristics of amorphous grain-boundary phases that either preexist or are formed by exposure to oxidizing environments. Specifically, low viscosity and low surface energy amorphous phases accelerate the crack growth and reduce the relative blunting threshold, K_{th}/K_c, as also established for various Al_2O_3[1-6] and Si_3N_4[11] materials. The present research is thus performed in an inert environment in an attempt to preserve the initial phase characteristics during testing.

An important constituent of the current research is the thorough characterization of the materials and the direct observation of crack blunting and of damage. These aspects of the research are presented first, followed by measurements of mechanical behavior and then interpretation of the brittle-to-ductile transition.

II. Experimental Procedure

(1) *Materials and Procedures*

One silicon carbide[†] was manufactured[16] by mixing a fine, high-purity silicon carbide powder with 0.5 to 5 wt% aluminum in a ball mill, using cobalt-bonded tungsten carbide grinding media, and hot-pressed at 2075°C and 18 MPa. The other material[‡] was sintered α-SiC containing boron and excess carbon as sintering aids.[17]

The surfaces subject to examination were first mechanically polished. The polishing procedure began with 15-μm diamond paste on glass, reduced to 9 μm and then 6 μm, the latter on a lapping wheel. Polishing was completed with 1-μm diamond paste on a vibration polisher. Several specimens were thermally treated to highlight grain boundaries prior to examination. Treatments were conducted under vacuum or in an argon atmosphere. Temperatures ranged from 1300° to 1600°C and times from 15 to 45 min.

K. T. Faber—contributing editor

Manuscript No. 198882. Received September 21, 1988; approved December 20, 1988.

[*] Member, American Ceramic Society.

[†] Norton Co., Worcester, MA.

[‡] Sohio Engineered Materials Co., Niagara Falls, NY.

Chemical analysis was performed to determine the total boron, silicon, carbon, and oxygen contents. For *boron* analysis, samples were crushed and the boron leached out into an acid solution. This solution was then plasma-heated and the photon intensities characteristic of boron determined. The *silicon* content was determined by fusing. The resultant glass was dissolved in a hydrochloric acid solution and the silicon evaluated using atomic absorption. The *carbon* content was determined by fusing with an oxidant to evolve carbon dioxide. The carbon dioxide content was then analyzed using a coulometer and a carbonate standard. Finally, the *oxygen* content was determined by neutron activation analysis. Other impurities were identified using semiquantitative spectroscopic procedures.

A microprobe was used to determine the composition of second-phase impurities from X-ray spectra and maps. The scanning electron microscope (SEM) was used to obtain information about porosity and carbon inclusions: the former on uncoated, mechanically polished surfaces and the latter on gold-coated fracture surfaces. Transmission electron microscopy (TEM) was used to examine grain-boundary phases, employing both light- and dark-field techniques. Electron energy loss spectroscopy also identified the principal second phases.

(2) *Microstructure*

(*A*) *Hot-Pressed Silicon Carbide:* Specimens having a light thermal etch observed in the optical microscope revealed a grain size of about 1.5 μm. The chemical analysis (Table I) indicated appreciable oxygen, aluminum, tungsten, and cobalt. The tungsten and cobalt were presumably introduced by the cobalt-bonded tungsten carbide grinding media used to mix the initial powders. Microprobe analysis confirmed appreciable quantities of second phases. Backscattered electron images and related X-ray spectra identified silicides having variable composition. Some of these are tungsten silicide while others are a mixture of tungsten, cobalt, and iron silicides. Attempts to image a grain-boundary phase in the TEM were unsuccessful, indicating that amorphous phases, if present, must be less than ~0.5 nm in width.

(*B*) *Sintered Silicon Carbide:* Optical observations of thermally etched specimens revealed a grain size of about 10 μm. Chemical analysis (Table I) indicated few impurities. However, residual carbon is implied. Specifically, by assuming that all the silicon and boron present are in the form of carbides, the residual carbon content can be estimated at 0.8 wt%. This estimate is confirmed by TEM, which reveals graphite inclusions (Fig. 2(A)). The graphitic structure is confirmed by the near-edge fine structure of the electron energy loss spectrum (Fig. 2(B)). The graphite is also well delineated on fracture faces (Fig. 2(C)).

(3) *Toughness Measurements*

Four-point flexure beams (3 by 3 by 30 mm) were indented on the tensile surface, with a 200-N Knoop indent, such that the long axis of the indenter was oriented perpendicular to the applied stress axis. The indent created a semicircular crack having 125- to 150-μm radius. The residual stress was removed by surface polishing. The edges of the tensile surface were also beveled to remove flaws that might cause premature failure.

Table I. Material Composition

Material (quantitative composition)	Major impurities (semiquantitative)
Hot-pressed SiC	1.50 wt% Al
29.84 wt% C	2.50 wt% W
64.89 wt% Si	0.10 wt% Co
50 ppm B	0.10 wt% Fe
	1.70 wt% O
Sintered α-Sic	0.18 wt% Al
30.50 wt% C	0.07 wt% Ca
69.40 wt% Si	0.06 wt% Cu
0.15 wt% B	0.16 wt% Fe
	0.23 wt% O

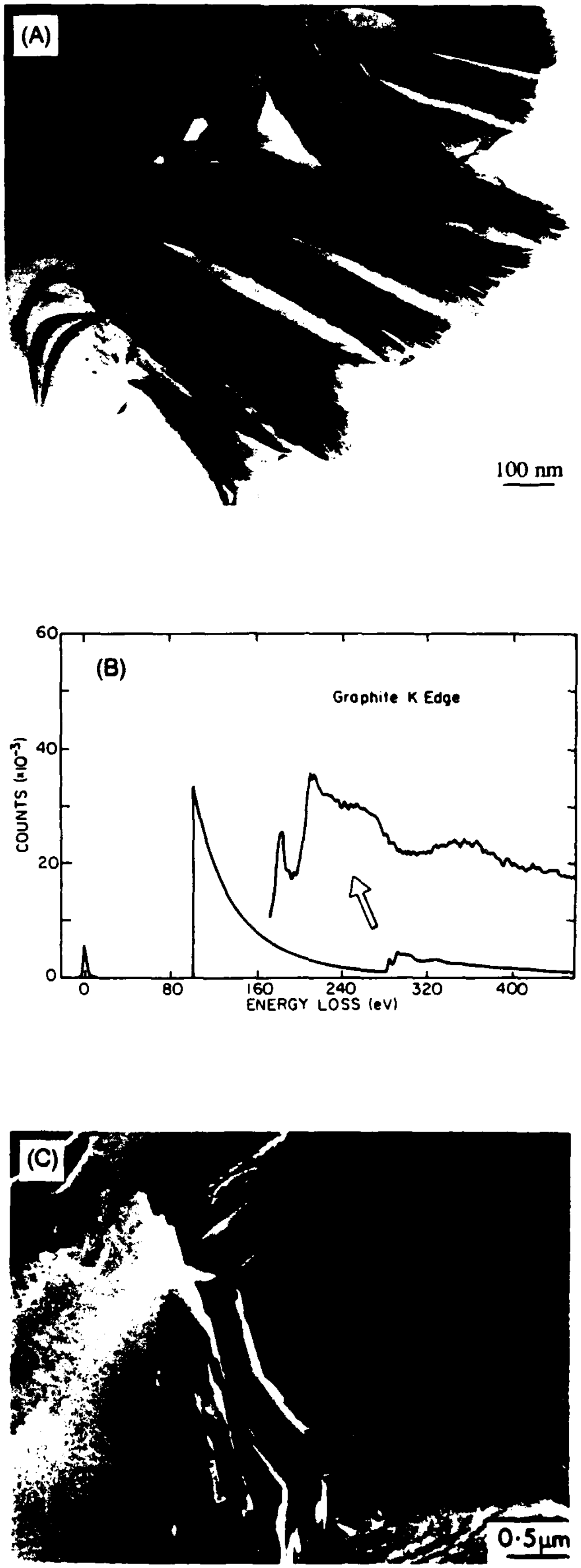

Fig. 2. (A) Transmission electron micrograph of sintered silicon carbide showing graphite inclusion. (B) Electron energy loss spectrum from inclusion with graphitic structure confirmed by near-edge fine structure. (C) Scanning electron micrograph of fracture surface with graphite inclusion.

Table II. Fracture Toughness as a Function of Temperature

Temperature (°C)	K_{IC} (MPa · m$^{1/2}$)	
	Sintered SiC	Hot-pressed SiC
RT[†]	2.7	3.9
1400		2.8
1500	2.7	2.7
1600	2.7	2.4
1700	2.9	2.6
1800	2.7	

[†] Room temperature.

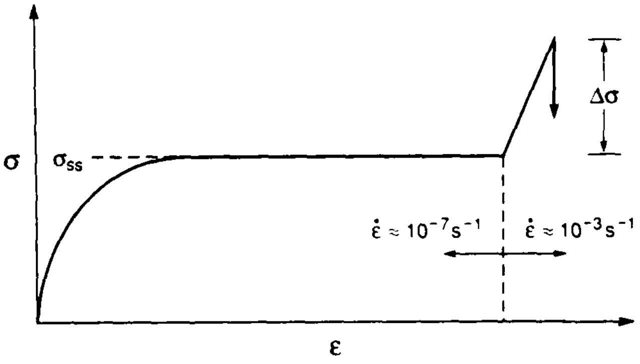

Fig. 3. Schematic stress–strain curve for tests used to evaluate creep damage. The sudden increase in strain rate at a certain level of strain causes the specimen to fracture at an overstress $\Delta\sigma$.

The fracture toughness was determined as a function of temperature by using indented beams tested at a strain rate of 6×10^{-5} s^{-1}. The initial flaw size due to the indent was measured on the fracture surface in the SEM after testing. The critical stress intensity factor was determined using the relation[18]

$$K_c = (2/\sqrt{\pi})\sigma_f\sqrt{a} \tag{1}$$

where σ_f is the fracture stress and a is the flaw radius.

The results (Table II) show that the sintered material has a temperature-insensitive toughness. The hot-pressed material has a somewhat higher room-temperature toughness, but the toughness diminishes at higher temperature to a level comparable to that of the sintered material.

(4) Deformation Measurements

Creep tests were performed at 1600° to 1800°C in an argon atmosphere and at constant displacement rates of 10^{-7} to 10^{-9} m/s and the "steady-state" creep properties characterized by

$$\dot{\varepsilon}_{ss} = \dot{\varepsilon}_0(\sigma_{ss}/\sigma_0)^n \tag{2}$$

where $\dot{\varepsilon}_{ss}$ is the strain rate and σ_{ss} the stress in steady state, n is the creep exponent, and $\dot{\varepsilon}_0$ and σ_0 are constants. The steady-state stress on the tensile surface was estimated using[19]

$$\sigma_{ss} = \frac{3(L - l)P_{ss}}{bh^2}\left(\frac{2n + 1}{3n}\right) \tag{3}$$

where L is the outer span in four-point bending, l is the inner span, P_{ss} is the steady-state load, b is the thickness, and h is the height. The use of Eq. (3) is justified by the absence of noticeable creep damage (see Fig. 8) and, hence, of obvious asymmetry in creep between tension and compression. Sequential testing was used in some cases, with SEM examinations conducted between each iteration. The evolution of damage and the behavior of indentation flaws could thereby be established. At the conclusion of sequential testing, the beams were fractured either by testing rapidly to failure (Fig. 3) or by cooling under stress to room temperature and then loading to failure. The material directly in front of the crack tip was then examined for damage in the SEM and a nominal toughness ascertained.

The testing revealed an abrupt transition from brittle to ductile behavior (Fig. 4) such that, in the ductile region, the strain on the tensile surface exceeded 10% without failure. Extensive creep ductility in SiC has also been noted in a previous study.[20] At strain rates of $\sim 10^{-7}$ s^{-1}, the transition for the hot-pressed material occurred between 1650° and 1700°C, and for the sintered material it occurred between 1750° and 1800°C. In the ductile range, the creep exponent of the hot-pressed silicon carbide was 2.3, and that for the sintered silicon carbide was 1.7. These values are in the range expected for superplastic behavior,[21] consistent with the extensive ductility observed above the transition temperature.

Above the transition temperature, precracks in the sintered material exhibited blunting and opening without growth (Fig. 5), such that the crack-tip opening b increased substantially with strain (Fig. 6). The blunting exhibits a functional dependence on strain (see Eq. (12a)): $b/a \sim \varepsilon_{ss}^{3/2}$ (Fig. 7). Furthermore, damage is evident in the vicinity of the blunt tip in the form of cavities that seemingly initiated at graphite inclusions (Fig. 8). These cavities are typically 1 μm in diameter, essentially independent of the creep strain. In the hot-pressed material, some slow crack growth occurred. Appreciable damage was also detected in a crack-tip zone (Fig. 9) consisting of lenticular-shaped facet cav-

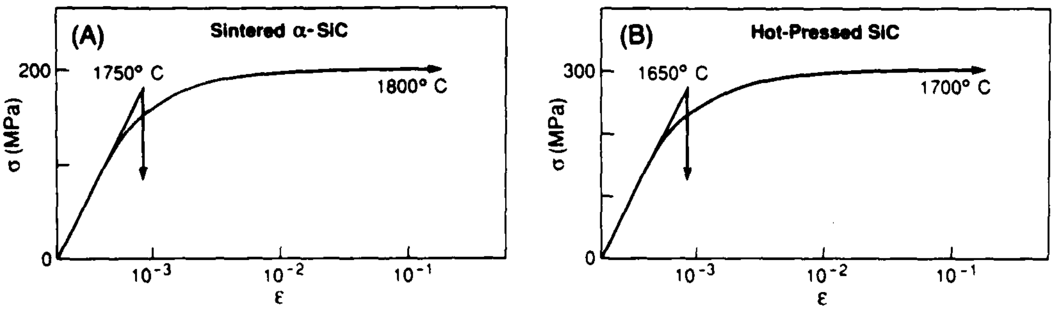

Fig. 4. Representative stress–strain curves illustrating the change in behavior of both materials over a small temperature range: (A) sintered, (B) hot-pressed.

ities typical of those apparent during creep-crack growth.[22] The incidence of slow crack growth caused the crack profile to evolve with complex geometry, and thus blunting measurements comparable to those obtained for the sintered material (Fig. 6) could not be obtained. Consequently, the study of blunting effects is restricted to the measurements obtained on the sintered material.

Specimens of the sintered material tested at room temperature after exposure to steady-state conditions at high temperature to cause crack blunting gave nominal toughnesses K_N larger than the sharp-crack toughness (Table III). Specimens tested rapidly to failure at temperature after steady-state creep also gave a relatively high nominal toughness. Furthermore, the toughness systematically increased with increase in creep strain and, hence, crack-tip opening, b (Table III).

III. Some Basic Mechanics

Stationary cracks in a body subject to steady-state creep generate displacement and strain fields directly analogous to the corresponding nonlinear hardening solutions.[23] The crack-tip stresses outside the blunting region in plane strain have the singular form[23]

$$\frac{\sigma_{ij}}{\sigma_0} = \left(\frac{C^*}{\sigma_0 \dot{\varepsilon}_0 I r}\right)^{1/(n+1)} \tilde{\sigma}_{ij} \tag{4a}$$

or

$$\sigma_{ij} = (C^* \sigma_{ss}^n / \dot{\varepsilon}_{ss} I r)^{1/(n+1)} \tilde{\sigma}_{ij} \tag{4b}$$

where C^* is the loading parameter, r is the distance from the crack tip, and I and $\tilde{\sigma}_{ij}$ are nondimensional coefficients tabulated by Hutchinson.[24] Then, by noting that, for a surface crack[25]

$$C^* = \sigma_{ss} \dot{\varepsilon}_{ss} a h_s \tag{5}$$

where h_s is a constant, Eq. (4) becomes

$$\frac{\sigma_{ij}}{\sigma_{ss}} = \left(\frac{h_s a}{I r}\right)^{1/(n+1)} \tilde{\sigma}_{ij} \tag{6}$$

At the crack tip, blunting occurs, and the stresses are locally reduced below the value predicted by Eq. (6). A peak stress occurs at r values of 1 to 2 times b.[26] However, the peak is substantially influenced by the shape of the blunting crack tip. Some solutions

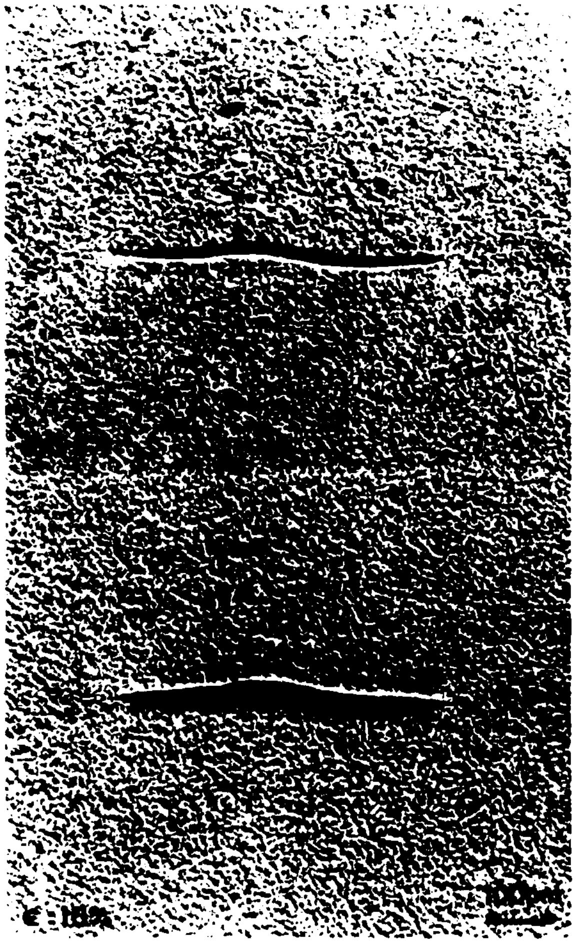

Fig. 5. Scanning electron micrograph of indentation crack in sintered material tested above the transition temperature.

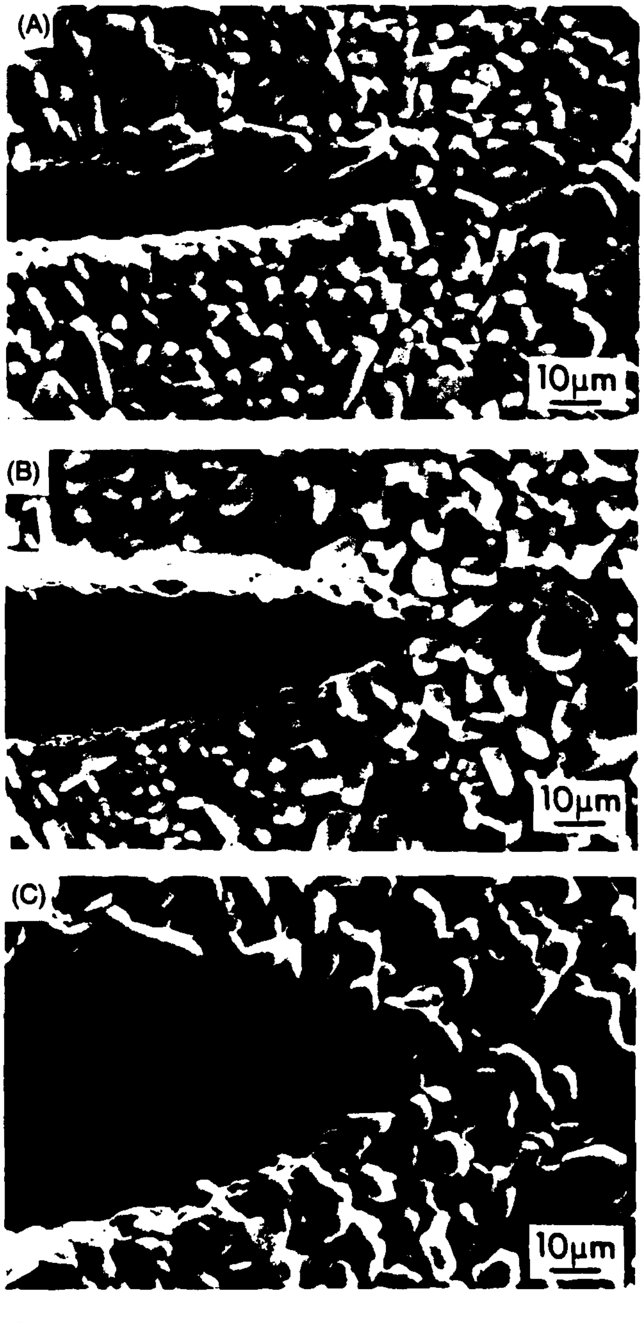

Fig. 6. Crack tip in sintered material tested above the transition temperature exhibiting blunting and opening with no propagation: (A) ε = 3.5%, (B) ε = 6%, (C) ε = 8.5%.

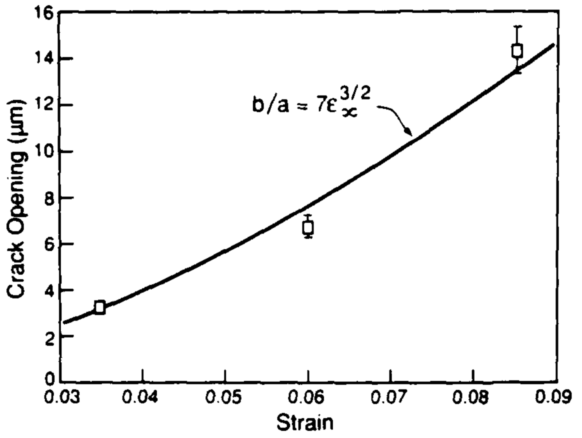

Fig. 7. Crack-tip opening as a function of strain for the sintered silicon carbide.

for *self-similar* shapes are first summarized, followed by approximate results that may apply when the blunting morphology changes (Fig. 6).

When the material ahead of the crack can be represented by a continuum constitutive law, the following expressions obtain:[26]

$$\hat{\sigma}/\sigma_0 = \xi(n) \tag{7a}$$

$$\dot{b} = 0.55C^*/\sigma_f \tag{7b}$$

where ξ is a function of the creep exponent only, $\hat{\sigma}$ is the peak value of σ_{yy}, and σ_f is the flow stress at a strain rate of $1/(n + 1)$. Inserting C^* from Eq. (5) into Eq. (7*b*) then gives, for steady state

$$b/a = 0.55h_s(n + 1)^{1/n}\dot{\varepsilon}_{ss}^{1/n}\varepsilon_{ss} \tag{8}$$

where ε_{ss} is the imposed creep strain. The crack opening is thus predicted to vary linearly with strain. This prediction is at variance with measurements (Fig. 7). The disparity arises because the crack-tip blunting does not develop with a self-similar shape, probably because of discrete grain-size effects that obtain at small b (Fig. 6). When self-similarity is violated, the coefficient ξ in Eq. (7) exhibits an additional dependence on b.[27] Explicit results for ξ are unavailable. Consequently, for present purposes, a simple *assumption* is made and justified by comparison with experimental results. Specifically, it is assumed that the peak stress develops at $r = 2b$, for all b. Then Eq. (6) gives

$$\hat{\sigma}/\sigma_{ss} \approx (h_s a/2Ib)^{1/(n+1)}\bar{\sigma}_{yy} \tag{9}$$

which for the present materials[24] ($n = 2$, $h_s = 1.4$, $I = 5.8$, $\bar{\sigma}_{yy} = 1.8$) gives

$$\hat{\sigma}/\sigma_{ss} \approx 0.89(a/b)^{1/3} \tag{10}$$

Consequently, this assumption predicts that the peak stress *diminishes* upon blunting. An analogous expression for the blunting rate is derived by also allowing the blunting to scale with the peak stress

$$\dot{b} \approx AC^*/\hat{\sigma} \tag{11}$$

where A is a nondimensional coefficient of order unity. Hence, inserting $\hat{\sigma}$ from Eq. (10) and C^* from Eq. (5), gives ($n = 2$)

$$b/a \approx 2A\varepsilon_{ss}^{3/2} \tag{12a}$$

such that

$$\hat{\sigma} \approx (0.7/A^{1/3})\sigma_{ss}\varepsilon_{ss}^{-1/2} \tag{12b}$$

The nonlinear dependence of b on ε_{ss} conforms well with experiment (Fig. 7).

When specimens with blunt cracks are either loaded rapidly to failure at elevated temperature or tested to failure at low temperature, a further elastic stress concentration S develops at the crack tip given by[27]

$$S = (1 + 2a/b)\Delta\sigma \tag{13}$$

where $\Delta\sigma$ is the incremental applied stress upon elastic loading.

IV. Brittle-to-Ductile Transition

The brittle-to-ductile transition involves *local* competition between flow and fracture. Flow at elevated temperature is

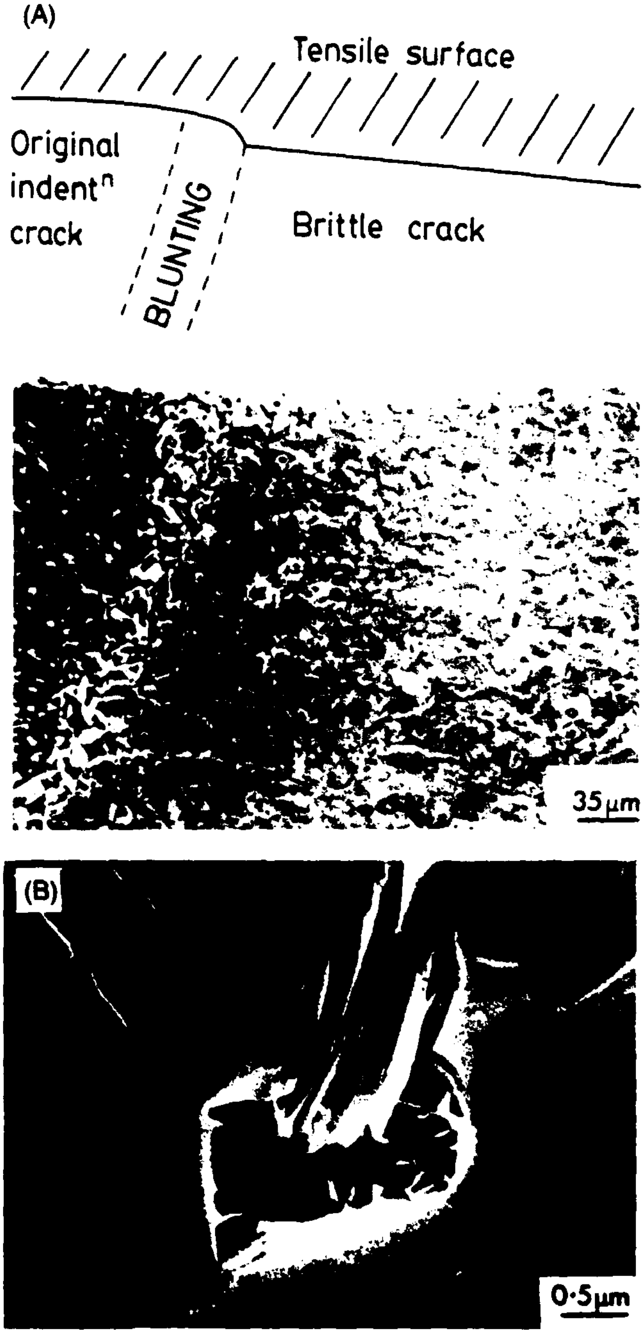

Fig. 8. (A) Scanning electron micrograph and schematic illustration of a sintered SiC fracture face of a bend beam deformed at a temperature above the transition and then fractured at room temperature. (B) Creep damage void nucleated at a graphite inclusion near the blunt indentation crack.

Table III. Nominal Toughness of Sintered SiC After Creep

Test temperature (°C)	Creep strain (%)	b/a	K_v (MPa·m$^{1/2}$)
RT[†]	6.0	0.067	5.5
1800	2.9	0.030	4.0
1800	6.0	0.067	4.9

[†] Room temperature.

governed by creep, while fracture involves propagation of an initial crack. A transition would be expected when the flow stress becomes smaller than the fracture stress. The most critical region is clearly within the crack-tip field. Further discussion thus involves consideration of the competing deformation and fracture processes near the crack tip.

Prediction of trends in the brittle fracture stress with temperature requires that the operative fracture mechanism in the presence of a blunt crack be established. Analysis of the fracture tests on cracks subjected to creep blunting provides pertinent information. In this regard, the transition from brittle to ductile behavior seems to have strong analogies with the corresponding transition in steels,[28] except that the rate dependence is stronger. The basic behavior is schematically illustrated in Fig. 10. At lower temperatures, the crack remains sharp and the toughness is insensitive to temperature. The onset of significant crack-tip creep during loading initiates tip blunting and changes the brittle fracture mechanism to one involving initiation ahead of the crack, at small microstructural flaws (Fig. 10). The fracture is then governed by the interaction of the crack-tip field with the population of flaws, such that the toughness varies strongly with temperature and strain rate and is microstructure-sensitive.[29] In the absence of a creep-damage mechanism in the material, a transition to superplasticity should occur when the peak stress in the crack-tip zone becomes less than the stress needed to activate the largest microstructural flaw.

The activation of flaws in the crack-tip zone is assumed to be governed by Eq. (3), reexpressed in the form

$$\sigma_c \approx \frac{\sqrt{\pi}K_{IC}}{2\sqrt{c}} \tag{14}$$

where σ_c is the critical stress that must be exceeded in the crack-tip zone to cause brittle fracture and c is the radius of the flaws in the damage zone. The ductility requirement is then simply

$$\sigma_f < \sigma_c \tag{15}$$

To further examine this premise, the crack-tip stress at fracture can be calculated for the tests depicted in Fig. 4 by summing Eqs. (10) and (13):

$$\sigma_f = 0.89(a/b)^{1/3}\sigma_{ss} + (1 + 2a/b)\Delta\sigma \tag{16}$$

Then, upon equating σ_f to σ_c, the radius of the flaws in the damage zone c can be calculated. The results for the sintered material (Table IV) yield a *constant* value, $c \approx 1$ μm. Furthermore, this value of c agrees well with measured values (Fig. 8). The results are thus consistent with the proposed criterion for brittle fracture after creep blunting.

With this background, it is now possible to address the ductility transition. Ultimately, this will require knowledge of the size distribution of the crack-tip damage in conjunction with a weakest-link statistical analysis within the crack-tip field.[28] Without this knowledge, an elementary transition criterion for constant displacement rate testing may be based on Eq. (12*b*), which implies that the peak stress decreases as the strain increases, during steady state. Consequently, creep *inhibits* fracture (at least when the damage size, c, is strain-insensitive), whereupon ductility obtains as soon as tip blunting initiates. Conversely, for materials in which the size of the flaws in the damage zone increases upon blunting, brittle fracture can occur during creep.

V. Conclusions

Silicon carbide exhibits a transition from creep brittleness to creep ductility. Below the transition temperature, the material fails by brittle crack extension. Above the transition temperature, the material is superplastic and can withstand strains in excess of 10%. Cracks in sintered silicon carbide open and blunt with damage around the crack tip characterized by cavities opening at graphite inclusions. Cracks in the hot-pressed material open, stay sharp, and propagate at a very slow rate accompanied by cavity formation on grain facets in front of the crack tip.

The brittle fracture stress at rapid strain rates is temperature-insensitive. However, the onset of blunting is strongly dependent on strain rate and temperature. When the crack blunts, the stress field around its tip is reduced and impedes brittle fracture.

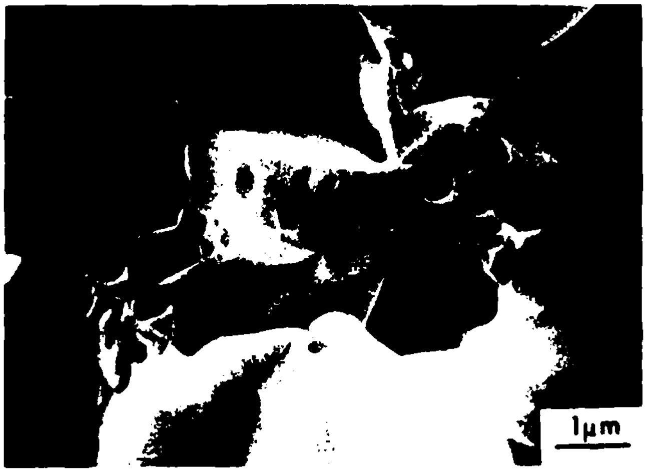

Fig. 9. Scanning electron micrograph of lenticular cavities formed in the region close to the tip of an indentation crack in the hot-pressed SiC which was crept to 10% strain above the transition temperature and subsequently fractured at room temperature.

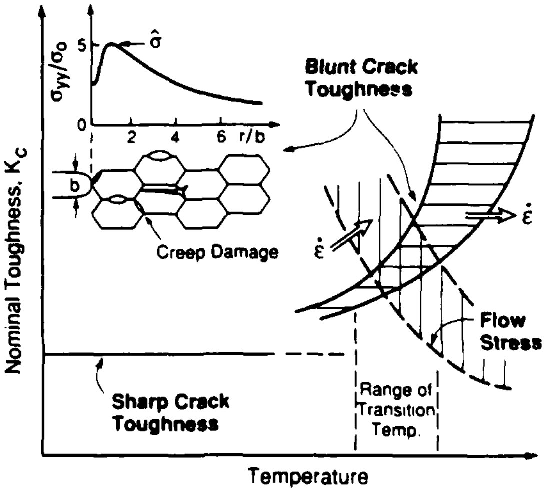

Fig. 10. Schematic representation of the competition between flow and fracture to produce a transition temperature, with a schematic of fracture initiated by creep damage. The strain rate ε arrows indicate the direction in which the flow and failure curves shift as the strain rate is increased.

Table IV. Calculation of Flaw Size in Damage Zone of Sintered SiC

Creep strain (%)	σ_{cs} (MPa)[*]	$\Delta\sigma$ (MPa)[†]	c (μm)[‡]
2.9	346 ± 3	60 ± 2	0.8
6.0	363 ± 23	136 ± 14	1.0

[*] Creep stress. [†] Brittle fracture stress increment. [‡] Calculated damage radius.

References

[1] W. Blumenthal and A. G. Evans, "High-Temperature Failure of Polycrystalline Alumina: II, Creep Crack Growth and Blunting," *J. Am. Ceram. Soc.*, **67** [11] 751–59 (1984).

[2] B. J. Dalgleish, S. M. Johnson, and A. G. Evans, "High-Temperature Failure of Polycrystalline Alumina: I, Crack Nucleation," *J. Am. Ceram. Soc.*, **67** [11] 741–50 (1984).

[3] S. M. Johnson, B. J. Dalgleish, and A. G. Evans, "High-Temperature Failure of Polycrystalline Alumina: III, Failure Times," *J. Am. Ceram. Soc.*, **67** [11] 759–63 (1984).

[4] B. J. Dalgleish and A. G. Evans, "Influence of Shear Bands on Creep Rupture in Ceramics," *J. Am. Ceram. Soc.*, **8** [1] 44–48 (1985).

[5] B. J. Dalgleish, E. B. Slamovich, and A. G. Evans, "Duality in the Creep Rupture of a Polycrystalline Alumina," *J. Am. Ceram. Soc.*, **68** [11] 575–81 (1985).

[6] K. Jakus, S. M. Weiderhorn, and B. J. Hockey, "Nucleation and Growth of Cracks in Vitreous-Bonded Aluminum Oxide at Elevated Temperatures," *J. Am. Ceram. Soc.*, **69** [10] 725–31 (1986).

[7] K. D. McHenry and R. E. Tressler, "High-Temperature Dynamic Fatigue of Hot-Pressed SiC and Sintered α-SiC," *Am. Ceram. Soc. Bull.*, **59** [4] 459–61 (1980).

[8] K. D. McHenry and R. E. Tressler, "Fracture Toughness and High-Temperature Slow Crack Growth in SiC," *J. Am. Ceram. Soc.*, **63** [3–4] 152–56 (1980).

[9] E. J. Minford and R. E. Tressler, "Determination of Threshold Stress Intensity for Crack Growth at High Temperature in Silicon Carbide Ceramics," *J. Am. Ceram. Soc.*, **66** [5] 338–40 (1983).

[10] E. J. Minford, D. M. Kupp, and R. E. Tressler, "Static Fatigue Limit for Sintered Silicon Carbide at Elevated Temperatures," *J. Am. Ceram. Soc.*, **66** [11] 769–73 (1983).

[11] G. Grathwohl, "Regimes of Creep and Slow Crack Growth in High-Temperature Rupture of Hot-Pressed Silicon Nitride"; pp. 573–86 in Deformation of Ceramic Materials II. Edited by R. E. Tressler and R. C. Bradt. Plenum Press, New York, 1984.

[12] F. Wakai, S. Sakaguchi, and H. Kato, "Compressive Deformation Properties of Microstructures in the Superplastic Y-TZP," *J. Ceram. Soc. Jpn.*, **94** [8] 721–25 (1986).

[13] F. Wakai, H. Kato, S. Sakaguchi, and N. Murayama, "Compressive Deformation of Y_2O_3-Stabilized ZrO_2/Al_2O_3 Composite," *J. Ceram. Soc. Jpn.*, **94** [9] 1017–20 (1986).

[14] B. J. Kellet and F. F. Lange, "Hot Forging Characteristics of Fine-Grained ZrO_2 and Al_2O_3/ZrO_2 Composites," *J. Am. Ceram. Soc.*, **69** [8] C-172–C-173 (1986).

[15] B. J. Kellet and F. F. Lange, "Hot Forging Characteristics of Transformation Toughened Al_2O_3/ZrO_2 Composites," *J. Mater. Res.*, **3** [3] 545–51 (1988).

[16] G. Q. Weaver and B. A. Olson, "Sintered Silicon Carbide," U.S. Pat. No. 3836673, Sept. 17, 1974.

[17] J. S. Coppola and R. H. Smoak, "Method of Producing High Density Silicon Carbide Product," U.S. Pat. No. 4080415, Mar. 21, 1978.

[18] P. C. Paris and G. C. Sih, "Stress Analysis of Cracks," *ASTM Spec. Tech. Publ.*, **381**, 30–81 (1965).

[19] G. W. Hollenberg, G. R. Terwilliger, and R. S. Gordon, "Calculation of Stresses and Strains in Four-Point Bending Creep Tests," *J. Am. Ceram. Soc.*, **54** [4] 196–99 (1971).

[20] C. Cary and A. Mocellin, "High Temperature Creep of Dense Fine Grained Silicon Carbide"; pp. 391–403 in Deformation of Ceramic Materials II. Edited by R. E. Tressler and R. C. Bradt. Plenum Press, New York, 1984.

[21] C. M. Packer and O. D. Sherby, "An Interpretation of the Superplasticity Phenomenon in Two-Phase Alloys," *Trans. Am. Soc. Met.*, **60**, 21–28 (1967).

[22] R. Raj and S. Baik, "Creep Crack Propagation by Cavitation Near Crack Tips," *Met. Sci. J.*, **14** [8–9] 385–94 (1980).

[23] H. Riedel and J. R. Rice, "Tensile Cracks in Creeping Solids," *ASTM Spec. Tech. Publ.*, **100**, 112–30 (1980).

[24] J. W. Hutchinson, "Singular Behavior at the End of a Tensile Crack in a Hardening Material," *J. Mech. Phys. Solids*, **16**, 13–31 (1968).

[25] M. Y. He and J. W. Hutchinson, "The Penny-Shaped Crack and the Plane Strain Crack in an Infinite Body of Power-Law Material," *J. Appl. Mech.*, **48**, 830 (1981).

[26] R. M. McMeeking, "Finite Deformation Analysis of Crack-Tip Opening in Elastic-Plastic Materials and Implications for Fracture," *J. Mech. Phys. Solids*, **25**, 357–81 (1977).

[27] C. E. Inglis, "Stresses in a Plate Due to the Presence of Cracks and Sharp Corners," *Trans. Inst. Naval Architects (London)*, **55**, 219–41, (1913).

[28] T. Lin, A. G. Evans, and R. O. Ritchie, "A Statistical Model of Brittle Fracture by Transgranular Cleavage," *J. Mech. Phys. Solids*, **34** [5] 477–97 (1986).

[29] R. O. Ritchie, J. F. Knott, and J. R. Rice, "On the Relationship Between Critical Tensile Stress and Fracture Toughness in Mild Steel," *J. Mech. Phys. Solids*, **21**, 395 (1973). □

MATERIALS

WHISKER TOUGHENING;
A COMPARISON BETWEEN
Al_2O_3 AND Si_3N_3 TOUGHENED WITH SiC

G. H. Campbell, *M. Rühle, B. J. Dalgleish and A. G. Evans
Materials Department
College of Engineering
University of California, Santa Barbara
Santa Barbara, California 93106

(Presented at the 91st Annual Meeting of the American Ceramic Society, Indianapolis, Indiana, April 25, 1989, Paper No. 57-SI-89)

---

* Now at Max-Planck-Institut für Metallforschung, Institut für Werkstoffwissenschaft, Seestraße 92, D-7000 Stuttgart, FRG

ABSTRACT

Two whisker toughened materials have been subject to study, with the objective of identifying the mechanism that provides the major contribution to toughness. It is concluded that, for composites with randomly oriented whiskers, bending failure of the whiskers obviates pull-out, whereupon the major toughening mechanisms are the fracture energy consumed in creating the debonded interface and the stored strain energy in the whiskers, at failure, which is dissipated as acoustic waves. The toughening potential is thus limited. High toughness requires extensive pull-out and hence, aligned whiskers with low fracture energy interfaces.

KEY WORDS: Ceramic, Composite, Toughness, Model, TEM

1. INTRODUCTION

The toughening of ceramics by whiskers typically includes contributions from debonding, crack bridging, pull-out and crack deflection.[1-3] It is important to ascertain the relative roles of these contributions, because each mechanism predicts very different dependencies of toughness upon microstructure. Crack deflection is ostensibly governed only by whisker shape and volume fraction[4]: albeit that the relative elastic moduli and thermal expansion coefficients may have implicit effects on the deflection path. Conversely, the other contributions depend sensitively upon the mechanical properties of the interface, the whisker strength/toughness, the whisker radius and the volume fraction, as elaborated below.

Toughening by bridging is induced by debonding along whisker/matrix interfaces[1] (Fig. 1). The debonding allows the whiskers to remain intact within a small bridging zone behind the crack.[1] The magnitude of the toughening involves considerations of the debond extent and the mode of fiber failure, as well as of residual stress effects.[1,5] Various attempts have been made to model the toughening and to compare the predictions with experiment. The most comprehensive and recent attempt[6] established many of the salient features. However, neither residual stress effects nor the contribution to toughness from the energy of the debonded surfaces were included and, furthermore, explicit determination of the debond extent was not used for comparison between experiment and theory. The present article examines these and related issues by further experimental investigation and by presenting a fully inclusive model in a form that provides direct physical insight. For this purpose, crack/microstructure interactions are investigated in two whisker-toughened systems: the Al_2O_3/SiC system which has interfaces subject to residual compression and Si_3N_4/SiC with interfaces in residual tension.

2. SOME RELEVANT MECHANICS

2.1 INTERFACE DEBONDING

Cracks on bimaterial interfaces are characterized by a strain energy release rate, $\mathcal{G}$, and a phase angle of loading, ψ.[7,8] The latter is a measure of the mode mixity, such that $\psi = 0$ refers to a pure crack opening mode and $\psi = \pi/2$ represents an interface crack subject to crack surface shear. Specifically, debonding along the interface occurs when $\mathcal{G}$ reaches the interface fracture energy Γ_i at the relevant phase angle, ψ. For a matrix crack subject to mode I loading, the incidence of *initial debonding,* rather than cracking into the fiber, is found to be governed by the ratio of interface to fiber fracture energies Γ_i/Γ_f and the whisker orientation (Fig. 2).[8] For the present composites, values of Γ_i/Γ_f needed to debond whiskers normal to the crack plane should be either $< 1/3$ for Si_3N_4/SiC or $< 1/4$ for Al_2O_3/SiC. Note that this prediction is *independent* of the residual stress.

Growth of the initial debond along the interface is influenced by additional variables, such as the residual stress and the whisker radius. Debond growth is most prevalent in the crack wake.[9,10] Analysis of wake debonding for interfaces under *residual tension*[9] indicates that debond growth in the wake occurs when the stress t on the fiber reaches a critical value t^*, given by,

$$t^* \approx 2.2 E_f e_T \tag{1}$$

where E_f is Young's modulus for the fiber and e_T is the misfit strain. When $t > t^*$, the debond propagates unstably up the interface.

Residual compression results in different behavior. In this case, $\mathcal{G}$ is strongly influenced by the friction coefficient μ along the previously debonded interface.[10] The basic debonding features indicate that again, a threshold stress must be exceeded before debonds can further propagate in the wake. However, for stresses in excess of the threshold, debonding occurs stably to an extent determined by the friction coefficient μ and the residual strain, until $t \rightarrow E_f e_T/\nu$ (with ν being Poisson's ratio for the fiber), whereupon the interface separates and further debonding occurs unstably. The debonding behavior is thus sufficiently complex that prediction of trends with e_T, Γ_i and other material variables is unlikely to be instructive. Instead, the preceding results may be used as the mechanics background needed to facilitate interpretation of observed trends in debonding, as elaborated below.

2.2 TOUGHENING

The steady-state toughening $\Delta\mathcal{G}_c$ imparted by whiskers can be considered to have four essential contributions, as elaborated in the Appendix. These contributions can be insightfully expressed in the simple form (Fig. 3);

$$\Delta\mathcal{G}_c/fd = S^2/E - Ee_T^2 \quad 4(\Gamma_i/R)/(1-f) + (\tau/d)\sum_i(h_i^2/R) \tag{2}$$

where d is the debond length, R the fiber radius, f the volume fraction and S the whisker "strength." The first term S^2/E is simply the *strain energy stored* in the whisker *over the debonded length* on both sides of the matrix crack, before the whisker fails ($S^2/2E$ on either side of the crack). This strain energy *dissipates* as acoustic waves and thus contributes *positively* to the toughening. The second term is the *residual strain energy* in each composite element *within the debond length*, as governed by the misfit strain e_T. This strain energy is *lost* from the system when the fiber fails and thus, *detracts* from the toughness, independently of the sign of e_T. The third term is the energy needed to create the *debond fracture surface*, with Γ_i

being the fracture energy per unit area. This term must be *positive*. The last term is the *pull-out contribution*, with h_i being the pull-out length and τ the sliding resistance of the debonded interface. This term is again positive, because heat is generated by the frictional sliding at the interfaces. The above result is all inclusive and has not been specifically presented elsewhere.‡ Furthermore, it deviates from certain of the other results reported in the literature for each of the individual terms, principally in the magnitude of the constants of proportionality. It is believed that Eqn. (2) is the simplest possible result that is also physically consistent with the mechanisms involved.

Optimization of toughness based on these terms is discussed later. Presently, it is noted that all contributions scale with the debond length d, *indicating that large d is desirable.* However, it is also recognized that d should have a functional dependence,

$$d/R = F(\Gamma_i, e_T, S) \tag{3}$$

where the function F has yet to be determined.

The present experimental results are examined using Eqn. (2) to assess the various contributions to toughness, based on direct measurements of h, d, R, f. Thereafter, implications for high toughness are discussed.

---

‡ The results are strictly applicable to reinforcements *normal to the crack plane*. Whiskers inclined to the crack are more likely to fail by bending and thus, result in smaller pull-out toughening.

3. MATERIALS

Four basic materials have been used for the present investigation: two whisker toughened materials and two reference matrix materials. One whisker toughened material is a commercial product, consisting of Al_2O_3 toughened with 20 vol. % SiC whiskers, prepared by hot pressing*. The other toughened material was a SiC toughened Si_3N_4** containing 20 vol. % SiC whiskers, 4 wt-% Y_2O_3 as a sintering aid and was densified by reaction bonding followed by HIPing. Microstructural investigations were performed, not only for the composites, but also for the matrices and those observations were used as reference. The Al_2O_3 matrix material was a hot pressed system containing 1/4 volume percent MgO, heat treated to create the corresponding grain size. The reference Si_3N_4** contained 4 wt % Y_2O_3.

The mode I toughnesses $\mathcal{G}_c$ of the four materials, evaluated using a surface flaw technique,[1] are summarized in Table I. A comparison with models requires evaluation of the increase in toughness caused by the whiskers, $\Delta\mathcal{G}_c$, which for Al_2O_3/SiC is 40–80 Jm^{-2} and for Si_3N_4/SiC is 25–55 Jm^{-2} (Table I).

4. CHARACTERIZATION

4.1 MICROSTRUCTURE OF WHISKERS

Characterization of two different as-received SiC whiskers*** indicated a broad distribution of length (1μm . 25μm) and diameter (0.1μm to 1.0μm). Quite frequently, clusters of whiskers and irregular, serrated-edged whiskers were found.

---

* Greenleaf, Inc.
** Norton Company
*** ARCO and Tateho whiskers

The average length and diameter were 17.5μm and 0.5μm, respectively, for ARCO whiskers and 11.7μm and 0.42μm for Tateho whiskers.

The whiskers had a high density of planar faults lying on the close-packed plane (basal plane) perpendicular to the long axis.[12] The faults resulted in a complex arrangement in thin lamellae of different α and β polytypes normal to the whisker axis. Furthermore, the core region of the ARCO whiskers contained a high density of small spherical impurity clusters and/or cavities. Half of the Tateho whisker are hollow. The outer skin of both types of whiskers was covered with a 2nm SiO_2 rich layer as revealed by defocus imaging (Fig. 4a)[13] and X-ray photoelectron spectroscopy (Fig. 6b).[14]

4.2 MICROSTRUCTURE OF THE COMPOSITES

Thin foils of each of the materials suitable for TEM have been prepared by mechanical polishing and dimpling followed by ion beam thinning. Transmission electron microscope (TEM) characterization of the materials has been accomplished using conventional, analytical and high resolution microscopy. From conventional TEM micrographs of the SiC *whisker toughened Al_2O_3 material*, a matrix grain size of ~ 1μm was determined. Dark field studies[15] have indicated the presence of a thin (< 5nm thickness) amorphous layer at the interface between the whiskers and the matrix, consistent with previous studies. The thickness of the amorphous layer at the whisker/matrix interface depends on the purity of the Al_2O_3. However, even in Al_2O_3-SiC composites processed using ultraclean materials,[16] a thin (1nm-thick) SiO_2 layer can be detected by TEM imaging. Specifically, by using a range of defocus conditions[13,15] (Fig. 5), the expected contrast reversal for different signs of defocusing can be observed. Furthermore, it is apparent that the contrast at the interface is not caused by preferential etching. Notably, the interface between the whiskers and the Al_2O_3 matrix in Fig. 5 is perpendicular to the edge of the foil and no preferential etching is visible close to the amorphous region near the edge, because the interface contrast disappears gradually in the amorphous part of the specimen.[‡] Occasionally, amorphous pockets also exist at junctions between matrix grain boundaries and the interface (Fig. 5b). However, within the resolution of dark field and high resolution procedures (~ 1nm), the matrix grain boundaries appear to be devoid of amorphous material.

Occasionally, a whisker is completely embedded in *one* Al_2O_3 grain. In such cases, strain contours become visible under dynamical TEM imaging (Fig. 6). A semi-quantitative evaluation of the strain perpendicular to the whisker diameter is possible by calculating the scattering of modified Bloch waves[17] in the thick foil approximation and evaluating the number and distance of contrast oscillations for different excitation errors. The observations confirm that a homogeneous compressive strain ε occurs in the whisker, with $2 \cdot 10^{-3} < \varepsilon < 6 \cdot 10^{-3}$: a result consistent with the known thermal expansion characteristics of Al_2O_3 and SiC and a cooling range $\Delta T \approx 1000°C$.

Studies conducted on the *Si_3N_4 reference material* have revealed several relevant microstructural features. Dark field and high resolution microscopy have indicated that an intercrystalline phase, presumably amorphous, is present as a thin continuous film of equilibrium thickness (Fig. 7a). Grain pockets are mostly crystalline, except for the thin, intercrystalline outer layer (Fig. 7b). Analytical microscopy and diffraction studies are consistent with α-$Y_2Si_2O_7$ being the predominant crystalline grain boundary phase. The crystalline pockets are typically 50–100nm in diameter. The whisker toughened Si_3N_4 had several different characteristics. The whiskers are typically 100–500nm in diameter. About half of the whiskers are hollow, in which case they become filled by the sintering-aid phase. This phase, which is also present at grain pockets, remains glassy upon cooling to room temperature. Analytical microscopy indicates a relatively high SiO_2 content in this phase. Presumably, the excess SiO_2 that prevents crystallization of this phase is introduced by the oxide layer that preexists on the SiC whiskers. High resolution microscopy shows that this intercrystalline phase is present as a thin film at *all* Si_3N_4 grain boundaries and, most importantly, at the interface between the Si_3N_4 grains and the SiC whiskers (Fig. 7c).

[‡] A hole would be visible at the site of the interface for the case of preferential thinning.

Finally, in order to clarify ambiguity, it is noted that it has been occasionally reported in the literature that *no* glassy phase can be observed at interfaces between SiC whiskers and the surrounding matrix.[18] A careful inspection of available micrographs[18] suggests that the interface plane in such studies was inclined to the electron beam, whereupon the glassy interphase would not be detected. Specifically, it is evident from Fig. 8 that an amorphous interface layer can only be imaged if the foil thickness t is such that $t \leq \sqrt{aD/2}$, with a being the thickness of the amorphous foil and D the diameter of the whiskers and if the interface is parallel to the electron beam.

4.2 DEBONDING AND BRIDGING

i) Transmission Electron Microscopy

Observations of debonding and of bridging zones have been made in the TEM. The procedure developed for studying these characteristics consists of indenting the material, mechanically dimpling in the region of the indentation crack tips and then ion thinning to a thickness in excess of the whisker diameter. This procedure ensures debonding and bridging representative of plane strain crack propagation in bulk material and avoids the anomalous crack extension and debonding that can occur upon thinning to less than the whisker diameter. In order to use these foils to investigate near tip phenomena, it is imperative that the specimens be subject to tilting through a large angular range, because the debond and matrix crack opening displacements are small and only detectable when the electron beam is essentially aligned with the crack plane. Some typical views of the bridge zone with schematic drawings used to highlight the salient features.

For Al_2O_3/SiC, the matrix cracks are mostly transgranular and conchoidal, while cracks in the whiskers are planar and always parallel to the basal plane of SiC. These distinctive fracture paths facilitate interpretation of the micrographs. The series of micrographs and schematical drawings summarized in Fig. 9 illustrate the salient features. Locations A and B refer to the crack/whisker interaction, which include whiskers having axis either normal or inclined to the crack plane. In both cases, the whiskers are debonded and are fractured. Near the crack tip (location C), a bridging zone with intact whiskers is apparent, with the crack tip located at the arrow. Tilting studies have revealed the extent of debonding at the whisker/matrix interface as illustrated in the accompanying schematic (Fig. 9d). Such observations are typical of whiskers that exist within a bridging zone that usually extends to about 4 to 6 whisker spacings. *The length of the debonds is variable and ranges between about 2R and 6R*, R being the whisker radius.

For Si_3N_4/SiC, the same general features noted for Al_2O_3 are again evident, as exemplified by Fig. 10a, wherein the debonds are between the arrows. The lengths of these debonds, which can be measured directly from the micrograph, range from R to 3R. Usually, the second whisker behind the crack tip is fractured, indicating that the bridging zone is very small. It is also noted that, because elongated Si_3N_4 grains are present, debonding along the grain boundaries with the equiaxed matrix grains is evident (Fig. 10b). Such debonding is exactly analogous to that occurring at whisker interfaces. Consequently, the debonds of the whisker interface are more difficult to detect than in the Al_2O_3 composite. An interesting sequence of events can be deduced from Fig. 10c, in which the main crack is clearly visible (large white gap). This crack propagated from the upper right to the lower left. It is surmised that, when the crack first interacted with the whisker, the interface debonded (to a length of about 3 whisker radii). The whisker then fractured within the debond length and pulled out by about 20nm (the width of the gap). While being pulled out, the whisker would be subject to bending, resulting in enhanced stresses, as manifest in strain fringes at the corner of the whisker (arrow in Fig. 10c). Consequently, the whisker fractured a second time in the plane of the matrix crack.

It is also of importance to examine whisker failure. In general, whisker fracture can either initiate at the end of the debond by kinking into the whisker,[5] or the debond cracks could remain at the interface such that the whisker fails by the propagation of a pre-existing flaw within the debonded length. The former mode has been rigorously verified in several cases (Figs. 9 and 10) by extensive tilting to confirm the absense of a debonded region beyond the location of the whisker fracture. The latter is much more difficult to unambiguously identify and cannot be substantiated at this juncture.

ii) Scanning Electron Microscopy

Polished surfaces containing indentation cracks have been examined in the scanning electron microscope. The residual crack opening allows observation of some aspects of bridging and debonding. For the Al_2O_3/SiC, a low accelerating voltage provides contrast between the Al_2O_3 and SiC and facilitates observation. Within the spatial resolution of the SEM, *debonds* are only occasionally evident, usually at intact inclined whiskers (Fig. 11a) remote from the crack front. Crack surface interlocking is also evident (Fig. 11b), caused by debonding around the whisker ends. In some cases, whisker cracks are apparent (Fig. 11a) again at inclined whiskers, with the crack often forming near the end of the debond. Measurements of *bridging* zones associated with intact whiskers are not possible by direct SEM, because of resolution limitations. However, for Al_2O_3/SiC, use of a dilute orthophosphoric acid etch allows dissolution of some of the matrix, preferentially around the crack (Fig. 12). Matrix removal permits both the intact (Fig. 12b) and fractured whiskers (Fig. 12c) to be identified, with reference to the crack front and thus, allows measurement of the bridging zone size, L. For this composite, L is about 3 to 4 whisker spacings.

Inspection of fracture surfaces by SEM provides complementary information regarding *pull-out* as well as debonding (Fig. 13). Studies on both composites reveal that inclined whiskers fracture on a plane normal to the whisker axis, such that the crack-surface is within one whisker radius of the matrix crack plane. *Pull-out is thus negligible.*

5. COMPARISON BETWEEN THEORY AND EXPERIMENT

Initial comparison between theory and experiment can be achieved based on measured values of the debond length and using Eqn. (2) for the toughness. The relative magnitudes of the four contributions to toughness from elastic bridging, residual strain, debond surface energy and pull-out can then be readily assessed, using the material properties listed in Table I and using $d/R = 2-6$ for Al_2O_3 and 1–3 for Si_3N_4 with $f = 0.2$ and $R = 0.25\mu m$ for both composites. The *pull-out* contribution is negligible since only a small fraction of whiskers exhibit this phenomenon. The reduction in toughness from the *residual strain*, $Ee_T^2 f d$, ranges between $0.3\ Jm^{-2}$ for Si_3N_4/SiC to $2\ Jm^{-2}$ for Al_2O_3/SiC and is thus of negligible importance (in part, accounting for the similar toughening levels measured for both composites). The toughening contribution from the *elastic strain energy* stored in the whiskers up to failure, S^2fd/E, is dominated by the choice of whisker "strength." The appropriate choice for S is unclear because the "gauge length" is small and because the whiskers may be subject to degradation upon composite processing. For initial purposes, it is *assumed* that S is in the range 4–8GPa,[6] whereupon this component of toughening is at most 45 Jm^{-2} for Al_2O_3/SiC and 25 Jm^{-2} for Si_3N_4/SiC. Finally, the *debonding energy* contribution is estimated by noting that amorphous silicates have a fracture energy, $\Gamma_i = 6-8\ Jm^{-2}$. The toughening caused by debonding is then of order 50 Jm^{-2} for Al_2O_3/SiC and 25 Jm^{-2} for Si_3N_4 /SiC. The energy needed to create the debond surface and the strain energy dissipated from elastic bridging thus appear to provide similar contributions to toughness. Furthermore, the toughness level provided by the combination of both processes is comparable to the measured values (Table I).

6. IMPLICATIONS AND CONCLUSIONS

The preceding experiments and calculations firstly indicate that *non-aligned*, inclined whiskers typically fail by bending and do not provide a pull-out contribution to toughening.* Consequently, composites with *randomly oriented whiskers cannot normally be expected to exhibit high toughness*. Subject to this limitation, useful toughness increases are still possible, as governed by an optimum combination of bridging and debonding. Since residual strain is invariably detrimental, *matched thermal expansions are desirable*. *Enhanced debonding* is also desirable, but then the relative contributions to toughness from bridging and from the debonded surfaces requires further elaboration. The debond length is expected to scale directly with the whisker radius, to increase with increase in S and to depend inversely on Γ_i (Eqn. 3). Consequently, d/R and Γ_i are coupled in such a way that the contribution to $\Delta \mathcal{G}_c$ from the *energy of the debonded surfaces* is expected to be weakly dependent on Γ_i and *insensitive to whisker radius*, but should *increase* as the *whisker strength* increases. A corresponding assessment of the *bridging contribution* yields very different conclusions. In this case, the direct dependence on debond length suggests that this contribution should *increase* appreciably as either *Γ_i decreases* or the *whisker radius increases* and should become the dominant contribution to toughness for small Γ_i and large R, provided that the *"strength" S is also high*. Indeed, it is important to note that careful experiments[6] indicate a systematic dependence of $\Delta \mathcal{G}_c$ on R, confirming an important contribution of elastic bridging to toughening. However, the whisker "strength" is not related in simple form to the uniaxial fracture strength of the whiskers. Further research is needed to understand the operative relationships.

---

* An exception may be graphite whiskers which can sustain very high bending strains and have debonded interfaces with a low sliding resistance.

The factors which govern the *debond length* merit brief additional consideration. While small Γ_i and large S clearly enhance debonding, such variables as residual strain, surface roughness and friction coefficient could be important. The available calculations (Appendix) indicate that, when the non-dimensional residual strain parameter Q $(= S\nu/E_f|e_T|)$ is much larger than unity, the Poisson contraction of the whisker is large compared with the misfit displacements. Then, residual strain is unimportant: instead, the amplitude of the roughness on the debond surface dominates debonding. Conversely, when $Q < 1$, residual strain effects dominate debonding in the sense that positive e_T (interface tension) enhances debonding and vice versa. For the present materials, the inverse trend with residual strain (*large* debond lengths for Al_2O_3/SiC in which e_T is *negative*) suggests that roughness effects and interface characteristics are more important in debonding than the residual strain. Indeed, consistent with this implication, Q is larger than unity. Whisker roughness effects would thus appear to merit further investigation.

APPENDIX

CRACK BRIDGING AND TOUGHNESS

Several aspects of crack bridging have been addressed by analysis, particularly the stress/crack opening relation t(u). For whiskers *normal* to the crack plane with interfaces subject to *residual tension*, u/t is linear when the debond length is constant and a threshold stress is needed to achieve initial opening of the crack, such that[9]

$$u/Re_T = (t/E_f e_T)(\lambda_1 + \lambda_2 d/R) + \lambda_3 + \lambda_4 d/R \tag{A1}$$

where λ_i (i = 1–4) are coefficient tabulated in Table II. When the whiskers fail at a critical axial stress t = S, the change in toughness imparted by the whiskers, $\Delta \mathcal{G}_c$, when d is fixed, becomes;[11]

$$\Delta \mathcal{G}_c \approx 2f \int_0^{t=S} t\,du + 4f\Gamma_i d/(1-f)R$$

$$\approx \frac{fS^2R\left[(\lambda_1+\lambda_2 d/R)^2-(E_f e_T/S)^2(\lambda_3+\lambda_4 d/R)^2\right]}{E_f(\lambda_1+\lambda_2 d/R)} + 4f\Gamma_i d/(1-f)R \tag{A2}$$

The first term is the contribution to toughness from elastic bridging, whereas the second term is the contribution from the debond surface energy. When d/R > > 1 and the material is elastically homogeneous, Eqn. (A2) reduces to

$$\Delta \mathcal{G}_c = \frac{fS^2d}{E}\left[1-(Ee_T/S)^2\right] + 4f\Gamma_i d/(1-f)R \tag{A3}$$

revealing that the toughness increases linearly with increase in the debond length and diminishes as the residual strain increases. Indeed, $\Delta \mathcal{G}_c \to 0$ as $E_f |e_T| \to S$ because then, the whiskers fail upon cooling from the processing temperature.

For composites containing whiskers normal to the crack and with interfaces in residual compression, t(u) is dependent on the friction coefficient as well as the debond length. For fixed d,[10]

$$\frac{u}{e_T R} = (d/R)(1+v)/v - (1-vF)(1-2v^2\phi)[\exp(2\mu d\phi/R)-1]/2\mu\phi\upsilon \qquad (A4)$$

where

$$\phi = v(1-f+f\Sigma)/[\Sigma(1+f)+(1-f)(1-2v)]$$

and $\Sigma = E_f/E_m$, with E_m being the matrix modulus.

For homogeneous elastic properties, Eqn. (A4) reduces to;

$$\frac{\upsilon u}{e_T R} = (1+\upsilon)d/R - (1-\upsilon F)[\exp(D)-1]/\mu\upsilon \qquad (A5)$$

where $D = \mu\upsilon d/R$. The toughness for constant d is thus;[10]

$$\Delta \mathcal{G}_c = \frac{fS^2R[\exp(D)-1]}{\mu\upsilon E}\left\{1-\left(\frac{e_T E}{\upsilon S}\right)^2\left[\frac{(1+\upsilon)D}{\exp(D)-1}-1\right]^2\right\} + 4f\Gamma_i d/(1-f)R \qquad (A6)$$

Furthermore, for small μ, the toughness reduces to Eqn. (A3).

The above results for $\Delta \mathcal{G}_c$ are clearly simplifications because the debonds are expected to extend in the crack wake and the integral should include this behavior.

Subject to this limitation, it is apparent that, for brittle whiskers which fail at a characteristic stress, S, the composite toughness invariably decreases with increase in misfit strain, e_T, whether tensile or compressive in sign, provided that the debond length is independent of e_T. Furthermore, when the friction coefficient is small, the toughness is also essentially independent of the sign of the residual stress.

TABLE I

Properties of Materials and Constituents

Material	$\alpha(C^{-1} \times 10^6)$	E(GPa)	$\mathcal{G}_c(Jm^{-2})$	$\Delta\mathcal{G}_c(Jm^{-2})$	
				Experiment	Theory
Al_2O_3	7.5	400	25 ± 5		
Si_3N_4	3.5	320	50 ± 10		
SiC	4.5	420	15 ± 5		
Amorphous Silicate Interphase	—	100	7 ± 1		
Al_2O_3/SiC		420	85 ± 15	60 ± 20	~ 80
Si_3N_4/SiC		350	90 ± 15	40 ± 15	~ 30

TABLE II

The Coefficients λ_i(i = 1,4), used in the expression for the Matrix Crack Opening: $\Sigma = E_f/E_m$

$\lambda_1(\Sigma,f)$								
$\Sigma \backslash f$	**0.05**	**0.1**	**0.2**	**0.3**	**0.4**	**0.5**	**0.6**	**0.7**
0.4	3.22	3.42	2.04	1.76	1.55	1.40	1.28	1.19
1.0	1.85	1.96	1.30	1.14	1.00	0.87	0.75	0.63
2.5	0.96	1.01	0.72	0.64	0.57	0.49	0.41	0.30

$-\lambda_3(\Sigma,f)$								
$\Sigma \backslash f$	**0.05**	**0.1**	**0.2**	**0.3**	**0.4**	**0.5**	**0.6**	**0.7**
0.4	2.59	2.75	1.64	1.42	1.25	1.12	1.03	0.95
1.0	1.73	1.84	1.23	1.07	0.94	0.81	0.70	0.59
2.5	1.05	1.11	0.79	0.71	0.62	0.54	0.44	0.33

Σ	$\lambda_2(\Sigma)$	$-\lambda_4(\Sigma)$
0.4	0.838	1.062
1.0	0.910	1.058
2.5	0.964	1.043

REFERENCES

[1] M. Rühle, B. J. Dalgleish and A. G. Evans, Scr. Metall. 21 (1987) 681.

[2] P. F. Becher and G. C. Wei, J. Am. Ceram. Soc. 67 (1984) C267.

[3] P. Becher, Mtls. Sci. Eng., in press.

[4] K. T. Faber and A. G. Evans, Acta Met. 31 (1983) 565.

[5] D. B. Marshall and A. G. Evans, Materials Forum, 11 (1988) 304.

[6] P. F. Becher, C. H. Hsueh, P. Angelini and T. N. Tiegs, J. Am. Ceram. Soc. 71 (1988) 1050.

[7] J. R. Rice, J. Appl. Mech. 110 (1988) 98.

[8] M. He and J. W. Hutchinson, Jnl. Appl. Mech, in press.

[9] P. G. Charalambides and A. G. Evans, Jnl. Am. Ceram. Soc., in press.

[10] L. S. Sigl and A. G. Evans, Mechanics of Materials, in press.

[11] P. G. Charalambides, to be published.

[12] S. R. Nutt, J. Am. Ceram. Soc. 67 (1984) 428.

[13] L. Reimer, Transmission Electron Microscopy, Springer Berlin (1986) p. 201.

[14] V. K. Sarin and M. Rühle, Composites 18 (1987) 129.

[15] D. R. Clarke, Ultramicroscopy 4 (1979) 33.

[16] J. R. Porter, unpublished.

[17] M. Wilkens and M. Rühle, phys. stat. sol.(b) 49 (1972) 749.

[18] W. Braue, R. W. Carpenter and D. J. Smith, Proc. 46th EMSA Conference, San Francisco Press, Inc. (1988) P. 734.

FIGURE CAPTIONS

Fig. 1. A schematic of a bridging zone in a reinforced composite

Fig. 2. A debond diagram: the dependency of fracture energy on elastic mismatch and whisker orientation

Fig. 3. A schematic representation of the four mechanisms that contribute to toughening by whiskers

Fig. 4. Analysis of outer layer on a Tateho SiC whisker

a) Through-focus images at the edge of a whisker (i) $\Delta f < 0$, (ii) $\Delta f \approx 0$, (iii) $\Delta f > 0$. The amorphous layer is clearly visible on the infocus image ($\Delta f = 0$). The defocus images indicate that the density (scattering power) of the outermost layer is less than that of SiC (bright contrast for negative defocusing)

b) XPS spectrum (courtesy Sarin and Rühle[14])

Fig. 5. TEM micrograph of interface between SiC whisker and Al_2O_3 matrix (i) $\Delta f = -96nm$, (ii) $\Delta f \approx 0$, (iii) $\Delta f = 96nm$. The interface is parallel to the electron beam. The contrast of the amorphous grain boundary phase is equivalent to that of the amorphous layer at the edge of the foil.

Fig. 6. Stress contours around whiskers: dynamical

a) Bright field and b) Dark field images. A quantitative evaluation the matrix strain can be obtained from the number and positions of contrast oscillations (micrograph taken by E. Bischoff)

Fig. 7. Transmission electron microscopy study of Si_3N_4 materials

a) High-resolution image revealing continuous thin amorphous layer in the matrix

b) High-resolution image of the interface of the crystalline phase at the matrix grain pockets and a Si_3N_4 grain

c) High-resolution image of the amorphous layer between a matrix grain and a SiC whisker

Fig. 8. Maximum allowed thickness, t, for imaging at amorphous layer of thickness a

Fig. 9. Transmission electron microscopy studies of the crack tip region in thick foils of Al_2O_3/SiC. A comprehensive visualization of debonding and cracking can only be achieved by imaging under different orientations by extensive tilting. Consequently, to assist in summarizing the behavior, a schematic drawing is shown in addition to *one* TEM micrograph of each crack/whisker interaction:

a) Overview of crack tip region
b) Region A with schematic 3-dimensional drawing
c) Region B with schematic 3-dimensional drawing
d) Region C bridging zone with schematic overview. The debonded interface zones between whiskers and matrix are hatched. The whiskers are not fractured.

Fig. 10 a) Transmission electron micrograph of a region close to crack tip in SiC/Si_3N_4. On the micrograph, the crack enters from the lower left and ends at the position of the uppermost arrow. Debond cracks are between arrows along the interfaces.
b) Transmission electron micrograph of Si_3N_4/SiC indicating grain boundary debonding in the matrix between an elongated grain and equiaxed grains
c) Transmission electron micrograph of a multiply-fractured whisker well into the crack wake

Fig. 11. Scanning electron microscope image of the crack tip region in Al_2O_3/SiC

a) Initiation of a whisker crack from the end of an inclined debond
b) Debonding around the whisker end resulting in crack surface interlocking

Fig. 12. SEM investigation of a crack in Al_2O_3/SiC after etching in orthophosphoric acid

a) Overview
b) Crack tip region showing intact whiskers

Fig. 13. Scanning electron microscope image of fracture surface of Si_3N_4/SiC

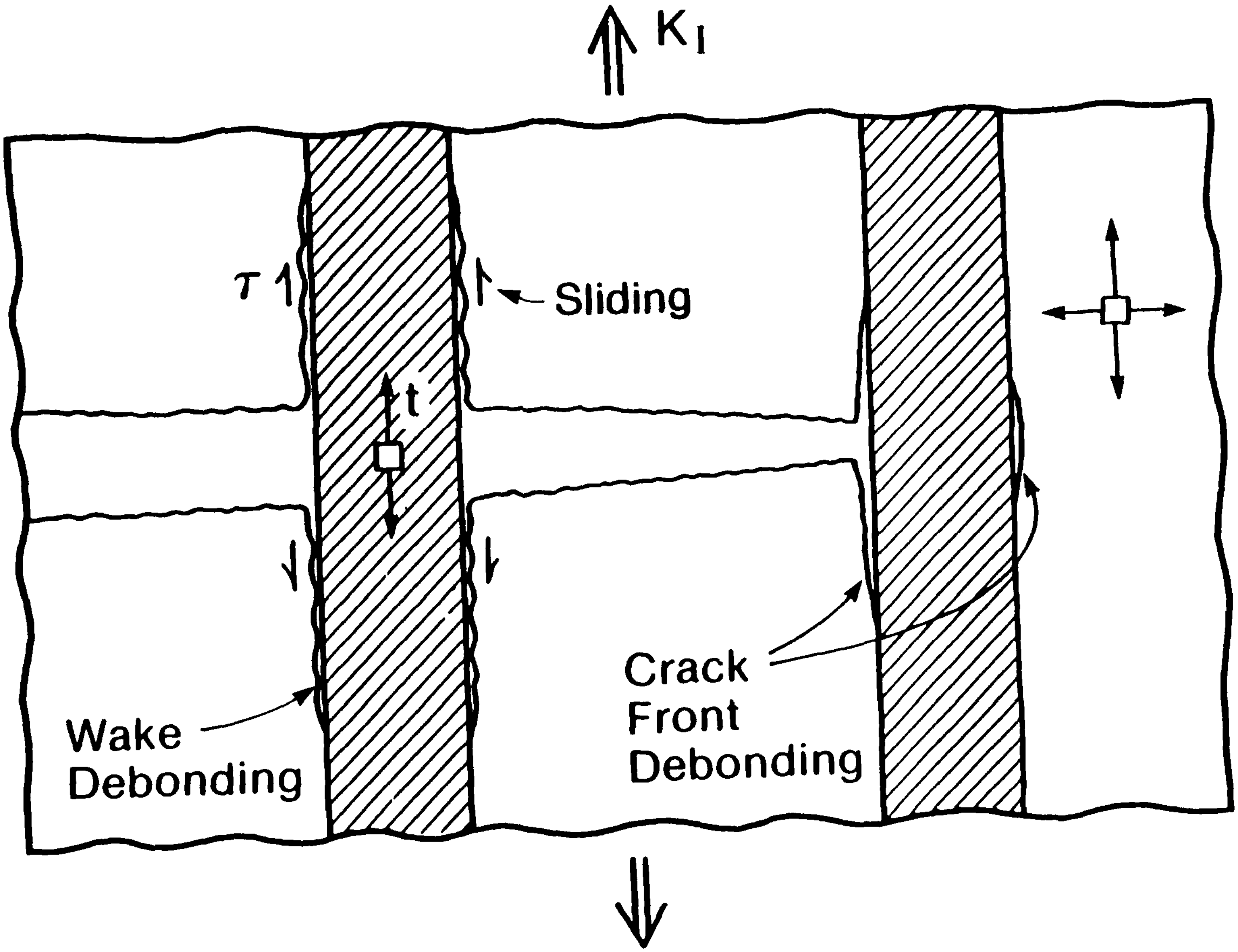
K_I
τ
Sliding
t
Wake
Debonding
Crack
Front
Debonding

Figure 1

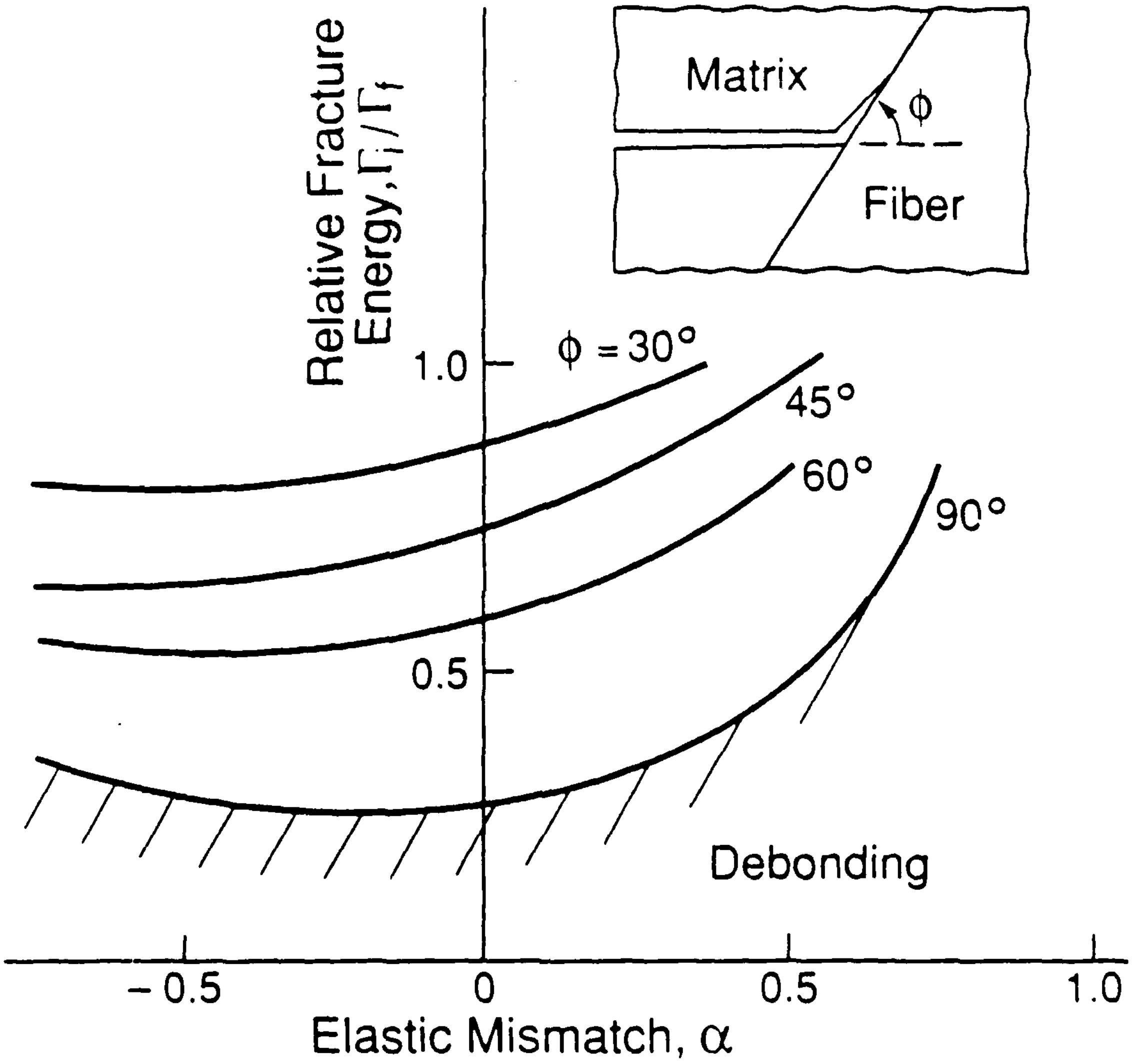

Matrix
φ
Fiber
Relative Fracture Energy, Γ_i/Γ_f
1.0
0.5
φ = 30°
45°
60°
90°
Debonding
−0.5
0
0.5
1.0
Elastic Mismatch, α

Figure 2

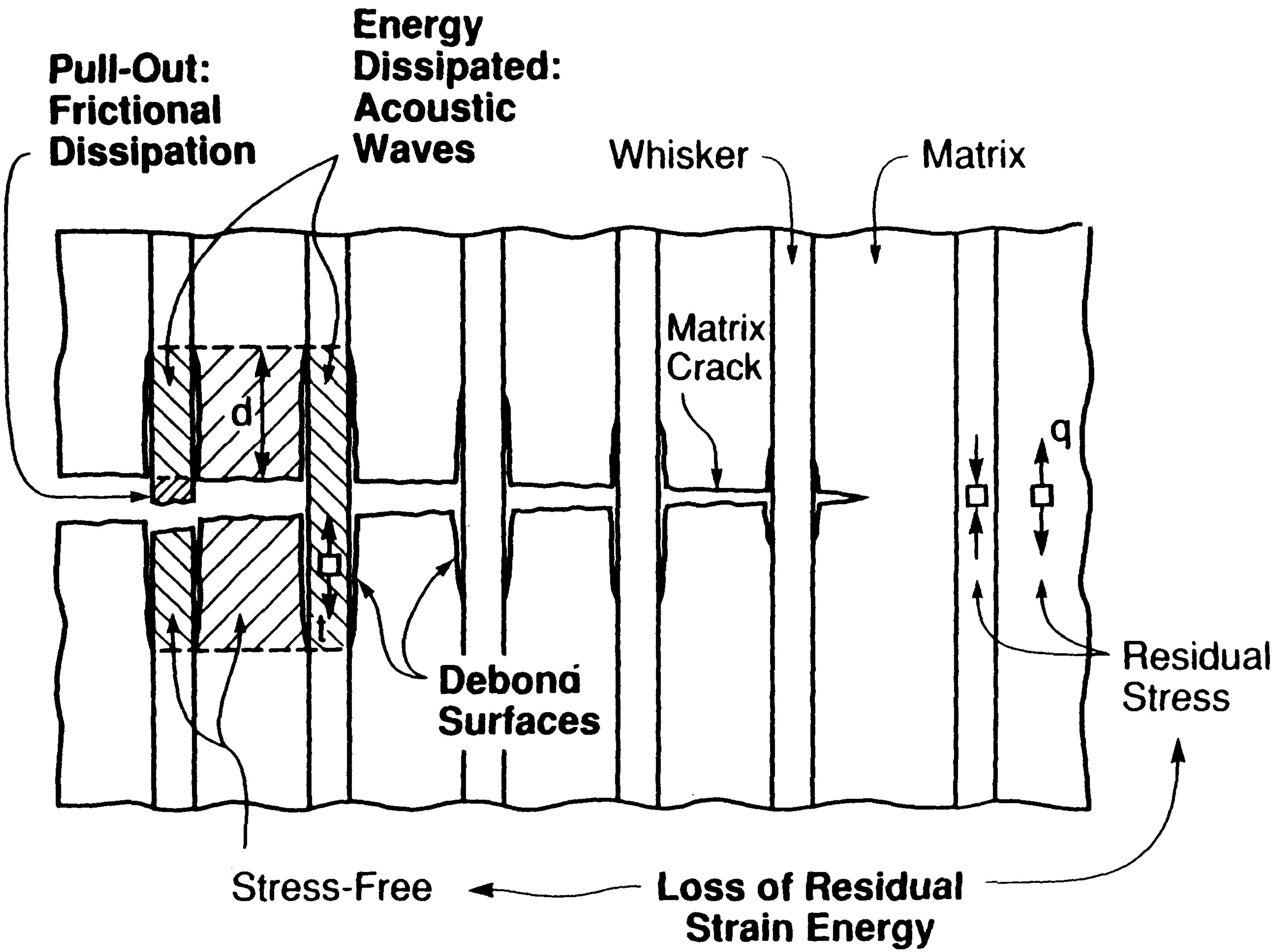
Pull-Out:
Frictional
Dissipation
Energy
Dissipated:
Acoustic
Waves
Whisker
Matrix
Matrix
Crack
d
t
q
Debond
Surfaces
Residual
Stress
Stress-Free
Loss of Residual
Strain Energy

Figure 3

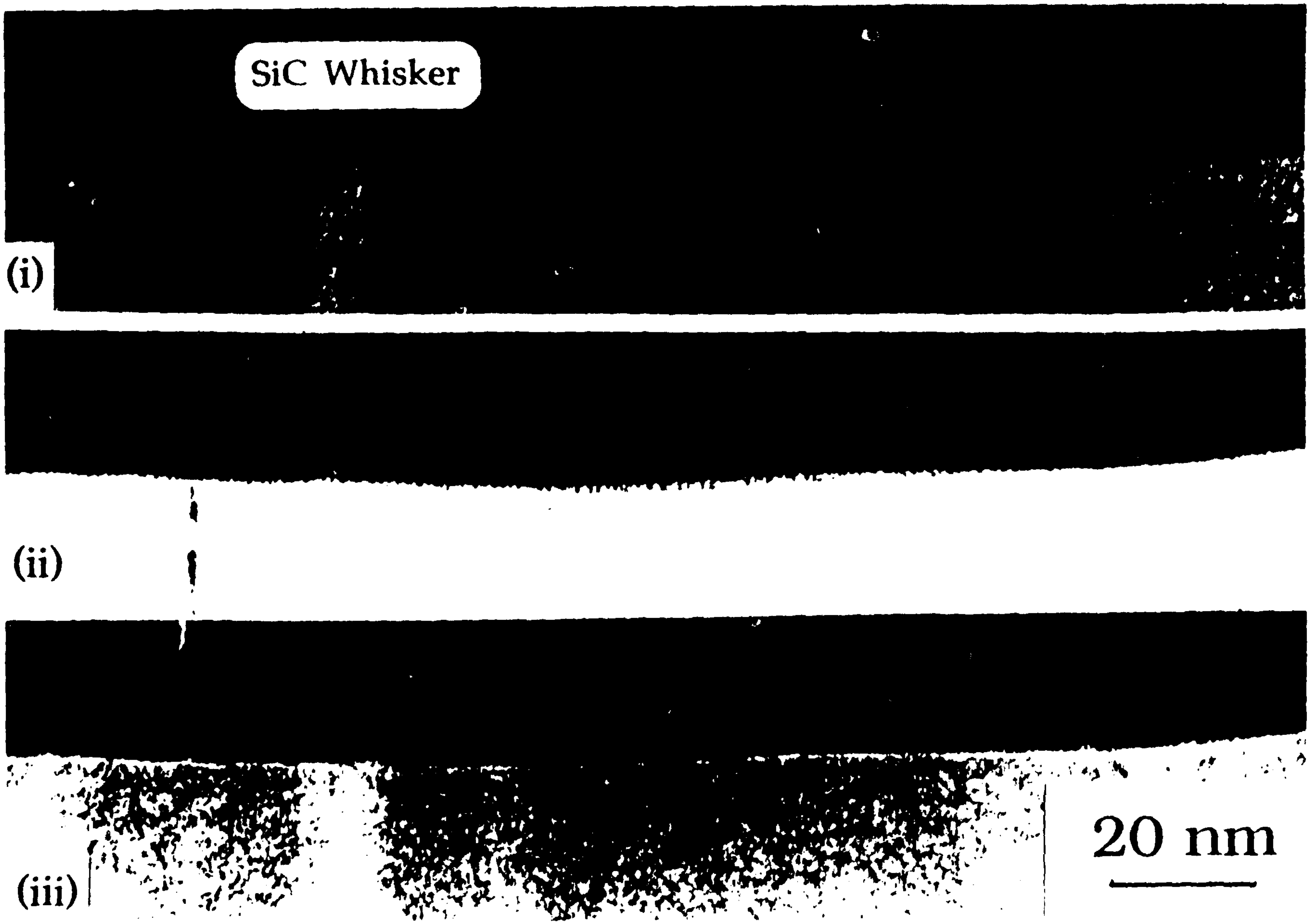
SiC Whisker
(i)
(ii)
(iii)
20 nm

Figure 4a

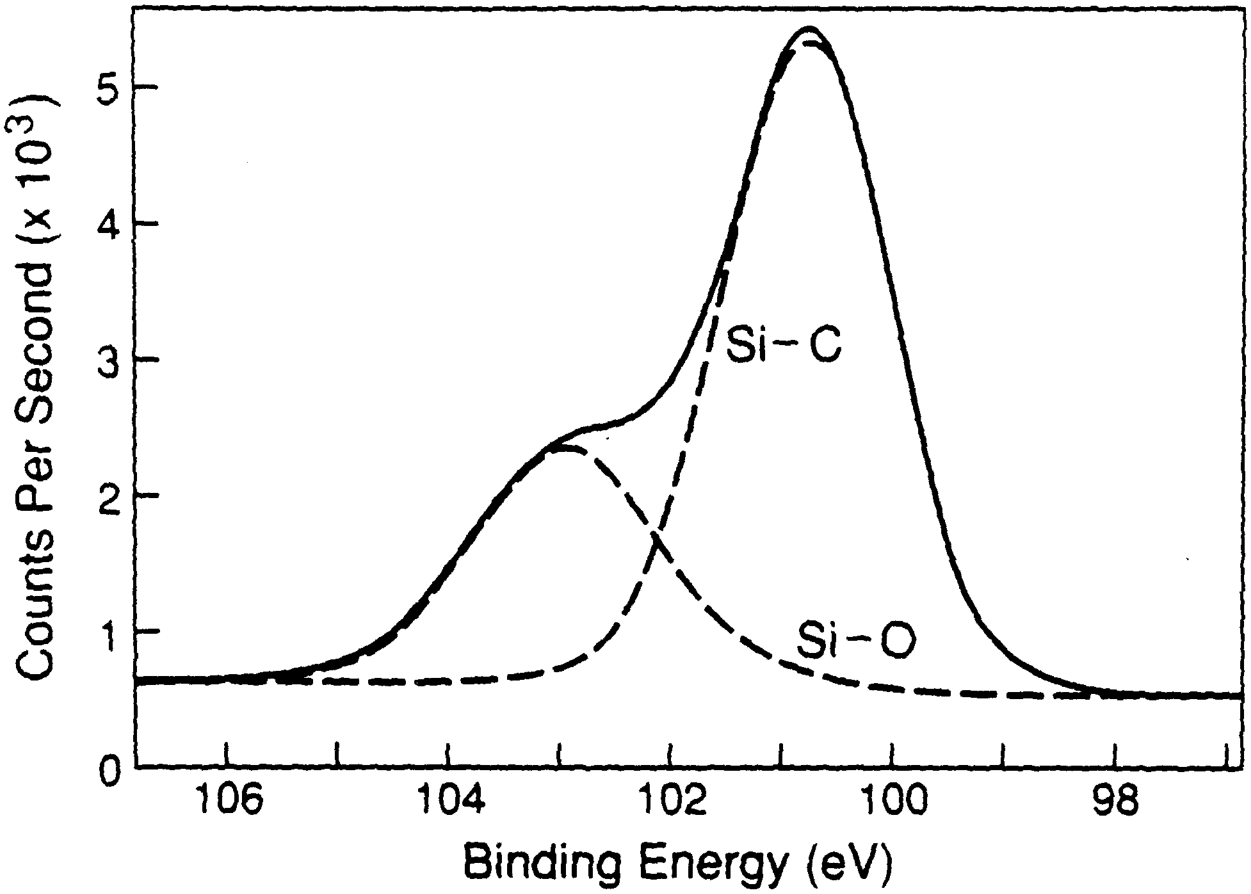
Counts Per Second (x 10^3)
0
1
2
3
4
5
106
104
102
100
98
Binding Energy (eV)
Si−C
Si−O

Figure 4b

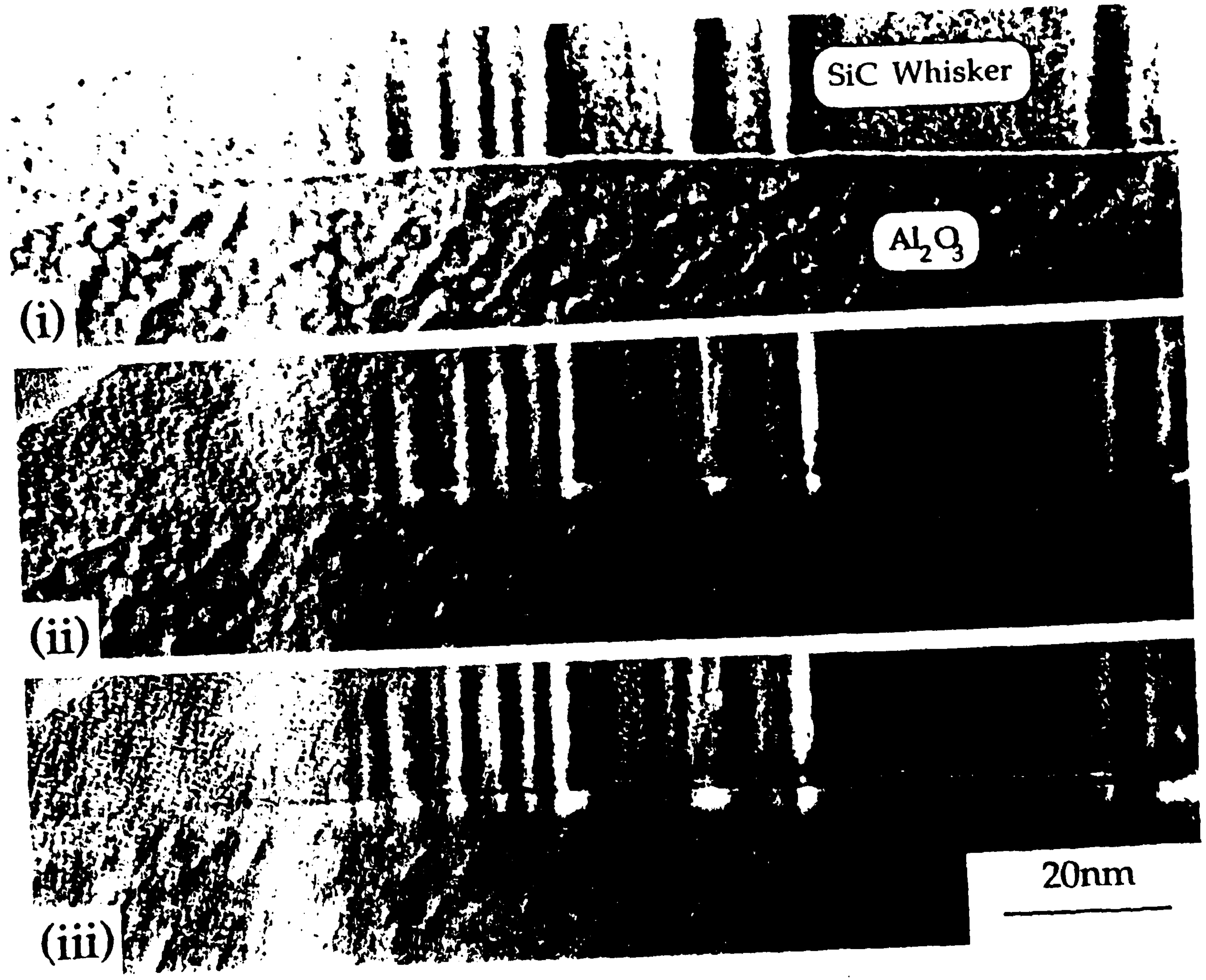
SiC Whisker
Al_2O_3
(i)
(ii)
(iii)
20nm

Figure 5

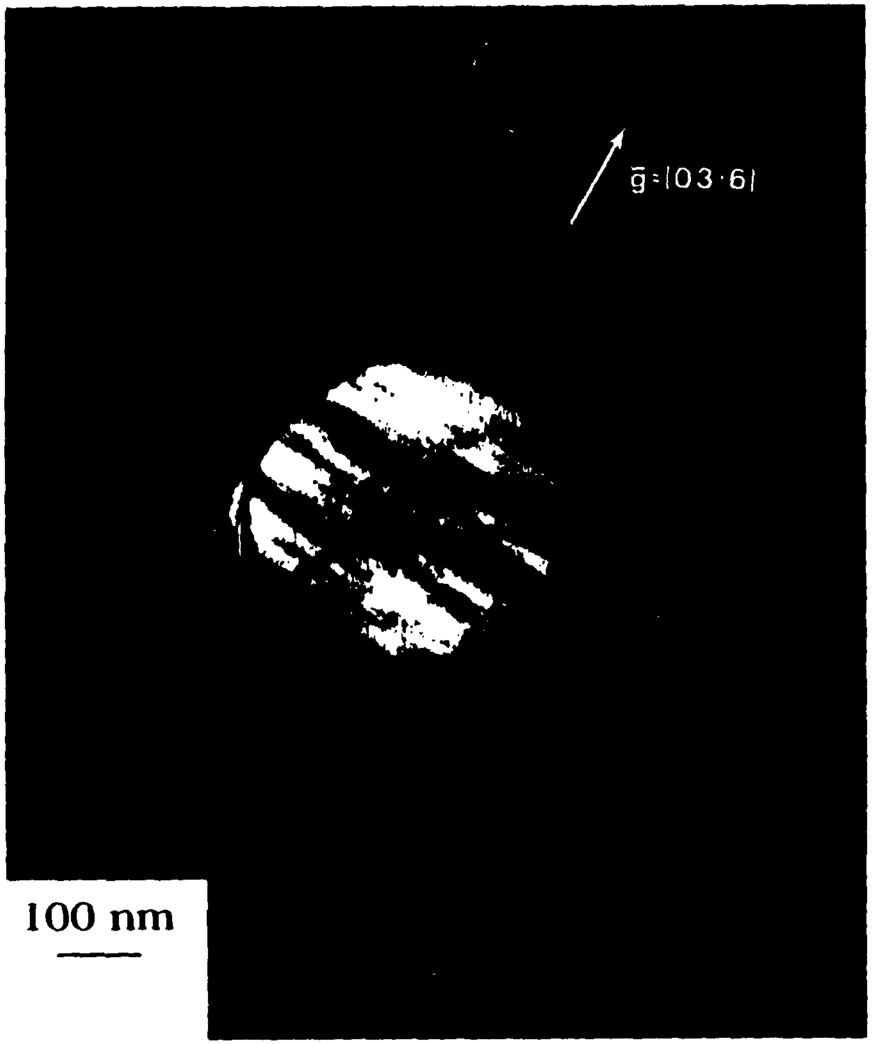
$\bar{g} = [03\cdot6]$
100 nm

Figure 6a

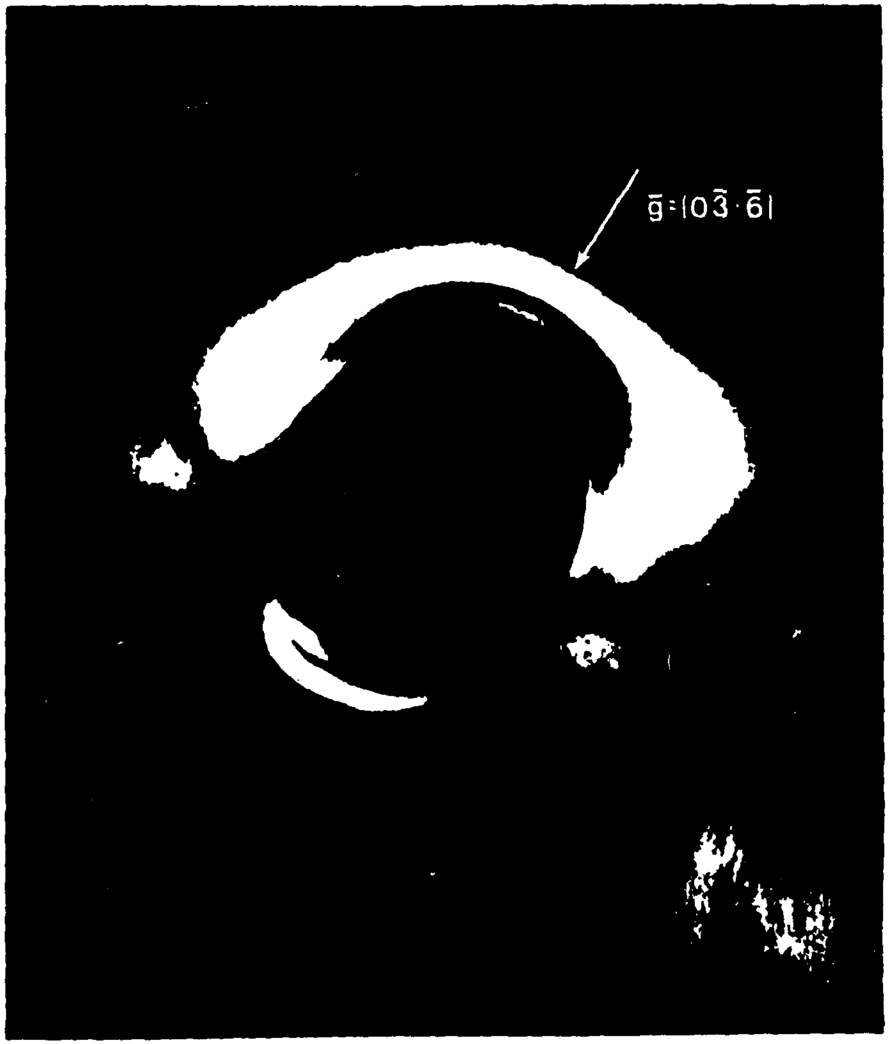
$\bar{g} = [0\bar{3}\cdot\bar{6}]$

Figure 6b

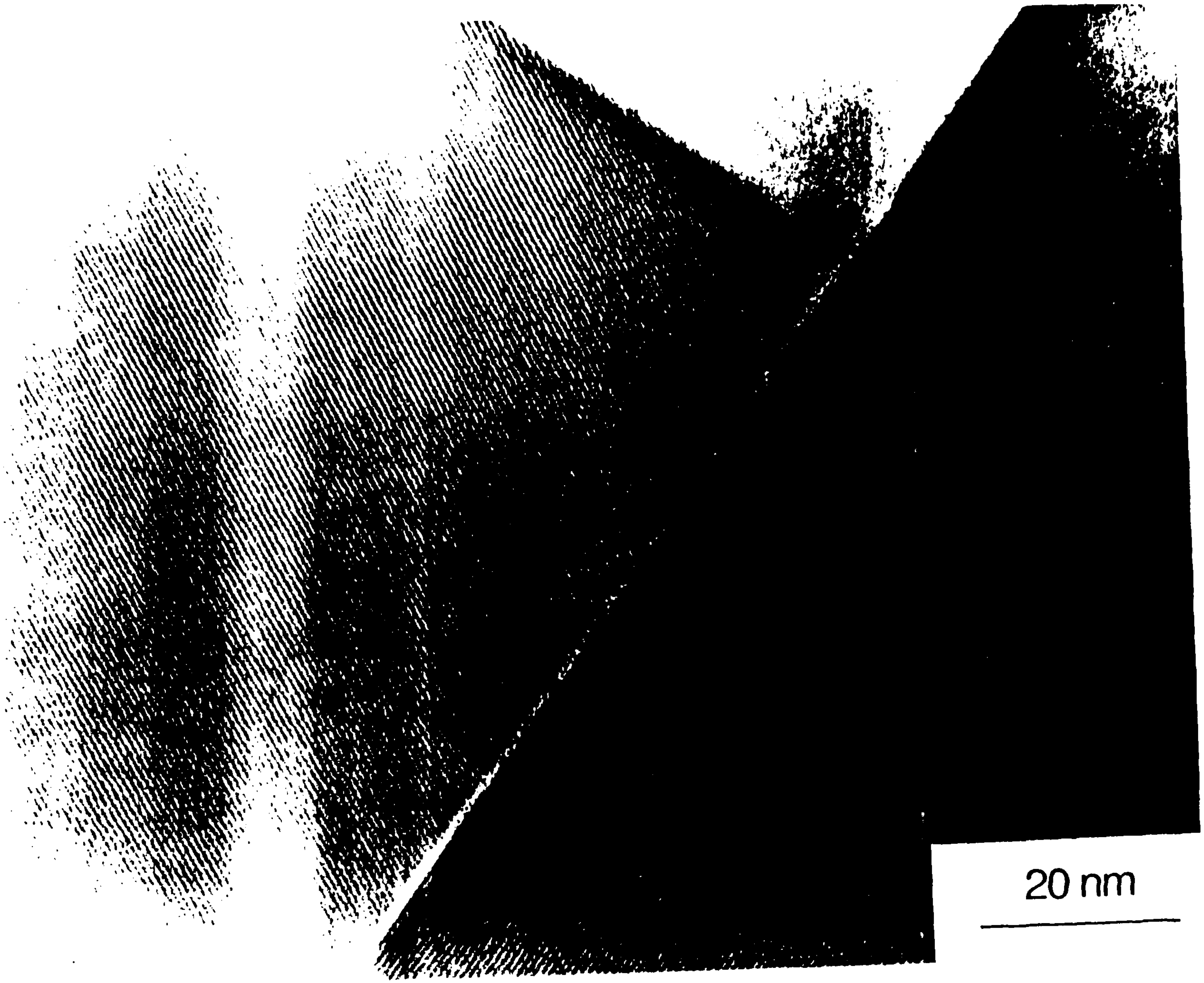

Figure 7a

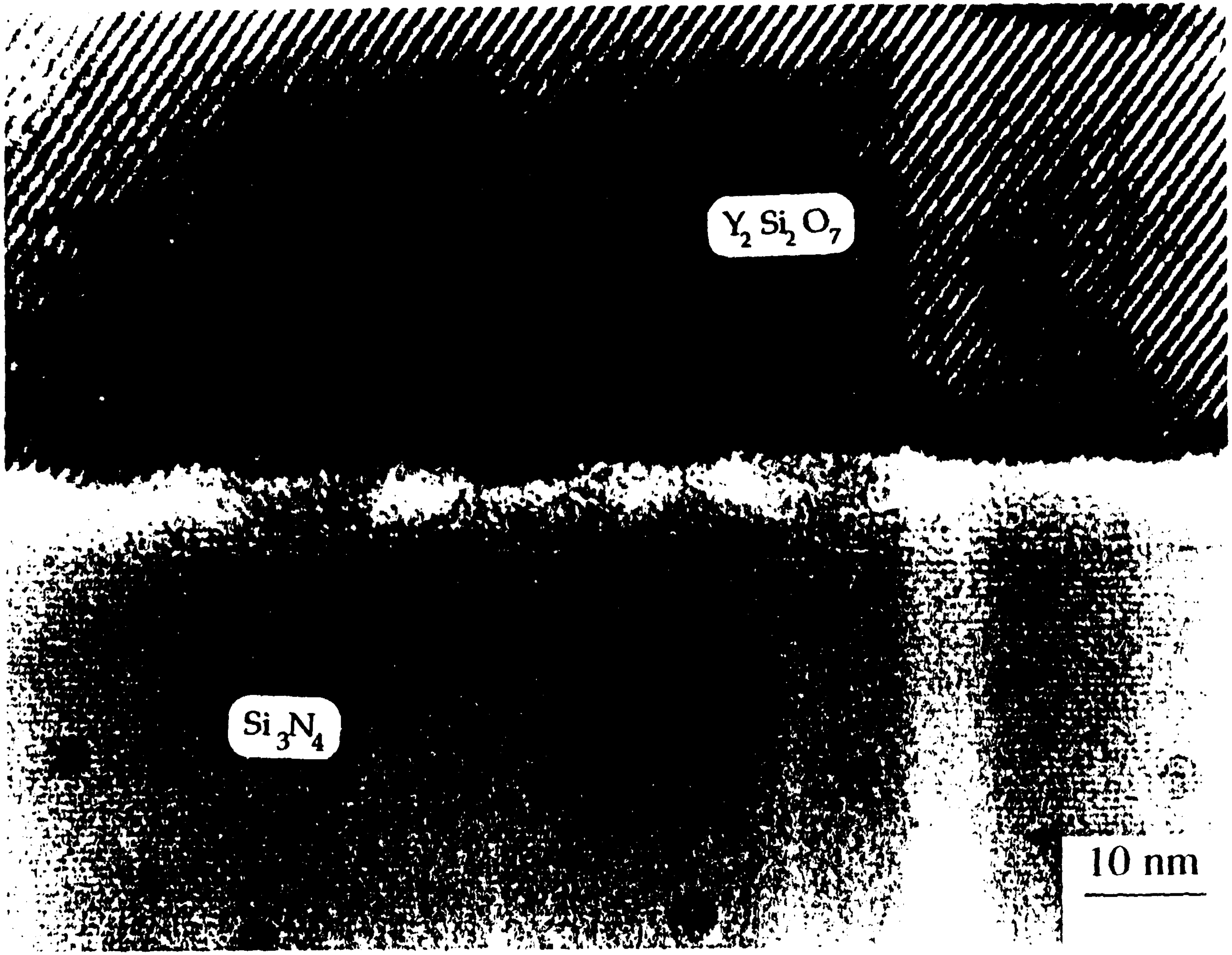
$Y_2Si_2O_7$
Si_3N_4
10 nm

Figure 7b

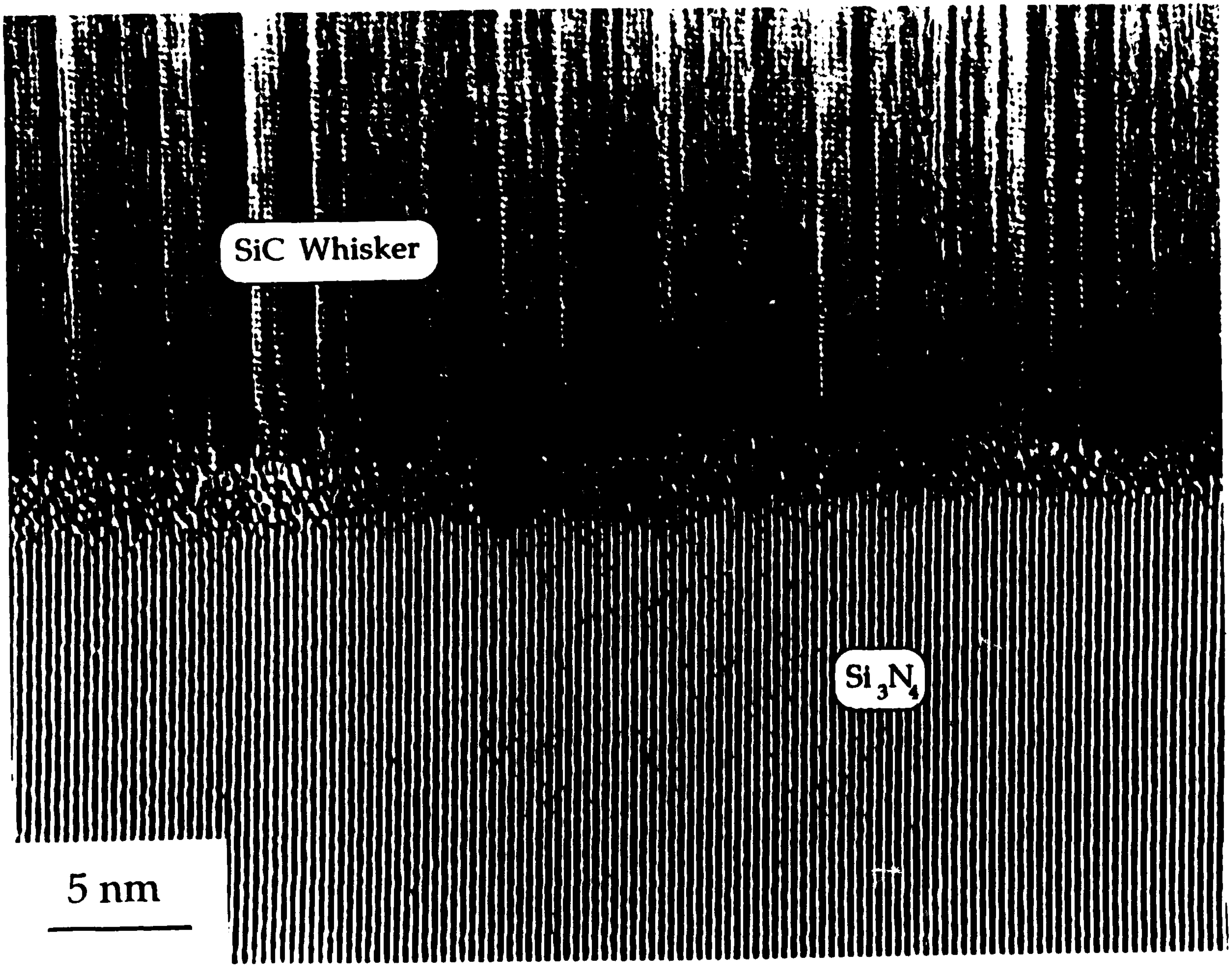
SiC Whisker
Si_3N_4
5 nm

Figure 7c

TEM of Amorphous Grain Boundary Phase
(thickness a)

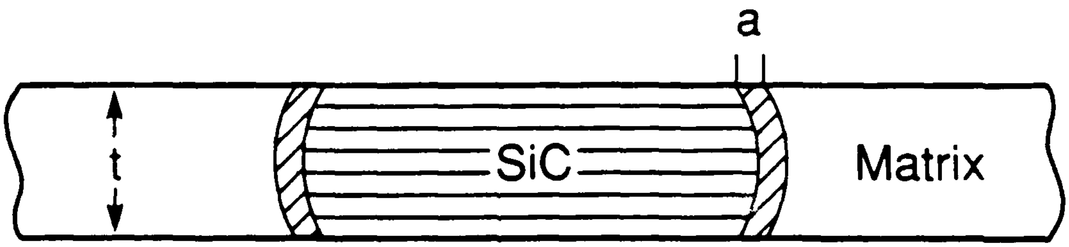
a
t
SiC
Matrix

Maximum Foil Thickness $t \leq \sqrt{a \cdot D/2}$
(D = fiber diameter)

Figure 8

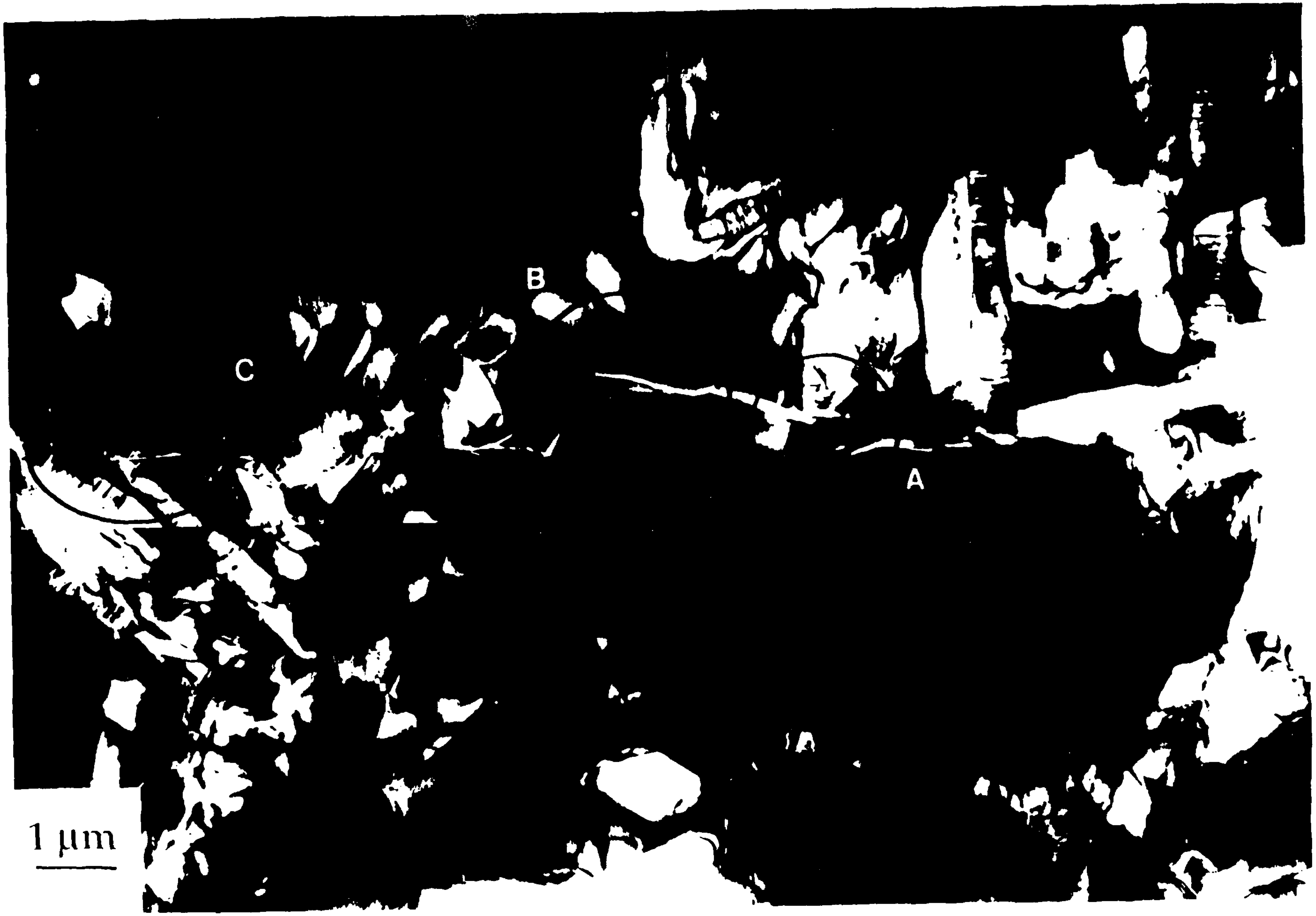

Figure 9a

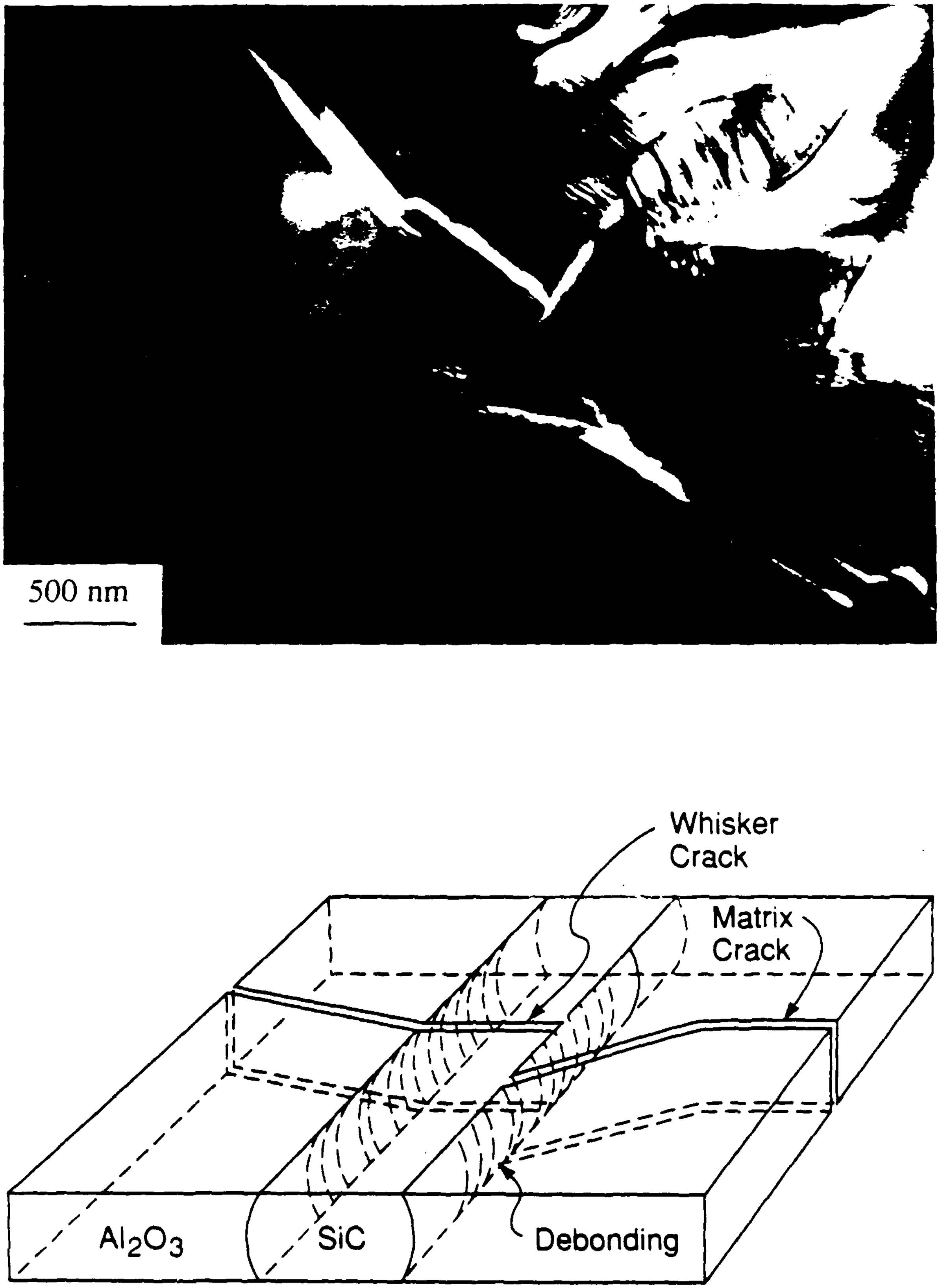
500 nm
Whisker Crack
Matrix Crack
Al_2O_3
SiC
Debonding

Figure 9b

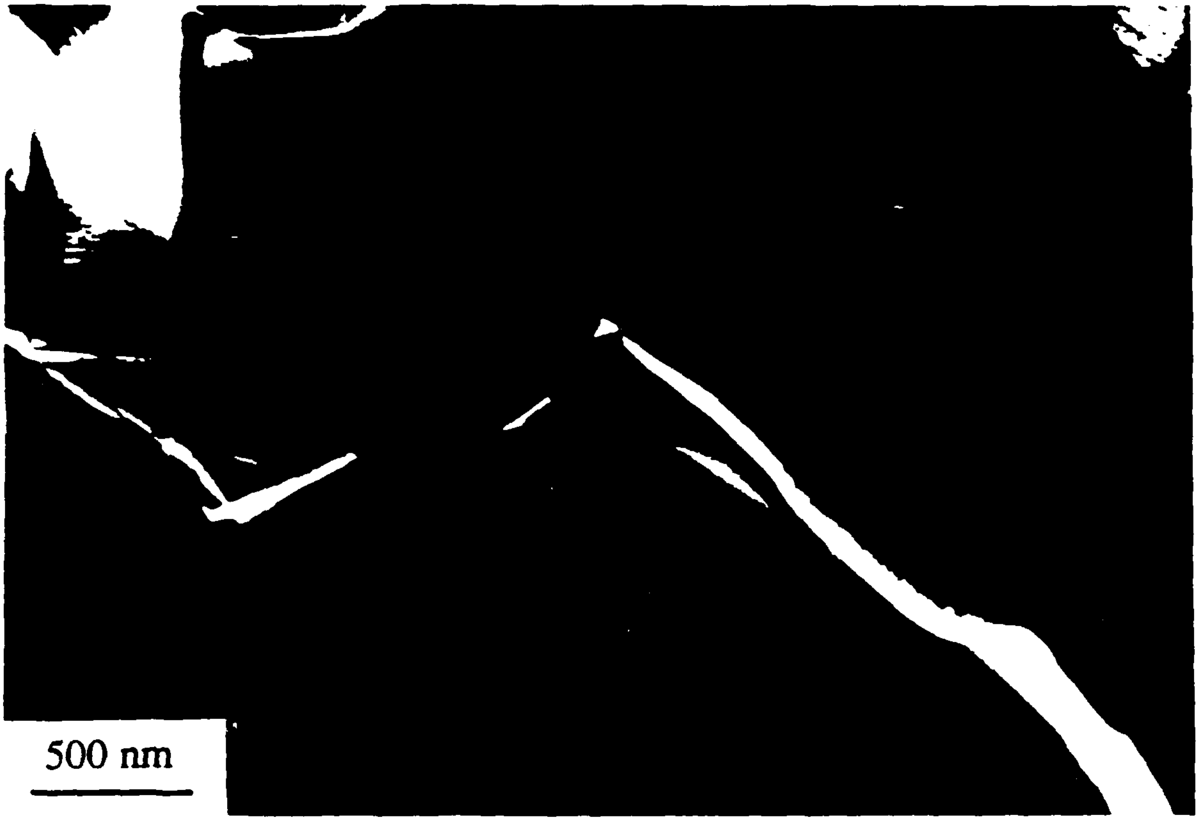

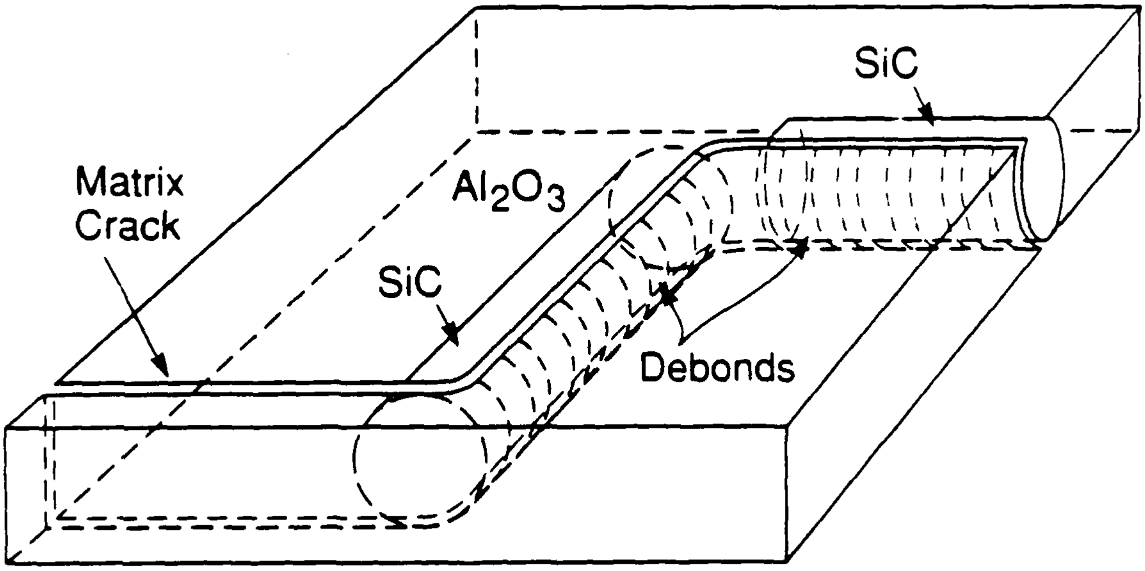
SiC
Matrix
Crack
Al2O3
SiC
Debonds

Figure 9c

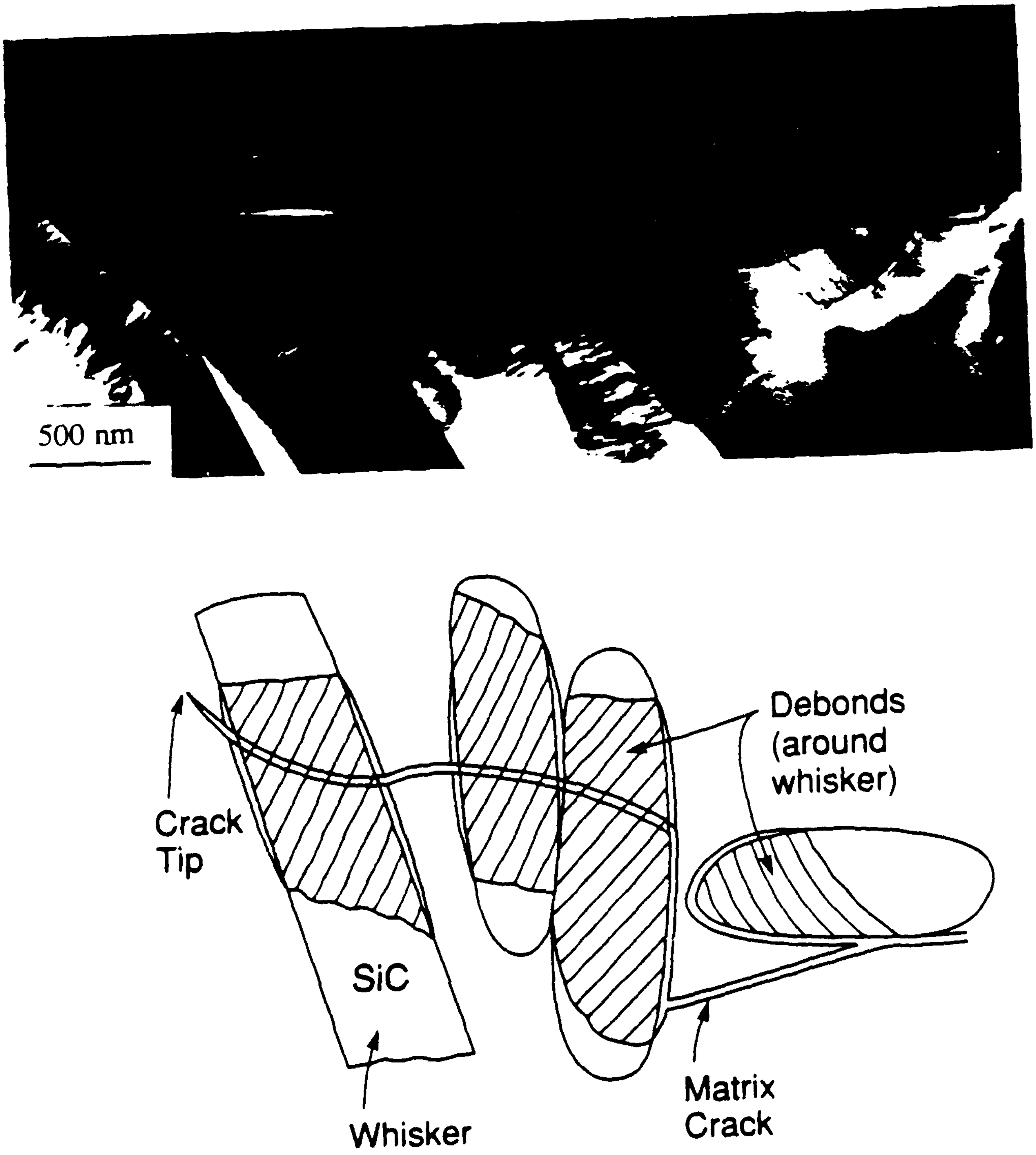
500 nm
Crack Tip
SiC
Whisker
Debonds (around whisker)
Matrix Crack

Figure 9d

Figure 10a

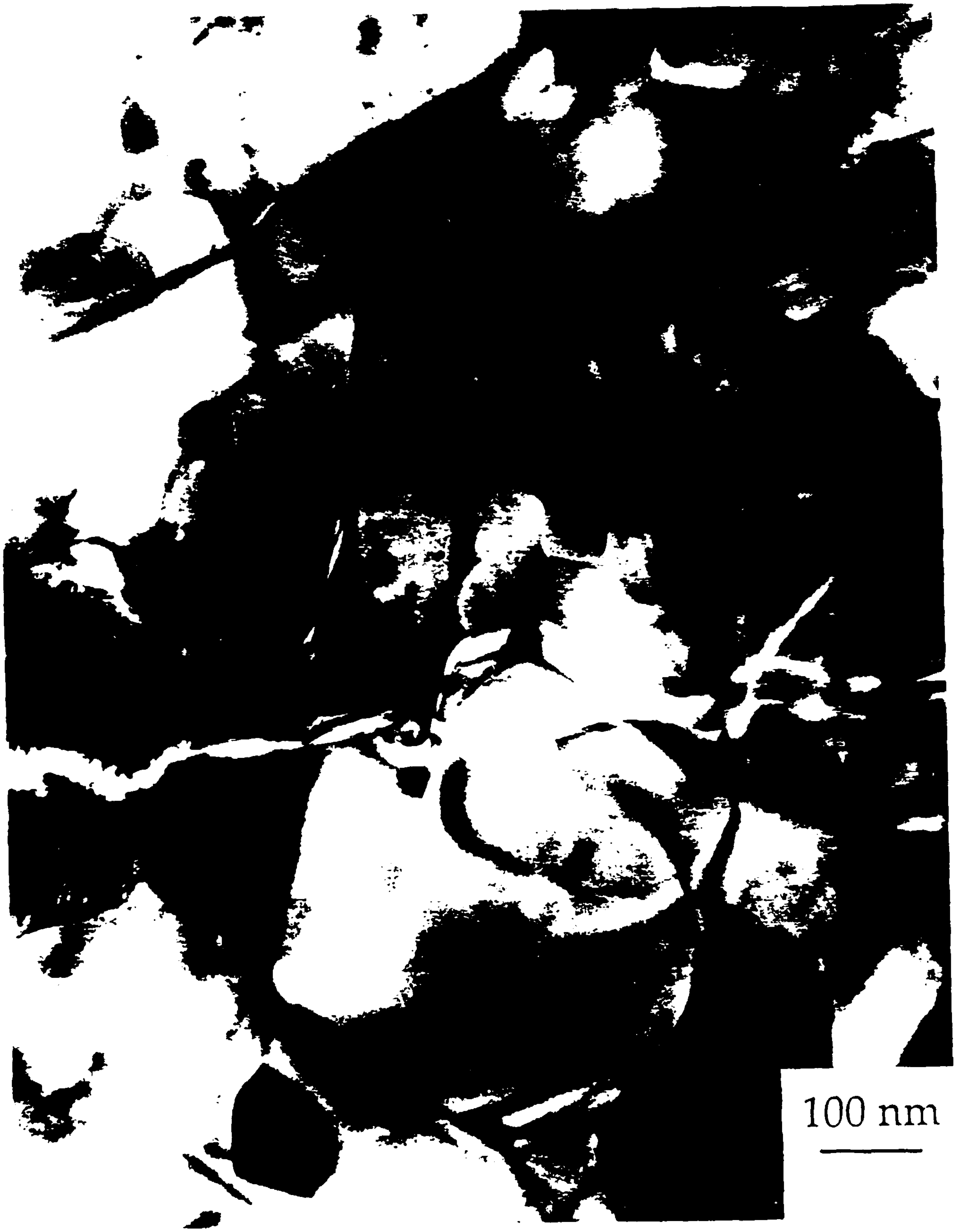

Figure 10b

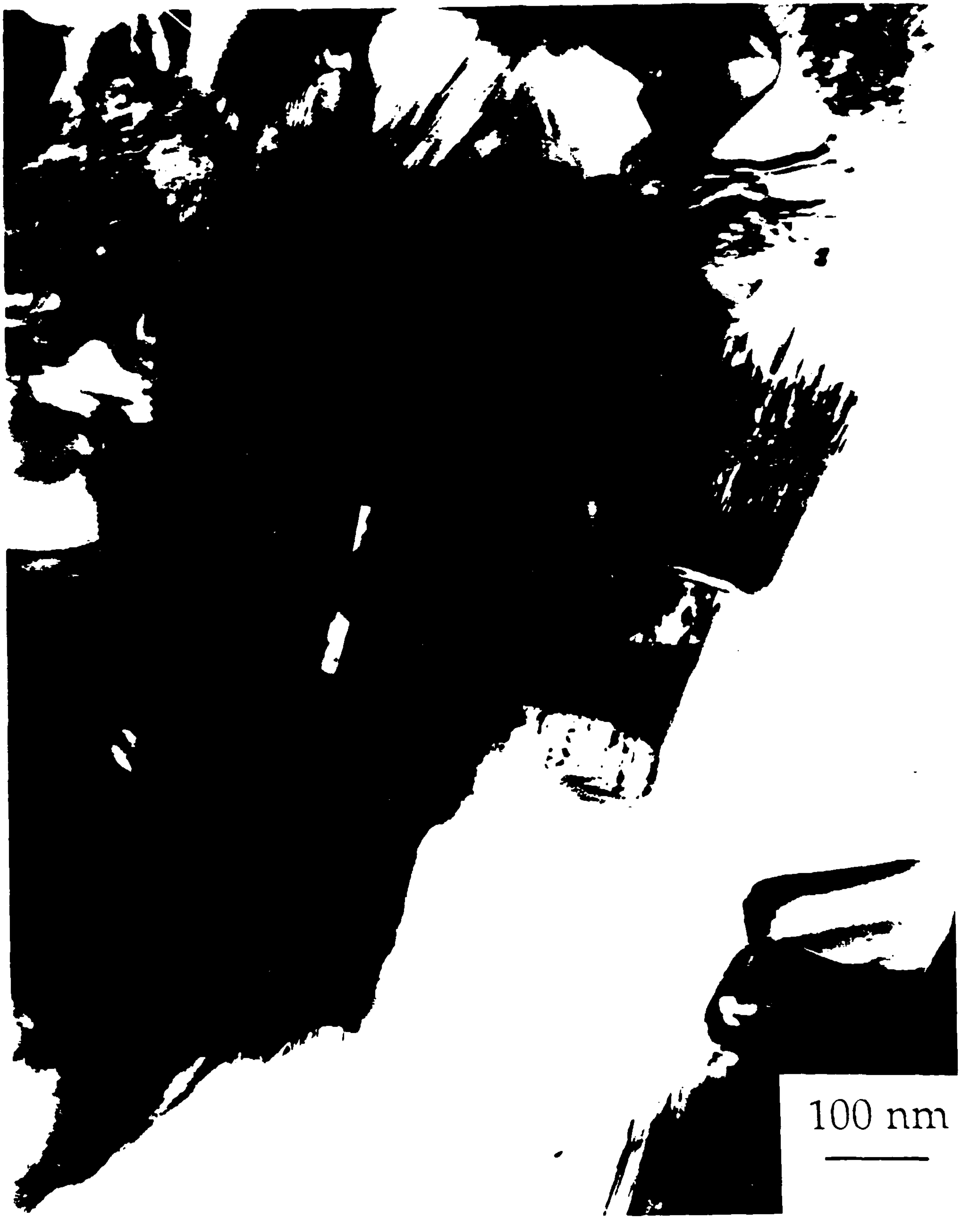

Figure 10c

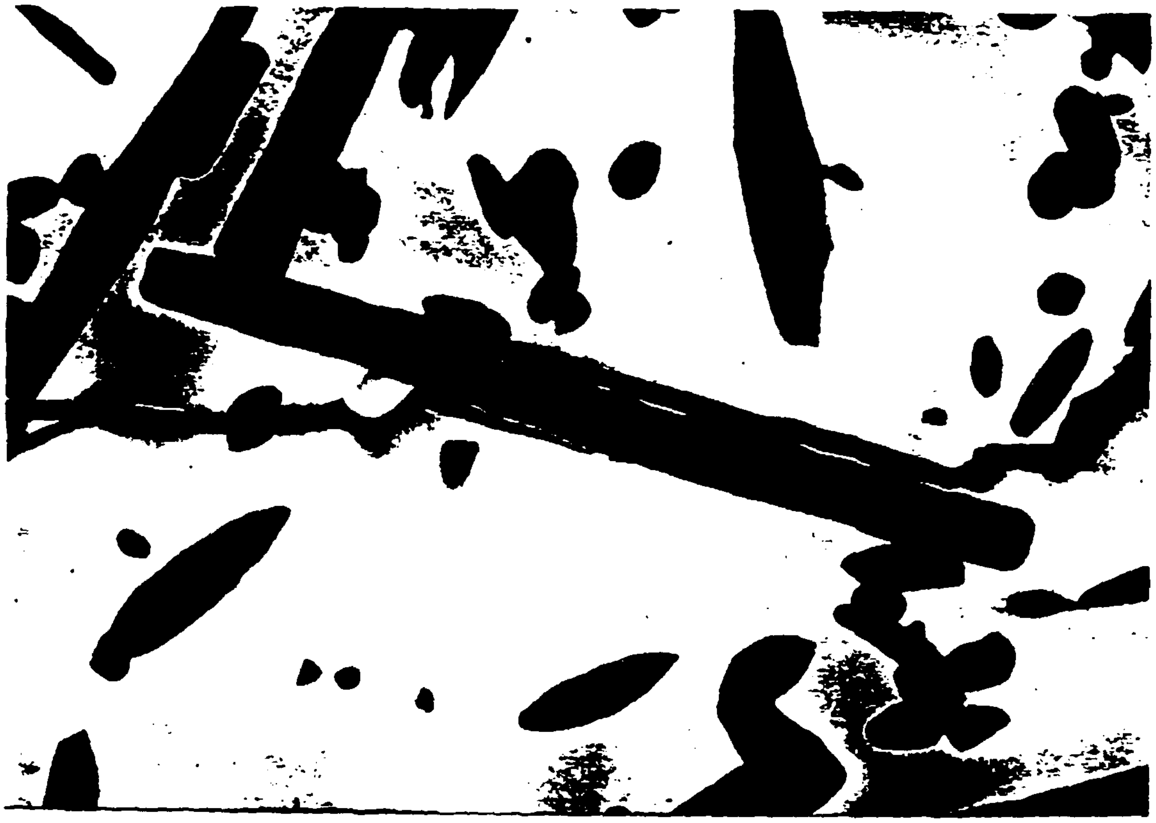

Figure 11a

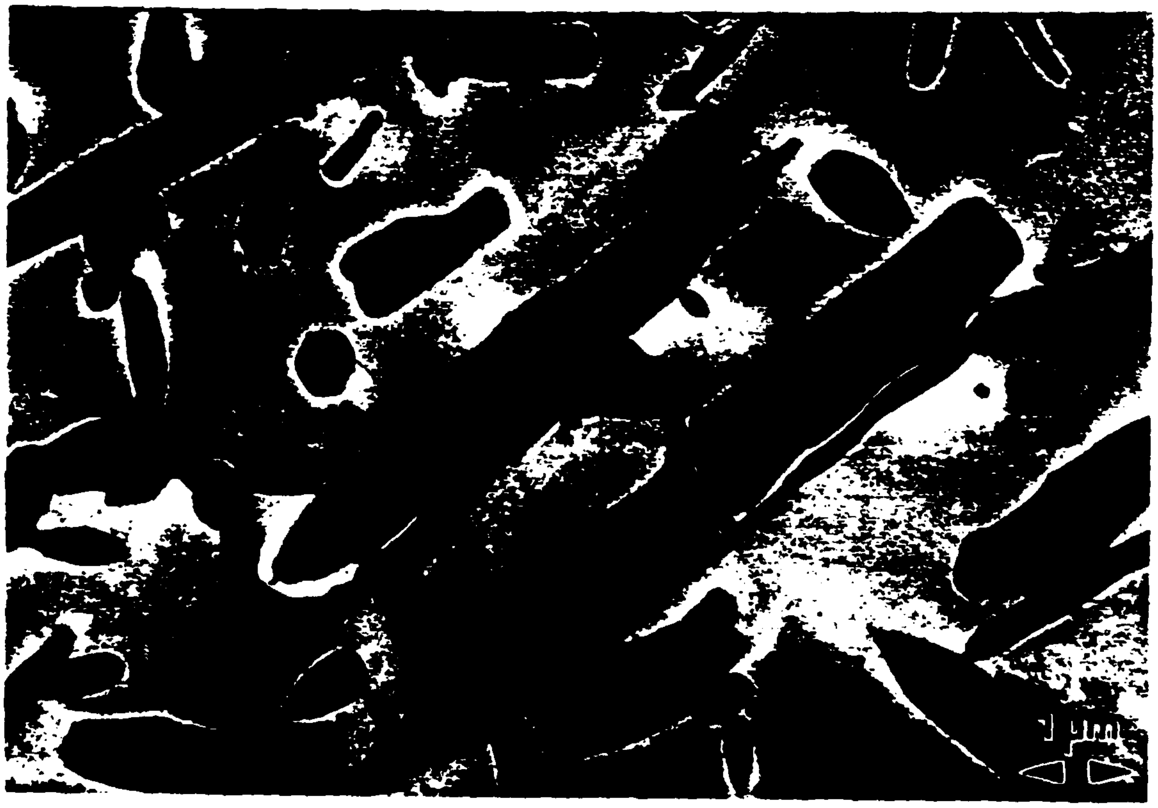

Figure 11b

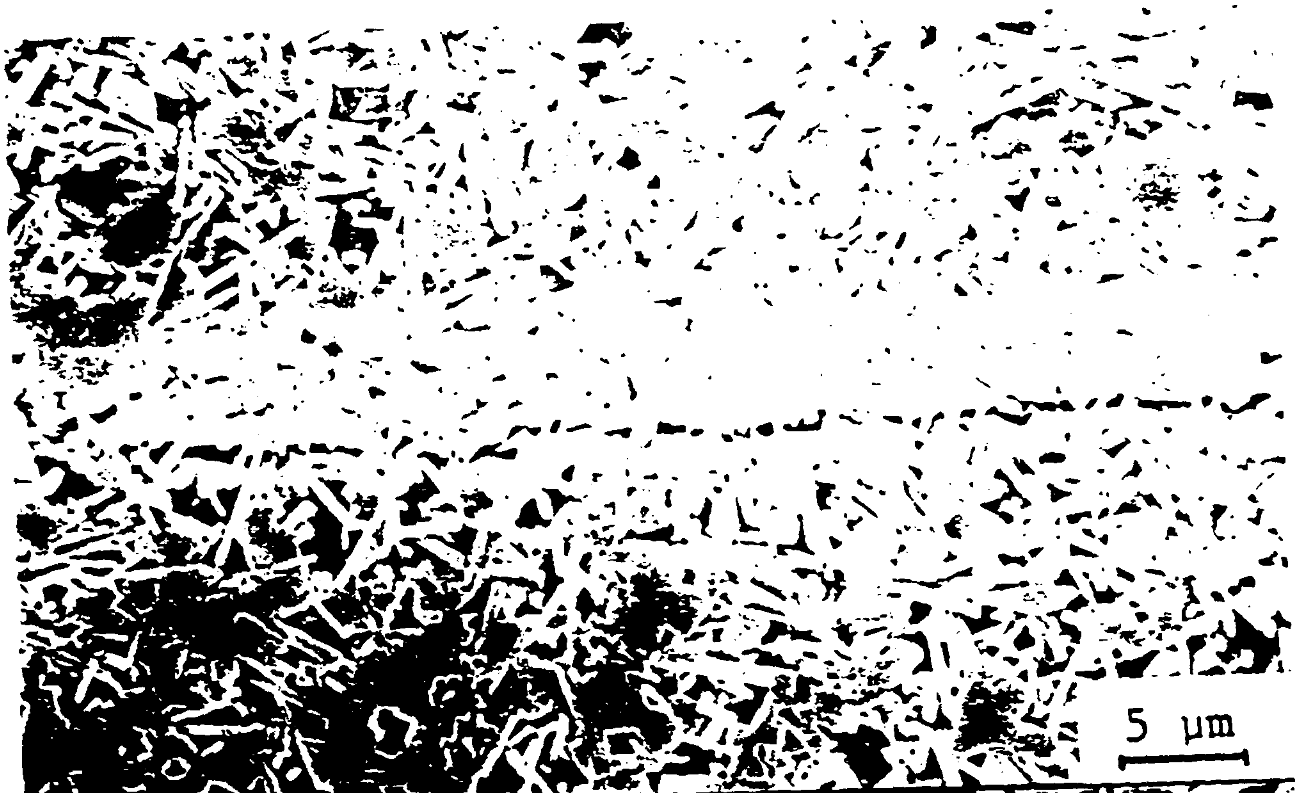

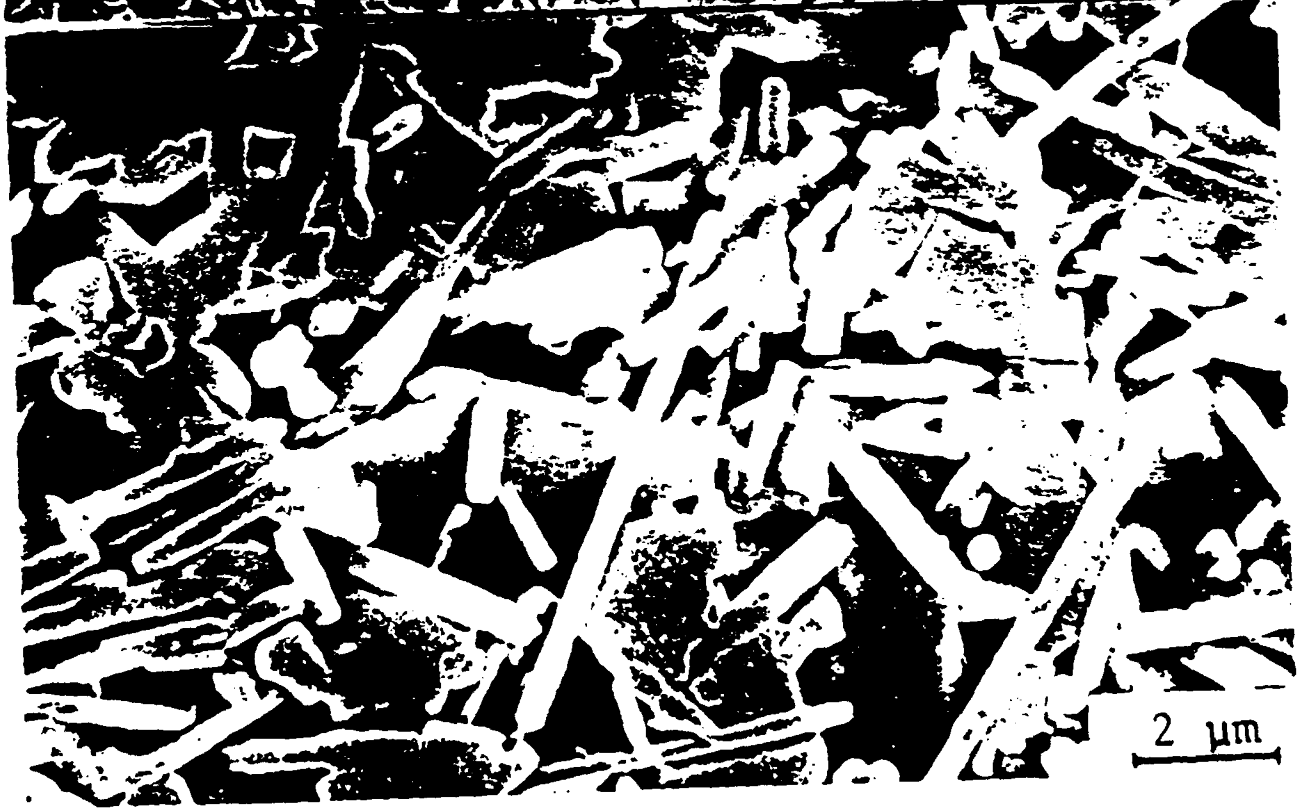

Figure 12a

Figure 12b

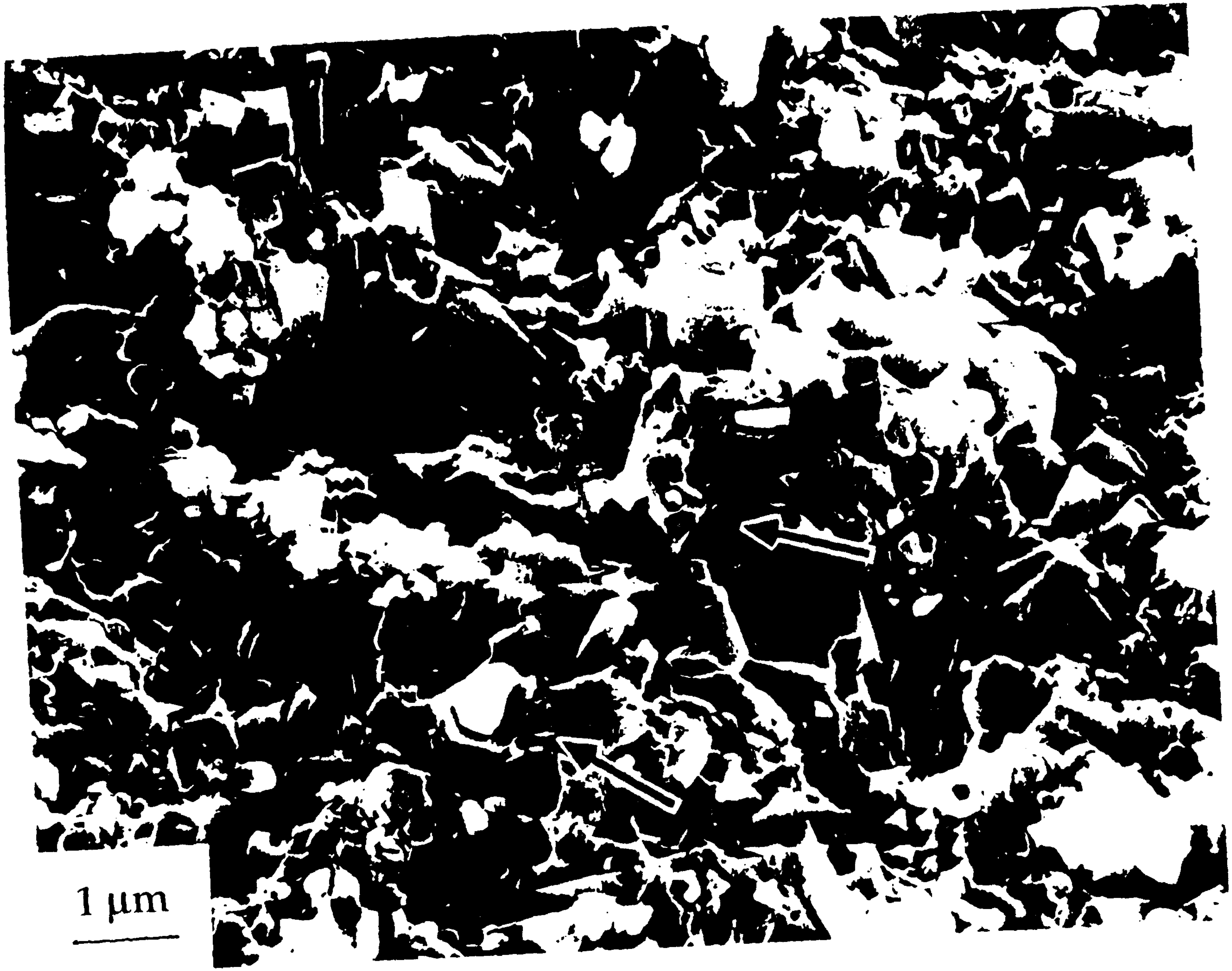

Figure 13

MECH-138

FINITE CRACKS IN TRANSFORMATION-TOUGHENED CERAMICS

David M. Stump and Bernard Budiansky

Division of Applied Sciences
HARVARD UNIVERSITY
Cambridge, Massachusetts 02138

February 1989

FINITE CRACKS IN TRANSFORMATION-TOUGHENED CERAMICS

David M. Stump and Bernard Budiansky

Division of Applied Sciences
Harvard University
Cambridge, MA 02138

February 1989

ABSTRACT

The dependence of the tensile fracture stress on crack length in dilatationally phase-transforming ceramics is studied by modeling the evolution of the transformed regions around the tips of finite cracks during crack growth. The presence of the transformation is found to reduce the stress required for crack-growth *initiation* . However, the peak, or "ultimate", tensile stress is found to occur during subsequent crack growth, and the *transformation-strengthening*, that is, the increase of tensile strength due to phase transformation, is found as a function of initial crack size.

INTRODUCTION

The fracture toughnesses of ceramics reinforced by partially-stabilized zirconia particles (PSZ) have been found to exceed the values for the unreinforced materials [1,2]. Experimental observations have revealed that a martensitic phase transformation occurs in the zirconia particles in the vicinity of the crack tip. As the crack advances into the material, a wake region of permanently transformed particles bordering the crack faces is left behind. Several analytical studies [3-6] of transformation toughening have been made on the basis of the assumption that the phase transformation is purely dilatant in nature and is triggered by a critical value of the mean stress. In these analyses, the growth of a semi-infinite plane-strain crack was contemplated and the toughening ratio $\lambda_s = K_s/K_m$ was calculated, where K_s is the "applied", mode-I, far-field stress intensity factor during steady-state crack growth, and K_m is the critical crack-tip stress intensity factor for fracture in the unreinforced material.

More recently, the transition due to increasing applied K from a semi-infinite stationary crack to steady-state growth was studied [7] and the dependence of the current value of $\lambda = K/K_m$ on crack extension calculated. Surprisingly, it was found that these *resistance curves* displayed peak values $\lambda_p > \lambda_s$ for finite amounts of crack extension.

While these studies are applicable to transformation toughening in the presence of "long" cracks, they may not be relevant to the effects of PSZ reinforcement on the nominal tensile strength of the material, which is governed by the unavoidable small flaws introduced during the manufacturing process. A tensile strength of 700 MPa, and a toughness ≈ 3 MPa$\sqrt{m}$ correspond to a critical flaw size estimate of $\approx 6\mu m$, which is comparable to transformation-zone wake heights ≈ 1-$10\mu m$ that have been observed during steady crack growth [2, 8]. Accordingly, the effects of phase-transforming particles on the growth of finite cracks appears to merit consideration and are studied in this paper. We will begin with a concise review of earlier results for semi-infinite cracks.

SEMI-INFINITE CRACKS

STEADY-STATE GROWTH

Steady-state crack growth under the "applied" stress intensity K_s is illustrated in Fig. 1. The region of transformed material is modeled as a continuum of uniform dilatation-transformation strain of strength $c\theta_p^T$ where c is the zirconia particle volume fraction and θ_p^T is the unconstrained volumetric dilatation of the particles (typically .04). The transformation is assumed to occur "supercritically", i.e. completely, when the mean stress $\sigma_m = \sigma_{kk}/3$ reaches the critical value σ_m^c. (The supercritical-transformation model is employed exclusively throughout this paper.) Thus, as crack growth proceeds, the mean stress just ahead of the leading boundary C_s (Fig. 1) due to the remote K-field and the transformation itself reaches σ_m^c, while the crack tip stress intensity factor is maintained at K_m. The results for the steady-state toughening ratio $\lambda_s = K_s/K_m$ depend on the *transformation-strength* parameter

$$\omega = \frac{Ec\theta_p^T}{\sigma_m^c}\left(\frac{1+\nu}{1-\nu}\right) \tag{1}$$

and are provided by the outer curve of Fig. 2, which shows λ_s^{-1} versus ω [6]. For $\omega > \omega_c = 29.99$, "lock-up" of the crack occurs [5,6].

RESISTANCE CURVES

The onset of growth of a semi-infinite crack occurs when $K = K_{tip} = K_m$, where K_{tip} is the stress intensity factor in the vicinity of the crack tip [3,4]. The problem of finding K as a function of subsequent crack growth Δa was addressed in [7] by imposing on the stationary crack a series of growth increments and modeling the evolution of the transformed region. Throughout the growth process $\sigma_m = \sigma_m^c$ was enforced on the moving part of the boundary of the transformed region, and K_{tip} was maintained at K_m. The characteristic length

$$L = \frac{2}{9\pi}\left[\frac{K_m(1+\nu)}{\sigma_m^c}\right]^2 \tag{2}$$

emerged from the analysis [7]. Nondimensional resistance curves of $\lambda = K/K_m$ versus $\Delta a/L$, as in Fig. 3, were found for various values of the transformation-toughening parameter ω. Results for peak toughening are given by the inner curve of Fig. 2, a plot of λ_p^{-1} versus ω. "Lock-up" for the advancing crack occurs at finite amounts of growth for $\omega > 20.15$.

The characteristic length L can be usefully related to the transformation-zone height H_s (Fig. 1) during steady growth of a semi-infinite crack. For $\omega \rightarrow 0$ [4]

$$L/H_s = \left(\frac{8\sqrt{3}}{9}\right) \tag{3}$$

and so L should be roughly in the aforementioned range of observed transformation-zone heights.

STATIONARY FINITE CRACKS

This section contemplates the *stationary*, mode-I, finite crack in an infinite body of supercritical material (Fig. 4). Under plane-strain conditions, the remote non-zero stresses are given by

$$\sigma_y = \sigma \quad , \quad \sigma_z = \nu\sigma \tag{4}$$

while near the crack tip at $x = a$, the stresses obey the asymptotic forms

$$\sigma_{\alpha\beta} = \frac{K_{tip}}{\sqrt{2\pi r}} f_{\alpha\beta}(\theta) \qquad \sigma_z = \nu\sigma_{\alpha\alpha} \tag{5}$$

where r and θ are crack-tip coordinates and Greek indices take on the values (1,2), with repetition implying summation. The $f_{\alpha\beta}(\theta)$ are the well-known trigonometric functions of the mode-I K-field. We can generally expect each crack tip to be surrounded by a region of supercritically transformed material (Fig. 4) with $\sigma_m = \sigma_m^c$ just outside its boundary.

In the presence of finite-strength transformations, $\omega \neq 0$, the crack-tip stress intensity factor K_{tip} differs from the "applied" stress-intensity factor $K = \sigma\sqrt{\pi a}$. Hence for imminent crack growth due to the applied stress σ, the combined effects of *both* the remote loading and the transformation itself must maintain σ_m at σ_m^c along the transformed-region boundaries while keeping K_{tip} at K_m. As a prelude to the finite-strength transformation analysis, we first study the limit of vanishing transformation strength, $\omega \to 0$, where only the effects of the remote tension σ apply.

WEAK TRANSFORMATIONS ($\omega \to 0$)

In the limit $\omega \to 0$, the transformation itself has no effect on K_{tip} , so that crack-growth initiation occurs when $K = K_{tip} = K_m$. Thus, the initiation stress is given by

$$\sigma_o \equiv K_m/\sqrt{\pi a} \tag{6}$$

The mean-stress field due to the remote loading σ is described in terms of the complex variable $z = x+iy$ by

$$\sigma_m = \frac{2(1+\nu)\sigma}{3}\left[\mathrm{Re}\left(\frac{z}{\sqrt{z^2-a^2}}\right) - \frac{1}{2}\right] \tag{7}$$

By setting $\sigma = \sigma_o$ and $\sigma_m = \sigma_m^c$ and using the nondimensional coordinate $Z = z/a$, the governing equation for the boundaries *at the instant of crack-growth initiation* is found to be

$$1 = \frac{2}{\gamma}\left[\mathrm{Re}\left(\frac{Z}{\sqrt{Z^2-1}}\right) - \frac{1}{2}\right] \tag{8}$$

where the parameter

$$\gamma = \frac{3\sigma_m^c}{\sigma_o(1+\nu)} \tag{9}$$

is the ratio of the critical mean stress to the remote mean stress. With the use of the definition (2) for the characteristic length L, the parameter γ may be put into the alternative form

$$\gamma = \sqrt{\frac{2a}{L}} \tag{10}$$

which is seen to be a nondimensional *crack-size* parameter.

Non-dimensional boundary shapes at crack-growth initiation are shown in Fig. 5 for various values of γ; in each case, the transformed region lies on the shaded side of the boundary. The transformed zones at each crack tip diverge in size and coalesce for $\gamma < 1$, i.e. when the applied remote mean stress exceeds the critical mean stress. The studies for $\omega > 0$ that follow will accordingly be limited to crack sizes for which $\gamma \geq 1$, or $a/L \geq \frac{1}{2}$.

FINITE-STRENGTH TRANSFORMATIONS ($\omega > 0$)

For $\omega > 0$, the transformed-zone boundaries $R(\theta)$ (see Fig. 4) at crack-growth initiation, and the initiation stress σ_i, are determined by the conditions $K_{tip} = K_m$, and $\sigma_m = \sigma_m^c$ just outside the zone boundaries $R(\theta)$.

Details of the calculations for the nondimensional radii $R(\theta)/a$ and normalized initiation stresses σ_i/σ_o, for prescribed values of the parameters ω and a/L, are given in Appendix A. Some of the resulting boundaries are shown in Fig. 6 for the value $\omega = 10$ and a variety of a/L. For a fixed value of a, the size of the transformed regions at initiation increases monotonically as the crack-length parameter a/L decreases. At $a/L = 1/2$, i.e., $\gamma = 1$, the transformed zone remains bounded, because, as will be shown, the initiation stress σ_i is *less* than σ_o, and transformation does not occur at infinity. The effect of crack length on boundary size and shape is seen in Fig. 7, which shows the zone boundaries $R(\theta)/L$ again for $\omega = 10$ and several values of a/L. The frontal boundary intercept $R(0)/L$ is plotted versus $\log(a/L)$ in Fig. 8 for various ω. Remarkably, at the value $a/L = 1.40$, the normalized frontal intercept $R(0)/L = 0.71$ is independent of the parameter ω even though the overall boundary shapes $R(\theta)/L$ remain distinctly different.

The normalized initiation strengths σ_i/σ_o are plotted versus ω for various values of a/L in Fig. 9. Recall that for semi-infinite cracks $K = K_{tip} = K_m$ at initiation, so that

$\sigma_i/\sigma_o \rightarrow 1$ for $a/L \rightarrow \infty$. However, for finite a/L, Fig. 9 reveals the surprising result that $\sigma_i/\sigma_o < 1$, thus indicating that the presence of the transformation *weakens* the material as far as crack growth *initiation* is concerned. Plots of σ_i/σ_o versus ω, shown in Fig. 10 over the extended range $0 < \omega < 160$, display the remarkable feature that for each value of a/L *self-cracking* at $\sigma_i/\sigma_o = 0$ can occur for a sufficiently high ω. In the limit $a/L \rightarrow \infty$, the critical ω for self-cracking approaches the value $\omega \approx 124.3$. However, the self-cracking values of ω are probably well beyond a practical range.

GROWING FINITE CRACKS

The right tip of the symmetrically growing finite crack of Fig. 4 is shown in Fig. 11. When the tip has advanced from its stationary position at $x = a$ by an amount Δa, a wake region of transformed material has been left behind. The boundary of the transformed region is modeled by three segments; active, passive and residual, as in the study of [7] for semi-infinite cracks. The instantaneous active segment MN, is the advancing part of the boundary along which material has just transformed according to the criterion $\sigma_m = \sigma_m^c$. The residual piece OP is a portion of the stationary-crack boundary that is left behind with the first increment of crack growth. The passive segment is a growth-dependent piece connecting O, the end of the residual piece, with N, the end of the current active segment.

This study employs the crack extension model introduced in [7] and described concisely below, to solve for the transition from the stationary, finite crack to large crack growth. In the limit of infinitesimal crack-growth increments, the passive segment continually extends while always providing a smooth connection to the active piece. In the numerical calculations, the crack tips were advanced symmetrically by a series of small, finite growth increments, for each of which the passive-zone boundary was extended by a straight-line increment tangent to the end of the *current* active boundary, and connected to the end of the *previous* active boundary. Again, the active-segment configuration $R(\theta)$ and the magnitude of the current applied stress were found by requiring that the combined effects of σ and the transformation itself maintain $\sigma_m = \sigma_m^c$ on MN, while keeping K_{tip} equal to K_m. The numerical solution procedure is discussed in Appendix B.

The results of calculations for σ/σ_0 versus $\Delta a/L$ are shown in Figs. 12 and 13 for $\omega = 5,10$ and various a/L. The normalized applied stress is seen to reach a peak value σ_p/σ_0 for finite amounts of crack growth. The value σ_p may be identified with the ultimate strength of the material in the presence of a "worst" flaw of size a. For very short cracks, σ_p/σ_0 occurs immediately after the onset of growth, while for "long" cracks, σ_p/σ_0 occurs for a crack advance $\Delta a/L$ well in excess of the initial intercept R(0)/L (Fig. 7). In the limit $a/L = \infty$, $\sigma/\sigma_0 = K/K_m$ is the non-dimensional "resistance curve" function of $\Delta a/L$ found for semi-infinite cracks in [7].

Two factors are responsible for peaks in the curves of σ/σ_0 vs. $\Delta a/L$. The contribution of σ to K_{tip} during crack extension is a monotonically increasing function of Δa given by

$$K_{nom} = \sigma\sqrt{\pi(a+\Delta a)} \tag{11}$$

whereas the reduction in K_{tip} provided by the transformation depends on both Δa and the starting crack length a. For small values of a/L, the transformation contribution to K_{tip} is never very large during the initial stages of growth so that the effects of σ dominate the strengthening behavior after only a very small amount of extension $\Delta a/L$. For sufficiently high a/L, the K_{tip} reduction due to the transformation increases during an initial period of crack growth, fighting both the material resistance K_m and the effect of σ due to increasing crack length, before reaching a maximum and eventually decreasing toward the steady-state level for very long cracks, at which point the effects of σ dominate the strengthening behavior.

The transformation-toughening effect for growing finite cracks may be isolated by using the results in Figs. 12-13 to plot K_{nom}/K_m vs. $\Delta a/L$, as in Figs. 14-15. These pseudo-resistance-curves, given by

$$\lambda_{nom} = \frac{K_{nom}}{K_m} = \left(\frac{\sigma}{\sigma_0}\right)\sqrt{\frac{a+\Delta a}{a}} \tag{12}$$

show that the weakening already observed for the stationary crack persists, in that crack-tip interaction makes the transformation-toughening less than it was for the semi-infinite crack, shown by the dotted curves. Peaks in the dependence of K_{nom}/K_m vs. $\Delta a/L$ still occur for sufficiently long cracks, but for short cracks K_{nom}/K_m approaches the steady-state toughening ratio λ_s monotonically .

Calculations of peak tensile-strength σ_p/σ_o are plotted versus log(a/L) in Fig. 16 for various ω. For $a/L \approx 1$, the presence of the transformation provides only slight fracture-stress enhancement, $\sigma_p/\sigma_o \approx 1$, and for low-enough ω, may even reduce the fracture strength, $\sigma_p/\sigma_o < 1$. As $a/L \to \infty$, the ratio σ_p/σ_o is given by the asymptotic expression

$$\frac{\sigma_p}{\sigma_o} \equiv \frac{K_p/K_m}{\sqrt{1 + \frac{(\Delta a/L)_p}{a/L}}} \tag{13}$$

where K_p/K_m and $(\Delta a/L)_p$ are the peak toughening and the corresponding normalized crack growth for the semi-infinite crack (Fig. 3) found in [7]. This estimate, shown by the dotted curves in Fig. 16, is useful only for sufficiently low ω and/or high a/L .

Finally, we wrap up the results for σ_p/σ_o in Fig. 17, which shows $(\sigma_p/\sigma_o)^{-1}$ vs. ω for various a/L. For $a/L = \infty$, the curve is the same as that given in Fig. 1 for λ_p^{-1} . The loss in transformation-*strengthening* associated with finite crack size is evident.

DISCUSSION

The calculations of this study indicate that transformation-*strengthening* in the presence of finite cracks occurs at finite amounts of crack growth, but will generally be substantially less than the transformation-*toughening* associated with long cracks. Thus, even for $\omega \approx 20$, corresponding to lock-up of a growing semi-infinite crack, it is unlikely that there would be improvement by more than a factor of two in the tensile fracture strength of the material. This conclusion presumes the existence of "small" cracks with $a/L = 10$ or less. Transformation-strengthening in the presence of large flaws, initial or otherwise, could approach the magnitude of the transformation-toughening associated with semi-infinite cracks. Thus we conclude that if the material is "good" to start with, transformation-toughening will not help to strengthen it much; but if it starts out "poor" because of large flaws, the transformations might be quite beneficial.

APPENDIX A

STATIONARY CRACKS

The solution for σ_i/σ_0 and $R(\theta)/a$ is accomplished by superposing the effects of the remote loading and the transformation itself to enforce the criterion $\sigma_m = \sigma_m^c$ along the outside of the phase-transformation boundary while maintaining $K_{tip} = K_m$. The mean stress field due to the remote loading $\sigma = \sigma_i$ is given by

$$\sigma_m = \frac{2(1+\nu)\sigma_i}{3}\left[\mathrm{Re}\left(\frac{z}{\sqrt{z^2-a^2}}\right) - \frac{1}{2}\right] \tag{A1}$$

and the corresponding "applied" crack-tip stress intensity factor is

$$K_{tip} = \sigma_i\sqrt{\pi a} \tag{A2}$$

The contributions to σ_m and K_{tip} due to the transformation are found by first considering the effects of a small circular spot of dilatation of area dA_0 and centered at the point $z_0 = x_0 + iy_0$. The plane-strain mean stress at z exterior to the spot can be found by complex-variable methods to be given by

$$\sigma_m = -\frac{Ec\theta_p^T}{9\pi}\left(\frac{1+\nu}{1-\nu}\right)\mathrm{Re}\,\frac{\partial}{\partial z_0}\left[\frac{z+z_0}{\sqrt{z^2-a^2}\left(\sqrt{z^2-a^2}+\sqrt{z_0^2-a^2}\right)}\right]dA_0 \tag{A3}$$

(Here a straight branch line connects the crack tips, with $\sqrt{z^2-a^2} \to z$ for $|z| \to \infty$; Eq. (A3) is consistent with formulas given by Rose in [9] .)

Integration over the transformed regions (Fig. 4) and use of Green's theorem then gives the following result for the mean stress at any z outside those regions:

$$\sigma_m = -\frac{Ec\theta_p^T}{9\pi}\left(\frac{1+\nu}{1-\nu}\right)\mathrm{Re}\left\{\frac{1}{\sqrt{z^2-a^2}}\oint_{C_+ + C_-}\frac{z+z_0}{\sqrt{z^2-a^2}+\sqrt{z_0^2-a^2}}\,dy_0\right\} \tag{A4}$$

where C_+ and C_- are the boundaries of the transformed zones surrounding the crack tips at $x = \pm a$. Similarly, the mode-I crack-tip stress-intensity factor due to the phase transformation is

$$K_{tip} = -\frac{Ec\theta_p^T}{6(1-\nu)\sqrt{\pi a}}\,\mathrm{Re}\oint_{C_+ + C_-}\sqrt{\frac{z_0+a}{z_0-a}}\,dy_0 \tag{A5}$$

The critical-mean-stress criterion is formulated by setting the sum of (A1) and (A4) equal to σ_m^c and allowing z to approach C_+ from the exterior of the transformed region. We introduce the notation (Fig. 4)

$$z_{+,-}(\theta) = aZ_{+,-}(\theta) = \pm[R(\theta)e^{\pm i\theta} + a] \tag{A6}$$

for the values of z on C_+ and C_-. Then, with the use of the definitions (1), (2), and (5) for ω, L, and σ_0, the governing integral equation for $R(\theta)$ becomes

$$1 = \left(\frac{\sigma_i}{\sigma_0}\right)\sqrt{\frac{2L}{a}}\left[\mathrm{Re}\left(\frac{Z_+(\theta)}{\sqrt{Z_+^2(\theta)-1}}\right)-\frac{1}{2}\right]$$

$$-\frac{\omega}{9\pi}\mathrm{Re}\left\{\frac{1}{\sqrt{Z_+^2(\theta)-1}}\int_{-\pi}^{\pi}[M_+(\theta,\theta')-M_-(\theta,\theta')]\,\frac{d}{d\theta'}\left[\frac{R(\theta')}{a}\sin\theta'\right]\right\}d\theta' \tag{A7}$$

where

$$M_{+,-}(\theta,\theta') = \frac{Z_+(\theta)+Z_{+,-}(\theta')}{\sqrt{Z_+^2(\theta)-1}+\sqrt{Z_{+,-}^2(\theta')-1}} \tag{A8}$$

The constraint on K_{tip} is formulated by setting the sum of (A2) and (A5) equal to K_m to get

$$1 = \frac{\sigma_i}{\sigma_o} - \frac{\omega}{18\pi}\sqrt{\frac{2a}{L}}\,\mathrm{Re}\int_{-\pi}^{\pi}\left[\sqrt{\frac{Z_+(\theta)+1}{Z_+(\theta)-1}} - \sqrt{\frac{Z_-(\theta)+1}{Z_-(\theta)-1}}\right]\frac{d}{d\theta}\left[\frac{R(\theta)}{a}\sin\theta\right]d\theta \qquad \text{(A9)}$$

Equations (A7) and (A9) constitute a nonlinear integral equation and constraint in the unknowns $R(\theta)/a$ and σ_i/σ_o for prescribed ω and a/L. Solution was accomplished by first expanding the radius vector in the form

$$R(\theta)/a = \sum_{n=0}^{N} a_n \cos(n\theta) \qquad \text{(A10)}$$

After substitution of (A10) into (A7)-(A9), a system of N+2 equations in the N+2 unknowns $(a_o,\ldots,a_N,\sigma_i/\sigma_o)$ was generated by collocating (A7) at the N+1 points $\theta_j = j\pi/N$ ($j=0,\ldots,N$) and enforcing (A9). The integrals of (A7) and (A9) were evaluated by Gauss quadrature, and a Newton-Raphson iterative scheme was used to find a solution, with convergence specified by a relative change of less than 0.1% in the values of each of the unknowns in successive iterations. It was found that 10-15 term expansions of $R(\theta)/a$ were sufficient to obtain a solution.

APPENDIX B

GROWING CRACKS

The solution for the stress ratio σ/σ_o and the transformed region as functions of the crack growth $\Delta a = a'-a$ (Fig. 11) was accomplished by adapting the analysis of Appendix A to enforce the criterion $\sigma_m = \sigma_m^c$ along the *active* boundary segments while maintaining K_{tip} at K_m. The coordinates of the points on the zone boundaries surrounding the crack tips at $x = \pm a'$ are now given by (Fig. 11)

$$z_{+,-}(\theta) = aZ_{+,-}(\theta) = \pm\,[R(\theta)e^{\pm i\theta} + a'] \qquad \text{(B1)}$$

on the *active* segments, $-\alpha \le \theta \le \alpha$, where the angular coordinate α of the transition point N is to be determined.

The mean-stress field exterior to the transformed regions of the growing crack is found by replacing a by a' in the sum of (A1) and (A4), which gives

$$\sigma_m = \frac{2(1+\nu)\sigma}{3}\left[\mathrm{Re}\left(\frac{z}{\sqrt{z^2-a'^2}}\right)-\frac{1}{2}\right]$$

$$-\frac{Ec\theta_p^T}{9\pi}\left(\frac{1+\nu}{1-\nu}\right)\mathrm{Re}\oint_{C_+ + C_-}\left[\frac{z+z_o}{\sqrt{z^2-a'^2}\left(\sqrt{z^2-a'^2}+\sqrt{z_o^2-a'^2}\right)}\right]dy_o \quad \text{(B2)}$$

Setting $\sigma_m = \sigma_m^c$ and letting z approach C_+ *for* $0 < \theta < \alpha$ gives the equation

$$1 = \left(\frac{\sigma}{\sigma_o}\right)\sqrt{\frac{2L}{a}}\left[\mathrm{Re}\left(\frac{Z_+(\theta)}{\sqrt{Z_+^2(\theta)-A^2}}\right)-\frac{1}{2}\right]$$

$$-\frac{\omega}{9\pi}\mathrm{Re}\left\{\frac{1}{\sqrt{Z_+^2(\theta)-A^2}}\int_{-\pi}^{\pi}[H_+(\theta,\theta')-H_-(\theta,\theta')]\,\frac{d}{d\theta'}\left[\frac{R(\theta')}{a}\sin(\theta')\right]d\theta'\right. \quad \text{(B3)}$$

where

$$A = a'/a \quad \text{(B4)}$$

and

$$H_{+,-}(\theta,\theta') = \frac{Z_+(\theta)+Z_{+,-}(\theta')}{\sqrt{Z_+^2(\theta)-A^2}+\sqrt{Z_{+,-}^2(\theta')-A^2}} \quad \text{(B5)}$$

The crack-tip stress-intensity factor for the growing crack is found by replacing a by a' in (A2) and (A5) to get

$$K_{tip} = \sigma\sqrt{\pi a'} - \frac{Ec\theta_p^T}{6\sqrt{\pi a'}\,(1-\nu)}\,\mathrm{Re}\oint_{C_+ + C_-}\sqrt{\frac{z_o+a'}{z_o-a'}}\,dy_o \quad \text{(B6)}$$

Setting $K_{tip} = K_m$, and non-dimensionalizing then gives

$$1 = \left(\frac{\sigma}{\sigma_o}\right)\sqrt{A} - \frac{\omega}{18\pi}\sqrt{\frac{2a}{AL}}\;\mathrm{Re}\int_{-\pi}^{\pi}\left[\sqrt{\frac{Z_+(\theta)+A}{Z_+(\theta)-A}}-\sqrt{\frac{Z_-(\theta)+A}{Z_-(\theta)-A}}\right]\frac{d}{d\theta}\left[\frac{R(\theta)}{a}\sin\theta\right]d\theta \quad \text{(B7)}$$

For a given value of A, equations (B2)-(B7) constitute a nonlinear integral equation and constraint in the unknowns $R(\theta)/a$, σ/σ_o, and α. Solutions for increasing values of A must be found on the basis of a series of small increments in A. With previous residual and passive boundaries (Fig. 11) OP and ON known, the new configuration of NM produced by the change in A must be found, and connected to the previous passive segment ON by means of a short straight-line segment. An additional constraint is introduced by enforcing the tangency condition

$$\left.\frac{dY}{dX}\right|_{ACTIVE} = \left.\frac{dY}{dX}\right|_{PASSIVE} \tag{B8}$$

at the juncture point N (Fig. 11). (For the very first crack increment the extra tangency condition at the juncture O

$$\left.\frac{dY}{dX}\right|_{PASSIVE} = \left.\frac{dY}{dX}\right|_{RESIDUAL} \tag{B9}$$

was also imposed.)

The solution of (B3), (B7) and (B8) for $R(\theta)/a$, σ_i/σ_0 and α was accomplished with a procedure analogous to that of Appendix A. The radius was expanded in the series

$$\frac{R(\theta)}{a} = \sum_{n=0}^{N} a_n T_{2n}(\theta/\alpha) \tag{B11}$$

in the range (o, α) where the T_{2n} are the even Tchebyshev polynomials. A system of N+3 equations for the N+3 unknowns ($a_0,\ldots,a_N$, σ/σ_0,α) was generated by collocating (B3) at the N+1 points $\theta_j = j\alpha/N$ ($j=0,\ldots,N$) while enforcing (B7) and (B8). The integrals in (B3) and (B7) were evaluated with Gauss quadrature, and the Newton-Raphson procedure outlined in Appendix A was then used to obtain a solution. A five term expansion of $R(\theta)/a$ was sufficient to achieve convergence for all growth increments. As a check on the accuracy of selected calculations for a prescribed sequence of crack growth increments, the solution procedure was repeated with the growth increment sizes halved, and only slight variations in results were detected.

ACKNOWLEDGEMENTS

This work was supported in part by the DARPA University Research Initiative (Subagreement P. O. #VB38639-0 with the University of California, Santa Barbara, ONR Prime Contract N00014-86-K-0753), the Office of Naval Research (Contract N00014-84-K-0510), and the Division of Applied Sciences, Harvard University. The work of DMS was partially supported by a National Science Foundation Graduate Fellowship.

REFERENCES

1. R. C. Garvie, R. H. J. Hannink and R. T. Pascoe, *Nature* **258**, 703 (1982).
2. A. G. Evans and R. M. Cannon, *Acta. Met.* **34**, 761 (1986).
3. R. M. McMeeking and A. G. Evans, *J. Amer. Cer. Soc.* **65**, 242 (1982).
4. B. Budiansky, J.W. Hutchinson and J. C. Lambropoulos, *Int. J. Solids Structures* 19, 337 (1983).
5. L. R. F. Rose, *J. Mech. Phys. Solids* **34**, 609 (1986).
6. J. C. Amazigo and B. Budiansky, *Int.. J. Solid Structure* **24**, 751 (1988).
7. D. M. Stump and B. Budiansky, to be published in *Int. J. Solids Structures.*
8. L. R. F. Rose and M. V. Swain, *J. Amer. Cer. Soc.* **69**, 203 (1986).
9. L. R. F. Rose, *Proc. of Royal Soc.* **A412**, 151 (1987).

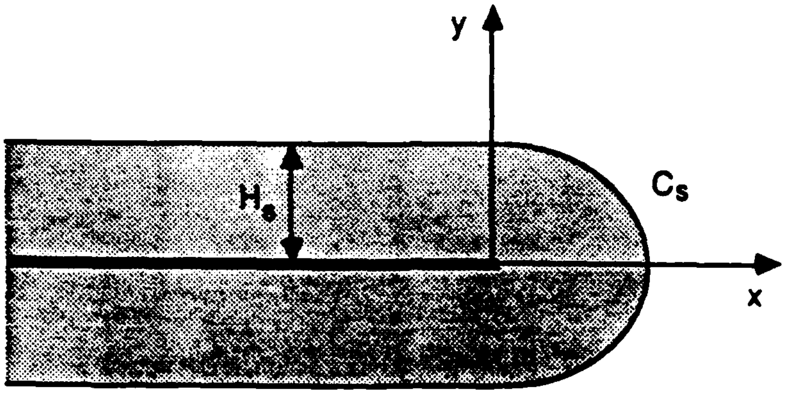

Fig. 1 Transformed zone during steady-state crack growth, semi-infinite crack.

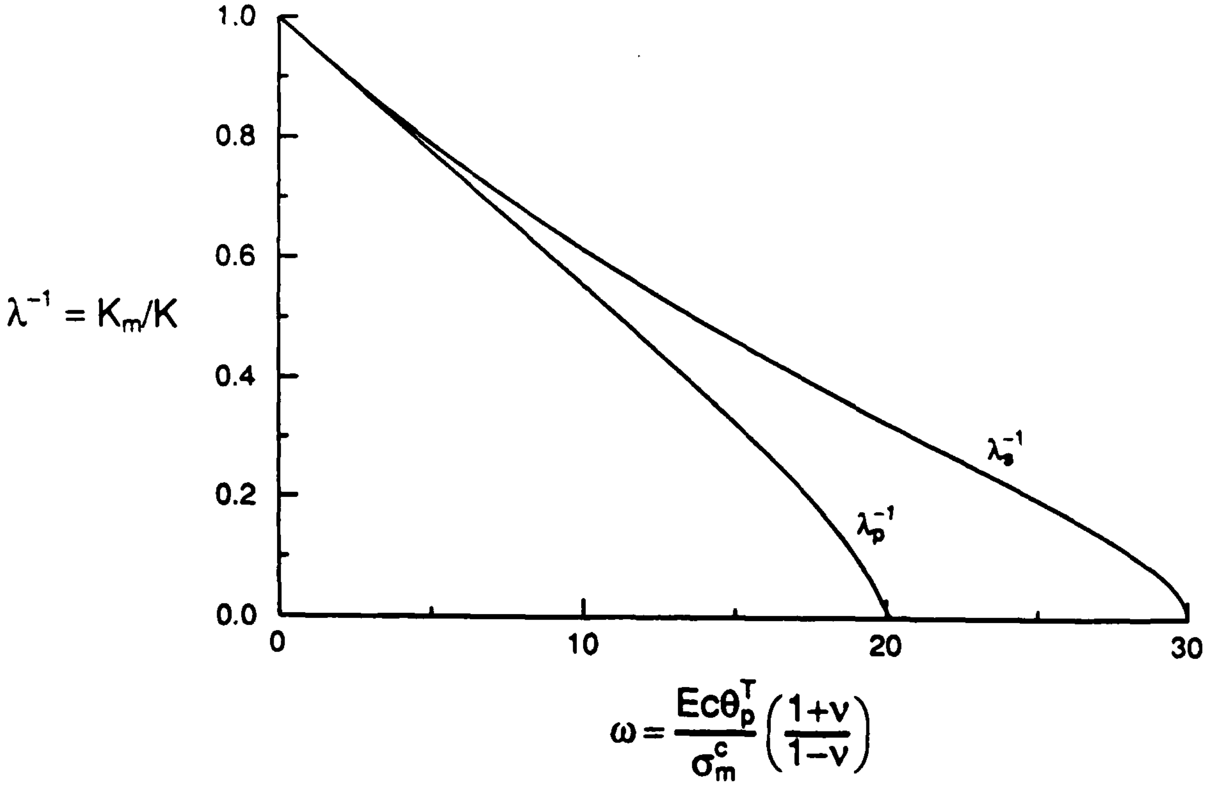

Fig. 2 Reciprocal of peak and steady-state toughening versus ω, semi-infinite crack.

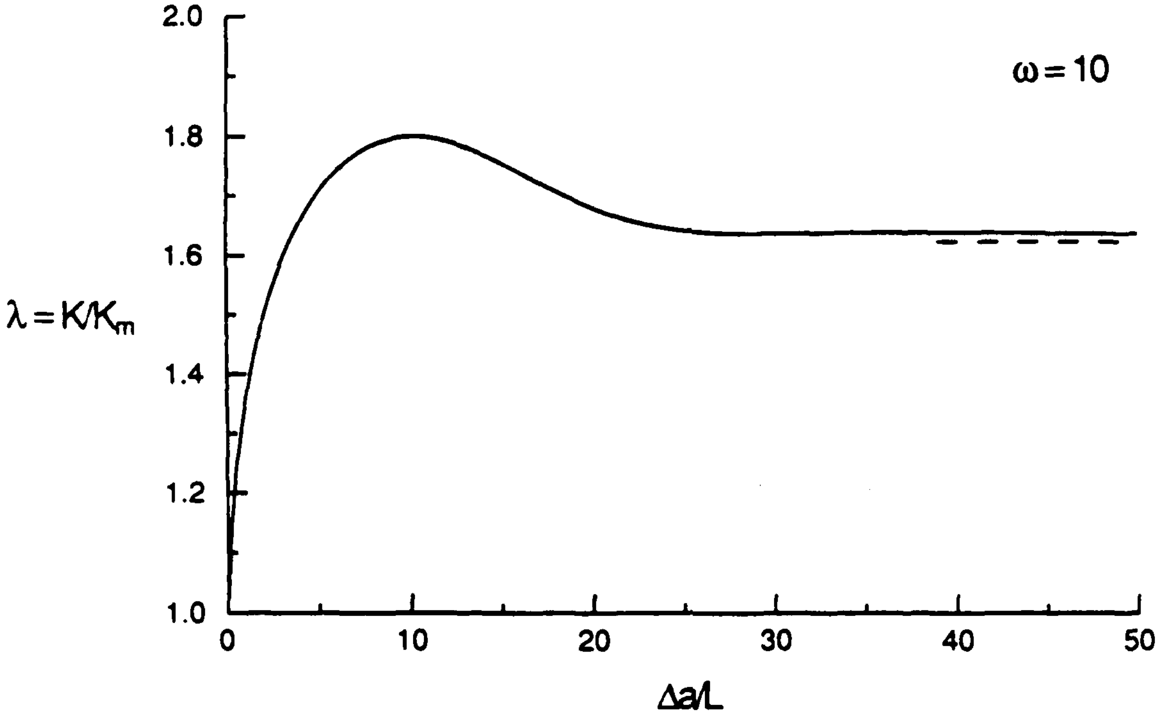

Fig. 3 Non-dimensional resistance curve, $\omega = 10$, semi-infinite crack.

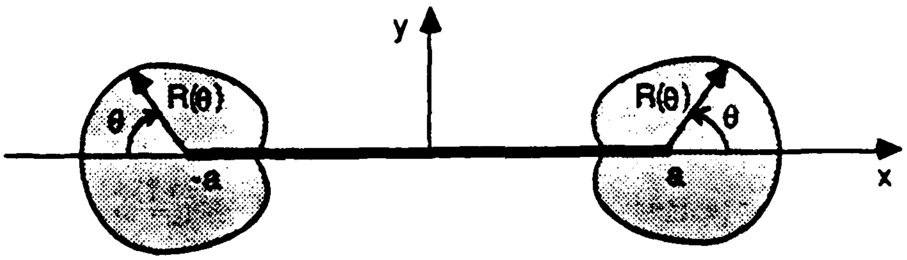

Fig. 4 Transformed zones just before crack-growth initiation, finite crack.

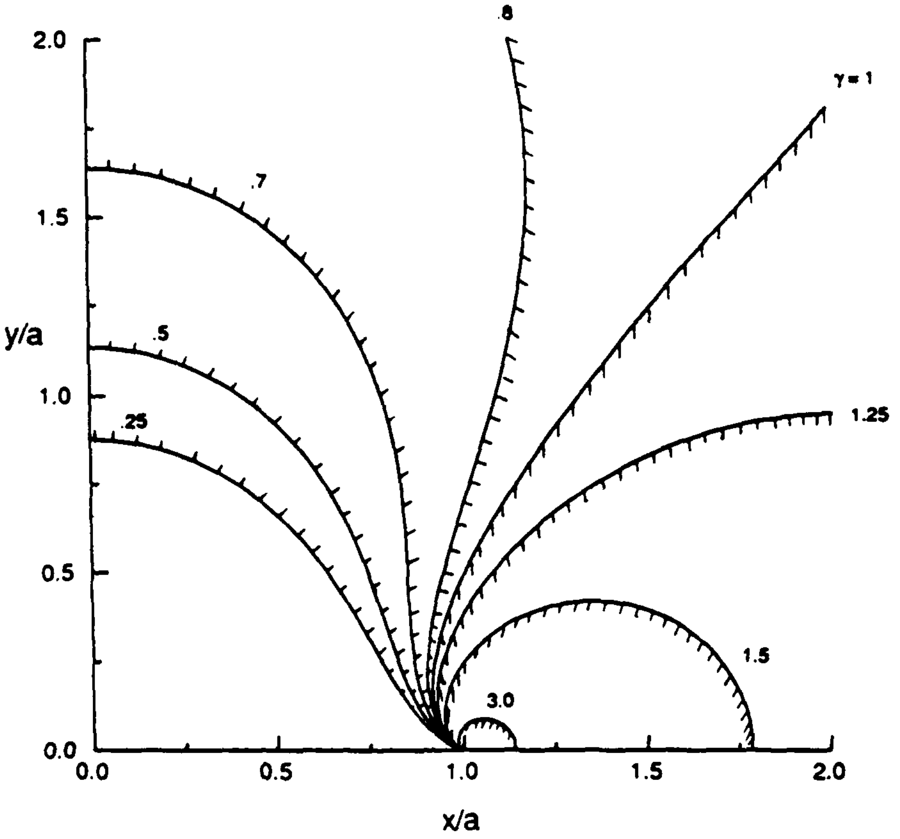

Fig. 5 Transformed-zone boundaries.

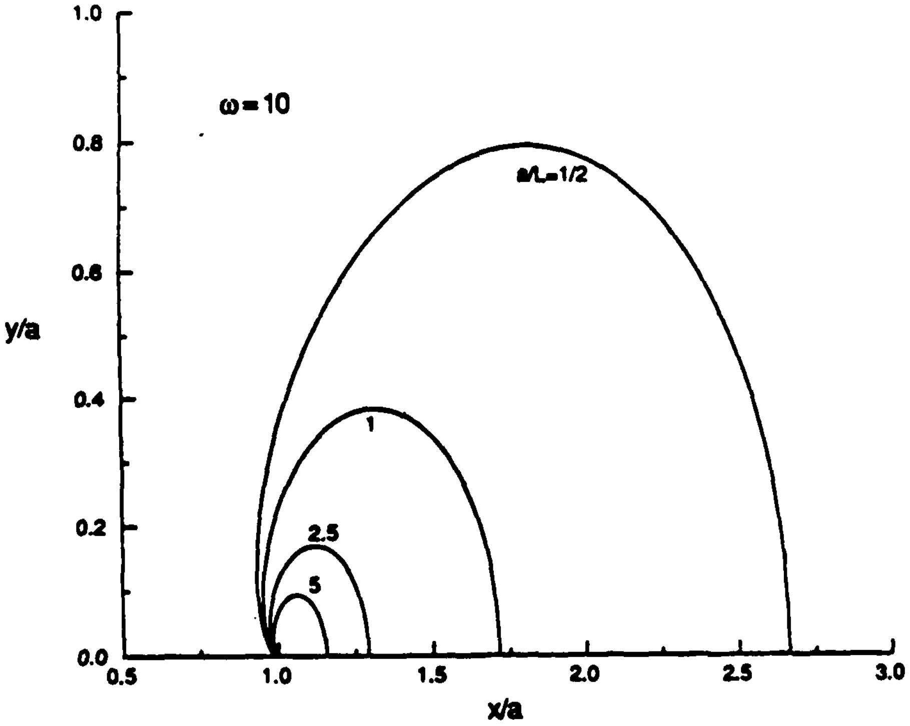

Fig. 6 Transformed-zone boundaries at crack-growth initiation, ω = 10; normalization length = a.

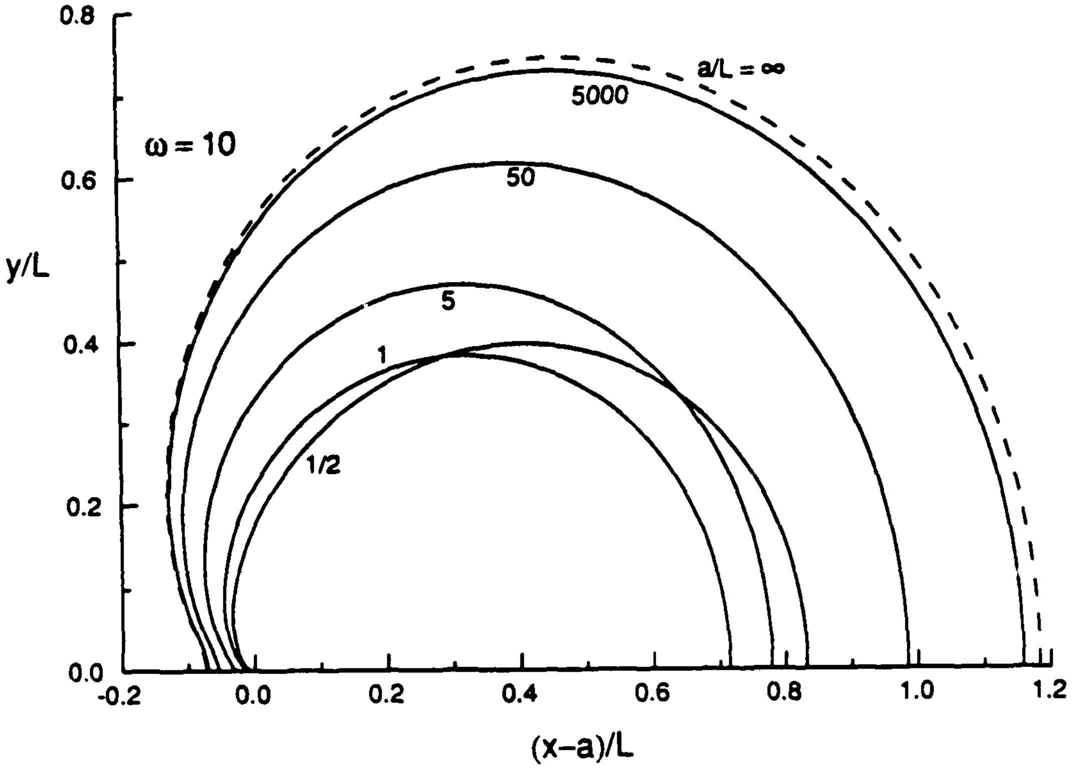

Fig. 7 Transformed-zone boundaries at crack-growth initiation, ω = 10; normalization length = L.

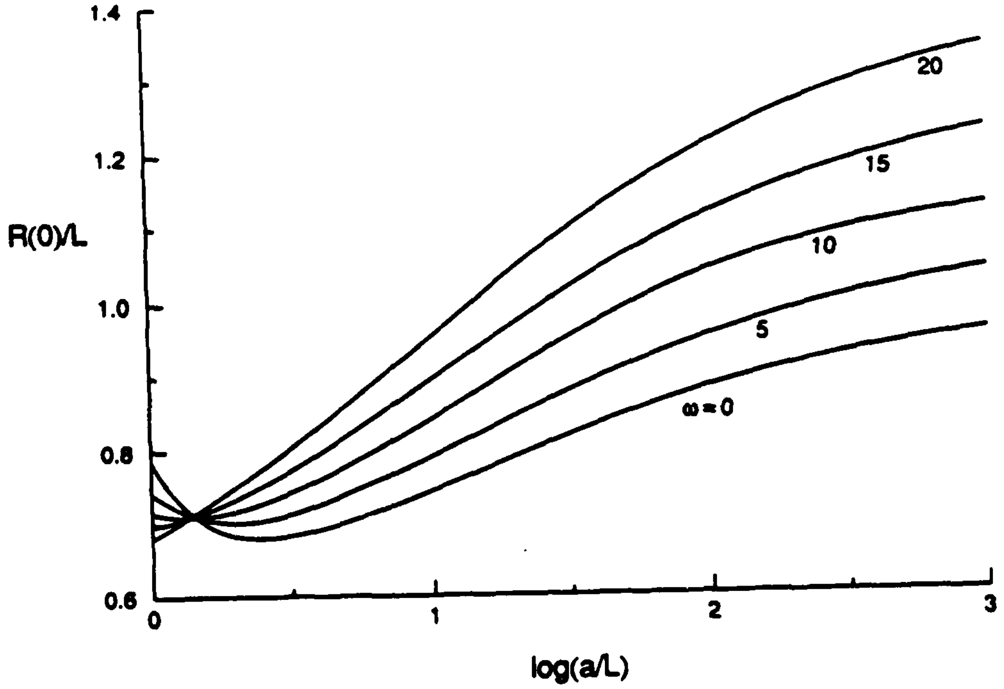

Fig. 8 Frontal zone-boundary intercept.

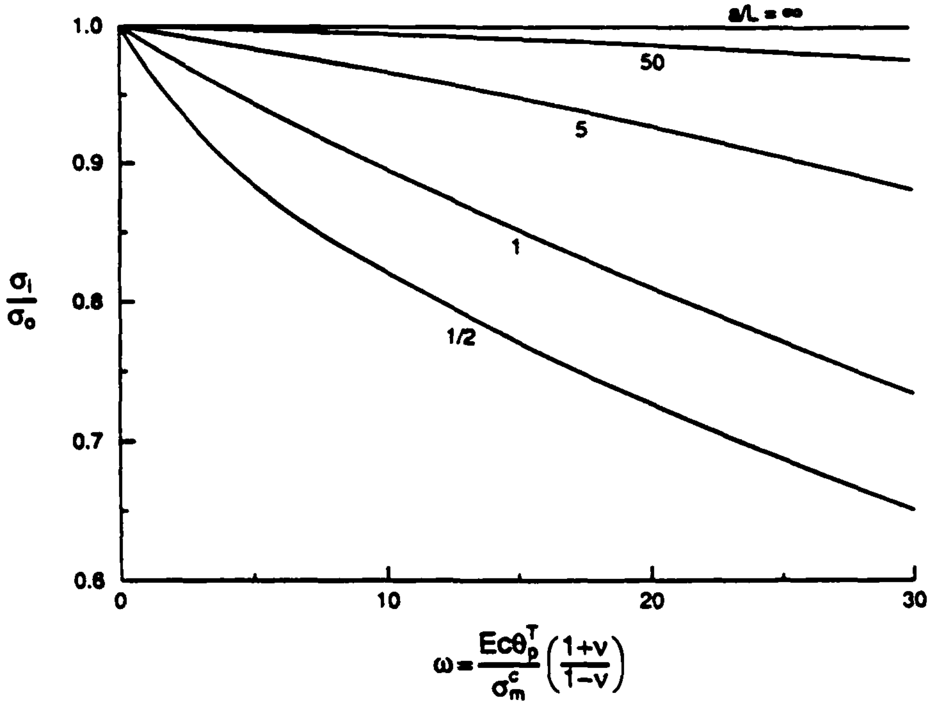

Fig. 9 Normalized crack-growth-initiation stress (0 < ω < 30).

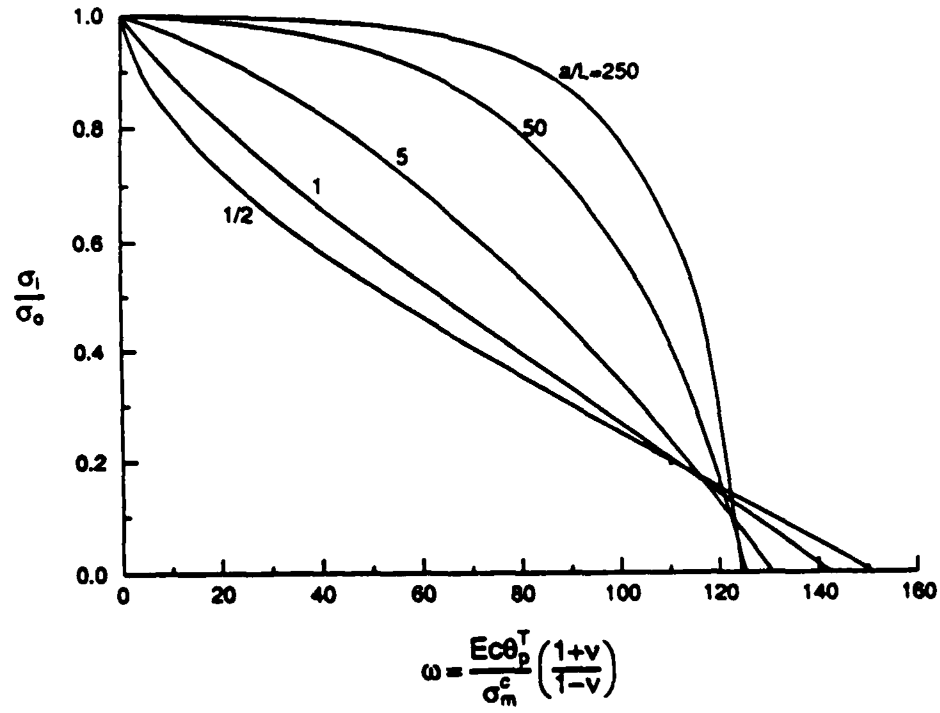

Fig. 10 Normalized crack-growth-initiation stress (0 < ω < 300).

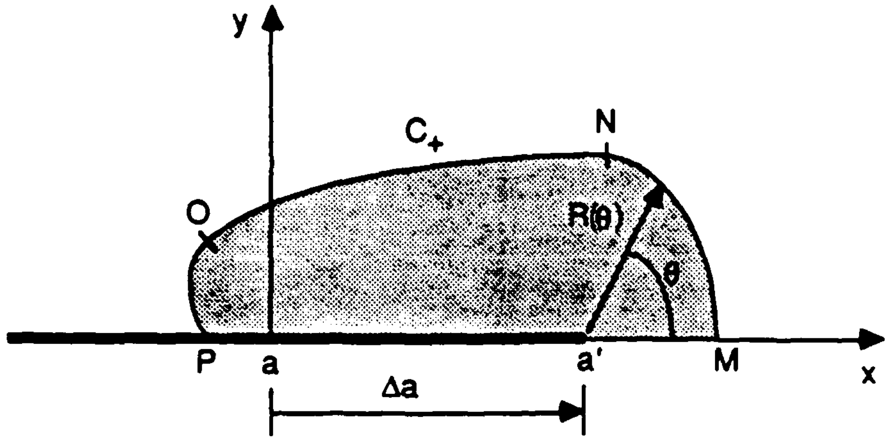

Fig. 11 Upper half of transformed region at right-hand tip of growing crack.

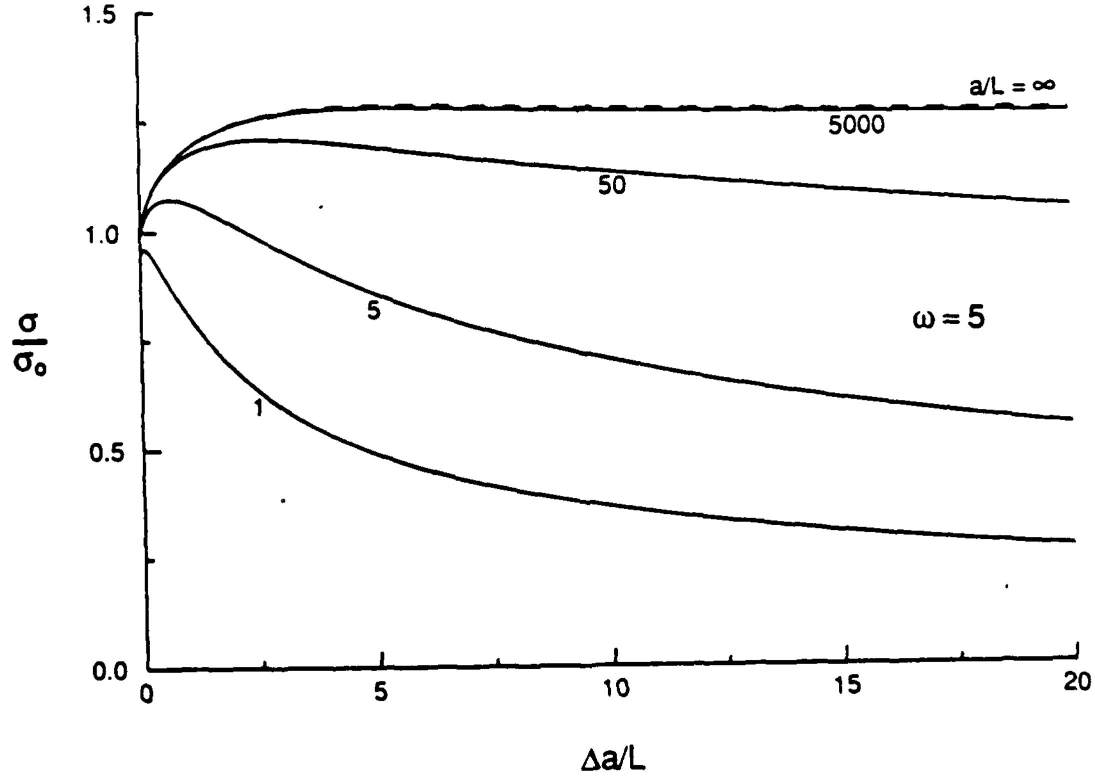

Fig. 12 Normalized applied stress versus non-dimensional crack growth ($\omega = 5$).

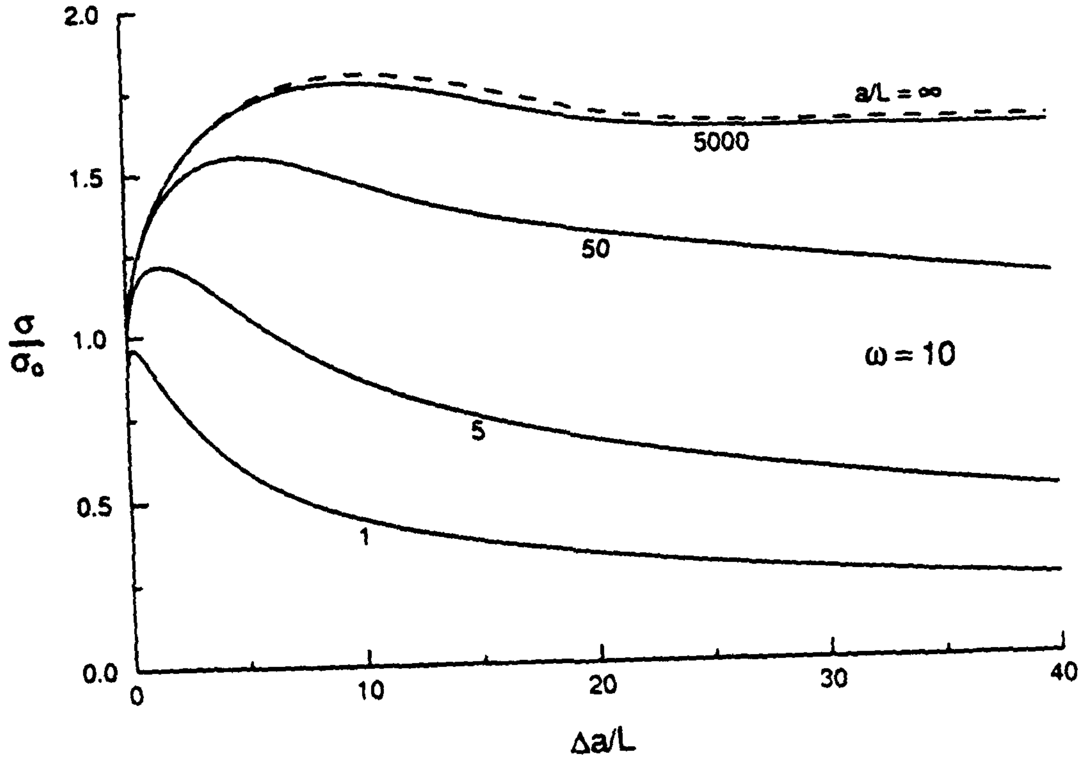

Fig. 13 Normalized applied stress versus non-dimensional crack growth (ω = 10).

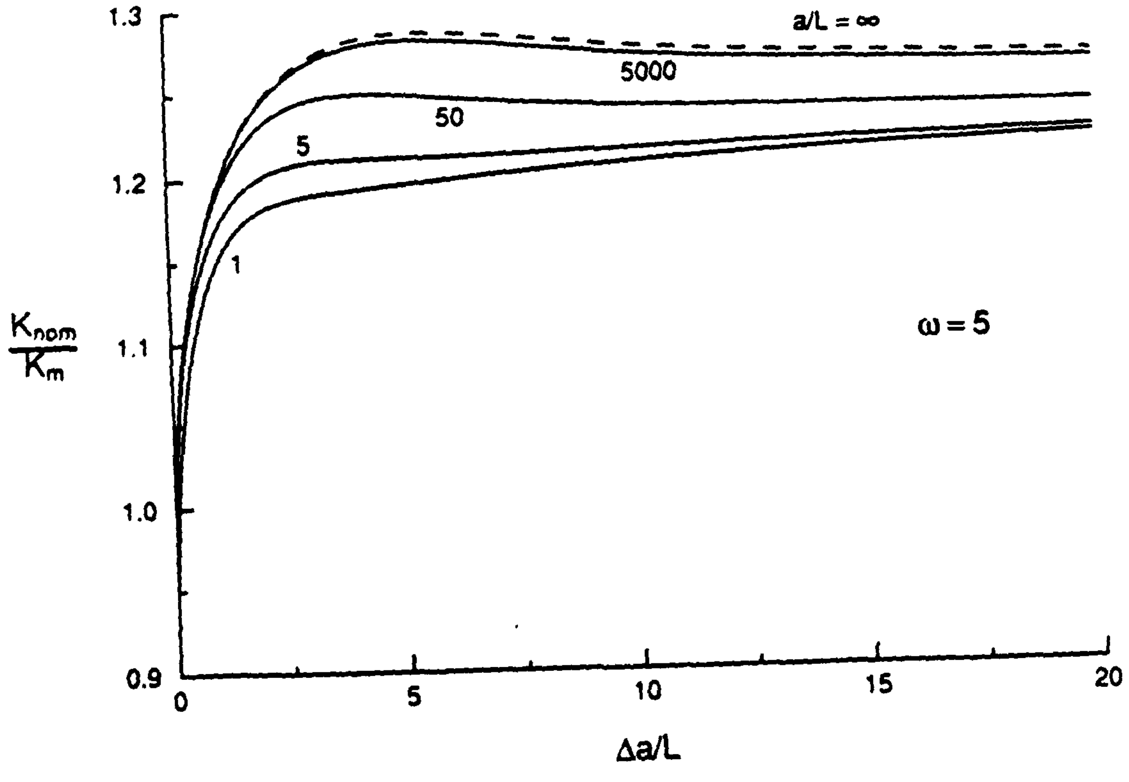

Fig. 14 Resistance curves for finite cracks: nominal toughening ratio, based on current crack length, versus crack growth (ω = 5).

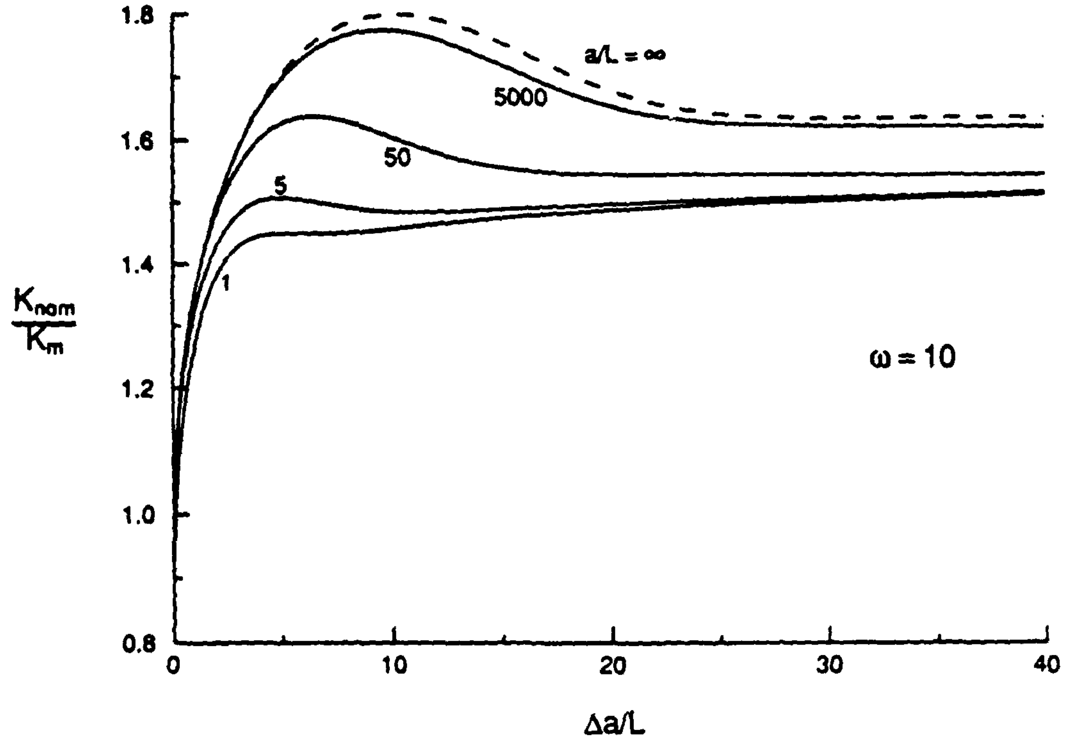

Fig. 15 Resistance curves for finite cracks: nominal toughening ratio, based on current crack length, versus crack growth (ω = 10).

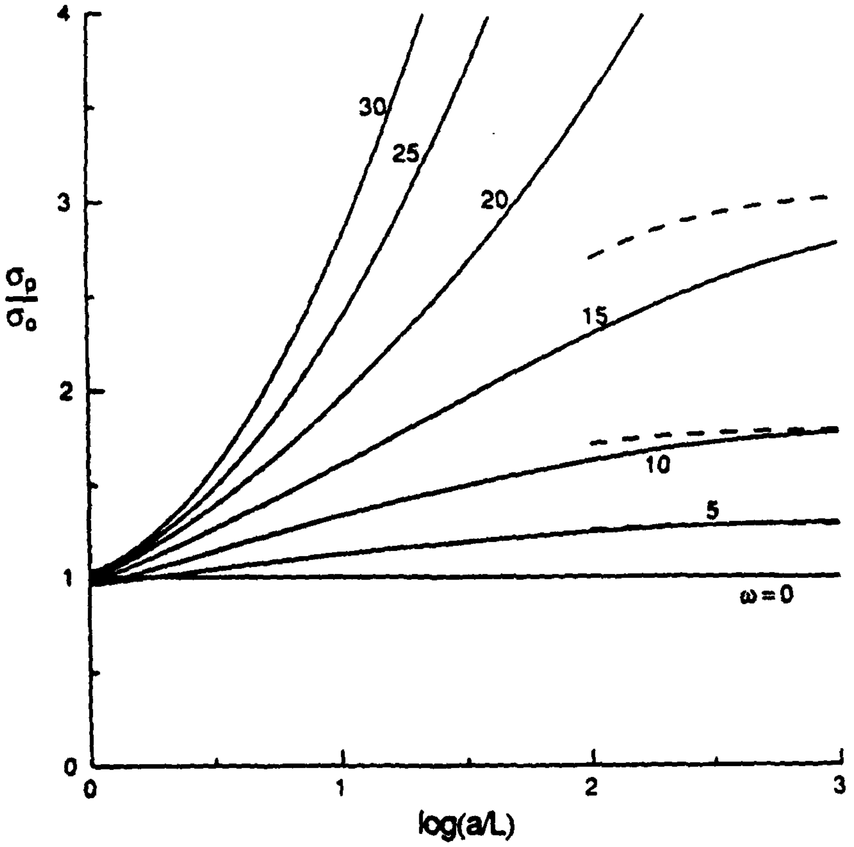

Fig. 16 Transformation strengthening: strengthening ratio versus crack-size parameter.

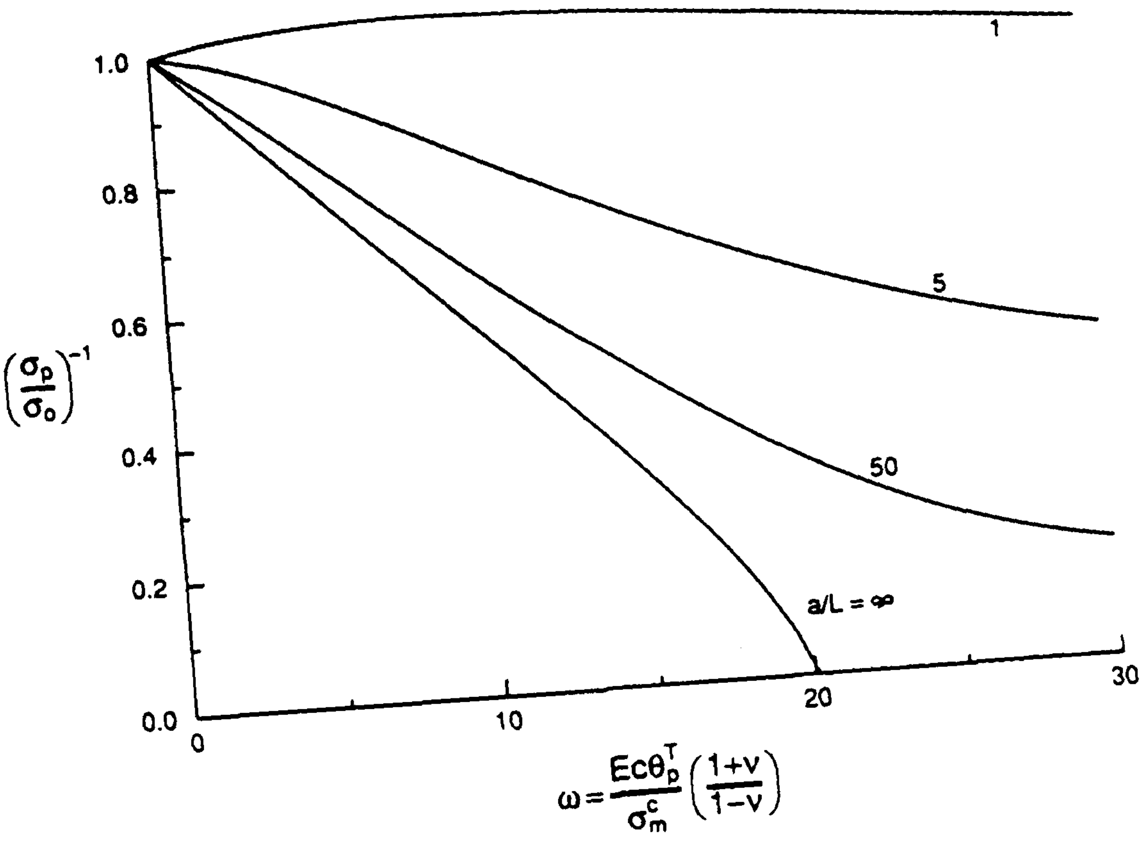

Fig. 17 Transformation strengthening: reciprocal of strengthening ratio versus ω.

MECH-151

ON TOUGHENING BY MICROCRACKS

David K. M. Shum and John W. Hutchinson

Division of Applied Sciences
HARVARD UNIVERSITY
Cambridge, Massachusetts 02138

October 1989

On Toughening By Microcracks

David K. M. Shum and John W. Hutchinson

Division of Applied Sciences
Harvard University
Cambridge, MA 02138

October 1989

Abstract

This study examines the phenomenon of microcrack toughening under the premise that toughening must entail mutual shielding of the main crack *and* the microcracks. Maximum toughening corresponds to the macrocrack/microcrack configuration that minimizes the maximum energy release rate (or stress intensity factor) among the various crack tips. Explicit results for the maximum toughening achievable and the corresponding optimal configuration are presented for a plane strain model of a macrocrack in the presence of either one or two microcracks.

1. Introduction

Some brittle single phase polycrystalline materials display a macroscopic fracture energy which is many times the fracture energy for cleavage of the single crystals or the fracture energy of grain boundary separation. Thus, even in the absence of any plastic deformation, the polycrystal can be much tougher than its constituent crystals or its grain boundaries. A number of toughening mechanisms have been suggested to account for this rather counterintuitive phenomenon. Each mechanism proposed is connected one way or another to heterogeneity on the scale of the grains. They include crack deflection, microcrack shielding, and crack bridging by uncracked grains. Quantitative toughening predictions for these mechanisms are not yet firmly established and a consensus on conditions when one mechanism is expected to dominate has not been reached.

This paper focuses on microcracking and addresses the question of the maximum toughening which can be expected from this mechanism. Considerable theoretical work has recently been devoted to the phenomenon of microcrack shielding in brittle materials. Some studies approach the problem on a continuum scale (Hoagland and Embury, 1980; Evans and Faber, 1980; Hutchinson, 1987; Ortiz, 1988) where a profusion of microcracks are imagined to participate in the process of shielding the main crack. Other studies (Rose, 1986; Rubinstein, 1986; Horii and Nemat-Nasser, 1987; Kachanov, 1987; Montagut and Kachanov, 1987; Gong and Horii, 1989) treat the microcracks as discrete entities interacting with the main crack tip. There are two potential contributions to toughening from microcracking. One is crack tip stress redistribution due to the release of residual stress when a microcrack is nucleated. This contribution is rather similar to plastic deformation at a crack tip in a metal or to dilatational transformation at the tip of a crack in a ceramic. The residual stress is present and varies from grain to grain when the crystals have thermal-expansion anisotropy. The other contribution results in stress redistribution at the main tip due to microcracking in the absence of residual stress. In the continuum approach this redistribution results due to the lowing of the stiffness of the microcracked material. In the discrete approach the redistribution occurs directly from the interaction of the microcracks with the main crack. It is this latter contribution which is of concern in this paper. The contribution due to release of residual stress is reasonably well in hand (Hutchinson, 1987) and does not present any major computational difficulties.

Specifically, in this paper, the interaction between one or two microcracks located near the tip of a macrocrack is considered. Optimal configurations are found which minimize the maximum energy release rates for *all* the crack tips involved. Although the outcome of a highly idealized model, these results supply insight into the maximum amount of toughening which can be expected from this contribution of microcracking. Prior work has primarily focussed on shielding of the main crack with no regard for any attendant amplification of the energy release rates of the microcracks. A toughening enhancement requires the *mutual shielding* of the main tip and the tips of the microcracks, otherwise crack advance will occur from one of the microcracks. This is the motivation for the search for the configuration with the lowest possible maximum energy release rate of all the crack tips involved.

This study is highly idealized in that attention is limited to plane strain cracks in an isotropic elastic solid. Microcracks in a brittle polycrystal usually nucleate on a grain boundary facet and arrest at a junction, or they may form on a crystal cleavage plane and arrest at the first grain boundary they encounter. In either case, the heterogeneity at the scale of the grains sets the size and orientation of the microcracks, and nucleation is usually assisted by residual stresses. Nevertheless, the results of this study do isolate an essential aspect of the interaction between a macrocrack and microcracks as it pertains to toughening.

A rationale for limiting attention to the one or two microcracks nearest the main crack tip can be found from both continuum and discrete interaction theories. Calculations using large arrays of discrete microcracks interacting with the macrocrack (Montagut and Kachanov, 1987) suggest that the locations of the nearest microcracks largely determine whether shielding or antishielding occurs. The details of the distribution of the microcracks outside the immediate tip region appear to be less important. The same conclusion can be drawn from continuum studies of the effect of zones of less stiff material surrounding a macrocrack tip (Hutchinson, 1987). Consider the semi-infinite crack tip in Fig. 1a which is surrounded by an annular circular zone with a reduced shear modulus $\bar{\mu}$ and an altered Poison's ratio $\bar{\nu}$. The crack is subject to a remote mode I loading characterized by K_I^0, and the stress intensity factor at the tip within the annular zone (with modulus μ and ν) is K_I^A. To lowest order in the differences in moduli, $\bar{\mu}-\mu$, and Poisson's ratio, $\bar{\nu}-\nu$,

$$K_I^A = K_I^0 \tag{1.1}$$

In other words, the annular zone of less stiff material surrounding the tip has neither a shielding nor an antishielding effect to lowest order. If the less stiff zone extends all the way to the tip such that the tip lies in the less stiff material, as shown in Fig. 1b, the crack tip stress intensity factor is altered according to

$$\frac{K_I^A}{K_I^0} = 1 - \frac{5}{8(1-\nu)}\left[\frac{\mu}{\bar{\mu}} - 1\right] + \frac{3}{4(1-\nu)}\left[\bar{\nu}\frac{\mu}{\bar{\mu}} - 1\right] \tag{1.2}$$

to lowest order in the moduli and Poisson's ratio differences (Hutchinson, 1987). Thus, it is the inner core of less stiff material, as opposed to the surrounding annular region, which mainly influences the stress level at the crack tip. Note also that the size of the circular zone does not enter into (1.2). Increasing the zone size does not alter the shielding.

2. Formulation of the problem

Consider the configuration in Fig. 2a where a single microcrack of length 2a is positioned near the tip of the main crack. The tip of the main crack is subject to a mode I stress intensity factor K_I^0 in the absence of the microcrack. When the size and distance of the microcrack from the tip is very small compared to the length of the macrocrack, one can consider an asymptotic problem where the semi-infinite main crack is remotely stressed consistent with the classical mode I crack tip field

$$\sigma_{ij} = \frac{K_I^0}{\sqrt{2\pi r}}\, \tilde{\sigma}_{ij}(\theta) \tag{2.1}$$

where (r,θ) are plane polar coordinates. The microcrack is arbitrarily positioned as characterized by the two angles, α and ω, and the distance, d, of its center from the main tip. Let

$$\mathcal{G}_0 = K_I^{0^2} \frac{(1-\nu^2)}{E} \tag{2.2}$$

be the energy release rate of the main tip in the absence of the microcrack, where E is Young's modulus and ν is Poisson's ratio. It will be referred to as the applied energy release rate. Denote the energy release rates of the three tips in the interaction problem in Fig. 2a by $\mathcal{G}_A$, $\mathcal{G}_B$ and $\mathcal{G}_C$. By dimensional considerations and the fact that a linear, plane strain problem is being analyzed, one concludes that

$$\mathcal{G}_A/\mathcal{G}_0 = f\,(d/a,\alpha,\omega) \tag{2.3}$$

with a functional dependence on the same variables for $\mathcal{G}_B/\mathcal{G}_0$ and $\mathcal{G}_C/\mathcal{G}_0$. Similarly the mode I or mode II stress intensity factor of any of the three tips must depend on the same three nondimensional position variables according to

$$K/K_I^0 = g\,(d/a,\alpha,\omega) \tag{2.4}$$

Thus, a small microcrack close to the tip has the same effect as a large microcrack farther from the tip with the same d/a ratio. More to the point for application to polycrystals, the influence of a microcrack of fixed size (e.g. the size of a grain facet) is larger the closer it is to the macrocrack tip. This observation is clearly related to the special role of the microcracks nearest the tip noted in the Introduction.

The two-microcrack configuration in Fig. 2b will also be considered. In this case the cracks will be restricted to be symmetrically positioned with respect to the semi-infinite main crack. Thus, by symmetry, only results for tips A, B and C need to be considered.

The solution to the interaction problem is obtained by numerical solution to an exact integral equation formulation similar to that used in (Kachanov, 1987; Hori and Nemat-Nasser, 1987; Gong and Horii, 1989). This formulation and the reduction for numerical analysis is given in the Appendix. The solution procedure leads to highly accurate results for the stress intensity factors and energy release rates. High accuracy is needed for the present minimization problem. Various approximate solutions, or solution procedures, have been proposed for the interaction problem. These approximations all tended to lose accuracy when $d/a < 1$ and the microcrack is located off the plane of the main crack as in Fig. 2a. In particular, they have large errors for the optimal crack configurations reported in the next section.

Two minimax problems are considered in this paper:

Problem No. 1

Minimize the maximum of $(\mathcal{G}_A/\mathcal{G}_0, \mathcal{G}_B/\mathcal{G}_0, \mathcal{G}_C/\mathcal{G}_0)$ with respect to all admissible d/a, α and ω. Admissible values of the position variables are those for which the cracks do not intersect.

Problem No. 2

Minimize the maximum of $\left(K_I^A/K_I^0,\ K_I^B/K_I^0,\ K_I^C/K_I^0\right)$ with respect to all admissible d/a, α and ω.

Solutions to the minimax problems are carried out using the Least Pth algorithm (Bandler and Charalambous, 1972) coupled with a Simplex search method (Press et al., 1986). In the terminology of optimization, the objective function to be minimized is either the maximum energy release rate or the maximum mode I stress intensity factor among all the crack tips.

3. Solutions, Optimal Solutions and Inferences

As an illustrative example, consider the special subset of configurations for the two-microcrack problem wherein the microcracks are parallel to the main crack ($\alpha = 0$) and d/a is fixed at the value 1.2. The dependence of the energy release rates of the tips on ω is shown in Fig. 3. When the microcrack is ahead of the macrocrack ($\omega < 60^0$) the energy release rate of the macrocrack tip is amplified above the applied value. Within this subset of configurations, the maximum shielding of the main tip A occurs when $\omega \cong 130°$ with $\mathcal{G}_A = .325$. However, in this configuration the energy release rate of tips C of the microcracks is larger than that of the main crack. Maximum mutual shielding (i.e. the minimum maximum energy release rate) in this subset of configurations occurs when $\omega \cong 140°$ with $\mathcal{G}_A = \mathcal{G}_C$.

The results of the solutions to the two minimax problems over the full range of admissible d/a, α and ω are presented in Table 1. The optimal configurations are shown in Fig. 4. Note that the differences between the optimal solutions and configurations are very small. Moreover, the optimal position parameters characterizing the one-microcrack problem are almost the same as for the two-microcrack problem. For Problem No. 1 where the objective function is based on the energy release rate the optimal solution gives

$$\mathcal{G}_A/\mathcal{G}_0 = \mathcal{G}_C/\mathcal{G}_0 = 0.468 \qquad \text{(one microcrack)} \tag{3.1}$$

$$\mathcal{G}_A/\mathcal{G}_0 = \mathcal{G}_C/\mathcal{G}_0 = 0.289 \qquad \text{(two microcracks)} \tag{3.2}$$

The objective function space is relatively flat in the neighborhood of the minimum solution. This holds true for each of the two objective functions and for the one- or two-microcrack problems. Thus there is a range of configurations about those listed in Table 1 for which the values of $\mathcal{G}_A$ and $\mathcal{G}_C$ are essentially the optimal values. For the same reason, the values of position variables for the optimal configurations are less accurate than the optimal values of the objective function, ie. $\mathcal{G}$ or K.

The optimal results are not entirely unexpected. Consider, for example, the configuration in the insert in Fig. 5 where a single microcrack is parallel to the main crack and the two lead tips, A and C, are equally extended. The variation of the energy release rates of the three tips with c/a is shown. As can be understood from elementary considerations, the applied energy release rate becomes equally partitioned between each of the lead tips when c/a << 1 and

$$\mathcal{G}_A/\mathcal{G}_0 \rightarrow \mathcal{G}_C/\mathcal{G}_0 \rightarrow 1/2 \qquad \text{as } c/a \rightarrow 0 \tag{3.3}$$

This arrangement is not far from optimal for the one microcrack case.

The two-microcrack case is not so easily understood. The analogous arrangement of two parallel microcracks has a variation of energy release rates shown in Fig. 6. In this case, the applied energy release rate is not equally partitioned as c/a → 0. Instead the main tip is shielded such that

$$\mathcal{G}_A/\mathcal{G}_0 \cong 0.1 \quad \text{and} \quad \mathcal{G}_C/\mathcal{G}_0 \cong 0.45 \qquad \text{as } c/a \rightarrow 0 \tag{3.4}$$

This configuration is quite far from optimal.

The optimal values of the mutually shielded tips in (3.1) and (3.2) suggest that the *largest* amount of microcrack toughening (excluding the contribution from the release of residual stress) that can be expected is 2 or 3 times the "intrinsic" toughness measured in surface energy units. That is, if crack advance of each of the tips is controlled by a critical value of energy release rate, $\mathcal{G}_{CRIT}$, then there exist one- or two-microcrack configurations for which the critical applied energy release rate, $\mathcal{G}_0$, is 2 or 3 times $\mathcal{G}_{CRIT}$. Whether optimal, or near optimal, configurations can actually control the overall toughness in a statistical sense along a crack front is an open issue.

The above conclusion is not only tempered by the fact that the calculation is a two dimensional one. As discussed in the Introduction, it is also premised on the assumption that shielding is dominated by the microcracks closest to the tip. In addition, the assumption of an "intrinsic" toughness, $\mathcal{G}_{CRIT}$, is obviously a simplification. Local conditions such as geometry, elastic anisotropy mismatches, and residual stresses at a grain boundary junction or grain boundary where a tip has arrested will influence the critical energy release rate for that tip at that location. The manner in which all these influences work to establish the polycrystalline toughness is extremely complex and difficult to model. The present results, though highly idealized, provide a reference for the effect of microcracking on toughness, excluding the contributions from the release of residual stress.

Acknowledgements

This work was supported by the Materials Research Laboratory (Grant NSF-DMR-86-14003) and DARPA University Research Initiative (Subagreement P.O. #VB38639-0 with the University of California, Santa Barbara, ONR Prime Contract N00014-86-K-0753) and the Division of Applied Sciences, Harvard University.

REFERENCES

Bandler J.W., Charalambous C., Practical Least Pth Optimization of Networks, *IEEE Trans. Microwave* **MTT-20**, 834 (1972).

Evans A.G., Faber K.T., Toughening of Ceramics by Circumferential Microcracking, *J. Am. Ceram. Soc.* **64**, 394 (1980).

Gong S., Horii H., General Solution to the Problem of Microcracks Near the Tip of a Main Crack, *J. Mech. Phys. Solids* **37**, 27 (1989).

Hoagland R.G., Embury J.D., A Treatment of Inelastic Deformation Around a Crack tip due to Microcracking, *J. Am. Ceram. Soc.* **63**, 404 (1980).

Hori M., Nemat-Nasser S., Interacting Micro-Cracks Near the Tip in the Process Zone of a Macro-Crack, *J. Mech. Phys. Solids* **35**, 601 (1987).

Hutchinson J.W., Crack Tip Shielding by Micro-Cracking in Brittle Solids, *Acta Metall.* **35**, 1605 (1987).

Kachanov M., Elastic Solids with Many Cracks: A Simple Method of Analysis, *Int. J. Solids Structures* **23**, 23 (1987).

Montagut E., Kachanov M., On Crack-Microcracks Interactions and Elastic Moduli of the Damage Zone, presented at ASME Winter Annual Meeting, Boston (1987).

Ortiz M., Microcrack Coalescence and Macroscopic Crack Growth Initiation in Brittle Solids, *Int. J. Solids Structures* **24**,231 (1988).

Press W.H. et al, Numerical Recipes, Cambridge University Press (1986).

Rose L.R.F., Microcrack Interaction with a Main Crack, *Int. J. Frac.* **31**, 233 (1986).

Rubinstein A.A., Macrocrack-Microcrack Interactions, *J. Appl. Mech.* **53**, 505 (1986).

Tada H., Paris P.C., Irwin G.R., Handbook for Stress Analysis of Cracks, Del Research, 2nd Edition (1985).

APPENDIX

Macrocrack/Microcrack Interaction Solution

The solution methodology is illustrated for the case of a one-microcrack system involving a semi-infinite crack and a microcrack of length 2a within an infinite body subject to remote loading as shown in Fig A1. Following the procedures in (Kachanov, 1987; Hori and Nemat-Nasser, 1987; Gong and Horii, 1989) the total problem in Fig. A1 is decomposed into three subproblems where each subproblem contains only one crack. Based on linear superposition principles, the stress intensity factors at the various crack tips in the total problem are found by summing the stress intensity factor contributions of the corresponding crack tips in the three subproblems. The macrocrack/microcrack interaction solution method involves constructing the integral equations governing pseudo-tractions $\tau^A_\beta(\rho)$ and $\tau^B_\beta(\eta)$ on the faces of the two cracks in subproblems 2 and 3. Here ρ is the lineal coordinate along the semi-infinite crack wake with $\rho = 0$ at the tip, and η is the lineal coordinate along the microcrack face, where $\eta = 0$ is midpoint of the microcrack.

In subproblem 1 the semi-infinite crack is subject to the same remote loadings as that found in the total problem. The resultant traction along the line segment BC has a component along the direction of BC denoted as $\sigma^*_1(\eta)$ and a component perpendicular to BC denoted as $\sigma^*_2(\eta)$. The location of the line segment BC corresponds to the location of the microcrack in the total problem.

In subproblem 2 the stress field within the infinite body is due to a traction distribution along the semi-infinite crack faces with a shear component $\tau^A_1(\rho)$ and a normal component $\tau^A_2(\rho)$. The traction distribution $\tau^A_\beta(\rho)$ is needed to maintain traction-free boundary condition along the semi-infinite crack faces in the total problem, the magnitudes of its components to be determined as part of the solution to the total problem. The resultant traction along the line segment BC has components $\sigma^B_\beta(\eta)$.

Similarly, in subproblem 3 the stress field within the infinite body is due to a traction distribution along the microcrack faces with a shear component $\tau_1^B(\eta)$ and a normal component $\tau_2^B(\eta)$. The resultant traction along the semi-infinite line segment has components $\sigma_1^A(\rho)$ and $\sigma_2^A(\rho)$ along directions that are parallel and perpendicular to the line segment.

Solution of the total problem is found by requiring the unknown tractions $\tau_\beta^A(\rho)$ and $\tau_\beta^B(\eta)$ in the subproblems to result in traction-free crack faces in the total problem such that

$$\begin{aligned} &\sigma_\beta^A(\rho) + \tau_\beta^A(\rho) = 0 && \text{for} \quad 0 \le \rho < \infty \\ &\sigma_\beta^B(\eta) + \tau_\beta^B(\eta) = -\sigma_\beta^*(\eta) && \text{for} \quad -a < \eta < a \end{aligned} \tag{A1}$$

From this point on our procedure departs somewhat from those in (Kachanov, 1987; Hori and Nemat-Nasser, 1987; Gong and Horii, 1989).

Subproblem 1

Let the applied K field for the *total* problem be expressed in complex form such that

$$K = K_I^0 + i K_{II}^0 \tag{A2}$$

where $i = \sqrt{-1}$ and K_{II}^0 has been included. The stresses $\sigma_\beta^*(\eta)$ then take the form

$$\begin{aligned} \sigma_2^* &= \mathrm{Re}[\, Z + iY \,] \\ \sigma_1^* &= \mathrm{Re}[\, Y \,] \end{aligned} \tag{A3}$$

where

$$\begin{aligned} Y &= -(\, \mathrm{Im}(Z) + y Z' \,)\, e^{i2\alpha} \qquad (\;)' \equiv \frac{d}{dz} \\ Z &= \frac{\bar{K}}{\sqrt{2\pi z}} \end{aligned} \tag{A4}$$

Here, $\bar{K}$ denotes the complex conjugate of K and z is the complex variable denoting the position of the point on BC.

Subproblem 2

The resultant stresses $\sigma_\beta^B(\eta)$ due to the pseudo-traction $\tau_\alpha^A(\rho)$ are defined as

$$\sigma^B_\beta(\eta) = -\int_0^\infty K^A_{\beta\alpha}(\eta;\rho)\ \tau^A_\alpha(\rho)\ d\rho \tag{A5}$$

where $K^A_{\beta\alpha}(\eta;\rho)$ is the β component of the resolved stresses on the line segment BC at location η due to a pair of unit line loads applied on the semi-infinite crack faces at location ρ. Here the repeated indice α is to be summed from 1 to 2. Explicit expressions for $K^A_{\beta\alpha}$ can be derived from results in (Tada et al, 1985). For numerical evaluation of the integrals in (A5) let

$$\tau^A_\alpha(u) = (1-u)^2 \sum_{j=1}^{N} A_{j\alpha} U_{j-1}(u) \qquad \frac{\rho}{a} = \frac{1+u}{1-u} \tag{A6}$$

where $U_{j-1}(u)$ is Chebyshev polynomial of the second kind of degree j-1 and u is the nondimensional distance variable defined such that $-1 \leq u \leq 1$. For admissible microcrack configurations where the microcrack and the semi-infinite crack do not overlap, (A5) can be integrated exactly in closed form giving

$$\sigma^B_\beta(\eta) = \sum_{j=1}^{N} A_{j\alpha} F_{\beta\alpha}(\eta) \tag{A7}$$

Subproblem 3

The resultant stresses $\sigma^A_\beta(\rho)$ due to the pseudo-traction $\tau^B_\alpha(\eta)$ are similarly defined as

$$\sigma^A_\beta(\rho) = -\int_{-a}^{a} K^B_{\beta\alpha}(\rho;\eta)\ \tau^B_\alpha(\eta)\ d\eta \tag{A8}$$

Explicit expressions for $K^B_{\beta\alpha}$ can also be derived from results in (Tada et al, 1985). For numerical evaluation of the integrals in (A8) let

$$\tau^B_\alpha(w) = \sum_{j=1}^{N} B_{j\alpha} U_{j-1}(w) \qquad \text{with} \qquad w = \frac{\eta}{a} \tag{A9}$$

Again, for admissible microcrack configurations (A8) can be integrated exactly in closed form giving

$$\sigma^{A}_{\beta}(\rho) = \sum_{j=1}^{N} B_{j\alpha} G_{\beta\alpha}(\rho) \qquad \text{(A10)}$$

Stress Intensity Factors

Substitution of (A3,A6,A7,A9 and A10) into (A1) results in a system of equations which are linear in the 4N-unknowns, $A_{j\alpha}$ and $B_{j\alpha}$, and which have an explicit, closed form dependence on ρ and η. Each of the four equations (A6,A9) are collocated at N points denoted as t_k where

$$U_N(t_k) = 0, \quad t_k = \cos\left(\frac{k\pi}{N+1}\right), \quad k = 1, \ldots, N \qquad \text{(A11)}$$

The stress intensity factors at the semi-infinite crack tip are found by combining the stress intensity factor contributions from subproblems 1 and 2 such that (Tada et al, 1985)

$$K^{A}_{\xi} = K^{0}_{\xi} - \sqrt{\frac{2a}{\pi}} \int_{0}^{\infty} \frac{1}{\sqrt{u}} \tau^{A}_{\xi}(u)\, du \qquad \text{(A12)}$$

where K^{0}_{ξ} are the magnitudes of the applied mode I and II stress intensity factors. The integrals in (A12) can be integrated exactly in closed form giving

$$K^{A}_{\xi} = K^{\infty}_{\xi} + 2\sqrt{2\pi a} \sum_{j=1}^{N} (-1)^{j} A_{j\xi} \qquad \text{(A13)}$$

The stress intensity factors at the microcrack tip C due to $\tau^{B}_{\xi}(\eta)$ take the form (Tada et al, 1985)

$$K^{C}_{\xi} = -\sqrt{\frac{a}{\pi}} \int_{-1}^{1} \sqrt{\frac{1+w}{1-w}}\, \tau^{B}_{\xi}(\eta)\, d\eta \qquad \text{(A14)}$$

which can be integrated exactly in closed form giving

$$K^{C}_{\xi} = -\sqrt{\pi a} \sum_{j=1}^{N} B_{j\xi} \qquad \text{(A15)}$$

Similarly, the stress intensity factors at the microcrack tip B take the form

$$K^{B}_{\xi} = -\sqrt{\frac{a}{\pi}} \int_{-1}^{1} \sqrt{\frac{1-w}{1+w}}\, \tau^{B}_{\xi}(\eta)\, d\eta \qquad \text{(A16)}$$

which can also be integrated exactly in closed form giving

$$K_{\xi}^{B} = \sqrt{\pi a} \sum_{j=1}^{N} (-1)^{j} B_{j\xi} \qquad (A17)$$

Since the integrals (A5, A8, A12, A14 and A16) that arise in this macrocrack/microcrack interaction formulation are integrated exactly, the accuracy of the crack interaction solution obtained using this method is limited only by the number of terms taken in the pseudo-traction series and the choice of collocation points.

TABLE 1

Optimal Solutions for one- and two-microcrack configurations

	one-microcrack		two-microcrack	
	objective function minimized			
optimal solution	G	K_I	G	K_I
ω	145.8	149.9	147.9	150.4
α	27.0	25.1	27.4	24.3
d/a	1.02	1.01	1.02	1.02
ϑ_A	0.468	0.429	0.289	0.246
ϑ_B	0.001	0.001	0.001	0.000
ϑ_C	0.468	0.502	0.289	0.312
K_I^A	0.683	0.652	0.538	0.496
K_I^B	0.031	0.025	0.023	0.020
K_I^C	0.623	0.653	0.475	0.495
K_{II}^A	0.042	-0.056	0.000	0.000
* K_{II}^B	0.017	0.007	-0.003	0.008
* K_{II}^C	0.283	0.276	0.252	0.259

* bottom crack

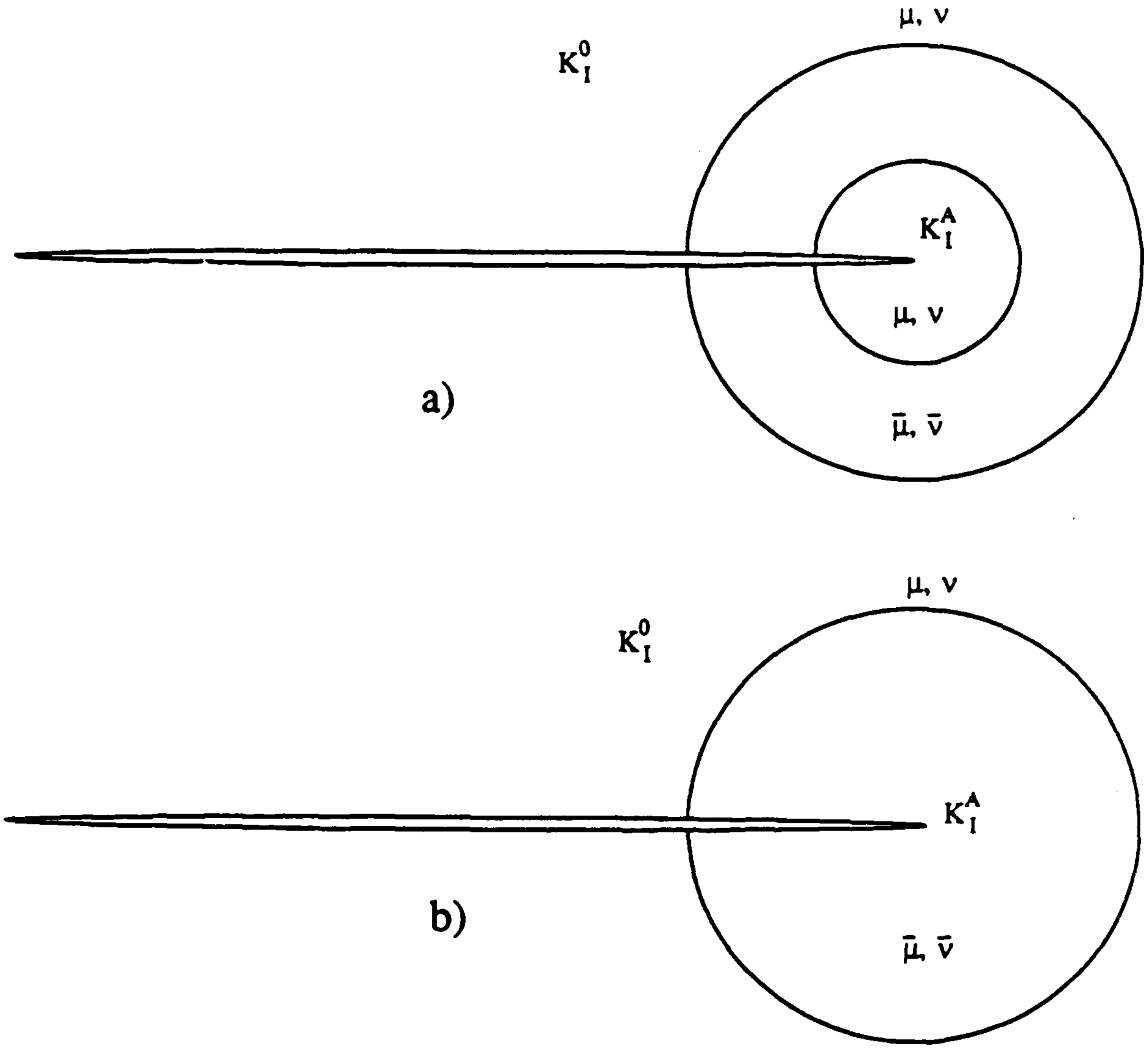

μ, ν
K_I^0
K_I^A
μ, ν
a)
$\bar{\mu}, \bar{\nu}$
μ, ν
K_I^0
K_I^A
b)
$\bar{\mu}, \bar{\nu}$

Fig. 1 Zone of reduced stiffness surrounding the tip of a semi-infinite crack: a) annular reduced stiffness zone, b) reduced stiffness zone extends all the way to crack tip.

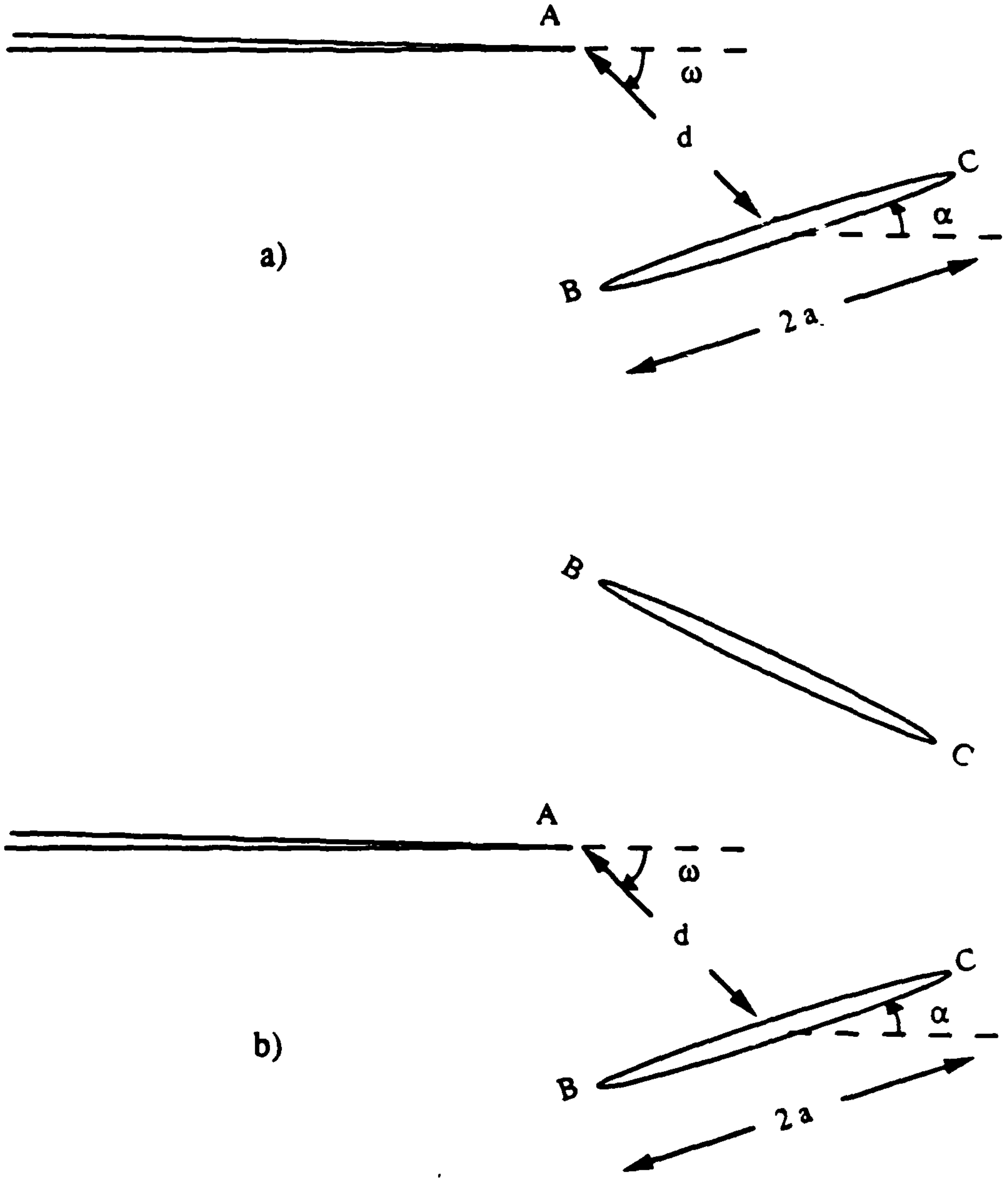
A
ω
d
C
α
a)
B
2a
B
C
A
ω
d
C
α
b)
B
2a

Fig. 2 Macrocrack/microcrack configurations: a) one microcrack, b) two symmetric microcracks.

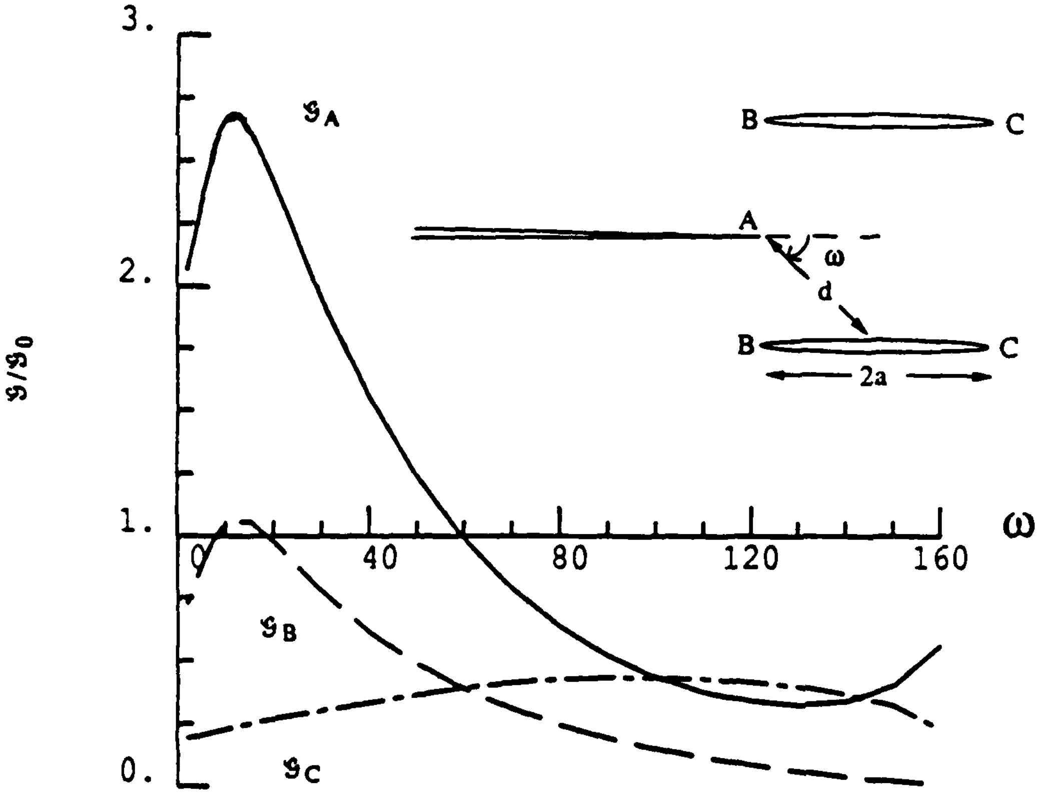

Fig. 3 Variation of energy release rates with ω for d/a = 1.2 and α = 0.

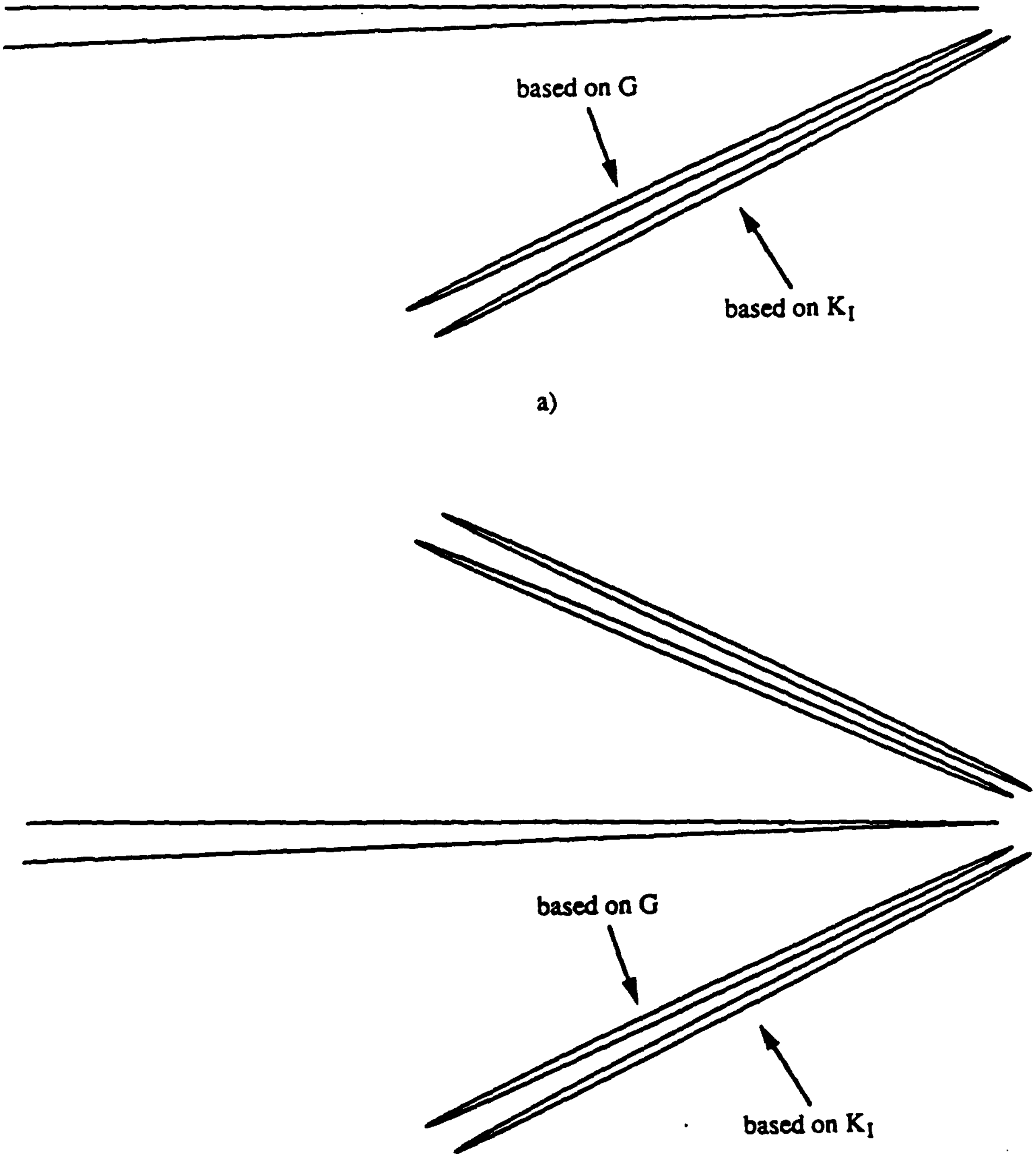
based on G
based on K_I
based on G
based on K_I

a)

b)

Fig. 4 Optimal one- and two-microcrack configurations.

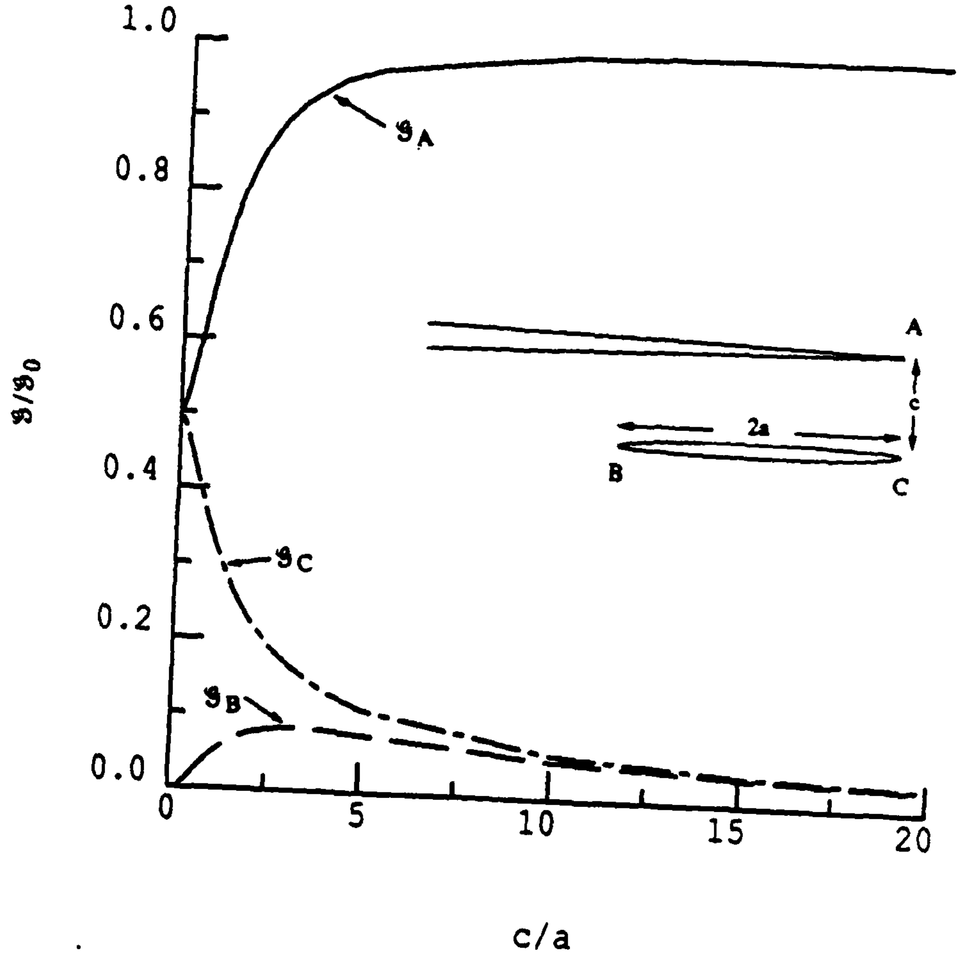

Fig. 5 Variation of energy release rates with c/a for a single microcrack parallel to main crack with aligned leading tips.

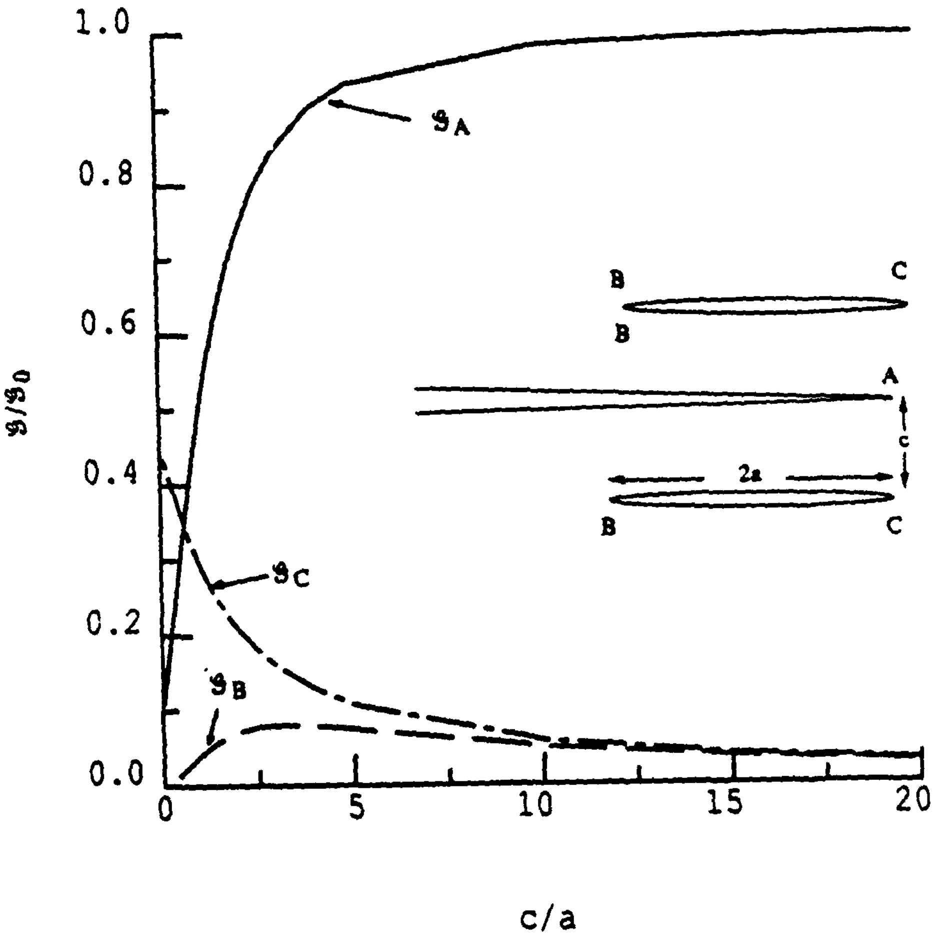

Fig. 6 Variation of energy release rates with c/a for two microcracks parallel to main crack with aligned leading tips.

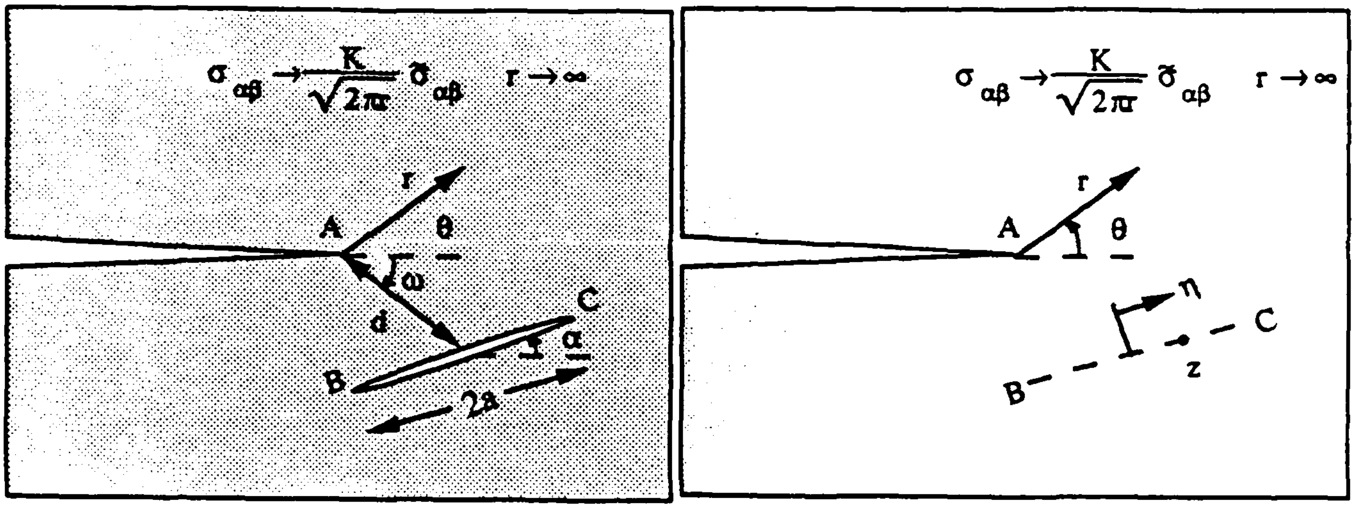
σ αβ → K/√2πr σ̃ αβ r → ∞
r
A
θ
ω
d
C
α
B
2a
σ αβ → K/√2πr σ̃ αβ r → ∞
r
A
θ
η
C
z
B

Total Problem

Subproblem 1

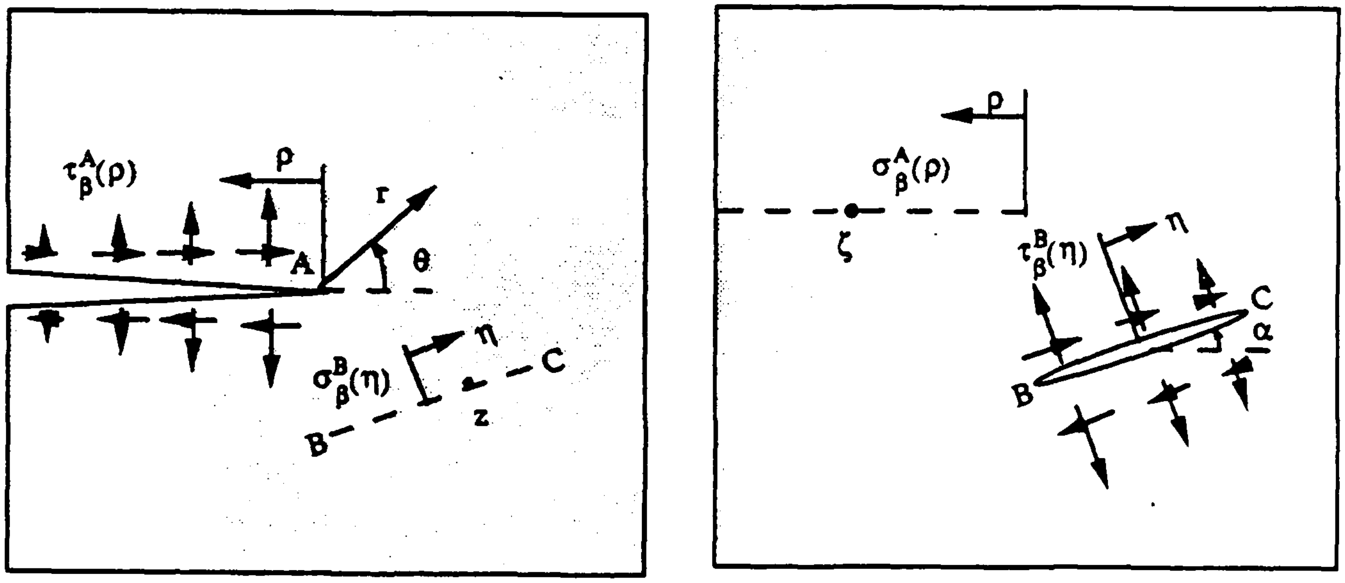
τ^A_β(ρ)
ρ
r
A
θ
σ^B_β(η)
η
C
z
B
ρ
σ^A_β(ρ)
ζ
η
τ^B_β(η)
C
α
B

Subproblem 2

Subproblem 3

Fig. A1 Decomposition of macrocrack/microcrack interaction problem into three subproblems.

MECH-145

FUNDAMENTAL SOLUTIONS FOR MICROCRACKING INDUCED BY RESIDUAL STRESS

David K. M. Shum
Yonggang Y. Huang

Division of Applied Sciences
HARVARD UNIVERSITY
Cambridge, Massachusetts 02138

June 1989

Fundamental Solutions for Microcracking Induced by Residual Stress

David K. M. Shum and Yonggang Y. Huang
Division of Applied Sciences
Harvard University
Cambridge, MA 02138

June 1989

Abstract. The problem studied is a spherical particle under residual compressive stress which subsequently nucleates an annular microcrack at its equator in the tensile stress field of the surrounding infinite matrix. This analysis provides fundamental solutions needed for continuum modelling of constitutive behavior of materials that undergo microcracking. The primary results of interest are the additional strains that show up at the macroscopic level via microcracking due to either release of residual stress or remote loading of the microcracked matrix. In addition, the stress intensity factor at the outer microcrack tip and the microcrack volume opening under these two loading conditions are evaluated. In presenting numerical results both particle and matrix are assumed to possess elastic isotropy, while the particle to matrix Young's modulus ratio assumes a range of values.

1. Introduction

In the absence of external loads microcracks form in polycrystalline and multi-phase materials when residual stress of sufficient magnitude develops within these materials. The residual stress can be due to a number of sources such as: thermal mismatch between phases of multi-phase materials, thermal anisotropy in the single crystals in polycrystalline materials, or crystallographic transformation of particles in a ceramic matrix [1-11]. In continuum modelling of the constitutive behavior of materials that undergo residual stress induced microcracking, the primary quantities of interest are the effective moduli of these microcracked materials [12,13] and the additional strains that show up at the macroscopic level due to microcracking [10].

In this paper an analysis of radial cracking around a spherical particle in an infinite matrix is performed. Specifically, the problem being considered is that of a spherical particle under residual compressive stress which subsequently nucleates an annular microcrack at its equator in the tensile stress field of the surrounding matrix as shown in Fig. 1. The configuration shown in Fig. 1 can be used to model either a circumferential-like microcrack around a particle such as those observed in zirconia toughened aluminas [9], or a microcrack that runs around a grain of a polycrystal along the grain boundaries the grain shares with its neighbors. Consequently, the radial extent of the microcrack in Fig. 1 is related to microstructural features of the surrounding matrix. This analysis thus provides fundamental solutions needed for continuum modelling of the constitutive behavior of materials that undergo microcracking.

The additional macroscopic strains due to microcracking mentioned previously arise from two distinct sources: 1) release of residual stress via microcracking, and 2) remote loading of the microcracked matrix. These additional strains are defined as the difference in macroscopic strains between the microcracked and the uncracked system due to either one of these sources of loading. With reference to Fig. 1, these additional strains, per unit volume of the particle, are denoted as ΔE_{ij} and are defined as [14]

$$\Delta E_{ij} = \frac{1}{2} \int_{A_R} \left\{ \left(u_i - u_i^o\right) n_j + \left(u_j - u_j^o\right) n_i \right\} dA \qquad (1.1)$$

where A_R denotes the outer boundary of the matrix, u_i denotes the displacement along A_R in the *presence* of the axisymmetric microcrack and u_i^o denotes the displacement along A_R in the *absence* of the microcrack. In continuum modelling of microcracking where the microcracks in the matrix are far enough apart so that interaction of the microcracks can be neglected, the total macroscopic strain contribution E_{ij} due to a volume fraction ρ of microcracked particles is simply [14]

$$E_{ij} = E_{ij}^o + \rho \left\langle \Delta E_{ij} \right\rangle \qquad (1.2)$$

where E_{ij}^o denotes the strain contribution in the absence of the microcracks and $\langle \Delta E_{ij} \rangle$ denotes an appropriate averaging of the extra strain contributions with respect to the orientations of the microcracks in the matrix.

In this study the additional macroscopic uniaxial (ΔE_{33}) and dilatational (ΔE_{kk}) strain contributions are presented for a number of loading situations to be specified. Note that (1.1) is not in a form suitable for numerical work. For actual computation of ΔE_{ij} (1.1) is transformed, as shown in the Appendix, into an expression over the microcrack surfaces which is convenient for numerical evaluation.

This paper is organized to first deal in Section 2 with the effects of release of residual compressive stress within the spherical particle in Fig. 1. For definiteness, the residual stress is henceforth assumed to be the consequence of transformation loading [1,2,8] of the particle. The uniform transformation strains, ε^T_{ij}, within the particle are taken to be either a pure dilatation of the form

$$\varepsilon^T_{ij} = \varepsilon^T \delta_{ij} \qquad i,j = 1,2,3 \tag{1.3}$$

or uniaxial in nature such that the only non-zero component of the transformation strain is

$$\varepsilon^T_{33} = \varepsilon^T \tag{1.4}$$

These two choices of transformation strains are motivated by their use in the majority of research works on brittle material systems such as ceramics.

In Section 3 the effects of remote loading of the microcracked matrix are analyzed. Specifically, the uniform remote stresses, Σ^∞_{ij}, are taken to be either hydrostatic tension in nature of the form

$$\Sigma^\infty_{ij} = \Sigma^\infty \delta_{ij} \qquad i,j = 1,2,3 \tag{1.5}$$

or uniaxial tension in nature such that the only non-zero component of the uniform remote stresses is

$$\Sigma^\infty_{33} = \Sigma^\infty \tag{1.6}$$

The extra macroscopic strains ΔE_{33} and ΔE_{kk} that result from these four loading situations will be presented in this study, along with results on the stress intensity factor at the outer microcrack tip and the microcrack volume opening under these loading conditions. Both particle and matrix are assumed elastically isotropic. The particle to matrix Young's modulus ratio assumes a range of values, but in the interest of reducing the number of parameters in the problem the Poisson's ratios are taken to be equal. For the case of common Young's modulus for particle and matrix, the stress intensity factor at the inner microcrack tip will also be calculated. Under the various loading conditions results for homogeneous material behavior ($E_1 = E_2$) will be presented first. For cases of inhomogeneous material behavior ($E_1 \neq E_2$), it is shown that the results can be represented by accurate formulae based on the homogeneous results. In interpreting the inhomogeneous material behavior results, note that the results from this study *cannot* be extended to the limit where the Young's modulus ratio E_1/E_2 approaches zero, since in the limit of a peripherally cracked spherical void the internal crack does not have an inner crack tip. The problem of a peripherally cracked spherical void in an infinite matrix is examined in [15,16].

2. Transformation Loading of Particle

2.1 Homogeneous material properties

We begin by considering transformation loading (1.3,1.4) of the particle in Fig. 1 where the particle and the matrix share the same Young's modulus. For the homogeneous problem solutions due to either dilatational or uniaxial transformation loading have been obtained based on a method detailed in [17]. As applied in the present context, this method involves formulating the singular integral equation governing the traction free boundary condition on the microcrack faces. The unknown function that arises naturally in this formulation is the crack opening displacement across the microcrack faces. The numerical solution of this integral equation involves expressing the unknown function as a Chebyshev series and then solving the integral equation via collocation in a standard way [18].

For this axially symmetric problem of transformation loading of the particle, the relations between the stress intensity factors and the microcrack length are presented in a normalized form in Fig. 2. The normalization factor K_0 will be introduced shortly. With reference to Fig. 1, note that values of the normalized microcrack length c/a between 0 and 1 span the complete range of crack geometry. The asterisks in Fig. 2 represent the numerical results to the singular integral equation mentioned previously, while the solid-line and dash-line curves are analytic approximations to be introduced later. With reference to Fig. 1, K_h^B and K_h^A denote the inner and outer microcrack tip stress intensity factors. The dependence of microcrack volume opening on crack length is presented in Fig. 3, in which the asterisks and the solid-line and dash-line curves again represent the numerical results and analytic approximations to this problem, with the normalization factor V_0 to be introduced shortly. For the present case where $E_1 = E_2$, it is shown in the Appendix that $\Delta E_{kk} = \Delta E_{33} = V$.

In Fig. 2, the normalization factor K_0 is the asymptotic form of both K_h^A and K_h^B as the normalized crack length c/a approaches zero, while in Fig. 3 the normalization factor V_0 is the asymptotic form of the microcrack volume opening as c/a approaches zero. For dilatational transformation loading K_0 and V_0 take the forms

$$K_0 = \frac{E\varepsilon^T}{3(1-\nu)}\sqrt{\frac{\pi c}{2}}$$
$$V_0 = (1+\nu)\,\frac{\pi^2}{3}\,b\,c^2\,\varepsilon^T \tag{2.1}$$

while for uniaxial transformation loading they take the forms

$$K_0 = \frac{7E\,\varepsilon^T}{15\,(1-\nu^2)}\sqrt{\frac{\pi c}{2}}$$
$$V_0 = \frac{7\pi^2}{15}\,b\,c^2\,\varepsilon^T \tag{2.2}$$

As expected, the inner microcrack tip stress intensity factor K_h^B is higher than the outer tip value K_h^A for both dilatational and uniaxial transformation loading. However, while the dilatational stress intensity results appear to be greater than their uniaxial counterparts, it must be noted that the net particle dilatation assumed in these analyses are not the same for the two transformation loading cases. Specifically, in the dilatational case

$$\left(\varepsilon_{kk}^T\right)_{dil} = 3\varepsilon^T \tag{2.3}$$

while in the uniaxial case

$$\left(\varepsilon_{kk}^T\right)_{uni} = \varepsilon^T \tag{2.4}$$

Consequently, for equal amount of particle dilatation, the stress intensity factors due to uniaxial transformation strains are much higher than their dilatational transformation strains counterparts. Similar caution must be applied when interpreting the microcrack volume opening results presented in Fig. 3.

Finally, the homogeneous material property results in Figs. 2 and 3 can be neatly approximated using formulae of the simple form

$$\frac{V_h}{V_0} = \left(1 - \frac{c}{a}\right)^p$$

$$\frac{K_h^A}{K_0} = \left(1 - \frac{c}{a}\right)^q \tag{2.5}$$

$$\frac{K_h^B}{K_0} = \left(1 - \frac{c}{a}\right)^r$$

where the best fits for dilatational transformation loading results correspond to

$$p = 1, \quad q = 2.4, \quad r = 0.55 \tag{2.6}$$

whereas for uniaxial transformation loading

$$p = 1.45, \quad q = 3.1, \quad r = 0.74 \tag{2.7}$$

The solid-line curves in Figs. 2 and 3 represent best fits for dilatational transformation loading results while the dash-line curves correspond to best fits for uniaxial transformation loading results. In addition to providing a check on the accuracy of the finite element results to be presented in Section 2.2 for the case $E_1 = E_2$, these approximate expressions will be used to unify the finite element results in a way that will be clear later in the paper.

2.2 Inhomogeneous material properties

In modelling material systems in which microcracking is seen to occur around inclusions or second phase particles, results are needed for the transformation loading problem in which the matrix and particle moduli are not the same. For this part of the investigation, finite element solutions using the ADINA computer code have been obtained for three microcrack length to particle size ratios (c/b = 0.1,1,4) which should span the range of most interest. In addition, ratios of particle to matrix Young's modulus E_1/E_2 from 0.1 to 10 have been incorporated into the calculations, as these values are representative of modulus ratios in brittle material systems such as those found in ceramics [1]. In this part of the study the common Poisson's ratio ν is restricted to 0.3 to limit the number of calculations.

The dilatational transformation loading results are presented in Figs. 4 to 6. In Fig. 4 the stress intensity factor K at the outer microcrack tip is normalized by the corresponding stress intensity factor for the homogeneous problem $K_h (= K_h^{\Lambda})$, where K_h is found by evaluating (2.1,2.5) using the matrix's Young's modulus such that $E = E_2$. The three curves in Fig. 4 correspond to results based on the three crack lengths mentioned previously. This normalized stress intensity factor is plotted first as a function of E_1/E_2 for $0.1 \leq E_1/E_2 \leq 1$, and then as a function of E_2/E_1 for $1 \geq E_2/E_1 \geq 0.1$. In addition to the stress intensity factors results, the present choice of abscissa nicely exhibits the modulus ratio dependence of other quantities of interest and is used in all subsequent data presentations.

By normalizing the stress intensity factor with respect to the homogeneous solutions as indicated, the results have very little additional dependence on the microcrack length to particle size ratio c/b. In other words, these normalized curves are, to a very good approximation, *geometry independent.* As a result of this normalization scheme, *the dependence of the outer microcrack tip stress intensity factor on microcrack geometry and material properties are decoupled*, so that microcrack length effects are wholly incorporated in the homogeneous solution while Young's modulus effects have the form shown in Fig. 4. Consequently, while numerical results have been generated for only three crack lengths, stress intensity factor results for any other crack length can be obtained using (2.1,2.5) and Fig. 4.

In Fig. 5 the microcrack volume opening V is similarly normalized by the corresponding microcrack volume opening for the homogeneous problem V_h, where V_h is also found by evaluating (2.1,2.5) using the matrix's Young's modulus such that $E = E_2$. Again, the universal nature of this normalization scheme is clearly evident. Consequently, the dependence of microcrack volume opening on microcrack geometry and material properties are also decoupled, and microcrack volume opening results for all crack lengths can be obtained.

As mentioned in Section 1, the release of residual stress due to microcrack formation creates additional macroscopic "inelastic" strains (1.1) in the material in which the particle is imbedded. In Fig. 6 the extra macroscopic dilatational (ΔE_{kk}) and uniaxial (ΔE_{33}) strain contributions due to dilatational transformation strains in the particle are plotted. In addition, the microcrack volume opening results from Fig. 5 are replotted here for comparison. In Fig. 6 V, ΔE_{33} and ΔE_{kk} are normalized with respect to the particle volume V_p and the magnitude of the transformation strain ε^T. However, the differences among V, ΔE_{kk} and ΔE_{33} are seen to be small when $c/b \geq 1$. Consequently, the microcrack volume opening V may be used to approximate ΔE_{33} and ΔE_{kk} when $c/b \geq 1$, and these additional macroscopic strain quantities for all crack lengths satisfying $c/b \geq 1$ can be obtained.

The uniaxial transformation loading results exhibit trends identical to those already mentioned due to dilatational transformation loading. In particular, previous comments on the universal nature of the normalization scheme used to present stress intensity factor and microcrack volume opening results apply to uniaxial transformation loading results also. The universal functions generated using (2.2,2.5) are presented in Figs. 7 and 8 for the uniaxial transformation loading results. The results for ΔE_{kk}, ΔE_{33} and V under uniaxial transformation loading are shown in Fig. 9, where the trends are seen to be similar to the trends for these quantities under dilatational transformation loading. Consequently, the microcrack volume opening V may also be used to approximate ΔE_{33} and ΔE_{kk} when $c/b \geq 1$, enabling determination of these additional macroscopic strain quantities for all crack lengths satisfying $c/b \geq 1$.

Finally, when the particle and matrix share the same Poisson's ratio, it can be shown that for transformation and remote loadings of the type specified in (1.3-1.6) the inequalities

$$V < \Delta E_{33} \qquad\qquad V < \Delta E_{kk} \tag{2.8}$$

hold when the particle is more compliant than the matrix such that $E_1/E_2 < 1$. When the particle is stiffer than the matrix such that $E_1/E_2 > 1$, the inequalities

$$V > \Delta E_{33} \qquad V > \Delta E_{kk} \tag{2.9}$$

are also satisfied. These general trends are apparent in Figs. 6 and 9 for transformation loading results, and will be apparent in Figs. 10 and 11 for remote loading results in the next section.

3. Remote Loading of Microcracked Matrix

3.1 Homogeneous material properties

When the particle and matrix share the same Young's modulus value, the magnitude of the stress intensity factors of the inner and outer microcrack tips as a function of the microcrack length can be found in [19]. In particular, the outer tip stress intensity factor due to either remote hydrostatic (1.5) or remote uniaxial (1.6) loading is the same and takes the form

$$\begin{aligned} K_h &= \Sigma^{\infty} \sqrt{\frac{\pi c}{2}}\, f\left(\frac{c}{a}\right) \\ f\left(\frac{c}{a}\right) &= 1 - .116\frac{c}{a} + .016\left(\frac{c}{a}\right)^2 \end{aligned} \tag{3.1}$$

The microcrack volume opening, while not given in [19], can be found via (3.1) and can be very accurately represented by the expression

$$V_h = \frac{\pi^2 (1 - \nu^2)\, \Sigma^{\infty}}{E}\, a c^2 \left(1 - 0.469\, \frac{c}{a}\right) \tag{3.2}$$

3.2 Inhomogeneous material properties

It is found that the normalization scheme used for the transformation loading results in Section 2, in which the inhomogeneous results are normalized with respect to the homogeneous results, does not produce universal functions that are essentially geometry independent under present loading conditions. However, it is found that results for both remote hydrostatic and remote uniaxial loading can be very accurately represented by simple expressions that *decouple* the dependence of the results on microcrack geometry and material properties. Specifically, for the case where the particle is more compliant than the matrix such that $E_1 < E_2$, the stress intensity factor and microcrack volume opening results take the simple form

$$\frac{K}{K_h} = 1 + \alpha_K \left(1 - \frac{E_1}{E_2}\right)^{\frac{3}{2}} \left(1 - \frac{c}{a}\right)^2$$

$$\frac{V}{V_h} = 1 + \alpha_V \left(1 - \frac{E_1}{E_2}\right)^{\frac{3}{2}} \left(1 - \frac{c}{a}\right)^{\frac{3}{2}} \tag{3.3}$$

For the case of remote hydrostatic loading

$$\alpha_K = 0.7 \qquad \alpha_V = 1.1 \tag{3.4}$$

while for the case of remote uniaxial loading

$$\alpha_K = 1.2 \qquad \alpha_V = 1.8 \tag{3.5}$$

When the particle is stiffer than the matrix such that $E_1 > E_2$, the stress intensity factor and microcrack volume opening results take the equally simple form

$$\frac{K}{K_h} = 1 - \beta_K \left(1 - \frac{E_2}{E_1}\right)^{\frac{3}{2}} \left(1 - \frac{c}{a}\right)^2$$

$$\frac{V}{V_h} = 1 - \beta_V \left(1 - \frac{E_2}{E_1}\right)^{\frac{3}{2}} \left(1 - \frac{c}{a}\right)^{\frac{3}{2}} \tag{3.6}$$

For the case of remote hydrostatic loading

$$\beta_K = 0.4 \qquad \beta_V = 0.5 \tag{3.7}$$

while for the case of remote uniaxial loading

$$\beta_K = 0.9 \qquad \beta_V = 1.0 \tag{3.8}$$

The average error associated with the use of (3.3-3.8) is less than 4%.

In Fig. 10 the microcrack volume opening, the additional macroscopic dilatational (ΔE_{kk}) and uniaxial (ΔE_{33}) strain contributions due to remote hydrostatic loading of the matrix are plotted as a function of the modulus ratio. In Fig. 10, V, ΔE_{kk} and ΔE_{33} are normalized with respect to the particle volume V_p and the ratio of the magnitude of the remote stress to the matrix Young's modulus Σ^{∞}/E_2. Using the present normalization scheme the differences among V, ΔE_{kk} and

ΔE_{33} are small when $c/b \geq 1$. Consequently, the simple expressions for V in (3.3,3.6) may be used to approximate ΔE_{33} and ΔE_{kk} when $c/b \geq 1$.

Analogous to the results plotted in Fig 10, corresponding remote uniaxial loading results shown in Fig. 11 also exhibit trends identical to those already mentioned for loading under remote hydrostatic tension. As a result, the simple expressions for V in (3.3,3.6) may also be used to approximate ΔE_{33} and ΔE_{kk} when $c/b \geq 1$.

4. Conclusion

The problem of a spherical particle under residual compressive stress which subsequently nucleates an annular microcrack at its equator in an infinite matrix is studied. This analysis provides fundamental solutions needed for continuum modelling of constitutive behavior of materials that undergo microcracking. The primary results presented in this work are the additional macroscopic strains that result from microcracking, along with results on the stress intensity factor at the outer microcrack tip and the microcrack volume opening. In all cases examined the results are presented in a way which decouples the geometry and material properties dependence of the problem.

Acknowledgements

This work was supported by the Materials Research Laboratory (Grant NSF-DMR-86-14003) and DARPA University Research Initiative (Subagreement P.O. #VB38639-0 with the University of California, Santa Barbara, ONR Prime Contract N00014-86-K-0753) and the Division of Applied Science, Harvard University. The authors would like to thank Professor John W. Hutchinson for suggesting this problem and for his comments on the paper, and Professor Isaac F. Silvera for the use of his computer facilities for the finite element portion of this work.

REFERENCES

1. A.G. Evans and A.H. Heuer, Review - Transformation Toughening in Ceramics: Martensitic Transformations in Crack-Tip Stress Field, *J. Am. Ceram. Soc.* 63, 241 (1980).

2. M. Rühle, N. Claussen and A.H. Heuer, Transformation and Microcrack Toughening as Complementary Processes in ZrO_2-Toughened Al_2O_3, *J. Am. Ceram. Soc.* 69, 195 (1982).

3. N. Claussen, R.L. Cox and J.S. Wallace, Slow Growth of Microcracks: Evidence for One Type of ZrO_2 Toughening, *J. Am. Ceram. Soc.* C-190 (1982).

4. A.G. Evans and K.T. Faber, Crack-Growth Resistance of Microcracking Brittle Materials, *J. Am. Ceram. Soc.* 67, 255 (1984).

5. Y. Fu and A.G. Evans, Some Effects of Microcracks on the Mechanical Properties of Brittle Solids - I. Stress, Strains Relations, *Acta Metall.* 33, 1515 (1985).

6. A.G. Evans and R.M. Cannon, Toughening of Brittle Solids by Martensitic Transformations, *Acta Metall.* 34, 761 (1986).

7. A. A. Rubinstein, Macrocrack-Microcrack Interaction, *J. Appl. Mech.* 53, 505 (1986).

8. J.W. Hutchinson, Advanced Materials for Severe Service Applications, (eds. K. Iida and A.J. McEvily) (1987).

9. M. Rühle, A.G. Evans, R.M. McMeeking, P.G. Charalambides and J.W. Hutchinson, Microcrack Toughening in Alumina/Zirconia, *Acta Metal.* 35, 2701 (1987).

10. J.W. Hutchinson, Crack Tip Shielding by Micro-Cracking in Brittle Solids, *Acta Metall.* 35, 1605 (1987).

11. S.X. Gong and H. Horii, General Solution to the Problem of Microcracks Near the Tip of a Main Crack, *J. Mech. Phys. Solids* 37, 27(1989).

12. B. Budiansky, R.J. O'Connell, Elastic Moduli of a Cracked Solid, *Int. J. Solids Structures* 12, 81 (1976).

13. N. Laws, J.R. Brockenbrough, The Effect of Microcrack Systems on the Loss of Stiffness of Brittle Solids, *Int. J. Solids Structures* 23, 1247 (1987).

14. J.W. Hutchinson, Micro-Mechanics of Damage in Deformation and Fracture, Dept. of Solid Mechanics, Technical University of Denmark (1987).

15. F.I. Baratta, Refinement of Stress Intensity Factor Estimates for a Peripherally Cracked Spherical Void and a Hemispherical Surface Pit, *J. Am. Ceram. Soc.* 64, C-4 (1981).

16. G.G. Trantina, M. Barishopolsky, Elastic-Plastic Analysis of Small Defects - Voids and Inclusions, *Engg Fract. Mech.* 20, 1 (1984).

17. J. Weaver, Three-Dimensional Crack Analyses, *Int. J. Solids Structures* 13, 321 (1977).

18. F.Erdogan, G.D. Gupta, On the Numerical Solutions of Singular Integral Equations, *Quart. Appl. Math.* 525 (1972).

19. H. Tada, P.C. Paris and G.R. Irwin, Handbook for Stress Analysis of Cracks, 2nd Ed.. Del Research (1985).

20. A.I. Lur'e, Three Dimensional Problems of the Theory of Elasticity, Interscience (1964).

21. J.D. Eshelby, The Determination of the Elastic Field of an Ellipsoidal Inclusion, and Related Problems, *Proc. Roy. Soc.* A241, 376 (1957).

APPENDIX

Numerical Evaluation of Macroscopic Strains ΔE_{ij}

While the formal definition of ΔE_{ij} in (1.1) involves a surface integral over the outer surface A_R in Fig. 1, for numerical purposes it proves more feasible to evaluate ΔE_{ij} over the microcrack surfaces. This reformulation requires that we consider two separate elasticity problems of a particle inside an infinite matrix where both particle and matrix are assumed to possess elastic isotropy.

Test Problem

The geometry of this problem is that in Fig. 1 except the annular ring crack is *absent*. Loading is applied via uniform remote stresses $\bar{\Sigma}^{\infty}_{ij}$. The resultant field quantities of stresses, strains and displacements everywhere are denoted as Σ_{ij}, E_{ij} and U_i, and may be evaluated in closed form using methods detailed in [20]. While this problem has no direct bearing on the definition of ΔE_{ij} in (1.1), the solutions to this test problem will be used to back out values for ΔE_{33} and ΔE_{kk} in a manner that will be apparent later.

Main Problem

Let the resultant field quantities of stresses, strains and displacements everywhere for the geometry shown in Fig. 1 due to loadings specified in (1.3-1.6) be denoted as σ_{ij}, ε_{ij} and u_i, where these quantities in general need to be evaluated using the finite element method. The corresponding quantities in the *absence* of the annular ring crack are denoted as σ^0_{ij}, ε^0_{ij} and u^0_i, and may be evaluated in closed form [20,21].

Reformulation of ΔE_{ij} begins by pre-multiplying (1.1) with the test stresses $\bar{\Sigma}^{\infty}_{ij}$ such that

$$\bar{\Sigma}^{\infty}_{ij}\Delta E_{ij} = \frac{1}{2}\int_{A_R} \Sigma_{ij}\left\{\left(u_i - u_i^o\right)n_j + \left(u_j - u_j^o\right)n_i\right\} dA \qquad \text{(A1)}$$

Keeping in mind that the stresses Σ_{ij} are symmetric and in equilibrium, and making use of the following notations

$\delta_i = u_i^+ - u_i^-$

A_c^+, A_c^- = top and bottom microcrack faces

it follows directly from successive applications of both the reciprocity and divergence theorems that

$$\bar{\Sigma}^{\infty}_{ij}\,\Delta E_{ij} = \int_V \Sigma_{ij}\left(\varepsilon_{ij} - \varepsilon^0_{ij}\right) dV + \int_{A_c^+} \Sigma_{ij}\,\delta_i\, n_j dA \qquad (A2)$$

where the unit normal vector n_j in the crack face integral points *into* the matrix. Now decompose the volume integral in (A2) into two integrals over the volume of the particle V_P and the volume of the matrix V_R such that

$$\int_V \Sigma_{ij}\left(\varepsilon_{ij} - \varepsilon^0_{ij}\right) dV = \int_{V_P} \Sigma_{ij}\left(\varepsilon_{ij} - \varepsilon^0_{ij}\right) dV + \int_{V_R} \Sigma_{ij}\left(\varepsilon_{ij} - \varepsilon^0_{ij}\right) dV \qquad (A3)$$

Next evaluate (A3) by first focusing on the parts of the integrands involving the strain quantities ε_{ij}. To evaluate the integral over the particle volume V_P, note that application of the reciprocity theorem for the case of uniform remote loading via $\bar{\Sigma}^{\infty}_{ij}$ results in

$$\int_{V_P} \Sigma_{ij}\varepsilon_{ij} dV = \int_{V_P} \sigma_{ij} E_{ij} dV \qquad (A4)$$

For the case of transformation loading of the particle, application of the reciprocity theorem results in

$$\int_{V_P} \Sigma_{ij}\varepsilon_{ij} dV = \int_{V_P} \sigma_{ij} E_{ij} dV + \int_{V_P} \Sigma_{ij}\varepsilon^T_{ij} dV \qquad (A5)$$

where ε^T_{ij} is the transformation strain. By repeating (A4,A5) for the strain quantities ε^0_{ij} and noting that the value of the second integral in (A5) involving ε^T_{ij} has the same value for both the cracked and the uncracked state, the particle volume integral in (A3) takes the form

$$\int_{V_P} \Sigma_{ij}\left(\varepsilon_{ij} - \varepsilon^0_{ij}\right) dV = \int_{V_P} E_{ij}\left(\sigma_{ij} - \sigma^0_{ij}\right) dV \qquad (A6)$$

A straightforward application of the reciprocity theorem for the the matrix volume integral also gives

$$\int_{V_R} \Sigma_{ij}\left(\varepsilon_{ij} - \varepsilon^0_{ij}\right) dV = \int_{V_R} E_{ij}\left(\sigma_{ij} - \sigma^0_{ij}\right) dV \tag{A7}$$

The volume integral in (A2) can thus be transformed using the divergence theorem into two surface integrals of the form

$$\int_{V} \Sigma_{ij}\left(\varepsilon_{ij} - \varepsilon^0_{ij}\right) dV = \int_{A_R} \left(\sigma_{ij} - \sigma^0_{ij}\right) U_i\, n_j\, dA - \int_{A_c^{\pm}} \left(\sigma_{ij} - \sigma^0_{ij}\right) U_i\, n_j\, dA \tag{A8}$$

By keeping in mind the fact that

$$\begin{aligned} &\text{on } A_R && \sigma_{ij} = \sigma^0_{ij} \\ &\text{on } A_c^{\pm} && \sigma_{ij} n_j = 0 \\ &&& (\sigma^0_{ij})^+ = (\sigma^0_{ij})^- \\ &&& U_i^+ = U_i^- \end{aligned} \tag{A9}$$

the integral over the volume V in (A8) is identically equal to zero. Finally, (A1) takes the form

$$\bar{\Sigma}^{\infty}_{ij} \Delta E_{ij} = \int_{A_c^+} \Sigma_{ij}\, \delta_i\, n_j dA \tag{A10}$$

The reason for solving the test problem is now clear. By evaluating (A10) using the solutions to the test problem corresponding to

$$\bar{\Sigma}^{\infty}_{ij} = \delta_{ij} \tag{A11}$$

the integral expression in (A10) reduces to the additional macroscopic dilatational strain quantity ΔE_{kk}. By evaluating (A10) using the solutions to the test problem where the only non-zero component of the uniform remote stresses is

$$\bar{\Sigma}^{\infty}_{33} = 1 \tag{A12}$$

the integral expression in (A10) reduces to the additional macroscopic uniaxial strain ΔE_{33}.

When the particle and matrix share the same Young's modulus value such that $E_1 = E_2$ the stresses $\bar{\Sigma}^{\infty}_{ij}$ and Σ_{ij} are identical and therefore ΔE_{kk} and ΔE_{33} reduce to the crack opening volume V.

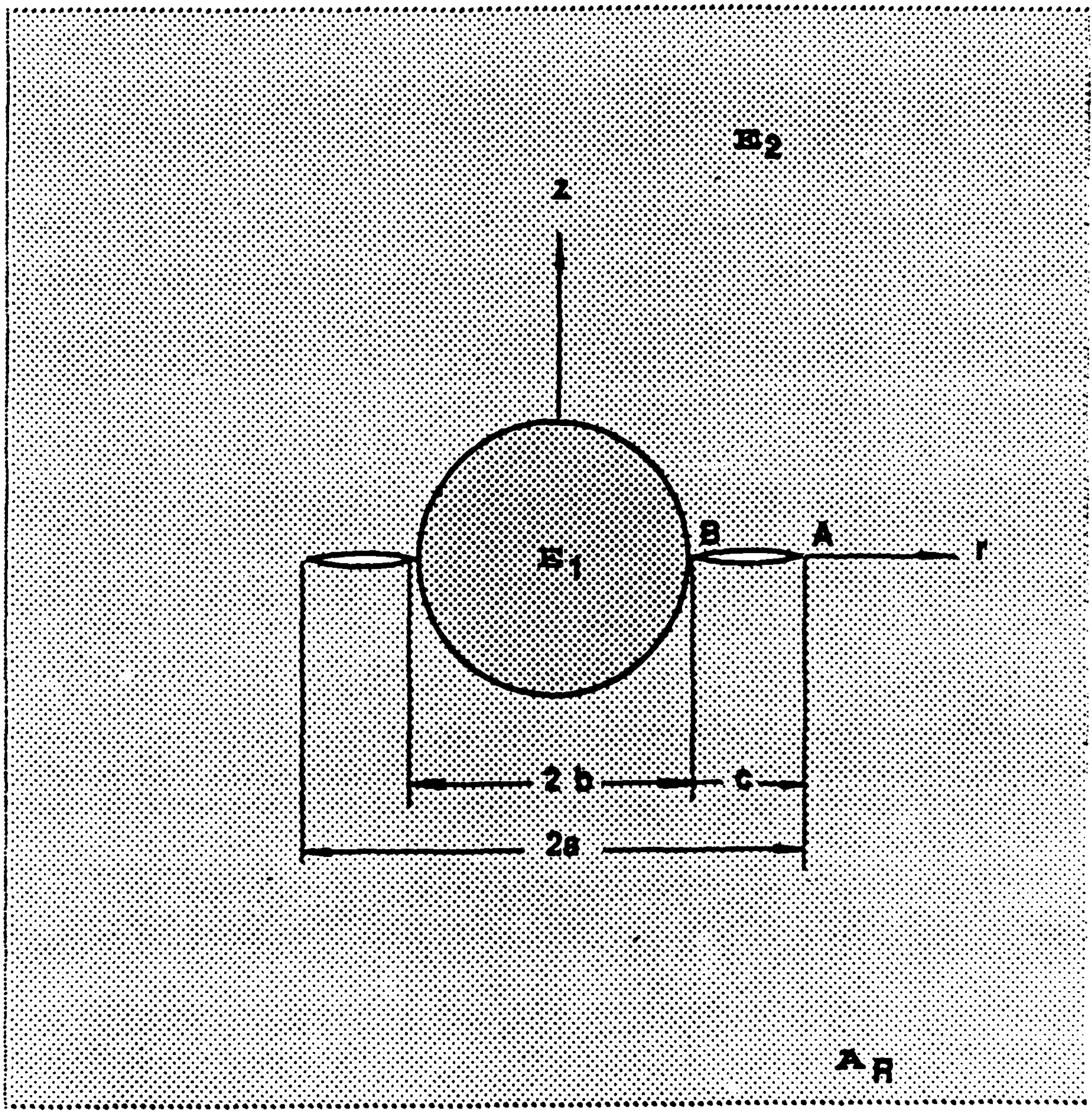
E2
z
B
A
r
E1
2 b
c
2a
A R

Fig. 1 Axisymmetric microcrack around particle in infinite matrix.

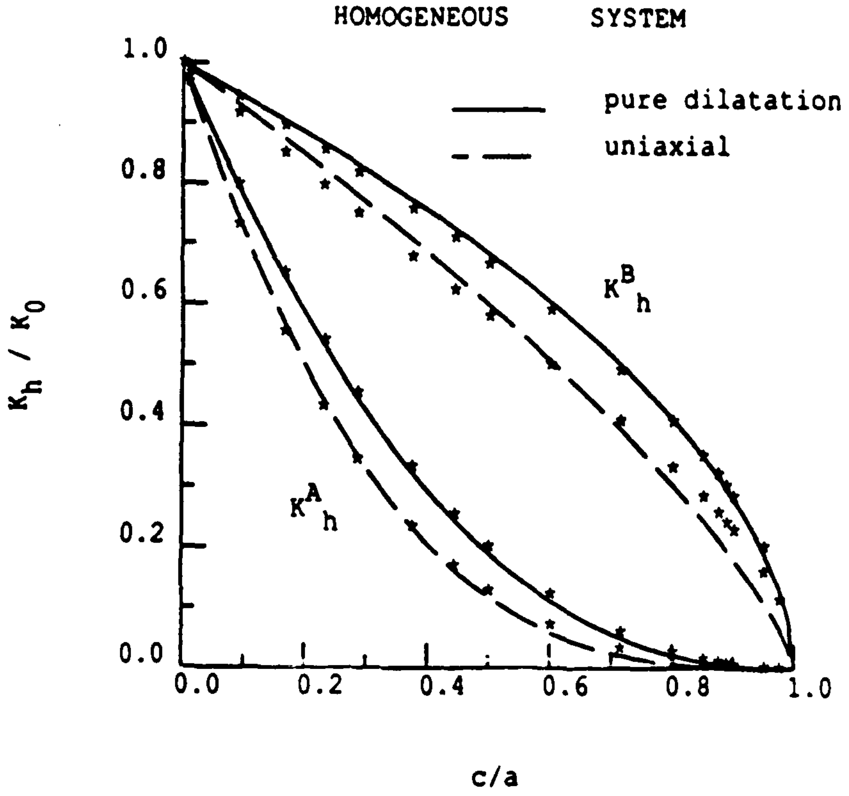

Fig. 2 Stress intensity factor results for dilatational and uniaxial transformation loading of particle when $E_1 = E_2$.

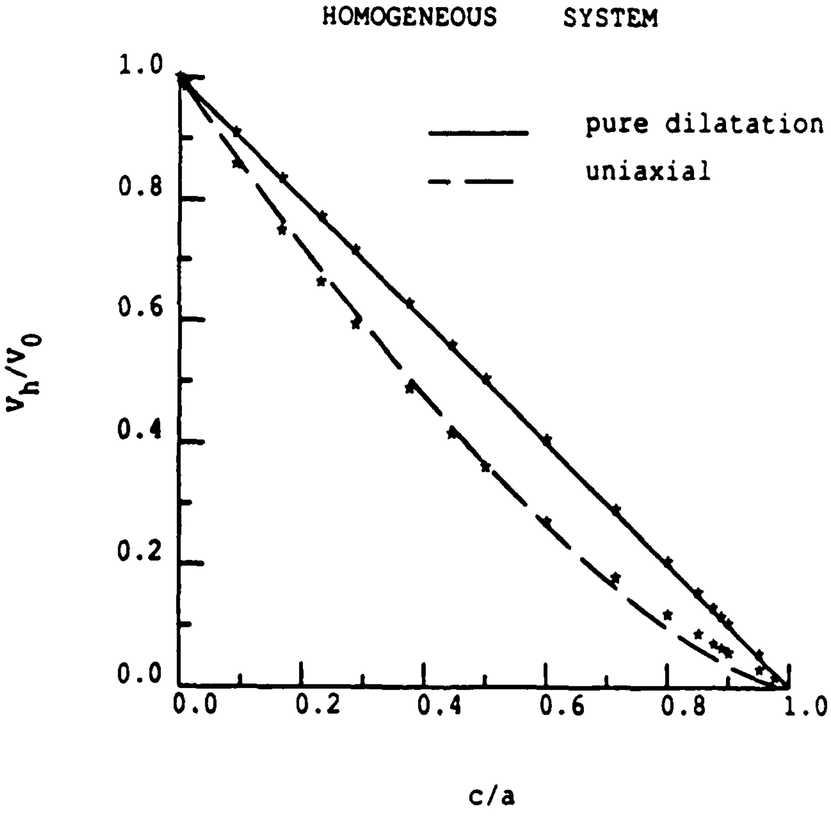

Fig. 3 Microcrack volume opening results for dilatational and uniaxial transformation loading of particle when $E_1 = E_2$.

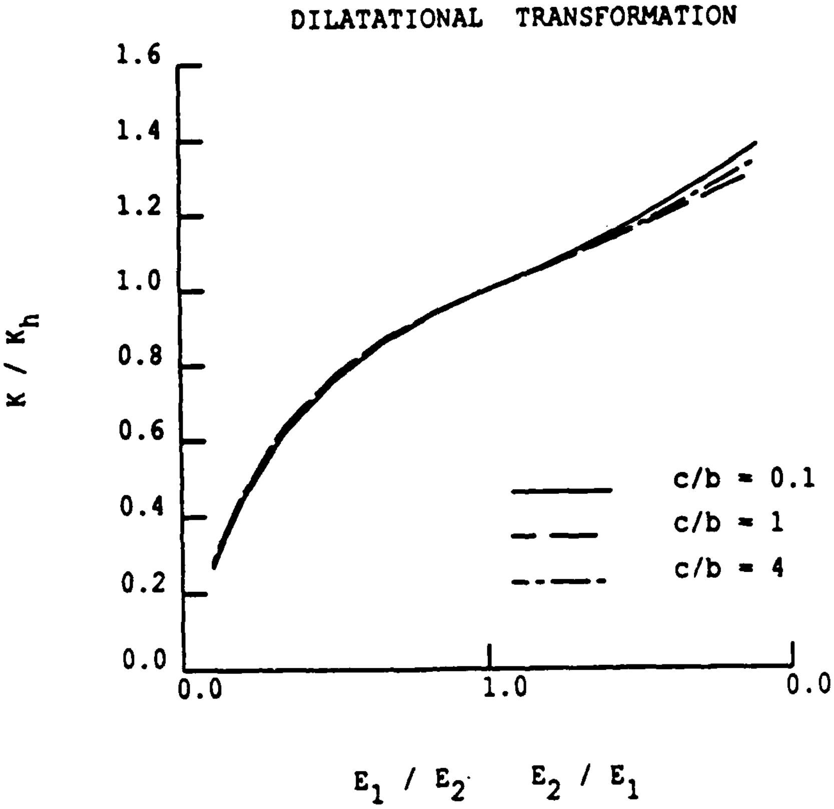

Fig. 4 Outer microcrack stress intensity factor as a function of modulus ratio for dilatational transformation loading of particle.

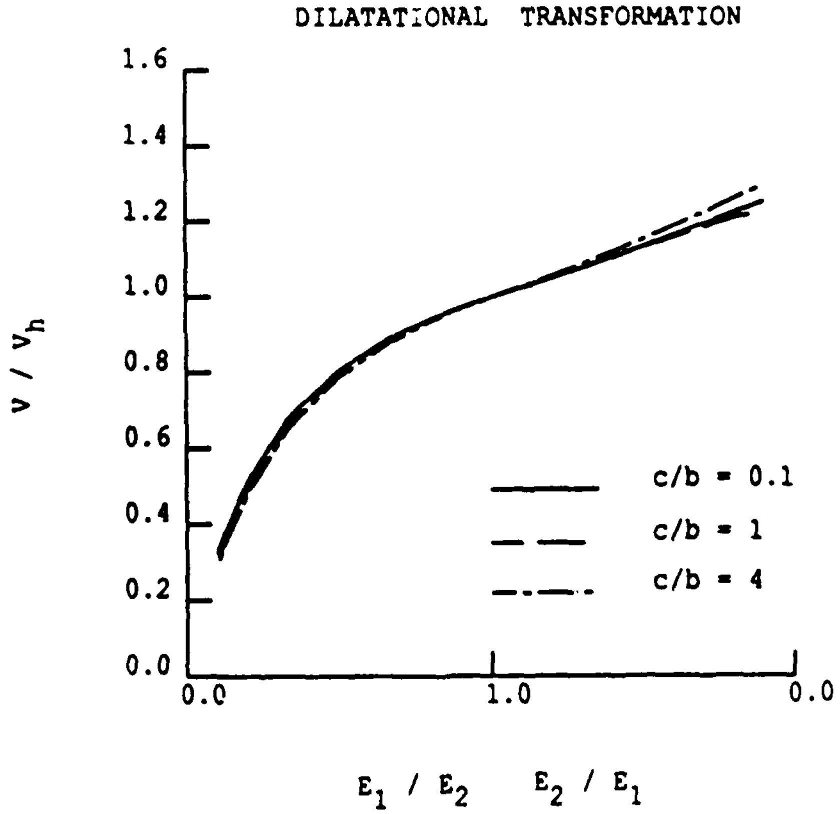

Fig. 5 Microcrack volume opening as a function of modulus ratio for dilatational transformation loading of particle.

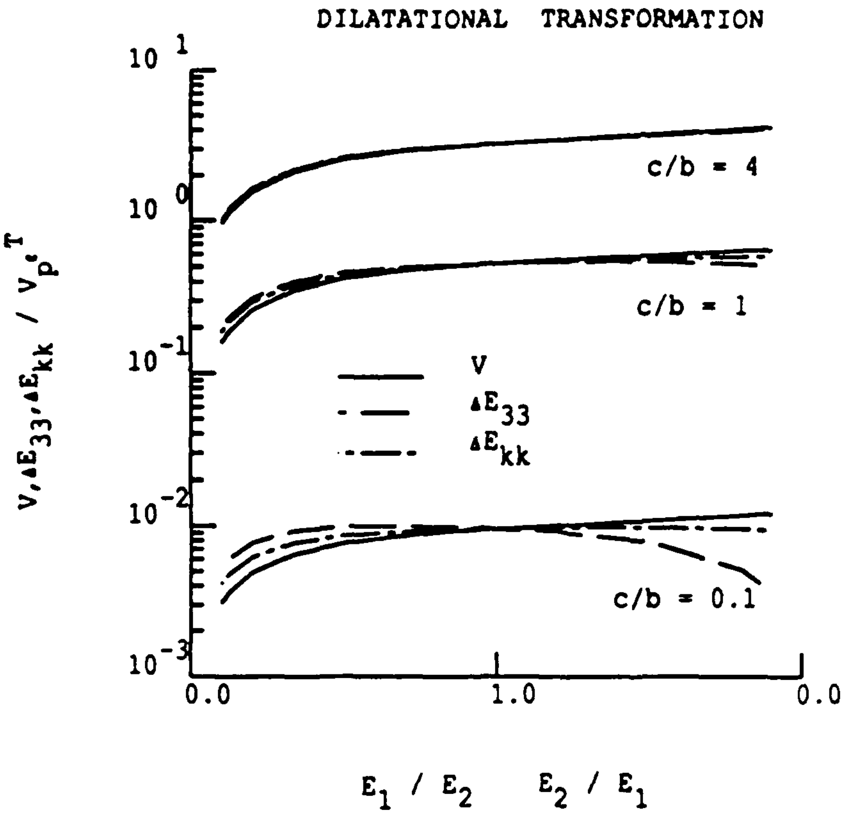

Fig. 6 Additional macroscopic strains as a function of modulus ratio for dilatational transformation loading of particle.

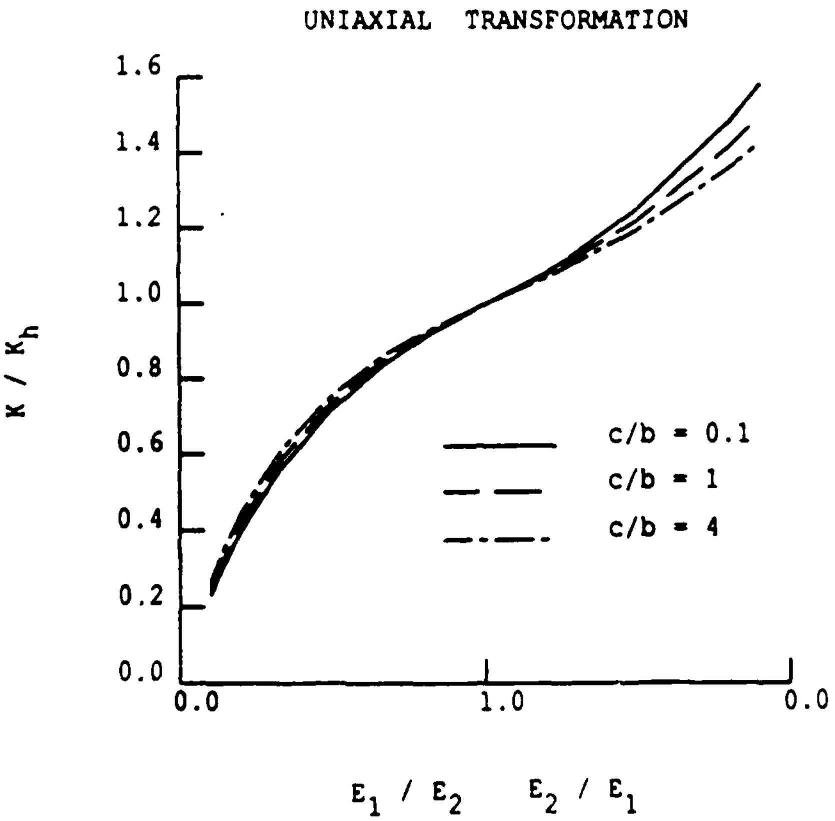

Fig. 7 Outer microcrack stress intensity factor as a function of modulus ratio for uniaxial transformation loading of particle.

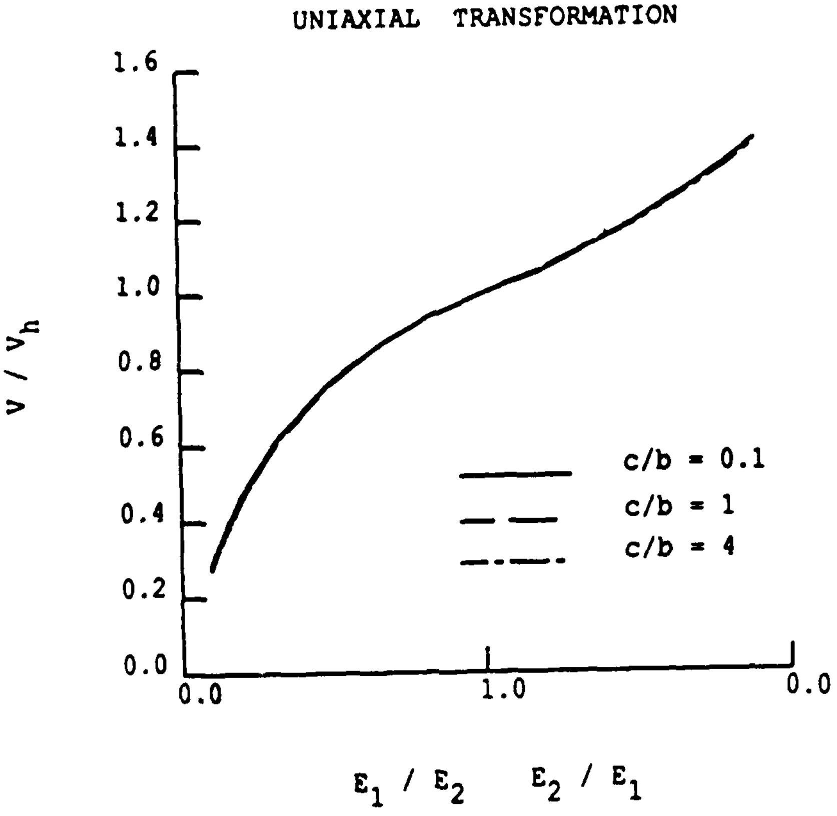

Fig. 8 Microcrack volume opening as a function of modulus ratio for uniaxial transformation loading of particle.

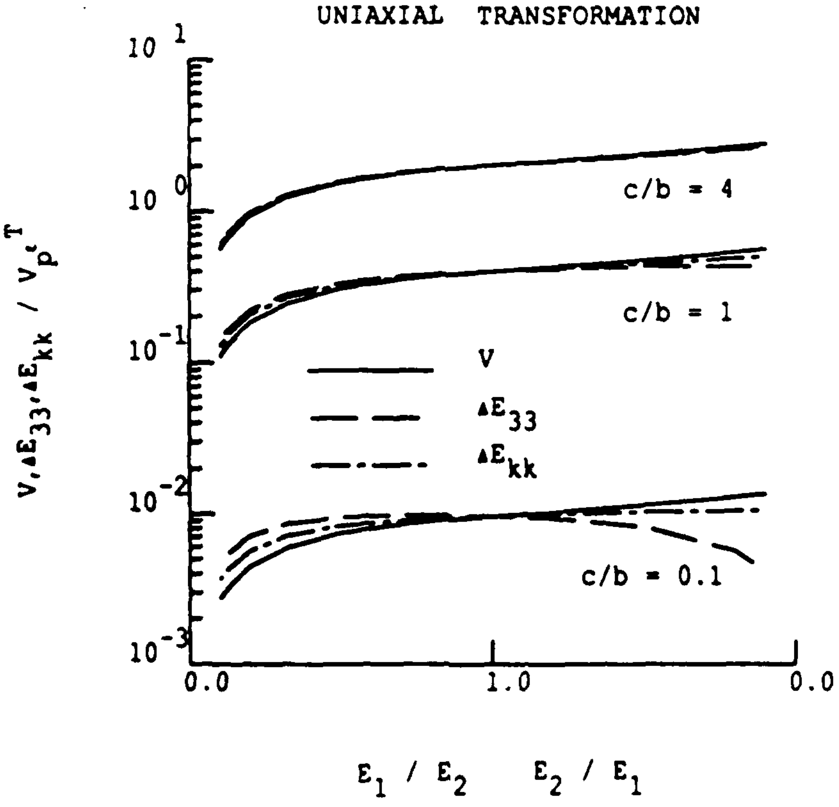

Fig. 9 Additional macroscopic strains as a function of modulus ratio for uniaxial transformation loading of particle.

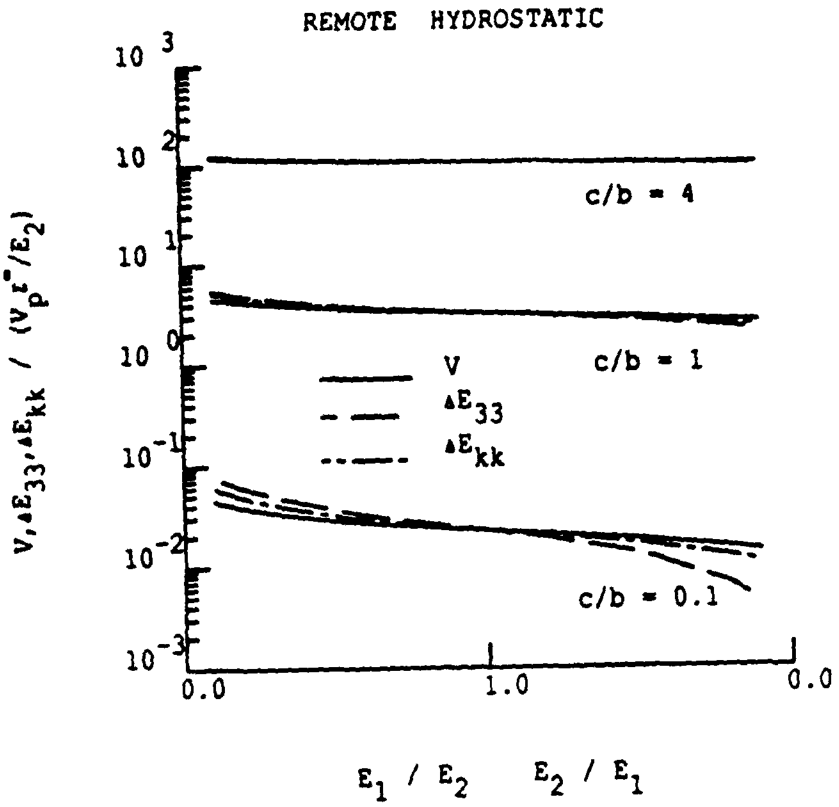

Fig. 10 Additional macroscopic strains as a function of modulus ratio for remote hydrostatic loading.

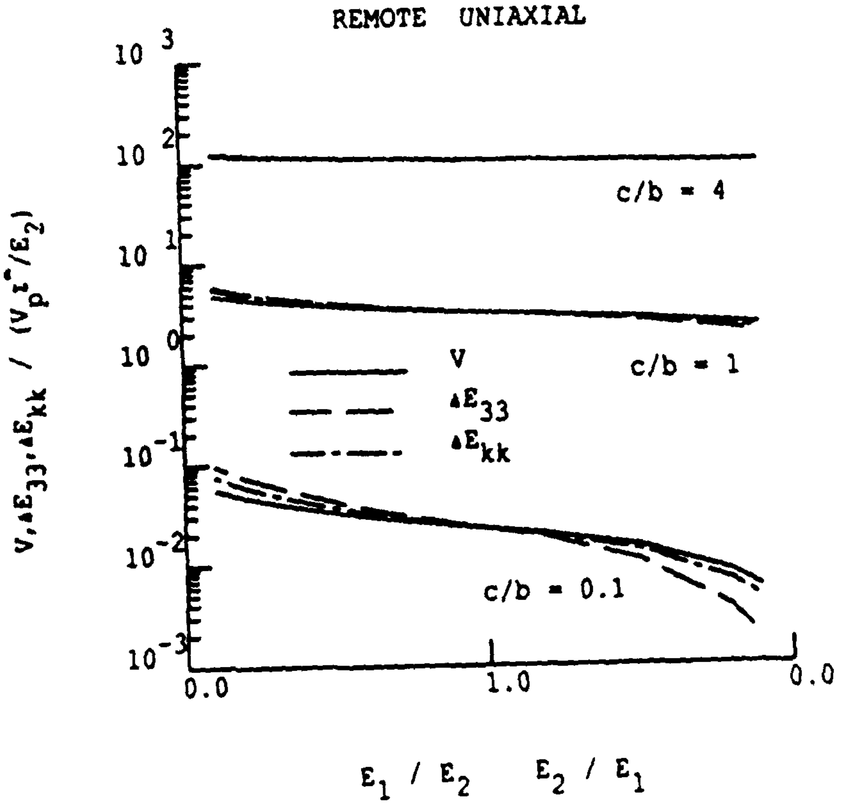

Fig. 11 Additional macroscopic strains as a function of modulus ratio for remote uniaxial loading.

MATERIALS

PHASE DIAGRAM AND SOLIDIFICATION MODELS FOR THE Nb-Al-Si SYSTEM

by

D. Tilly, T. Lu, A. Paul, R. Mehrabian

Materials Department
College of Engineering
University of California
Santa Barbara, California 93106

ABSTRACT

The solidification "paths" of ternary Nb-Si-Al alloys, near to the Nb_5Si_3 composition with various Al additions, were investigated. This work was motivated by recent recognition that ternary alloys in this system are potential candidates for high temperature aerospace applications. It is also recognized that the initial alloy composition is a controlling variable in determining the cast microstructure, which, after heat treatment, controls the properties. Furthermore, homogenization of cast microstructures in this system may not always be practical because of low diffusivities of species in the ordered compounds, and volatility of Al which limits homogenization temperatures to below ~1400°C. Thus, an understanding of the various solidification "paths" should permit optimization of initial alloy compositions to tailor the as-cast microstructures to meet applications requirements, e.g. oxidation resistance.

Solidification "path" calculations require relevant equilibrium phase diagram data, liquidus surfaces and solid-liquid tie lines. An extensive literature review of the Nb-Si-Al phase diagram was conducted with the data evaluated using a reaction flow chart. The two major discrepancies in the literature concerning the relevant phase fields in the 1400°C to 1500°C and 1820°C to 1850°C temperature ranges were resolved, and a liquidus projection diagram was generated incorporating specific findings from the experimental studies. Unfortunately, lack of reliable thermodynamic data did not permit modelling of the appropriate phase fields and tie lines. As a consequence, the various phases forming were modelled as line compounds in the solidification "path" calculation, with experimentally determined average compositions as input variables.

Two groups of alloys, one above and one below the 62.5at%Nb composition line, were studied. Furthermore, initial alloy compositions, selected during the course of the investigation, were such that the solidification "path" in each group would remain the same while the amount of the various phases

forming varied. In both alloy groups b-Nb_5Si_3 (T_1) phase, with various Al contents, solidified as the primary (facetted) dendritic phase. Group 1 alloys with Nb<62.5at%, followed the sequence:

$L \rightarrow L+T1 \rightarrow L+T1+NbAl_3 \rightarrow$ eutectic $[T1+NbAl_3+Nb_2Al]$

The solidification sequence for group 2 alloys, with Nb>62.5%, was predicted to be:

$L \rightarrow L+T1 \rightarrow L+T1+Nb_3Al \rightarrow L+T1+Nb_2Al \rightarrow$ eutectic $[T1+NbAl_3+Nb_2Al]$

Experimentally, only T_1+Nb_3Al phases solidified on the line of two-fold saturation. Calculations, based on the initial alloy compositions, showed this to be due to lack of remaining liquid, ~1 to 3wt%, at the intersection of the $L+T_1+Nb_3Al$ and $L+T_1+Nb_2Al$ two-fold saturation lines.

In general, predicted solidification "paths" and calculated weight fractions of the various phases were in reasonable agreement with the experimental findings. This agreement not only lends credence to the various assumptions made, but permits prediction of cast microstructures in significant composition ranges of the Nb-Si-Al system.

Table of Contents

I. Introduction....1

II. Literature Review....3

Niobium-Aluminum-Silicon Phase Diagram....3

III. Experimental Techniques....7

1. Alloy Preparation....7
2. Microstructure Characterization....8

IV. Solidification Models....10

V. Results and Discussion....18

1. Nb-Si-Al Phase Diagram Evaluation....18
2. Experimental Observations....26
3. Solidification "Path" Calculations....32

VI. Concluding Remarks....37

VII. References....41

VIII. Appendix A- Phase Diagram Information....44

IX. Appendix B- Solidification "path" Calculations....52

X. Tables....56

XI. Figures....68

I. INTRODUCTION

Recent emphasis on the development of Nb alloys and Nb-based intermetallics has been motivated by the need for new higher temperature materials for turbine, nozzle and re-entry vehicle technologies in the aerospace industry. The efforts have been plagued with many problems; e.g. oxidation resistance, embrittlement by interstitials and creep resistance. Alloys in the Nb-Al-Si system have shown reasonable oxidation resistance making them candidate materials for these technologies. The oxidation resistance is due to the formation of adherent protective oxides at high temperatures. For example, It was shown [1] that the $NbAl_3$ and the $NbSi_2$ compounds exhibit significantly better oxidation behavior with additions of Si and Al, respectively (Fig.1). It is recognized that initial alloy composition and the phases present in the solidified microstructure have an important influence on the oxidation behavior of these alloys. Furthermore, by determining the solidification "path" of an alloy it is possible to both optimize the initial composition and taylor the final microstructure. To achieve this goal a predictive model based on solidification theory coupled to phase diagram information is needed. This information is invaluable for the design of optimum microstructures to produce high temperature oxidation resistant materials not only in the Nb-Al-Si ternary system, but also in other systems (e.g. Ti-Al-Ta) requiring designer microstructures to meet mechanical and corrosive property goals.

An integral part in determining the solidification "path" in a ternary alloy system is the necessary information regarding the equilibrium phase diagram, particularly the liquidus surfaces, the lines of two-fold saturation and the tie lines between the liquidus and the solidus surfaces. A problem with ternary systems is the lack of phase diagram information. Consequently, a review of the literature on the Nb-Al-Si phase diagram is presented first. Included in this review are the available experimental data and thermodynamic phase diagram models for the relevant binary systems. In the body of the thesis the available solidification models for ternary alloys are combined with the appropriate phase diagram information to predict the evolution of solidification microstructures and compare same with the experimental findings of this work. It should be noted that the solidification "path" calculations are simplified since most phases of interest in this study can be approximated as line compounds.

II. LITERATURE REVIEW

The Nb-Si-Al Phase Diagram

When reviewing a ternary phase diagram it is best to start with the constituent binaries. For the Nb-Si-Al system, these are the Al-Si, Nb-Si and the Nb-Al binaries. The Al-Si diagram is a simple eutectic systems with the eutectic at 12.2at% Si and 577°C [2] (Fig. 2). The Nb-Si system [3-7] diagram used in this study is by L.M.Yupkol et al. [7] see (Fig. 3). There are three intermetallic phases; Nb_3Si (Ti_3P-type), Nb_5Si_3 with two crystal structures, a high temperature phase β (W_5Si_3-type) and a low temperature phase α (Cr_5B_3-type), and finally the $NbSi_2$ phase ($CrSi_2$-type). Both the Nb_5Si_3 and the $NbSi_2$ phases form congruently while the Nb_3Si phase forms peritectically. The Nb-Al system [8-12] was recently reviewed [8]. However, the evaluated diagram used in the present study is from U.Kattner et al. [13] (Fig. 4). The Nb-Al system also has three intermetallic phases; Nb_3Al (Cr_3Si-type), Nb_2Al (σ-CrFe-type), and the $NbAl_3$ phase ($TiAl_3$-type). Both the Nb_3Al and the Nb_2Al phases form peritectically, while the $NbAl_3$ phase forms congruently. Summaries of invariant reactions, and crystal structures of the phases in the three binaries are given in Appendix A.

The ternary system will be reviewed in three sections; section 1 will include alloys containing less than 33at%Nb, section 2 will include alloys containing 33 to 62.5at%Nb, and the third section will include alloys that contain more than 62.5at%Nb. The reported phases present in the system are those contained in the binaries as well as a ternary C-54 phase.

(a) Section 1

A paper by C. Allibert et al. [14] presents two partial isothermal sections; one at 1300°C (Fig.5) and the other at 1500°C (Fig.6). Both of these sections contain the same phase fields. The C-54 phase is based on the $NbSi_2$ compound with Al substituting for Si. The solubility range is 15 to 20at%Al. DTA experiments indicate that the C-54 phase undergoes a decomposition at 1145°C ($\pm$10°C) - possibly a transitional reaction ($L + C\text{-}54 \Leftrightarrow NbAl_3 + NbSi_2$). The authors assumed that this transition reaction is the reason for the major changes in the size and thickness of the two fields ($L+NbSi_2+C\text{-}54$) and (C-54+L). Both phase fields become very thin with decreasing temperature, to the point that the investigators found it difficult to distinguish the boundaries between the two fields. As for the other multi-phase fields, they all increase in size with the receding liquidus. It should be noted that this is the only ternary liquidus data for this system.

(b) Section 2

This region is bounded by $NbAl_3$, Nb_2Al, T1, T2, $NbSi_2$ and $Nb(Si,Al)_2$ (C-54). Where T1 and T2 are ternary phases based on the high and low temperature allotropes, respectively, of the Nb_5Si_3 phase in the Nb-

Si binary. Two isothermal sections are available; one at 1400°C (Fig.7), and the other at 1500°C (Fig.8). The paper containing the isothermal section at 1500°C, by V.M.Pan et al. [15], indicates the existence of a quasi-binary eutectic at 1660°C between $NbAl_3$ and Nb_5Si_3 (T2) at no less than 60 mol% T2. This explains the two phase field ($NbAl_3$ + T2) at 1500°C. The papers on the 1400°C isothermal section by H.Nowotny et al. [16,17] show no indication of the $NbAl_3$ phase in equilibrium with the T2 phase, presumably the C-54 phase prevents the $NbAl_3$ phase from being in equilibrium with the T2 phase at this temperature. Thus, the two studies present significantly different phase fields for this region. One possible explanation is the different sample preparation techniques of the two studies. The study at 1400°C [16] used a reaction sintering method with a final homogenization treatment at 1400°C. The 1500°C data [15] came from cast and homogenized alloys, with final annealing at 1500°C for 40hr. The different methods may have different phase forming sequences. If the specimens in either or both studies did not reach equilibrium, then the observed phases could be different. This region is of great importance due to the oxidation resistant $NbAl_3$ and $NbSi_2$ phases, and more work is needed to verify the exact nature of the phase equilibria.

(c) Section 3

The final region of interest is that bounded by Nb, Nb_2Al, T1 and T2. There are several papers that contain work in this region [15-20]. The isothermal sections are; 1400°C (Fig.7), 1500°C (Fig.8), 1700°C (Fig.9), 1820°C (Fig.10), and 1840°C (Fig.11). The five phases present are α-Nb solid solution, Nb_3Al, Nb_2Al, Nb_3Si (which only exists in a limited temperature range), T1 and T2. Most of the work in this region was done to evaluate the effect of Si additions on the superconducting transition temperature (T_c) of the Nb_3Al (A15) phase . The Nb_3Si phase, with the Ti_3P type crystal structure, only exists in the Nb-Si binary between 1720°C and 1960°C (Fig.3). The solubility of Al in this phase is very low-less than 1at%. Other phases of interest are the T1 and T2 phases. The crystal structure of the T2 is the same as the low temperature α-Nb_5Si_3 binary (Cr_5B_3 type). The crystal structure of the T1 is identical to that of the high temperature β–Nb_5Si_3 binary (W_5Si_3 type). The paper by A.Muller [19], 1840°C isothermal section (Fig.11), indicates a solid solution phase based on the Nb_5Si_3 with a maximum Al solubility of 21at%. On the other hand, the 1820°C section (Fig. 10), by V.M.Pan et al. [15], shows the existence of the two phases T1 and T2. Thus, there is a discrepancy on whether two separate $Nb_5(Si, Al)_3$ phases exist at high temperatures. This will be further discussed in Chapter V, section 1 entitled "Nb-Si-Al phase Diagram Evaluation". A summary of all the phase diagram data, i.e. invariant reactions , crystal structures ,ect. is given in Appendix A.

III. EXPERIMENTAL PROCEDURE

1. Alloy Preparation

The alloys were produced from a master alloy (62.5 at%Nb 27.5 at%Si 10 at%Al), which was donated by Pratt and Whitney. This was modified to the desired compositions, listed below, with the appropriate additions of Nb, Si and Al, in the form of Nb wire (99.98%), Si chunks (99.999%), and Al pellets (99.99%).

Alloy#	Al (at%)	Si (at%)	Nb (at%)
7	7.2	25.8	Balance
8	14	31	Balance
10	9	19.6	Balance
11	29.5	20.5	Balance
12	51.7	11.6	Balance
12b	44.6	10.4	Balance
13	13.1	12.8	Balance

All alloys were melted in an arc furnace on a copper chill mold, under an atmosphere of purified Ar (10^{-11} ppm O_2), to produce 20 gram buttons approximately 3 cm in diameter. The samples were flipped several times to insure adequate mixing. The main problem in producing these alloys was Al loss, which was minimized by first melting at low power to react the Al with the base alloy. With the Al in solution, the losses due to evaporation were reduced. These alloys are also susceptible to cracking during remelting and cooling - a tendency that can be minimized by controlling the power input to the melt. Heat treatments were conducted in a Vacuum Industries vacuum furnace at 1400 and 1500°C for 100 hours , in an atmosphere of purified Ar (< 10^{-7} ppm of O_2). The samples were wrapped in Ta foil and Ti chips were placed in the chamber to further reduce the O_2 level.

2. Microstructure Characterization

Samples were cut from the arc-melted buttons using an isomet wafer-blade diamond saw and mounted in bakelite prior to polishing. Microstructures were characterized using SEM, Microprobe,TEM, and X-ray techniques. The SEM was a JEOL 840 with a Tracor Northern EDX system with backscattered electron imaging capabilities, the TEM was done with a JEOL 2000FX equipped with a Tracor Northern EDX system. TEM specimens were prepared by cutting 3mm diameter discs out of as- cast ingots, ground down to 100μm thick, final thining was conducted with a twin jet electropolisher. SEM and TEM were used to identify phases and their volume fractions, hence phase sequencing during solidification. Both average compositions of phases and composition profiles of the primary phase were obtained with the microprobe and EDX system. The microprobe was a CAMECA model CMB located at the University of California Los Angeles (UCLA). An operating voltage of 15 KV, with a probe current of 8-10 mA and a probe size of 0.5 μm were employed. All spectrums were collected for 100 sec. live time, and ZAF[*] corrections were used for the compositional calculation. Standards used were pure Nb, Al and Si. Samples from the arc-melted buttons and heat treated material were crushed (with a mortar and pestle) into very fine powders for X-ray analysis with a Scintag PAD-10 diffractometer, operated in the θ-θ mode, at a scan rate of 2° per minute.

---

[*] ZAF corrections are for atomic number (Z), absorption (A) and fluorescence (F).

IV. SOLIDIFICATION MODEL

In deriving the general expressions for the solidification "path" of a three component alloy, we follow essentially an identical procedure to that previously employed for calculation of macrosegregation in ternary alloy systems [21]. Consider first a small volume element within a solidifying ingot. No material enters or leaves the element during solidification - neither interdendritic fluid flow nor solidification shrinkage are taken into consideration. There is no diffusion in the solid and the liquid composition is taken as uniform at any time. Equilibrium is maintained at the solid-liquid interface. Hence, liquid composition and temperature within the element are related to the liquidus surface of the ternary alloy, and solid composition at the interface is given by the appropriate tie line. During solidification, one, two or three phases can form from the liquid. The solute composition of the phases will, in general, be different. In this type of situation the solidification "path" has several stages.

Figure (12) shows schematically the solidification of a ternary alloy starting with the nucleation of a single phase. For this alloy composition, dendrites of primary α phase form first. At a later stage, a second phase β nucleates and solidifies. When two phases form simultaneously from a melt in a ternary system, the liquid composition is a direct function of the temperature, as given by the line of two-fold saturation in the phase diagram. Hence, in the schematic of Figure (12) the two phases α and β solidify by a cooperative growth mechanism over a range of temperatures and compositions given by the line of two-fold saturation. At the end of solidification the residual liquid solidifies as a ternary eutectic.

(a) Solidification of a Single Phase in a Ternary System

Consider the formation of a single phase α in a three component system. A local "solute redistribution" equation is readily written for each component, n and m, similar to Schiel's equation for solidification of a two component system.

The solute balance for component n is :

$$(C_{Ln} - C_{\alpha n})\, df_s = f_L\, dC_{Ln} \qquad [1a]$$

and the companion equation for element m is :

$$(C_{Lm} - C_{\alpha m})\, df_s = f_L dC_{Lm} \qquad [1b]$$

Where:

f_L = molar fraction of liquid

f_α = molar fraction of solid α

C_{Ln}, C_{Lm} = composition of liquid for components n and m in wt%

$C_{\alpha n}$, $C_{\alpha m}$ = composition of solid α for components n and m in wt%

and :

$$f_L + f_\alpha = 1.0 \qquad [2].$$

Next, we define the equilibrium partition ratios $k_{\alpha n}$, and $k_{\alpha m}$ at the solid-liquid interface as:

$$k_{\alpha n} = \frac{C_{\alpha n}}{C_{Ln}} \qquad [3a]$$

$$k_{\alpha m} = \frac{C_{\alpha m}}{C_{Lm}} \qquad [3b].$$

To evaluate the equilibrium partition ratios in a ternary system, the tie lines between the liquidus and corresponding solidus surfaces need to be known. Unfortunately, the tie lines in ternary systems are often not known, but may be obtained from experiments or calculated using thermodynamic models.

Substitution of equation [3a] into [1a], using equation [2], yields :

$$-\frac{dC_{Ln}}{C_{Ln}} = \left(1 - k_{\alpha n}\right) \frac{df_L}{f_L} \qquad [4]$$

In the terminology used previously [21], and in this work, the "path" of solidification is defined by the ratio dC_{Ln} / dC_{Lm} during solidification. By dividing equation [4] with its companion equation for element m the solidification "path" is obtained:

$$\frac{dC_{Ln}}{dC_{Lm}} = \frac{(1 - k_{\alpha n})}{(1 - k_{\alpha m})} \frac{C_{Ln}}{C_{Lm}} \qquad [5]$$

In general, equation [5] is solved using the tie lines from the ternary phase diagram. Next, equation [4], or its companion equation for element m, is used to calculate the molar fraction solid along this "path". If the partition ratios are assumed constant, then one may integrate equation [5] and solve for C_{Ln}:

$$C_{Ln} = C_{On} \left(\frac{C_{Lm}}{C_{Om}} \right)^{\left[\frac{(1-k_{\alpha n})}{(1-k_{\alpha m})} \right]} \qquad [6]$$

Where C_{On} and C_{Om} denote the initial composition of the alloy. By defining the solidification "path" in this way it is readily seen that the composition of the liquid at any time is a unique function of the initial composition of the alloy.

In the Nb-Si-Al system many of the phases formed are compounds, consequently, $k_{\alpha n}$ and $k_{\alpha m}$ are not constant. If one assumes the compounds are line compounds, $C_{\alpha n}$ and $C_{\alpha m}$ in equations [2a and b] are constant, the values of $k_{\alpha n}$ and $k_{\alpha m}$ will only vary with the composition of the liquid. The resulting equation for the solidification "path" can then be determined:

$$\frac{C_{Ln} - C_{\alpha n}}{C_{On} - C_{\alpha n}} = \frac{C_{Lm} - C_{\alpha m}}{C_{Om} - C_{\alpha m}} = \frac{1}{f_L} \qquad [7]$$

As before, the solidification "path" is a unique function of the initial composition, C_{On} and C_{Om}. These equations can now be used to quantitatively define where the liquid composition will intersect the line for two-fold saturation; hence, when a second phase will nucleate and grow.

(b) Simultaneous Solidification of Two Phases

The equations used to derive the "solute redistribution" expressions for the simultaneous solidification of two phases are essentially the same as those for single phase solidification with added terms to account for the formation of the second phase, β. The conservation equation is:

$$f_L + f_\alpha + f_\beta = 1.0 \tag{8}$$

The solute balance equations for two phases solidifying simultaneously are:

$$\left(C_{Ln} - C_{\alpha n}\right) df_\alpha + \left(C_{Ln} - C_{\beta n}\right) df_\beta = f_L dC_{Ln} \qquad [9a]$$

$$\left(C_{Lm} - C_{\alpha m}\right) df_\alpha + \left(C_{Lm} - C_{\beta m}\right) df_\beta = f_L dC_{Lm} \qquad [9b].$$

where the added terms are:

f_β = molar fraction of solid β

$C_{\beta n}$, $C_{\beta m}$ = composition of the β phase for component n and m in wt%

Using $k_{\alpha n}$ and $k_{\beta n}$ for the equilibrium partition ratios at the α and β interfaces with the liquid respectively, equations [8] and [9] are combined to give:

$$\frac{df_L}{dC_{Ln}} = -\left(\frac{1}{1-k_{\alpha n}}\right)\frac{f_L}{C_{Ln}} - \left(\frac{k_{\beta n}-k_{\alpha n}}{1-\ k_{\alpha n}}\right)\frac{df_\beta}{dC_{Ln}} \qquad [10]$$

The companion equation for element m may also be written.

Again, since in the Nb-Si-Al system many of the phases are line compounds, a set of equation similar to equation [10] may be written for the case of two line compounds solidifying simultaneously. In this case, both the α and β phases are compounds of constant composition, $C_{\beta n}$ and $C_{\alpha n}$ are constant. The equations that describe this are:

$$\frac{df_L}{dC_{Ln}} = -\frac{f_L}{C_{Ln}-C_{\alpha n}} - \left(\frac{C_{\beta n}-C_{\alpha n}}{C_{Ln}-C_{\alpha n}}\right)\frac{df_\beta}{dC_{Ln}} \qquad [11a].$$

$$\frac{df_L}{dC_{Lm}} = -\frac{f_L}{C_{Lm}-C_{\alpha m}} - \left(\frac{C_{\beta m}-C_{\alpha m}}{C_{Lm}-C_{\alpha m}}\right)\frac{df_\beta}{dC_{Lm}} \qquad [11b].$$

In general, equations [11 (a) and (b)] can be solved simultaneously using a relationship between C_{Ln} and C_{Lm} given by the line of two-fold saturation. During the solidification of two phases simultaneously, the solidification "path" follows along this line. The solution would yield the weight fractions of the β-phase, the liquid and hence the α-phase as a function of composition along the line of two-fold saturation (see Appendix B for derivation). It is quite likely that various solid phases, e.g. through peritectic reactions, may form as the liquid composition moves along this line. The weight fractions of these phases can be simply calculated using the same methodology once the liquid composition for the reactions are known.

To summarize, a knowledge of the tie lines between the liquidus surfaces and the various solidus surfaces and the equations for single phase and two-phase solidification in a ternary alloy given above provide the necessary information for the determination of solidification "paths" and weight fractions of various phases in a ternary alloy. In cases where both equilibrium partition ratios at the solid-liquid interface during solidification of a single phase are constant or where a compound of uniform composition forms, the solidification "path" is given by equation [6] or [7]. When the liquid composition intersects a line of two-fold saturation a second phase nucleates and grows, and the solidification "path" follows this line until the liquid is exhausted or it reaches an invariant temperature, e.g. a ternary eutectic point. There are occasions when one is only interested in determining the weight fraction of liquid as a function of liquid composition in order to compare the theoretical calculations with observed microstructures, e.g. weight fractions of the second phases. If the equilibrium partition ratios of the various phases forming are constant, and/or compounds of constant composition solidify, then using the known functional relationship between C_{Ln} and C_{Lm} defining the line of two-fold saturation, one may obtain analytical solutions for the cases represented by equations [10] and [11]. The details of the derivation of these equations is given in Appendix B.

V. RESULTS AND DISCUSSION

1. Nb-Si-Al Phase Diagram Evaluation

In this section we discuss the method for evaluating the available phase diagram data. This was done by using reaction flow charts. A simple explanation of a reaction flow chart is presented first, section (a), and then the phase diagram data (presented in the literature review) is analyzed. There were two main temperature ranges where discrepancies were cited, 1400-1500°C and 1820-1840°C. Isothermal diagrams in these temperature ranges are shown in the section (b) "evaluation of phase diagram data". Then the best estimate of the liquidus projection diagram is presented. Finally, the thermodynamic models for the three binaries are assembled and a short summary of the ternary information needed to model the system is given.

(a) Reaction Flow Charts

An excellent tool for evaluating the thermodynamic consistency of a ternary phase diagram is the reaction flow chart, which is a way to represent the connections between all the three and four phase equilibria (see Fig.13 a, b). To formulate such a chart, one first identifies the binary three phase fields, the invariant reactions, Appendix A, and projects them onto the ternary. These fields must either meet another three phase field or end at a binary diagram. Where two three phase fields meet, there exists a four phase equilibrium reaction. For example, in the Nb-Si system, if one follows the two three phase fields (L ⇔ α-Nb + Nb_3Si) and (L + β - Nb_5Si_3 (T1) ⇔ Nb_3Si) out into the ternary, they meet and produce a four phase equilibrium (L + Nb_3Si ⇔ α-Nb + β - Nb_5Si_3 (T1)). From thermodynamics it is known that four three phase equilibria meet at a four phase equilibrium, e.g. the two that project from the binary in the above example, plus the two that make up the other two sides of the four phase field. In turn, these ternary three phase fields meet other three phase fields to produce another four phase equilibrium, etc., a list of all four phase reactions is given in Appendix A. By following this procedure it is possible to produce a reaction flow chart for the whole system (Figs. 13 a, b). Furthermore, one can easily assess whether a given phase diagram falls within the constraints of thermodynamics, since a series of reactions must exist to produce a given three phase field. Also by looking at the reaction flow chart and following it across at a constant temperature, each three phase field one crosses will exist at that temperature. In this way one can easily check if a diagram agrees with the predicted flow chart.

(b) Evaluation of Phase Diagram Data

The evaluation of the ternary phase diagram data (presented in the literature review) was carried out with the aid of the reaction flow charts noted above. In the literature review discrepancies between papers were noted. The first of these was between the 1500°C section (Fig.8) by V. Pan et al. [15], and the 1400°C section (Fig.7), by H. Nowotny et al. [16]. The phase fields bounded by Nb_2Al, $NbAl_3$, C-54, $NbSi_2$, α - Nb_5Si_3 (T2) and β - Nb_5Si_3 (T1) in these two diagrams do not match. The phase fields in the 1400°C isothermal section are in agreement with the proposed reaction flow chart (Fig. 13 a). When evaluating the 1500°C section, no series of reactions could be formulated to produce the $NbAl_3$ and the T2 phases in equilibrium together. Thus, for this study, the 1500°C (Fig.8) diagram will not be used. An estimate of an isothermal section in the 1400-1500°C range is presented in Figure (14). This is very similar to that presented in the H. Nowotny paper with the addition of the results from the paper by C.Allibert [14]. This addition of the liquidus surface and the corresponding fields in the region below 33at%Nb is the only liquidus data available in this system.

The second area of uncertainty is around the T1 phase. There are two relevant isothermal sections reported in the literature: the 1840°C section (Fig.11), by A. Muller [19] and the 1820°C (Fig.10), by V. Pan et al. [15]. The former shows T1 phase as a solid solution based on the Nb_5Si_3 phase, while the latter shows the existence of a two phase field (T1 + T2) and T1 only as a ternary phase. Data from the paper by H. Nowotny et al. [16] shows that the T1 phase has the same crystal structure as the binary high temperature allotrope, β - Nb_5Si_3; indicating that the T1 is a solid solution of this binary phase. It is thus expected that the β - Nb_5Si_3 (T1) be in contact with the binary down to the reaction β - Nb_5Si_3 (T1) $\Leftrightarrow$ α -

Nb_5Si_3 (T2) + $NbSi_2$ at 1650°C (see Fig. 3). The isothermal section presented by V. Pan et al. [15] shows the β - Nb_5Si_3 (T1) is not connected to the binary, thus it will not be used in this study. The best estimate of this region in the temperature range of 1800°C to 1850°C is given in Figure (15). This isothermal section is based on the section presented by Muller [19]. The main additions to the Muller diagram are the phase fields that contain the T2 phase. From the binary diagram (Fig.3) it is seen that α - Nb_5Si_3 (T2) comes into existence through a peritectoid reaction at 1940°C; hence a two phase region between T1 and T2 should exist. Figure (16) shows a possible set of phase fields for a region close to the T1 composition at these temperatures.

(c) Liquidus Projection

By using the reaction flow chart, solidification results and phase diagrams from the literature, an overall picture of the liquidus surface of the Nb-Si-Al system may be synthesized. The liquidus projection is an excellent way to represent the information necessary in determining the solidification "path" of ternary alloys. Figure (17) is our best estimate of the liquidus projection for the Nb-Si-Al system. The phases listed in the different sections, separated by two-fold saturation lines, are the primary phases that will solidify first if an alloy composition falls in that section. The two phases that solidify along any two-fold saturation line are the adjacent phases to the line. Details of the liquidus projection diagram are discussed below. This entails following the projected three phase fields which contain liquid and discussing what four phase reactions occur when they meet other three phase fields. It should be noted that there are two types of four phase reactions seen in this diagram, these are defined by Rhines [22] as type I and type II.

Starting with the upper section of the diagram, alloys > 60%Nb, there exists a very deep trough between the Nb liquidus and the β-Nb_5Si_3 (T1) liquidus, Figure (17). The reaction flow chart shows that there are three four phase equilibria that contain liquid in a very small temperature range, around 1900°C:

$L + Nb_3Si \Leftrightarrow T1 + Nb$ $\quad II_1 \quad$ ~1915°C
$L + Nb \Leftrightarrow T1 + Nb_3Al$ $\quad II_2 \quad$ ~1900°C
$L + Nb_3Al \Leftrightarrow Nb_2Al + T1$ $\quad II_3 \quad$ ~1880°C

The first of these four phase equilibria was deduced by starting at the Nb-Si binary and projecting the eutectic $L \Leftrightarrow Nb_3Si + Nb$ and the peritectic $L + T1 \Leftrightarrow Nb_3Si$ into the ternary and meeting to form the type II reaction:

$L + Nb_3Si \Leftrightarrow T1 + Nb$ $\quad II_1 \quad$ ~1915°C

This should occur at a composition near the Nb-Si binary and at a temperature just below the eutectic temperature of 1920°C. An estimate of where this four phase equilibrium exists is Nb-17at%Si-(1 to 2)at%Al at ~1915°C. The three phase field L + Nb + T1 adjacent to the above four phase reaction will meet the three phase field $L + Nb \Leftrightarrow Nb_3Al$, which is a peritectic projected from the Nb-Al binary, forming the type II reaction:

$L + Nb \Leftrightarrow T1 + Nb_3Al$ $\quad II_2 \quad$ ~1900°C

This should happen at a temperature near 1900°C and composition of approximately Nb-12at%Si-7.5at%Al. If we follow the L + Nb_3Al + T1 two-fold saturation line it should meet the three phase field L + Nb_3Al $\Leftrightarrow$ Nb_2Al, which is a peritectic projected from the Nb-Al binary, and forms the type II reaction:

$$L + Nb_3Al \Leftrightarrow Nb_2Al + T1 \qquad II_3 \qquad \sim 1880°C$$

The temperature and composition of this reaction is estimated to be 1880°C and Nb-7at%Si-30at%Al, respectively. The adjacent three phase field will be L + Nb_2Al + T1. This two-fold saturation line has a very steep thermal gradient which drops from 1880°C to ~1550°C and meets the three phase field L $\Leftrightarrow$ Nb_2Al + $NbAl_3$ projected from the Nb-Al binary. The reaction formed here is a ternary eutectic, which is a type I reaction:

$$L \Leftrightarrow NbAl_3 + Nb_2Al + T1 \qquad I_1 \qquad \sim 1550°C$$

This was established from the results of our microstructural analysis of alloys #8, #11, #12 and #12b see next section entitled "Experimental Observations". The ternary eutectic composition was determined experimentally as (Nb-2at%Si-58at%Al) at an estimated temperature of ~1550°C. It follows that the three phase field L + $NbAl_3$ + T1 contains a saddle point and this was approximated at Nb-8at%Si-61at%Al and ~1625°C. This saddle point forms when the T1 liquidus surface meets the $NbAl_3$ liquidus surface resulting in the ternary eutectic on one side and another four phase reaction on the other. This saddle point was noted in the paper by Pan et al. [15] the 1500°C isothermal section (Figure 8) shows a quasi-binary between the T2 and the $NbAl_3$ phases.

Moving to the Nb-Si binary and following the projection of the eutectic L ⇔ β-Nb_5Si_3 + $NbSi_2$ out into the ternary it will intersect the three-phase field L + $NbSi_2$ + C-54 producing a type II four phase reaction:

$$L + NbSi_2 \Leftrightarrow T1 + C\text{-}54 \qquad II_4$$

The position of this reaction depends on how the C-54 phase comes into existence, congruently or peritectically. Since, the C-54 phase is reported as a plane compound, restricted in Nb content to 33at%Nb [16], a saddle point may exist along the 33at%Nb isoconcentration line where the three phase field L + $NbSi_2$ + C-54 forms. An isopleth along the 33at%Nb isoconcentration line is constructed (Fig. 18) to aid in the description of how the C-54 phase formation results in the two-fold saturation line with a saddle point. The formation of the C-54 phase is assumed to be around 22at%Al. If it forms congruently, then the saddle point, represented as the eutectic point between the C-54 and the $NbSi_2$ phases in Figure (18), will exist at a composition <22at%Al. If C-54 forms through a peritectic reaction, the saddle point composition will be >22at%Al. This will affect the composition of the four phase reaction (L + $NbSi_2$ ⇔ T1 + C-54) by moving it toward the Nb-Si (if the C-54 phase forms congruently) or away from this binary (if C-54 forms by a peritectic reaction). Either way, the temperature of the four-phase reaction could not be estimated. The saddle point is arbitrarily positioned at Nb-45at%Si-22at%Al in the liquidus projection diagram (Fig. 17). An estimate for the composition of the above four phase reaction is Nb-35at%Si-25at%Al; which could change once the composition and temperature for the formation of the C-54 phase is determined. The three phase field L + T1 + C-54 produced through this reaction will descend down and meet the three phase field L + T1 + $NbAl_3$ producing the type II reaction:

$$L + T1 \Leftrightarrow NbAl_3 + C\text{-}54 \qquad II_5 \qquad \sim 1550°C$$

This reaction occurs at a temperature between ~1500-1550°C and a composition near Nb-13at%Si-62at%Al. The three phase field L + C-54 + $NbAl_3$ produced here drops further down to a point where it meets the three phase field L + $NbSi_2$ + C-54 and produces the type II reaction:

$$L + C\text{-}54 \Leftrightarrow NbSi_2 + NbAl_3 \qquad II_6 \qquad \sim 1145°C$$

This is in agreement with the DTA experiments of C.Allibert [14] which established that the above four phase reaction occurs at 1145°C. The three phase field that continues is L + $NbSi_2$ + $NbAl_3$ which decends toward the Al corner.

Now, let us look at the Nb-Si binary once again, projecting the L ⇔ $NbSi_2$ + Si eutectic into the ternary it follows along the Si-Al binary until it runs into the three phase L ⇔ Si + Al field projected from the Si-Al binary. The result is the type II reaction:

$$L + Si \Leftrightarrow Al + NbSi_2 \qquad II_6 \qquad <577°C$$

The three phase L + Al + $NbSi_2$ field now intersects the three phase L + $NbAl_3$ + $NbSi_2$ field to produce the four phase type I reaction:

$$L \Leftrightarrow NbSi_2 + Al + NbAl_3 \qquad I_2$$

This ternary eutectic has the lowest temperature in this diagram.

(d) Phase Diagram models for the Nb-Si-Al system

During the literature search, thermodynamic models for the three binaries were assembled, see Appendix A, and an attempt at modeling the ternary was made. Due to the lack of ternary data available on many of the phases, the results were inconclusive. The two phases that needed significantly more ternary thermodynamic data to properly model this system were β-Nb_5Si_3 (T1) and C-54 , with little or no data being available for the latter. Some basic information, such as how this phase comes into existence, congruently or peritectically, would have been very helpful. The T1 phase has a very strong effect on all its surrounding fields, thus much more data is needed to properly model this phase with any confidence. The temperatures of the solid four phase equilibria are also very sensitive to the description of the T1 phase. Without adequate ternary thermodynamic data on these phases this system could not be modeled.

2. Experimental Observations

The alloys studied (#7, #8, #10, #11, #12, #12b, and #13) are divided into two groups: group 1 alloys with <62.5at%Nb (#8, #11, #12, and #12b), and group 2 alloys with >62.5at%Nb (#7, #10, and #13), see Figure (19). The main difference between these two groups lies in their general solidification sequence, Figure (20). This is described below along with the appropriate microstructural morphologies, phase compositions, and variations in volume fractions of the phases present.

(a) Group 1 Alloys

The primary dendritic phase of all these alloys was identified as β-Nb_5Si_3 (T1), using X-ray diffraction, electron microprobe analysis and EDS analysis in the SEM. The photomicrograph in Figure (21), taken of a shrinkage cavity in the arc-melted button of alloy #8, shows this faceted primary dendritic phase. In the polished cross sections Figures (22 to 25), these dendrites appear as light gray blocky structures with sharp edges, again indicating the faceted growth morphology. The second phases solidified in group 1 alloys were identified, using both microprobe and EDS analyses, as $NbAl_3$, Nb_2Al and β-Nb_5Si_3 (T1). The second phase morphologies are readily seen in photomicrographs of alloys #12 and #12b, where the volume fraction of these phases are the largest. In alloy #12, Figure (24), one can identify all three solidification stages. In the first stage, the primary β-Nb_5Si_3 (T1) phase solidifies as faceted dendrites. In the second stage, two phases solidify simultaneously, along a line of two-fold saturation. This region in Figure (24) is made up of a black phase ($NbAl_3$) with ribbons of a light gray phase (β-Nb_5Si_3 (T1)) through it. The third stage, comprises the final solidification of the remaining liquid as a ternary eutectic, seen in Figure (24) as regions of fine eutectic morphology. The phases in the ternary eutectic were identified as $NbAl_3$, Nb_2Al and β-

Nb_5Si_3 (T1), using the EDS system on the TEM. The eutectic structure is best seen in Figure (26) (alloy #12b) where β-Nb_5Si_3 (T1) appears as isolated islands between the ribbons of $NbAl_3$ and Nb_2Al. Using the ternary lever rule the expected volume fractions of each phase in this ternary eutectic were estimated as 11% T1, 40% Nb_2Al and 49% $NbAl_3$. The volume fractions of phases shown in Figure (26) are in qualitative agreement with this prediction.

In summary, the solidification phase sequence in alloys #8, #11, #12, and #12b, Figure (20), starts with the nucleation of the β-Nb_5Si_3 (T1) primary phase, which solidifies until the liquid composition intersects the line of two-fold saturation between I_1 and II_5 in Figure (19), but on the I_1 side of the saddle point. At this junction the $NbAl_3$ phase nucleates and grows along with T1. The liquid composition now follows down this line until it reaches the ternary eutectic, I_1, where the three phases, $NbAl_3$, Nb_2Al and β-Nb_5Si_3 (T1), solidify. Differences between the microstructures of these alloys are in primary phase compositions, volume fractions of the various phases and second phase morphologies.

Primary dendrite compositions, listed in Table 1, depend directly on the initial alloy composition. All the primary dendrites have approximately the same Nb content (58~60at%Nb). Composition profiles for this phase are flat, as seen in the composition line scan taken across a dendrite arm of alloy #8, Figure (27). This supports the assumption that primary dendritic phases in these alloys may be estimated as line compounds in calculations of solidification "paths". Table 1 also indicates alloys closer to the Nb-Si binary, #8 and #11, have dendritic phases with lower Al contents, while alloys that are further away, #12 and #12b, have dendrites with higher Al contents. The composition of the phases solidifying along the line of two-fold saturation and in the ternary eutectic, are relatively consistent from one alloy to another, see Tables (2-5). These compositions are used for calculations of solidification "paths" in the next section.

Measured volume fractions of primary and secondary phases are strongly dependant on initial alloy composition (Table 6). Alloys closer to the Nb-Si binary, #8 and #11, have higher volume fractions of the dendritic phase than alloys closer to the line of two-fold saturation, #12 and #12b. The volume fractions of $NbAl_3$ and β-Nb_5Si_3 (T1) that solidify along the line of two-fold saturation are dependent on where the liquid composition intersects this line; i.e. the transition from single-phase solidification to two-phase solidification. This can be qualitatively seen in alloys #12 and #12b. Alloy #12b has large amounts of ternary eutectic, Figure (25), hence, the liquid composition intersected the line nearly at the eutectic point, while alloy #12 contains larger amounts of T1 and $NbAl_3$ phases that solidified along the line of two-fold saturation, Figure (24) and Table 4.

(b) Group 2 Alloys

Group 2 alloys contain more than 62.5at%Nb. These alloys have the same dendritic phase, β-Nb_5Si_3 (T1), as group 1 alloys. The dendritic phase was again identified using X-ray diffraction, EDS and electron microprobe analysis. However, the morphology of this phase appears to changes with increasing Al content in the initial alloy composition. This is seen in Figure (28 a,b,c), where the dark phase is the primary dendritic phase, β-Nb_5Si_3 (T1), and the light phase is Nb_3Al. The sharp edges of the primary dendrites become rounded and smoother with increasing the Al content, i.e. decreasing volume fraction of this phase. These figures also show that dendrite arms are first surrounded by Nb_3Al prior to formation of cellular T1/Nb_3Al on the line of two-fold saturation. This can be attributed to the liquid composition over-shooting the line of two-fold saturation, i.e. difficulty in nucleating Nb_3Al. The liquid is then undercooled with respect to the liquidus surface of the two phase [L+Nb_3Al] field. The Nb_3Al phase nucleates and the interface recalesces up to the liquidus temperature. Solidification of Nb_3Al drives the liquid composition back to the line of two-fold saturation, where the β-Nb_5Si_3 (T1) nucleates and grows simultaneously with Nb_3Al in a cooperative growth mode. The recalesence may remelt the edges of the primary dendrites, leading to a more rounded morphology.

The composition of the various phases are given in Tables (7-9). The morphology of the two-phase eutectic structure is clearly noted in

Figure (29). Again, the dendritic phase is, β-Nb_5Si_3 (T1), surrounded by a light Nb_3Al phase, followed by fine β-Nb_5Si_3 (T1)/Nb_3Al eutectic structure. The cellular (colony) structure of the eutectic in Figure (29) is analogous to the way some eutectics grow because of the presence of impurities, e.g. Sn-Pb structures shown in Ref. [23]. In the present case, the cellular structure is attributed to constitutional supercooling that develops due to the changing liquid composition along the line of two-fold saturation - as the liquid moves down the line it rejects more solute than it uses and forms a boundary layer in front of the solid/liquid interface. The cooperative growth mechanism continues until the boundary layer in front of the liquid/solid interface becomes too large. The phases then solidify as larger chunks at a slower rate. It should also be noted that no ternary eutectic was observed in these alloys. The TEM photomicrograph of alloy #13 in Figure (30) shows a typical region where both T1 and Nb_3Al phases were found. In general, complete solidification requires that the liquid go through an invariant reaction, e.g. ternary eutectic. On the other hand, the available liquid may be exhausted before such a composition/temperature is reached. It appears that this was the case for the group 2 alloys.

Finally, the measured volume fraction of the dendritic phase decreases as the initial alloy composition moves further away, from the Nb-Si binary and closer to the line of two-fold saturation, Table (10).

3. Solidification "Path" Calculations

Solidification "path" calculations were carried out using the equations described in chapter IV. As previously noted it was assumed that only line compounds form from the melt. Equations that permit direct calculation of molar and weight fractions of the primary phase, the phases formed on the line of two-fold saturation and the ternary eutectic are derived in Appendix B. In this section the equation for the appropriate line of two-fold saturation is estimated, and a comparison is made of the calculated results with the experimental observations.

(a) Group 1 Alloys

The assumption that all the phases solidified are line compounds, is certainly supported for the case of T1 dendrites - note the rather flat composition profile in Figure (27). Furthermore, the $NbAl_3$ phase, which solidifies along the line of two-fold saturation and in the ternary eutectic, contains little or no Si, Table (2-5). Thus, for the calculations, the composition of Nb-75at%Al was used. The Nb_2Al phase only comes out in the ternary eutectic and the composition used for the calculation was Nb-1.5at%Si-34.3at%Al, in agreement with experimental observation, Table 5.

The line of two-fold saturation, $L+NbAl_3+T1$, intercepted during solidification of these alloys was estimated with a linear approximation:

$$wt\%Nb = M \times wt\%Si + N \qquad [12]$$

where: $M = -2.84$ $N = 0.731$

The T1 liquidus slope is steep and the $NbAl_3$ liquidus surface is rather flat, when these two surfaces meet two approximate straight lines are produced that meet at a saddle point, Figure (31). In general, lines of two-fold saturation have curvature and higher order polynomials are needed to properly describe them.

By combining the equation for the line of two-fold saturation, equation [12], and the single phase solidification equation for ternary alloys, equation [7], one can obtain the molar or weight fractions of liquid and liquid composition where the two-fold saturation line is intercepted, e.g. equation [B2] in Appendix B. The calculated solidification "paths" for group 1 alloys are plotted on the liquidus projection diagram, Figure (31), as a dashed lines. The molar fractions of the phases that solidify along the line of two-fold saturation and the ternary eutectic are calculated as described in Appendix B. The trends observed in the measured volume fractions are compared with calculated molar and weight fractions in Table 11. Two observations are noteworthy. Firstly, as previously noted, the primary dendritic volume fraction decreases with increasing Al content in the initial alloy composition. A comparison of the calculated weight and molar fractions of the primary dendritic phase with experimental results, given below, shows good agreement. Considering no correction is made for the density differences between the various phases, i.e. volume fraction is compared to weight fraction.

Alloy # Composition	Measured Volume Fractions	Calculated Weight Fractions
#8 - $Nb_{55}Si_{31}Al_{14}$	0.88	0.852
#11 - $Nb_{50}Si_{20.5}Al_{29.5}$	0.7	0.613
#12b - $Nb_{45}Si_{10.4}Al_{44.6}$	0.42	0.349
#12 - $Nb_{36.7}Si_{11.6}Al_{51.7}$	0.33	0.197

The second observation relates to the dependence of the amount and type of second phases on the Nb content in the initial alloy composition. This is best seen in alloys #12 and #12b. The calculated fractions of the different types of second phase, i.e. ternary eutectic or those solidifying on the line of two-fold saturation, show poor agreement with the observed trends (Table 11). Alloy #12 was observed to have 24% ternary eutectic and 43% second phases solidified along the line of two-fold saturation, the corresponding calculated weight percentages are 9.7% and 70.6%, respectively. In alloy #12b only ternary eutectic was discernable at a volume fraction of 58%. On the other hand, the calculated percentages are 37.6% ternary eutectic and 27.5% solidified along the line of two-fold saturation. Calculations for alloys #12 and #12b, due to their proximity to the line of two-fold saturation, are very sensitive to the values used for their initial alloy compositions. The EDS system used to determine the initial compositions of these alloys has an error of <5%, and this error can profoundly effect the calculated results. For example, by varying the initial composition of alloy #12b from $Nb_{45}Si_{10.4}Al_{44.6}$ to $Nb_{46.2}Si_{9.5}Al_{44.3}$ the calculated weight fractions of ternary eutectic and phases solidified on the line of two-fold saturation become 58% and 5.24%, respectively, which are in much better agreement with observations.

(b) Group 2 Alloys

Group 2 alloys were observed to end solidification along the line of two-fold saturation, with the simultaneous formation of T1 and Nb_3Al. Hence, either little or no liquid was left for the formation of the Nb_2Al phase at the four phase reaction [$L+Nb_3Al \Leftrightarrow T1 + Nb_2Al$], II_3, Figure (32), or this phase had difficulty nucleating. The calculated solidification "paths" for alloys #7, #10, and #13 using a procedure identical to the previous section are shown in Figure (32). In this case, the first two-fold saturation line intercepted by group 2 alloys, is the $L + Nb_3Al + T1$ line, between reactions II_2 and II_3. A linear approximation was again used to estimate the line:

$$\text{wt\%Nb} = M1 \times \text{wt\%Si} + N1 \qquad [13]$$

where: $M1 = 5.94$ and $N1 = 0.683$

This alloy group is predicted to hit reaction II_3 and then travel down the $L + Nb_2Al + T1$ line of two-fold saturation. This line was also estimated with a linear approximation:

$$\text{wt\%Nb} = M2 \times \text{wt\%Si} + N2 \qquad [14]$$

where: $M2 = 8.66$ and $N2 = 0.605$

The solidification "path" ends at the ternary eutectic, reaction I_1.

The measured volume fractions of various phases are compared to calculated molar and weight fractions in Table 12. As previously noted, no Nb_2Al phase was noted in the microstructure. Calculations show that the weight fraction of remaining liquid at point II_3 along the line of two-fold saturation was, 0.022, 0.033 and 0.01 for alloys #7, #10 and #13, respectively. It is clear that very little liquid was available for nucleation of Nb_2Al, hence, simultaneous formation of T1 and Nb_2Al as anticipated in Figure (20). Extensive characterization was not carried out to determine the existence of this phase in the microstructures. On the other hand, the predicted trends are in close agreement with the observations for the amounts of primary dendritic phase T1, and the T1 plus Nb_3Al phases forming simultaneously along the line of two fold saturation between II_2 and II_3 in Figure (32), see Table 12.

In summary, the solidification sequence of alloys above and below the 62.5at%Nb line can be generalized using the specific data for group 1 and 2 alloys. Two distinct regions, shaded in Figure (33), are defined. The predictability of these calculations is insured by the experiments conducted on the seven alloy compositions noted in Figure (19). It is expected that alloys with initial compositions in both regions will initially form T1 dendrites. Subsequently, group 1 alloys form $NbAl_3$ and T1, while, group 2 alloys form Nb_3Al and T1. Whether or not group 2 alloys form Nb_2Al depends on the fraction of liquid remaining as the liquid composition moves down the L + Nb_3Al + T1 line to point II_3 on the liquidus diagram of Figure (33).

VI. CONCLUDING REMARKS

The evolution of solidification microstructures in a number of Nb-Si-Al alloys were studied. Specific information about the phase diagram of the system is imperative for an intelligent solidification analysis. For this reason, the phase diagram was evaluated. To facilitate the evaluation of the available phase diagram data a reaction flow chart was constructed. Two discrepancies were noted in isothermal sections available in the literature. The first was between the 1500°C section by V. Pan et al. [15], and the 1400°C section by H. Nowotny et al. [16]. The phase fields bounded by Nb_2Al, $NbAl_3$, C-54, $NbSi_2$, α - Nb_5Si_3 (T2) and β - Nb_5Si_3 (T1) in these two diagrams do not match. Using the flow chart and the available data on the ternary and the relevant binaries, it was established that the probable phase fields are those presented by Nowotny et al.. The second uncertainty relates to the areas around the T1 phase. The two noteworthy isothermal sections reported in the literature for this region are: the 1840°C section by A. Muller [19] and the 1820°C section by V. Pan et al. [15]. The former shows T1 as a solid solution based on the binary Nb_5Si_3 phase, while the latter shows the existence of a two phase field (T1+T2), and T1 only as a ternary phase. Data from the paper by H. Nowotny et al. [16] shows that the T1 phase has the same crystal structure as the binary high temperature allotrope, β - Nb_5Si_3; indicating that the T1 is probably a solid solution of this binary phase. It was concluded that the T1 phase must be in contact with the binary down to a temperature of ~1650°C, where the β -

Nb_5Si_3 phase decomposes through a peritectoid reaction. An estimated 1850°C isothermal section was configured to better clarify this region.

Another useful diagram for solidification analysis configured from the above information was the liquidus projection diagram. This is the first estimate of the complete liquidus surface available. The liquidus surface is dominated by the T1 liquidus hill centered around the 62.5at% Nb isoconcentration line. The upper region, >62.5at% Nb , is a deep valley with several type II four phase reactions along it. The lower region is bounded by a quasi-binary between $NbAl_3$ and T1, which contains a saddle point, with one side of it decending into a ternary eutectic $L \Leftrightarrow NbAl_3 + Nb_2Al + T1$. Finally, the remainder of the diagram is dominated by the C-54 and $NbSi_2$ liquidus surfaces centered around the 33 at% Nb isoconcentration line. The two-fold saturation lines in this region have several type II transition reactions along them, and drop into the Al-rich corner. Using this information one may qualitatively deduce the primary and possible secondary phases that would form during solidification of a given alloy. On the other hand, quantitative analysis requires data on the liquid-solid tie lines which is not available. A reasonable compromise was reached by assuming the phases forming to be line compounds, with their compositions given by experimental measurements. Using the liquidus projection diagram and the ternary equations for solidification, with Schiel-type assumptions, the microstructure evolution "paths" and amounts of various phases for a number of alloys were predicted.

Two alloy groups close to the 62.5at% Nb isoconcentration line were studied. In group 1 alloys, with compositions below this line, the solidification sequence is:

$L \rightarrow L+T1 \rightarrow L+T1+NbAl_3 \rightarrow$ eutectic $[T1+NbAl_3+Nb_2Al]$

In group 2 alloys, with compositions above this line, the solidification sequence is:

$L \rightarrow L+T1 \rightarrow L+T1+Nb_3Al \rightarrow L+T1+Nb_2Al \rightarrow$ eutectic $[T1+NbAl_3+Nb_2Al]$

This difference in the solidification sequences stems from the shape of the liquidus surface of the T1 phase. One may visualize this surface as a hill with a crest that runs along the 62.5at%Nb isoconcentration line. The liquid compositions of the two alloy groups move down opposite sides of this T1 liquidus hill during primary solidification. Thus, with just a few atomic % difference in initial alloy composition the solidification "path" changes with the liquid composition intersecting a different "valley" line of two-fold saturation. The main variable in the determining the as-cast microstructure is the initial alloy composition. Because of constraints on homogenization heat treatments of high temperature Nb-Si-Al alloys, the properties (e.g.oxidation resistance, mechanical properties, etc.) are dominated by the phases that make up this microstructure. It is thus imperative to select the initial alloy composition using an approach similar to the one developed in this study, and hence, optimize the as-cast microstructure for specific applications.

ACKNOWLEDGEMENTS

The authors are grateful to Pratt & Whitney aircraft for supplying the alloys used in this study. The support of the Defense Advanced Research Projects Agency (DARPA) through contract N00014-86-K-0178, supervised by Dr. Ben A. Wilcox and monitored by Dr. Steven G. Fishman of the Office of Naval Research is also gratefully acknowledged.

References

1) R.J. Hecht, Pratt and Whitney Aircraft, West Palm Beach, Fl. (Private communication).

2) "Binary Alloys Phase Diagrams", American Society For Metals, T.B.Massalski, Vol.1, p. 164-165.

3) A.B.Gokhal, G.Sarkar, G.J.Abbaschian, J.C.Haygarth, C.Wojcik, R.E.Lewis."Supercooling Effect in Faceted Eutectic Niobium-Silicon Alloys", Solidification Processing of Eutectic Alloys,University of Florida,Gainsville FL. 32611 (1988).

4) S.I.Alyamouskiii, P.V.Gel'd, I.I.Matueenko. Russian Journal of Inorganic Chemistry. Vol.7, No. 4, p. 432-435 (1962).

5) A.G.Knapton, "The System Niobium-Silicon and the Effect of Carbon on the Structure of Certain Silicides", Nature. Vol. 175, p. 730 (1955).

6) D.K.Deardorff, R.E.Siemens, P.A.Romans and R.A.McCune, "New Tetragonal Compounds Nb_3Si and Ta_3Si", J. of Less Common Metals. 18, p. 11-26 (1969).

7) Y.A.Kocherzhiuskeiy, L.M.Yupkol, "The Nb-Si Phase Diagram", Russ. Metall., No. 1, p. 184-188 (1980).

8) Bulletin of Alloy Phase Diagrams, "The Al-Nb System", Vol. 2 No. 1, p. 75-81 (1981).

9) C.E.Lundin, A.S.Yamamoto, "The Equilibrium Phase Diagram, Niobium-Aluminum", Trans. AIME , Vol. 236, p. 863-872 (1966).

10) S.Steeb, R.Keppeler. Z.Natarforsch, "Diffusionuntersuchungen in den Systemen Mo-Nb, Mo-Al, und Nb-Al Mittels Microsonde", 24A, p. 1601-1609 (1969).

11) J.L.Jorda, R.Flukiger, J.Muller, "A New Metallurgical Investigation of the Niobium-Aluminum System", J. of Less Common Metals, 75, p. 227-239 (1980).

12) M.A.Wicker,C.Allibert, J.Driole, "Thermodynamique Metallurgique - Contribution a l'etude du diagramme de Phases $NbAl_3$-Al", C.R.Acad.Sc. Paris, t.272, S'erie C p. 1711-1713 (1971).

13) U.Kattner, To be published in "Bulletin of Alloy Phase Diagrams"

14) C. Allibert, A. Wicker, J. Driole and E. Bonnier, "Etude du Systemme Niobium Aluminum-Siliciun", J. of Less Common Metals, 31, p. 221228 (1973).

15) V.M.Pan, V.I.Latyshera, O.G.Kulik, A.G.Popov and E.N.Lituineko, "The Nb-$NbAl_3$-Si_3 Phase Diagram", IZV. Akad Nank SSSR Metally, 4, p. 225-226 (1984).

16) H.Nowotny, F.Benesousky, "Der Dreistoff: Nb-Al-Si", C. Brukl. Monash. Chem., 92, p. 193-196 (1961).

17) C.Brukl, A.Nowotny, F.Benesousky, "Untersuchungen in den Dreistoff Systemen: V-Al-Si, Nvb-Al-Si, Cr-Al-Si, Mo-Al-Si bzw Cr(Mo)-Al-Si", Monatsh. Chem., 92, p. 967-980 (1961).

18) V.M.Pan, V.I.Latysheva, A.I.Sudovtsov, "Superconductivity of Nb-Al-Si Alloys", Fiz. Metal. Metallov. 33, No. 6, p. 1311-1313 (1972).

19) A.Muller, Z. Naturforsch., "Supraleitung dur Al5-Phase in System Nb-Al-Si", 26A, p. 1035-1039 (1971).

20) H.J.Goldschmidt, "Interstitial Alloys", New York Plenum Press, London Butterworths, p. 294-444.

21) R.Mehrabian and M.C. Flemings, "Macrosegregation in Ternary Alloys", Met. Trans., Vol. 1, p. 455 (1970).

22) F.N.Rhines, "Phase Diagrams in Metallurgy", McGraw Hill Book Co., (1956).

23) R.Elliot, "Eutectic Solidification Processing", Butterworths & Co, (1983).

24) P.Doemer, "Konstitutionsuntersuchungen an Hochtemperaturkeramiken des Systems B-AL-=C-Si-N-O mit Hilfe Thermodynamischer Berechnungen", Ph.D Thesis, University Stuttgart, F.R. Germany, (1982).

Appendix A: Phase Diagram Information

Nb-Al Crystal Structure Data

Phase	Composition at%Al	Péarson symbol	Space group	Prototype
(Nb)	0-21.5	cI2	Im-3m	W
Nb_3Al	18.6-25	cP8	Pm-3n	Cr_3Si
Nb_2Al	30-42	tP30	$P4_2/mnm$	σ-CrFe
$NbAl_3$	75	tI8	I4/mmm	$TiAl_3$
(Al)	100	cF4	Fm-3m	Al

Nb-Si Crystal Structure Data

Phase	Composition at%Al	Pearson symbol	Space group	Prototype
(Nb)	0-1.2	cI2	Im-3m	W
Nb_3Si	25	tP32	$P4_2/n$	Ti_3P
β-Nb_5Si_3	37.5-39.5	tI32	I4/mcm	W_5Si_3
α-Nb_5Si_3	37.5-40.5	tI32	I4/mcm	Cr_5B_3
$NbSi_2$	66.7	hP9	$P6_222$	$CrSi_2$
(Si)	100	cF8	Fd-3m	C

Al-Si Crystal Structure Data

Phase	Composition at%Al	Pearson symbol	Space group	Prototype
(Al)	0-2.2	cF4	Fm-3m	Al
(Si)	100	cF8	Fd-3m	C

Nb-Si-Al Crystal Structure Data

T1	same as β-Nb_5Si_3
T2	same as α-Nb_5Si_3
$Nb(Si,Al)_2$	C-54 phase

Binary Invariant reactions

Type of reaction	Binary	atomic %	Temperature (°C)
Eutectics			
e_1: L ⇔ Al + Si	Al-Si	12at%Si	577°C
e_2: L ⇔ $NbSi_2$ + Si	Nb-Si	96at%Si	1400°C
e_3: L ⇔ β-Nb_5Si_3 + $NbSi_2$	Nb-Si	57at%Si	1900°C
e_4: L ⇔ Nb_3Si + α-Nb	Nb-Si	17.5at%Si	1920°C
e_5: L ⇔ $NbAl_3$ + Nb_2Al	Nb-Al	42at%Nb	1590°C
Peritectics			
p_1: L + β-Nb_5Si_3 ⇔ Nb_3Si	Nb-Si	19at%Si	1980°C
p_2: L + α-Nb ⇔ Nb_3Al	Nb-Al	72at%Nb	2060°C
p_3: L + Nb_3Al ⇔ Nb_2Al	Nb-Al	65at%Nb	1940°C
p_4: L + $NbAl_3$ ⇔ Al	Nb-Al	99at%Al	661°C
Congruent Melting Compounds			
$NbSi_2$	Nb-Si	33at%Nb	1940°C
β–Nb_3Si_3	Nb-Si	62.5at%Nb	2525°C
$NbAl_3$	Nb-Al	25at%Nb	1680°C

Four Phase Reactions
in the Nb-Si-Al System.

Type of Reaction		at%Si	at%Al	Temp. (°C)
Type I				
$L \Leftrightarrow NbAl_3 + Nb_2Al + T1$	I_1	2.2	57.5	~1550°C
$L \Leftrightarrow NbSi_2 + Al + NbAl_3$	I_2	8	90	<570
Type II				
$L + Nb_3Si \Leftrightarrow T1 + Nb$	II_1	18	1-2	~1910°C
$L + Nb \Leftrightarrow T1 + Nb_3Al$	II_2	12	7.5	~1900°C
$L + Nb_3Al \Leftrightarrow Nb_2Al + T1$	II_3	7	30	~1880°C
$L + NbSi_2 \Leftrightarrow T1 + C\text{-}54$	II_4	35	25	
$L + T1 \Leftrightarrow NbAl_3 + C\text{-}54$	II_5	12	62	~1550°C
$L + C\text{-}54 \Leftrightarrow NbSi_2 + NbAl_3$	II_6	115	80	~1145°C
$L + Si \Leftrightarrow Al + NbSi_2$	II_7	11	88	<577°C
Ternary Saddle Points				
$L+NbAl_3+T1$		7	62	1625°C
$L+NbSi_2+C\text{-}54$		~45	~22	

Solid State Reaction
in the Nb-Si-Al System

Nb-Si Binary Invarient Reactions (solid).

$Nb_3Si + T1 \Leftrightarrow T2$	ps1	1940°C	peritictiod
$Nb_3Si \Leftrightarrow T2 + Nb$	es1	1770°C	eutectiod
$T1 \Leftrightarrow T2 + NbSi_2$	es2	1650°C	eutectiod

Ternary Four Phase Reaction (solid).

Type II

$T1 + Nb_3Si \Leftrightarrow T2 + Nb$	II_{s1}
$T1 + Nb \Leftrightarrow Nb_3Al + T2$	II_{s2}
$T1 + NbSi_2 \Leftrightarrow T2 + C\text{-}54$	II_{s3}

Analytical Description of the Nb-Al System

General formula for the Gibbs energy:

$$G = \sum_i X(x,n)_i * (H_i - S_i * T)$$

The reference states for all the phases are bcc Nb and liquid Al.
The lattice stabilities for the pure elements are from Saunders et al. (24).
Coefficients adjusted in the optimization are underlined.

Liquid, Substitutional Solution (Nb,Al)

$X(x,n)_i$	H_i	S_i
x_{Nb}	30000.00	10.90900
x_{Al}	0.00	0.00000
$\sum_j x_j * \ln(x_j)$	0.00	-8.31451
$x_{Nb}x_{Al}$	$\underline{-133412.60}$	$\underline{-32.63330}$
$x_{Nb}x_{Al}(x_{Nb}-x_{Al})$	$\underline{6327.70}$	$\underline{8.28036}$
$x_{Nb}x_{Al}(x_{Nb}-x_{Al})^2$	$\underline{27496.90}$	0.00000

bcc (Nb), Substitutional Solution (Nb,Al)

$X(x,n)_i$	H_i	S_i
x_{Nb}	0.00	00.00000
x_{Al}	-628.00	-6.66300
$\sum_j x_j * \ln(x_j)$	0.00	-8.31451
$x_{Nb}x_{Al}$	$\underline{-149317.10}$	$\underline{-40.74840}$

fcc (Al), Substitutional Solution (Nb,Al)

$X(x,n)_i$	H_i	S_i
x_{Nb}	22000.00	2.20000
x_{Al}	-10711.00	-11.47300
$\sum_j x_j * \ln(x_j)$	0.00	-8.31451
$x_{Nb}x_{Al}$	-80000.00	0.00000

Nb_3Al, Wagner-Schottky Compound $(\mathbf{Nb},\mathrm{Al})_3(\mathbf{Al},\mathrm{Nb})_1$

$X(x,n)_i$	H_i	S_i
$\sum_l \sum_j n_j^l * \ln(n_j^l)$	00.00	-8.31451
1	37335.20	-8.77215
n_{Nb}^2	151000.00	30.00000
n_{Al}^1	53098.20	11.50000

Nb_2Al, Wagner-Schottky Compound $(\mathbf{Nb},\mathrm{Al})_{16}(\mathbf{Al},\mathrm{Nb})_{10}(\mathbf{Nb})_4$

$X(x,n)_i$	H_i	S_i
$\sum_l \sum_j n_j^l * \ln(n_j^l)$	00.00	-8.31451
1	-49113.10	-12.51828
n_{Nb}^2	141000.00	23.30000
n_{Al}^1	52946.80	4.00000

$NbAl_3$, Stoichiometric Compound $\mathbf{Nb_1Al_3}$

$X(x,n)_i$	H_i	S_i
1	-48626.20	-15.31191

note: where $\sum_l n_j^l = x_j$

Analytical Description of the Nb-Si System

General formula for the Gibbs energy:

$$G = \sum_i X(x,n)_i * (H_i - S_i * T)$$

The reference states for all the phases are bcc Nb and liquid Si.
The lattice stabilities for the pure elements are from Saunders et al. (24).
Coefficients adjusted in the optimization are underlined.

Liquid, Substitutional Solution (Nb,Si)

$X(x,n)_i$	H_i	S_i
x_{Nb}	30000.00	10.90900
x_{Si}	0.00	0.00000
$\sum_j x_j * \ln(x_j)$	0.00	-8.31451
$x_{Nb} x_{Si}$	-197387.10	-42.33861
$x_{Nb} x_{Si} (x_{Nb} - x_{Si})$	-116757.40	-58.17759

(Nb), Stoichiometric Compound $\mathbf{Nb_1Si_0}$

$X(x,n)_i$	H_i	S_i
1	00.00	00.00

(Si), Stoichiometric Compound $\mathbf{Nb_0Si_1}$

$X(x,n)_i$	H_i	S_i
1	-50208.00	-29.76200

Nb3Si, Stoichiometric Compound $\mathbf{Nb_3Si_1}$

$X(x,n)_i$	H_i	S_i
1	-36991.30	-5.45877

α-Nb_5Si_3, Stoichiometric Compound Nb_5Si_3

$X(x,n)_i$	H_i	S_i
1	-61964.80	-11.35889

β-Nb_5Si_3, Stoichiometric Compound $Nb_{31}Si_{19}$

$X(x,n)_i$	H_i	S_i
1	-58966.70	-9.78875

$NbSi_2$, Stoichiometric Compound Nb_1Si_2

$X(x,n)_i$	H_i	S_i
1	-93405.20	-27.02926

Analytical Description of the Al-Si System

General formula for the Gibbs energy:

$$G = \sum_i X(x,n)_i * (H_i - S_i * T)$$

The reference states are liquid Al and Si .
Lattice stabilities for the pure elements are from Saunders et al. (24).
Description was taken from Doemer (25)
Coefficients adjusted in the optimization are underlined.

Liquid, Substitutional Solution (Al,Si)

$X(x,n)_i$	H_i	S_i
x_{Al}	00.00	0.00000
x_{Si}	00.00	0.00000
$\sum_j x_j * \ln(x_j)$	0.00	-8.31451
$x_{Al}x_{Si}$	-133412.60	-32.63330
$x_{Al}x_{Si}(x_{Al}-x_{Si})$	6327.70	8.28036
$x_{Al}x_{Si}(x_{Al}-x_{Si})^2$	27496.90	0.00000

Appendix B: Solidification "path" Calculations

For the Nb-Si-Al system the phases that come out during solidification can be estimated as line compounds. Thus, for the calculations of the solidification "paths" the equations used are based on the assumption that phases of constant composition are solidifying. The solidification "path" is the path which the liquid composition follows throughout solidification. This starts with the primary phase solidifying, the path is described by the ternary single phase solidification equation, equation [7] in chapter IV. The next point of interest along the solidification "path" is the point where the liquid composition hits the line of two-fold saturation. This can be obtained by substituting in the single phase solidification equations for solute n and m into the equation for the line of two-fold saturation and solving for fraction liquid. The equation for the line of two-fold saturation was estimated with a linear approximation as described in secion 3 of chapter V. The equation of the line is:

$$C_{Ln} = M * C_{Lm} + N \qquad [B1]$$

substituting in equation [7] from the text and solving for the molar fraction of liquid left at the point where the liquid composition intersects the line of two-fold saturation (f_{LTF}), yields:

$$f_{LTF} = \frac{M*(C_{om} - C_{\alpha m}) - (C_{on} - C_{\alpha n})}{C_{\alpha n} - M*C_{\alpha m} - N} \qquad [B2]$$

The composition of the intersection is obtained by solving the single phase solidification equations using the value of fraction liquid at the point of intersection (f_{LTF}). The next calculation is to determine the amount of eutectic in the final microstructure. This is done by solving equation [11a,b] in the text for df_{β} and dividing the two equations, which will eliminate the df_{β} term:

$$1.0 = \left(\frac{C_{\alpha m} - C_{\beta m}}{C_{\alpha n} - C_{\beta n}} \right) \left(\frac{f_L \, dC_{Ln} + (C_{Ln} - C_{\alpha n}) \, df_L}{f_L \, dC_{Lm} + (C_{Lm} - C_{\alpha m}) \, df_L} \right) \qquad [B3]$$

To simplify define a constant X as:

$$X = \frac{C_{\alpha m} - C_{\beta m}}{C_{\alpha n} - C_{\beta n}}$$

rearranging and separating variables yields:

$$-\frac{df_L}{f_L} = \frac{dC_{Lm} - X \, dC_{Ln}}{(C_{Lm} - C_{\alpha m}) - X \, (C_{Ln} - C_{\alpha n})} \qquad [B4]$$

differenciating the equation for the line of two-fold saturation [B1], results in:

$$dC_{Ln} = M * dC_{Lm} \qquad [B5]$$

substituting equations [B1] and[B5] into equation [B4] and rearranging, yields:

$$-\frac{df_L}{f_L} = \frac{(1 - XM)\, dC_{Lm}}{(1 - XM)C_{Lm} - (C_{\alpha m} - XC_{\alpha n} + XN)} \qquad [B6]$$

This equation may be integrated and solved for the molar fraction eutectic. The integration is from C_{LTFm} to C_{LEm} and f_{LTF} to f_{LE}.

Where:

C_{LTFm} - liquid composition at the intersection point with line of two-fold saturation.

C_{LEm} - ternary eutectic composition.

f_{LTF} - molar fraction of liquid remaining at the intersection point with the line of two-fold saturation.

f_{LE} - molar fraction ternary eutectic

$$f_{LE} = f_{LTF}\left[\frac{(1-MX)C_{LTFm} - (C_{\alpha m} - XC_{\alpha n} + XN)}{(1-MX)C_{LEm} - (C_{\alpha m} - XC_{\alpha n} + XN)}\right] \qquad [B6]$$

The molar fraction of the primary dendritic phase and second phases solidifying along the line of two-fold saturation are then determined from:

$$f_D = 1 - f_{LTF} \qquad \text{[B7a]}$$

and

$$f_{TF} = 1 - f_D - f_{LE} \qquad \text{[B7b]}$$

Table 1: Dendritic Phase Composition

	atomic %		
Alloy #	Nb	Si	Al
8	60.3	36.8	2.9
11	57.9	34.6	7.5
12	57.6	32.4	10.0
12b	60.43	24.6	14.97

Table 2: Experimental Summary Alloy #8

	atomic %		
	Nb	Si	Al
Co	55.0	31.0	14.0
Dendrite T1	60.3	36.8	2.9
T1 (Eutectic)	60.5	17.2	22.3
$NbAl_3$	24.5	0.5	75
Eutectic	40.0	2.0	58.0

Volume Fraction:

Dendrite = 0.88
Second Phases =0.12

Line of Two-fold Saturation = 0.05
Eutectic = 0.07

Table 3: Experimental Summary Alloy #11

	atomic %		
	Nb	Si	Al
Co	50.0	20.5	29.5
Dendrite T1	57.9	34.6	7.5
T1 (Eutectic)	61.8	13.5	24.7
$NbAl_3$	25.0	0.4	74.6
Eutectic	40.0	2.0	58.0

Volume Fraction:

Dendrite = 0.7
Eutectic = 0.3

Table 4: Experimental Summary Alloy #12

	atomic %		
	Nb	Si	Al
Co	36.7	11.6	51.7
Dendrite T1	57.6	32.4	10.0
T1 (Eutectic)	57.33	22.17	20.5
$NbAl_3$	22.6	0.1	77.3
Eutectic	40.5	2.2	57.3

Volume Fraction:

Dendrite = 0.33
Second
Phases =0.67

Line of
Two-fold
Saturation = 0.43
Eutectic = 0.24

Table 5: Experimental Summary Alloy #12b

	atomic %		
	Nb	Si	Al
Co	45.0	10.4	44.6
Dendrite T1	60.43	24.6	14.97
T1 (Eutectic)	60.7	18.8	20.5
$NbAl_3$	25.2	0.3	74.5
Nb_2Al	64.2	1.5	34.3
Eutectic	40.0	2.0	58.0

Volume Fraction:

Dendrite = 0.42
Eutectic = 0.58

Table 6

Volume Fraction
Data Group 1 Alloys

Alloy #	Dendrite	Second Phases
8	0.88	0.12
11	0.7	0.3
12	0.33	0.67
12b	0.42	0.58

Table 7: Experimental Summary Alloy #7

	atomic %		
	Nb	Si	Al
Co	67.0	25.8	7.2
Dendrite T1	64.1	32.2	3.7
Nb_3Al	77.0	6.5	16.5

Volume Fraction:

Dendrite = 0.71
Second
Phases =0.29

Table 8: Experimental Summary Alloy #10

	atomic %		
	Nb	Si	Al
Co	71.4	19.6	9.0
Dendrite T1	65.2	31.8	3.0
Nb_3Al	77.8	9.1	13.1

Volume Fraction:

Dendrite = 0.54
Second
Phases =0.46

Table 9: Experimental Summary Alloy #13

	atomic %		
	Nb	Si	Al
Co	74.1	13.1	12.8
Dendrite T1	64.9	27.9	7.2
Nb_3Al	77.2	8.4	14.4

Volume Fraction:

Dendrite = 0.26
Second
Phases =0.74

Table 10

Volume Fraction
Data Group 2 Alloys

Alloy #	Dendrite	Second Phases
7	0.71	0.29
10	0.54	0.46
13	0.26	0.74

Table 11

	Calculated Molar Fraction	Calculated Weight Fraction	Observed Volume Fraction
Alloy #8			
	$f_D = 0.81$	$f_D = 0.852$	$V_D = 0.88$
	$f_{TF} = 0.146$	$f_{TF} = 0.111$	$V_{TF} = 0.05$
	$f_E = 0.044$	$f_E = 0.037$	$V_E = 0.07$
	$f_{SP} = 0.19$	$f_{SP} = 0.148$	$V_{SP} = 0.12$
Alloy #11			
	$f_D = 0.563$	$f_D = 0.613$	$V_D = 0.7$
	$f_{TF} = 0.012$	$f_{TF} = 0.008$	
	$f_E = 0.425$	$f_E = 0.379$	$V_E = 0.3$
	$f_{SP} = .0437$	$f_{SP} = 0.387$	
Alloy #12			
	$f_D = 0.162$	$f_D = 0.197$	$V_D= 0.33$
	$f_{TF} = 0.745$	$f_{TF} = 0.706$	$V_{TF} = 0.43$
	$f_E = 0.093$	$f_E = 0.097$	$V_E = 0.24$
Alloy #12b			
	$f_D = 0.294$	$f_D = 0.349$	$V_D= 0.42$
	$f_{TF} = 0.314$	$f_{TF} = 0.275$	
	$f_E = 0.392$	$f_E = 0.376$	$V_E = 0.58$

where:

f_D - fraction primary dendrite

f_{TF} - fraction of phases that solidify along the line of two-fold saturation, L+ $NbAl_3$ + T1.

f_E - fraction eutectic

f_{SP} - fraction of all second phases

V_D - volume fraction of primary dendrite

V_{TF} - volume fraction of phases that solidify along the line of two-fold saturation, L+ $NbAl_3$ + T1.

V_E - volume fraction eutectic

V_{SP} - volume fraction of all second phases

Table 12

	Calculated Molar Fraction	Calculated Weight Fraction	Observed Volume Fraction
Alloy #7			
	$f_D = 0.709$	$f_D = 0.691$	$V_D = 0.71$
	$f_{TF1} = 0.268$	$f_{TF1} = 0.287$	$V_{TF1} = 0.29$
	$f_{TF2} = 0.022$	$f_{TF2} = 0.021$	
	$f_E = 0.001$	$f_E = 0.001$	
	$f_{SP} = 0.291$	$f_{SP} = 0.309$	$V_{SP} = 0.29$
Alloy #10			
	$f_D = 0.422$	$f_D = 0.4$	$V_D = 0.54$
	$f_{TF1} = 0.542$	$f_{TF1} = 0.567$	$V_{TF1} = 0.46$
	$f_{TF2} = 0.034$	$f_{TF2} = 0.0315$	
	$f_E = 0.002$	$f_E = 0.0015$	
	$f_{SP} = 0.578$	$f_{SP} = 0.6$	$V_{SP} = 0.46$
Alloy #13			
	$f_D = 0.144$	$f_D = 0.1326$	$V_D = 0.26$
	$f_{TF1} = 0.847$	$f_{TF1} = 0.8573$	$V_{TF1} = 0.74$
	$f_{TF2} = 0.0085$	$f_{TF2} = 0.0097$	
	$f_E = 0.0005$	$f_E = 0.0004$	
	$f_{SP} = 0.856$	$f_{SP} = 0.8674$	$V_{SP} = 0.74$

where:

f_{TF1} - fraction of phases that solidify along the line of two-fold saturation, L+ Nb_3Al + T1.

f_{TF2} - fraction of phases that solidify along the line of two-fold saturation, L + Nb_2Al + T1.

V_{TF1} - volume fraction of phases that solidify along the line of two-fold saturation, L+ Nb_3Al + T1

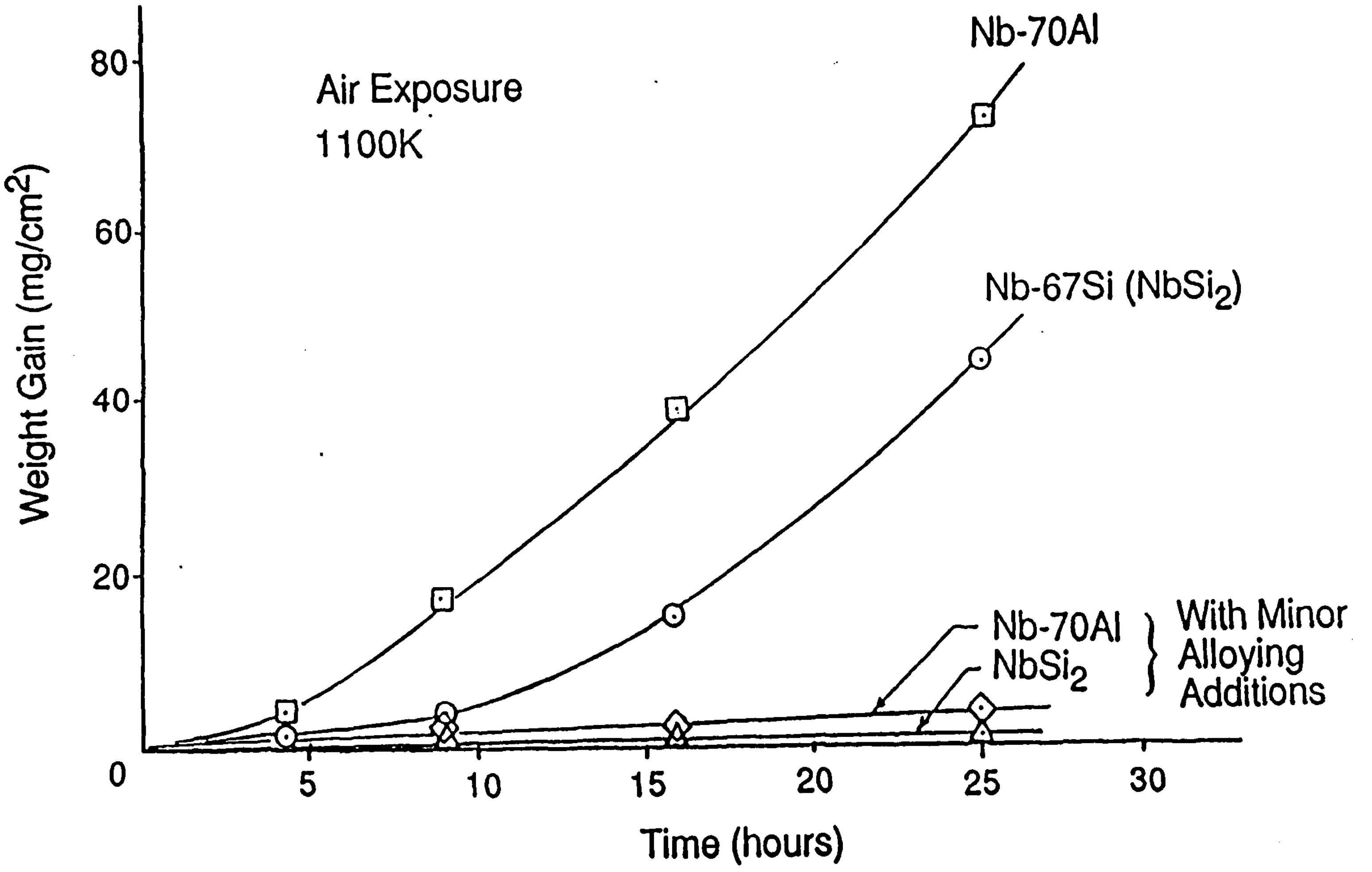

Figure 1: Low temperature oxidation of Nb-Si-Al alloys, form Reference [1]

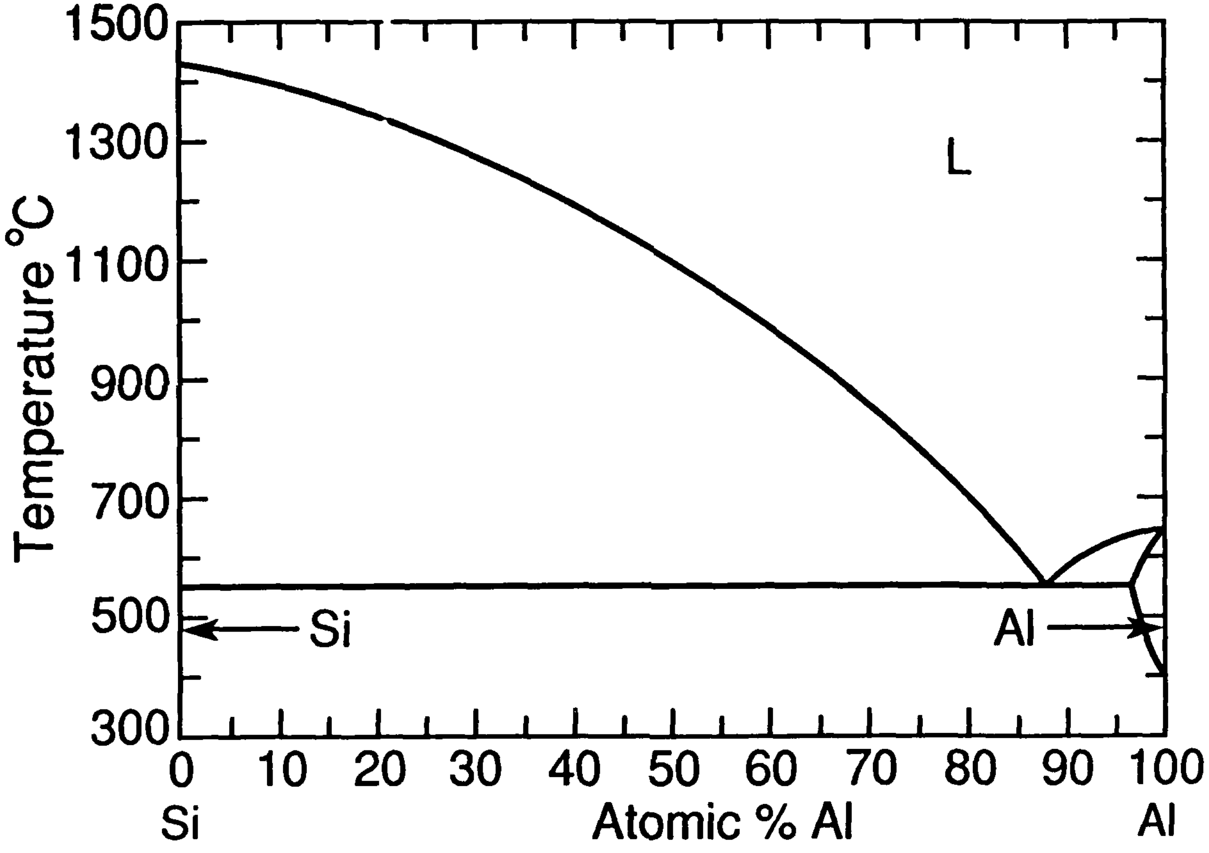

Figure 2: Al-Si binary, from Reference [2].

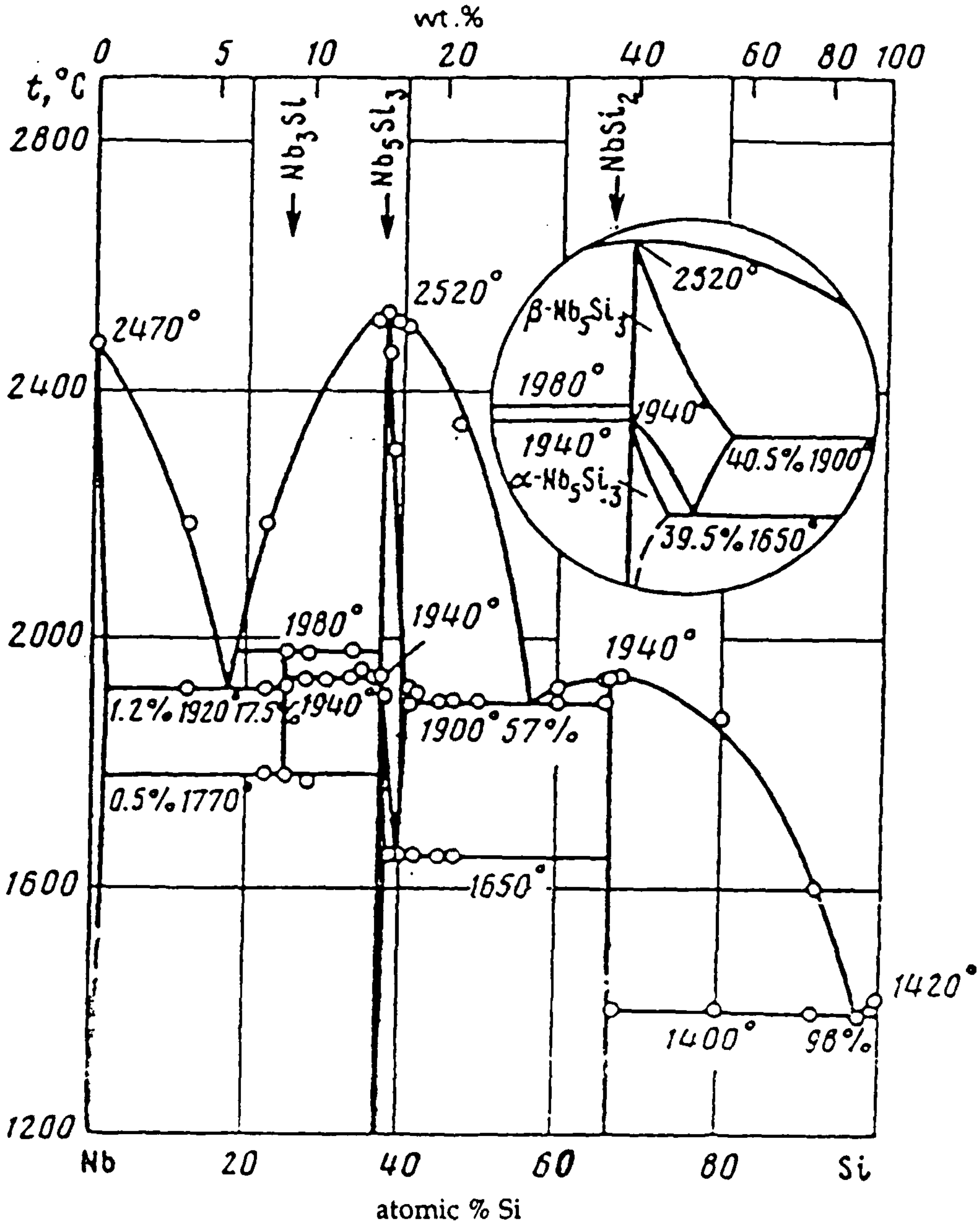

Figure 3: Nb-Si binary, from Reference [7]

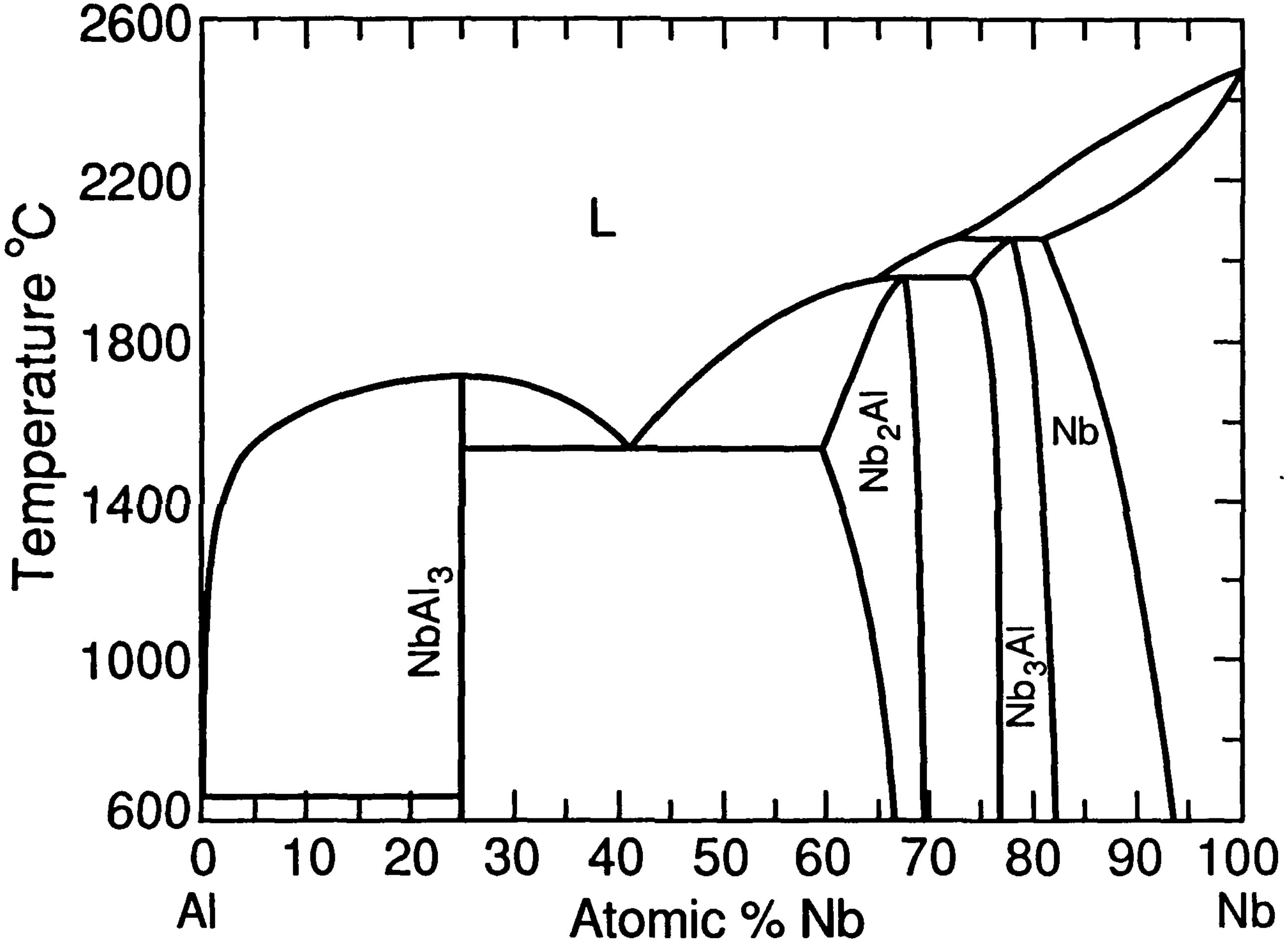

Figure 4: Nb-Al binary, form Reference [13].

D24 A89-183a'9/25

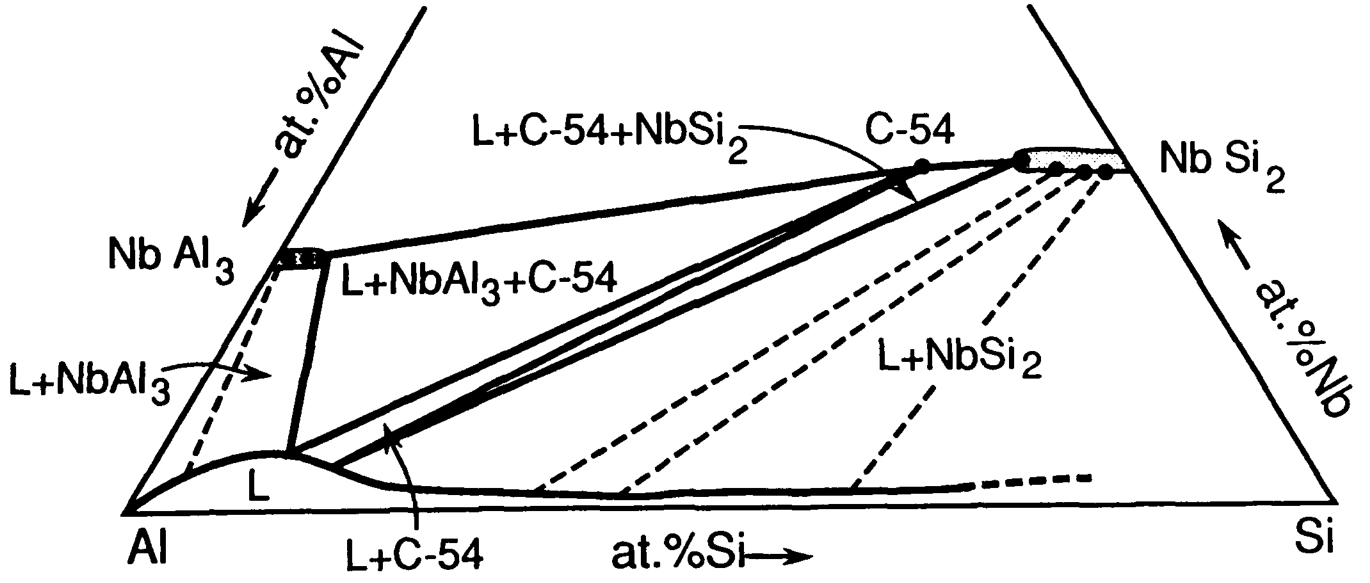
at.%Al
Nb Al$_3$
L+NbAl$_3$
L+C-54+NbSi$_2$
C-54
Nb Si$_2$
L+NbAl$_3$+C-54
L+NbSi$_2$
at.%Nb
L
Al
L+C-54
at.%Si
Si

Figure 5: 1300°C Isothermal section, from Reference [14].

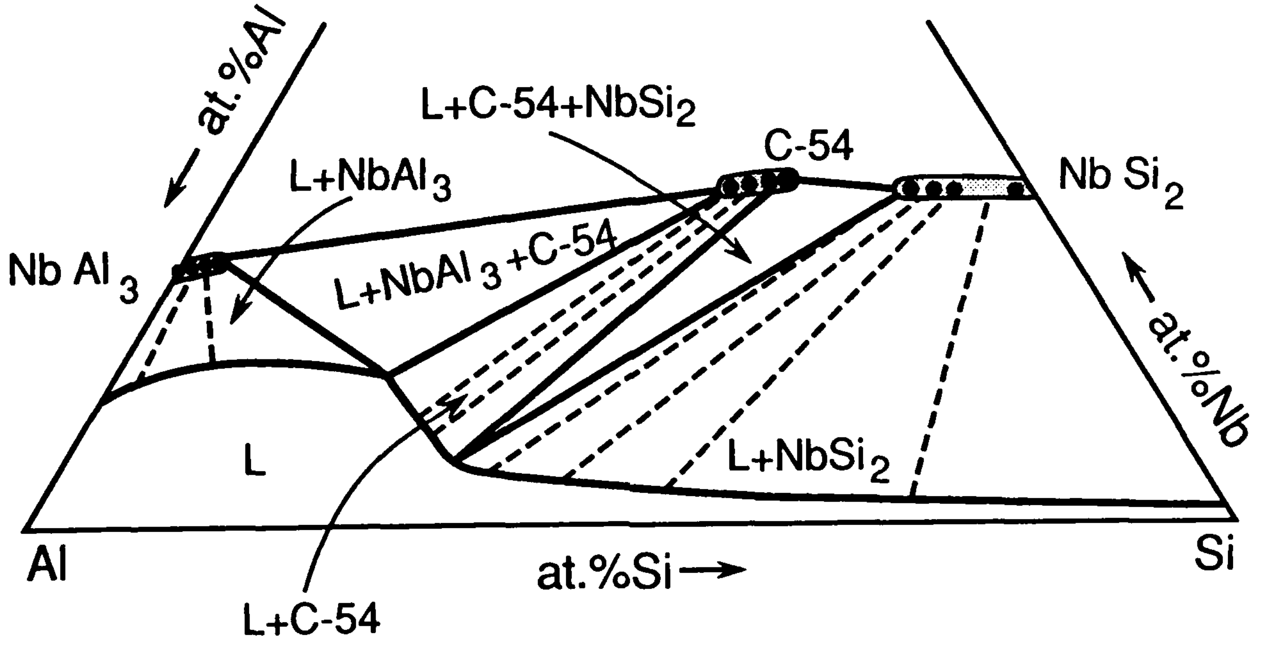
at.%Al
L+NbAl3
L+C-54+NbSi2
C-54
Nb Si2
Nb Al3
L+NbAl3+C-54
at.%Nb
L+NbSi2
L
Al
at.%Si ⟶
Si
L+C-54

Figure 6: 1500°C Isothermal section, from Reference [14].

DWG A89 246'11/16

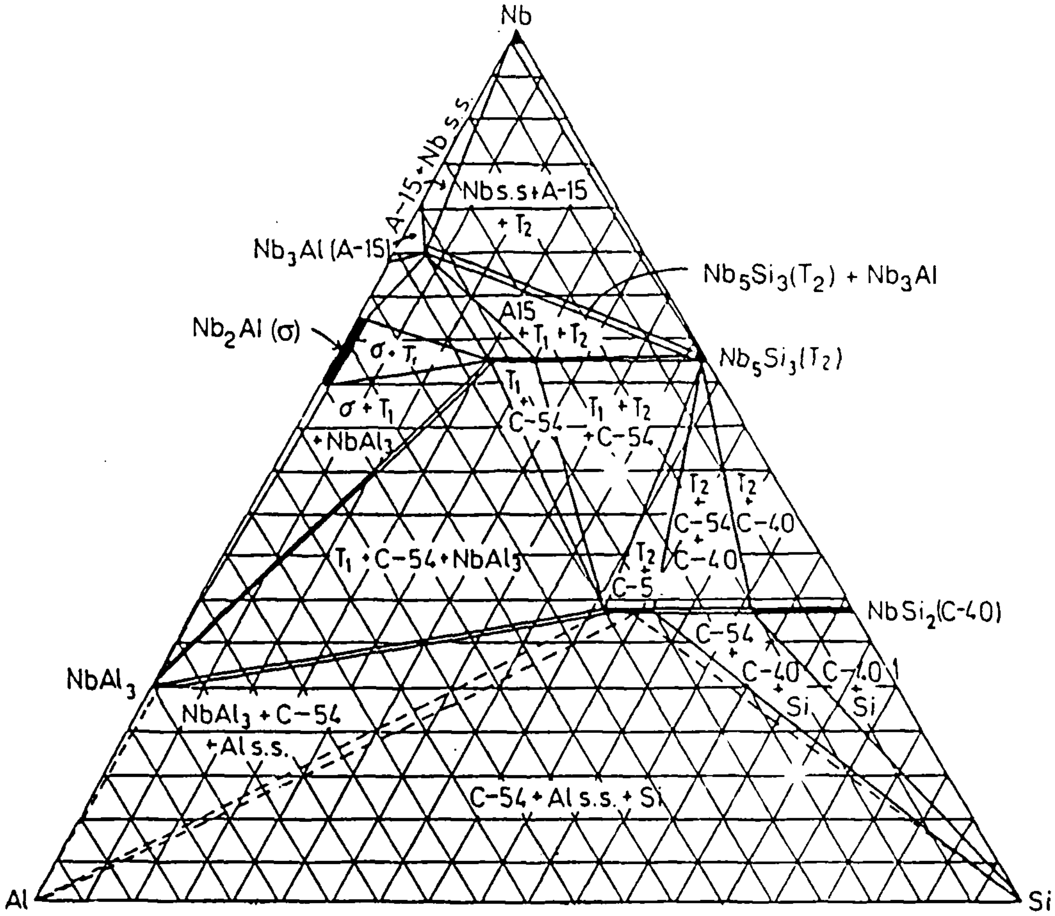
Nb
A-15+Nb s.s.
Nb s.s+A-15
+ T_2
Nb_3Al (A-15)
$Nb_5Si_3(T_2)$ + Nb_3Al
Nb_2Al (σ)
A15
+ T_1 + T_2
σ + T_1
$Nb_5Si_3(T_2)$
σ + T_1
+ $NbAl_3$
T_1
+
C-54
T_1 + T_2
+ C-54
T_2
+
C-54
T_2
+
C-40
T_2
+
C-40
T_1 + C-54 + $NbAl_3$
C-5
$NbSi_2$(C-40)
C-54
+
C-40
+
Si
C-40
+
Si
$NbAl_3$
$NbAl_3$ + C-54
+ Al s.s.
C-54 + Al s.s. + Si
Al
Si

Figure 7: 1400°C Isothermal section, form Reference [16]. Moinor modifications have been made in the Nb_2Al and Nb_3Al phase fields to match the evaluated Nb-Al binary diagram.

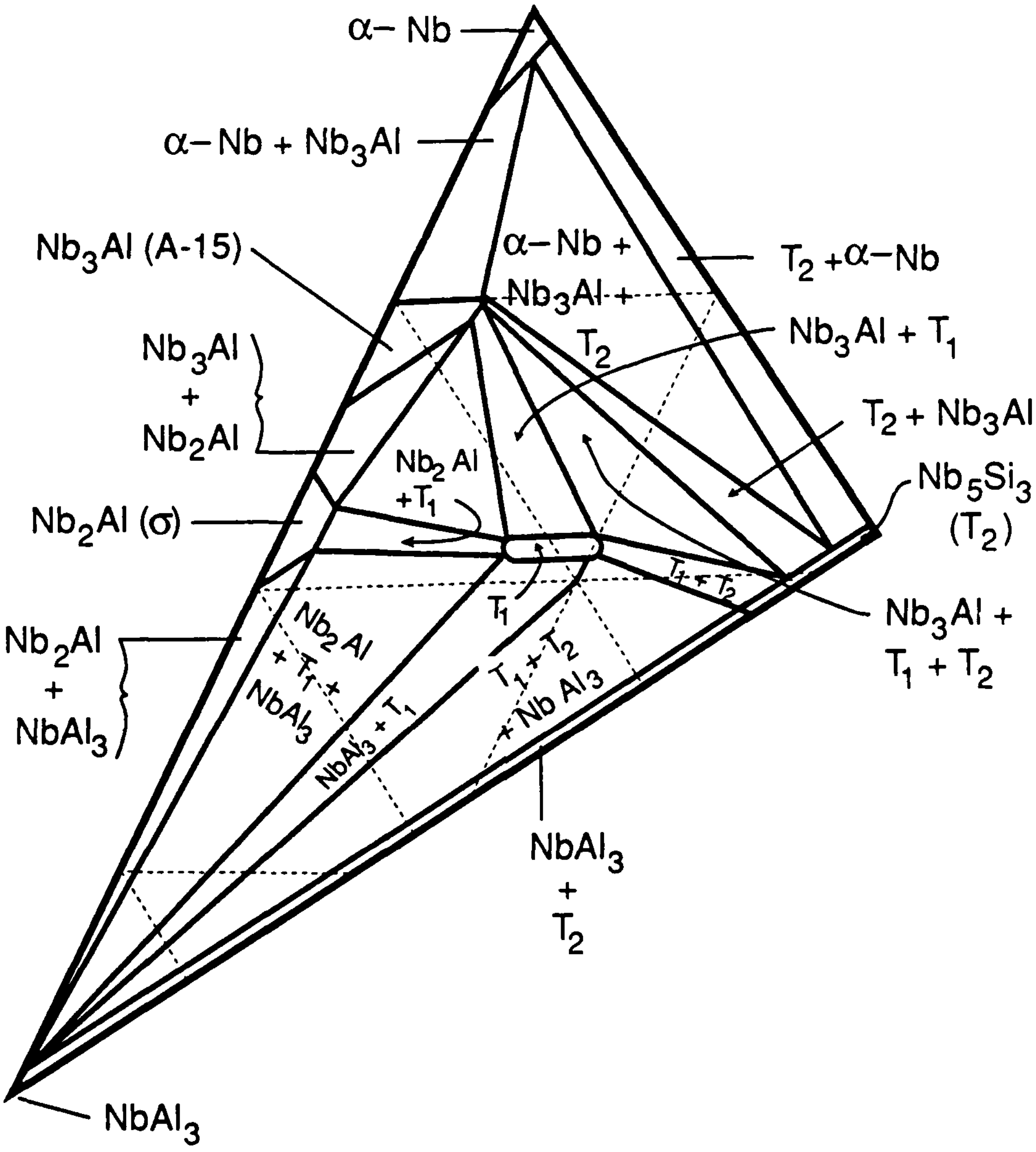
α− Nb
α− Nb + Nb_3Al
Nb_3Al (A-15)
α− Nb + Nb_3Al + T_2
T_2 +α−Nb
Nb_3Al + T_1
Nb_3Al + Nb_2Al
T_2 + Nb_3Al
Nb_2Al + T_1
Nb_5Si_3 (T_2)
Nb_2Al (σ)
T_1 + T_2
T_1
Nb_3Al + T_1 + T_2
Nb_2Al + $NbAl_3$
Nb_2Al + T_1 + $NbAl_3$
T_1 + T_2 + $NbAl_3$
$NbAl_3$ + T_1
$NbAl_3$ + T_2
$NbAl_3$

Figure 8: 1500°C Isothermal section, from Reference [15]. Minor modifications have been made to the Nb_2Al and Nb_3Al phase fields to match the evaluated Nb-Al binary diagram.

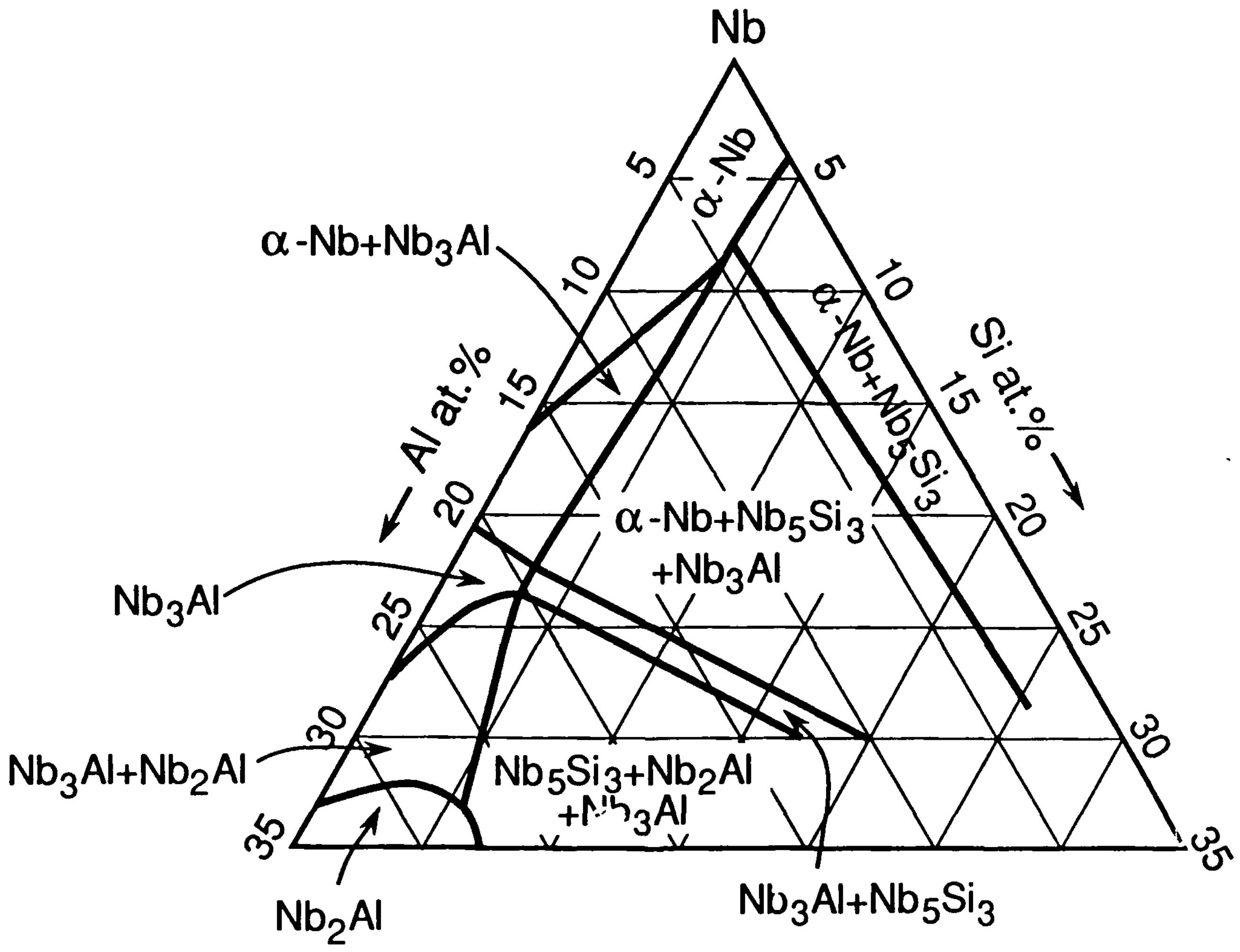
Nb
α-Nb
α-Nb+Nb$_3$Al
α-Nb+Nb$_5$Si$_3$
α-Nb+Nb$_5$Si$_3$
+Nb$_3$Al
Al at.%
Si at.%
5
10
15
20
25
30
35
Nb$_3$Al
Nb$_3$Al+Nb$_2$Al
Nb$_5$Si$_3$+Nb$_2$Al
+Nb$_3$Al
Nb$_2$Al
Nb$_3$Al+Nb$_5$Si$_3$

Figure 9: 1700°C Isothermal section, from Reference [18].

Figure 13a: Reaction Flow Chart for the Nb-Si-Al System

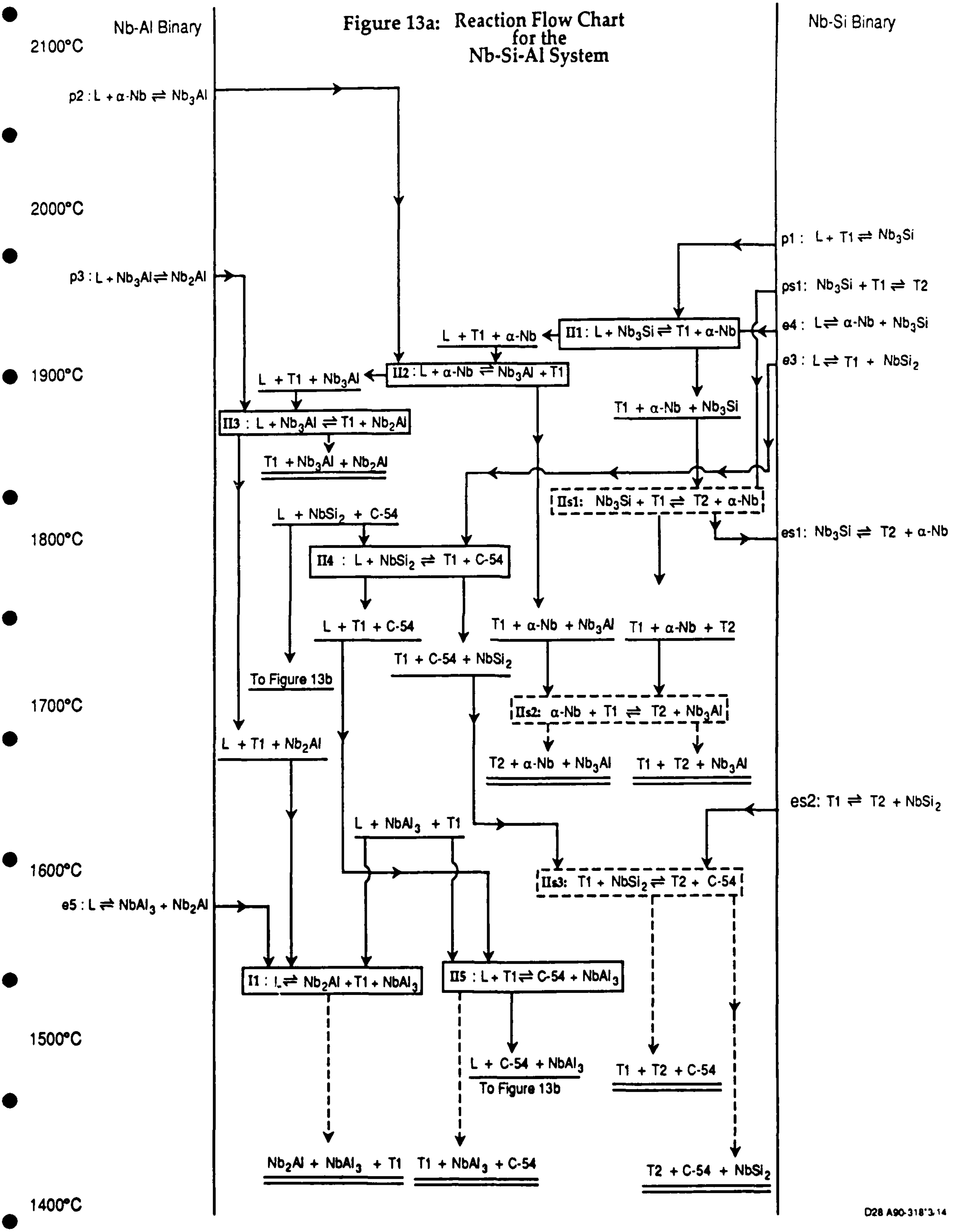
Nb-Al Binary
Nb-Si Binary
2100°C
2000°C
1900°C
1800°C
1700°C
1600°C
1500°C
1400°C
p2 : L + α-Nb ⇌ Nb3Al
p3 : L + Nb3Al ⇌ Nb2Al
e5 : L ⇌ NbAl3 + Nb2Al
p1 : L + T1 ⇌ Nb3Si
ps1: Nb3Si + T1 ⇌ T2
e4 : L ⇌ α-Nb + Nb3Si
e3 : L ⇌ T1 + NbSi2
es1: Nb3Si ⇌ T2 + α-Nb
es2: T1 ⇌ T2 + NbSi2
II1 : L + Nb3Si ⇌ T1 + α-Nb
L + T1 + α-Nb
II2 : L + α-Nb ⇌ Nb3Al + T1
L + T1 + Nb3Al
II3 : L + Nb3Al ⇌ T1 + Nb2Al
T1 + Nb3Al + Nb2Al
T1 + α-Nb + Nb3Si
IIs1: Nb3Si + T1 ⇌ T2 + α-Nb
L + NbSi2 + C-54
II4 : L + NbSi2 ⇌ T1 + C-54
L + T1 + C-54
T1 + C-54 + NbSi2
T1 + α-Nb + Nb3Al
T1 + α-Nb + T2
To Figure 13b
IIs2: α-Nb + T1 ⇌ T2 + Nb3Al
T2 + α-Nb + Nb3Al
T1 + T2 + Nb3Al
L + T1 + Nb2Al
L + NbAl3 + T1
IIs3: T1 + NbSi2 ⇌ T2 + C-54
I1 : L ⇌ Nb2Al + T1 + NbAl3
II5 : L + T1 ⇌ C-54 + NbAl3
L + C-54 + NbAl3
To Figure 13b
T1 + T2 + C-54
Nb2Al + NbAl3 + T1
T1 + NbAl3 + C-54
T2 + C-54 + NbSi2
D28 A90-318'3.14

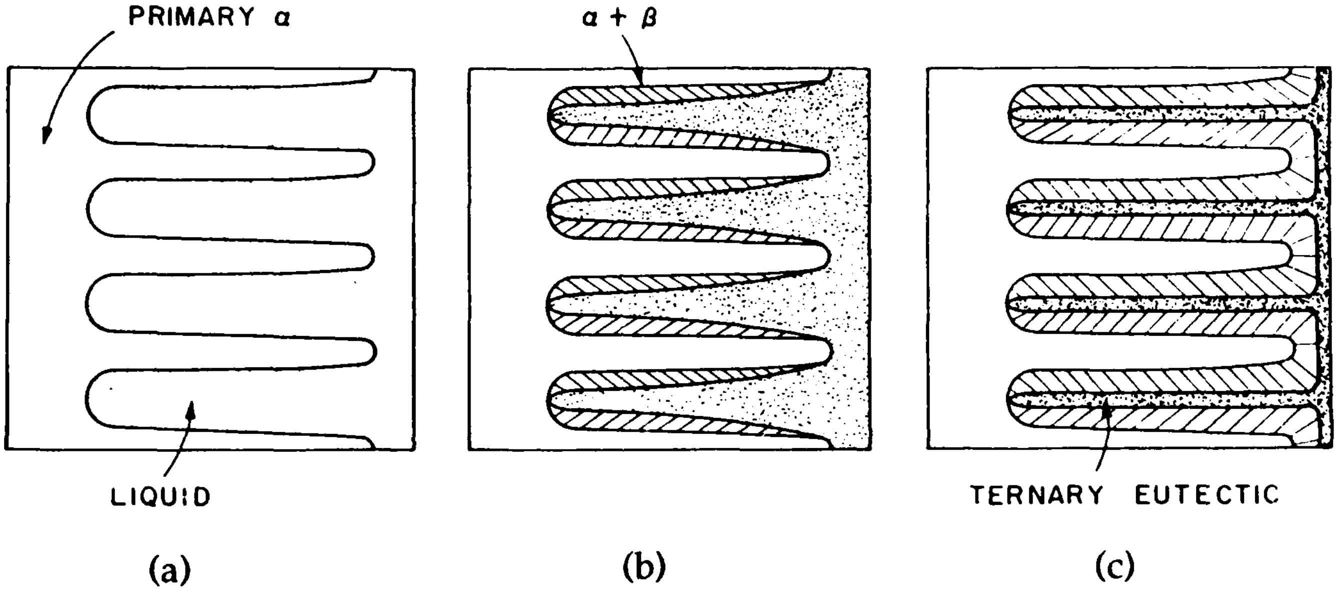
PRIMARY α
α + β
LIQUID
TERNARY EUTECTIC
(a)
(b)
(c)

Figure 12: Schematic illustration of a small "volume element" of a ternary alloy during solidification of
(a) primary phase,
(b) the line of two-fold saturation and
(c) ternary eutectic. From Reference [21].

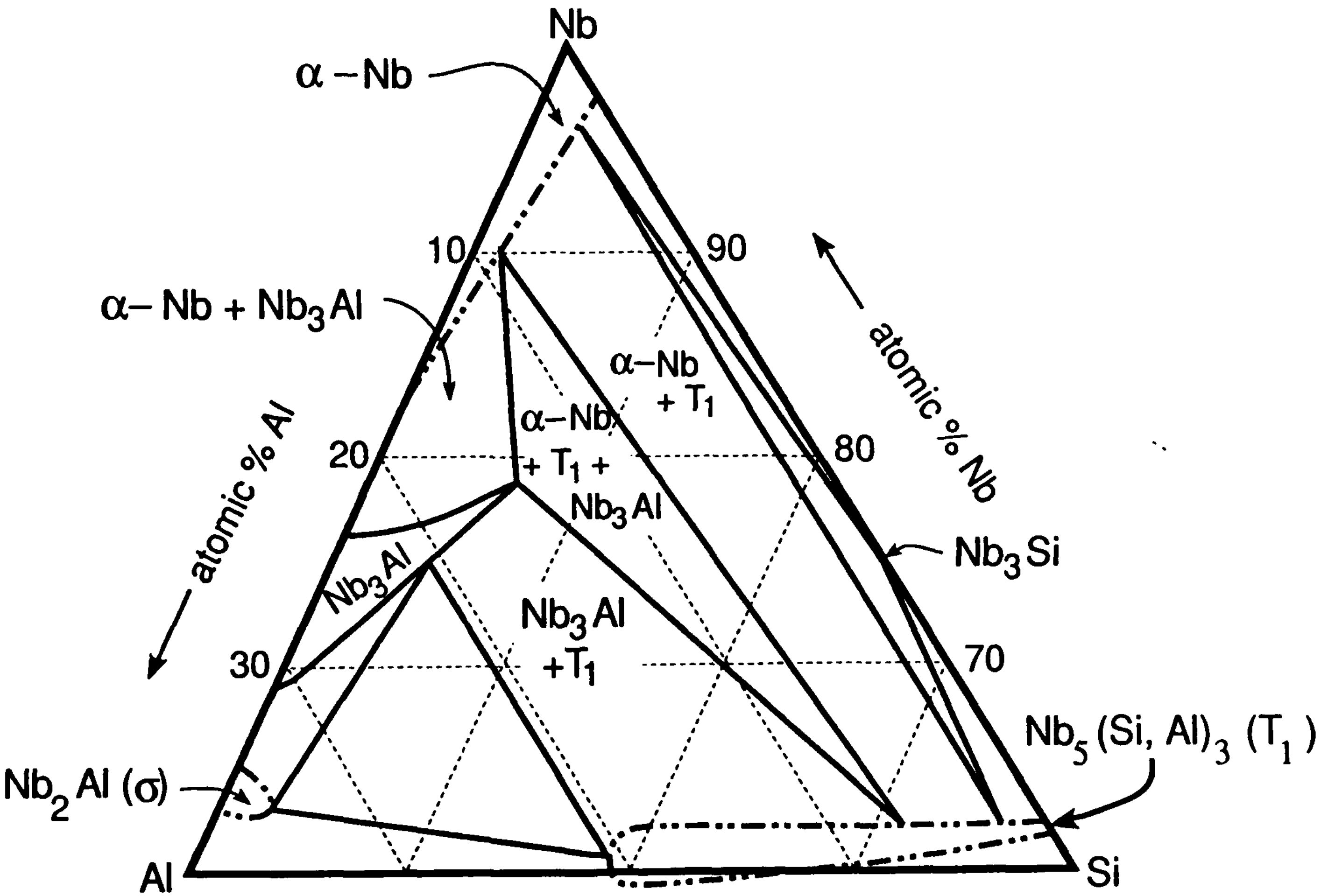
Nb
α −Nb
10
90
α− Nb + Nb_3Al
α−Nb
+ T_1
atomic % Al
atomic % Nb
α−Nb
+ T_1 +
Nb_3Al
20
80
Nb_3Si
Nb_3Al
Nb_3Al
+T_1
30
70
Nb_5(Si, Al$)_3$ (T_1)
Nb_2Al (σ)
Al
Si

Figure 11: 1840°C Isothermal section, from Reference [19]. Minor modifications have been made to Nb_2Al and Nb_3Al phase fields to match evaluated Nb-Al binary diagram.

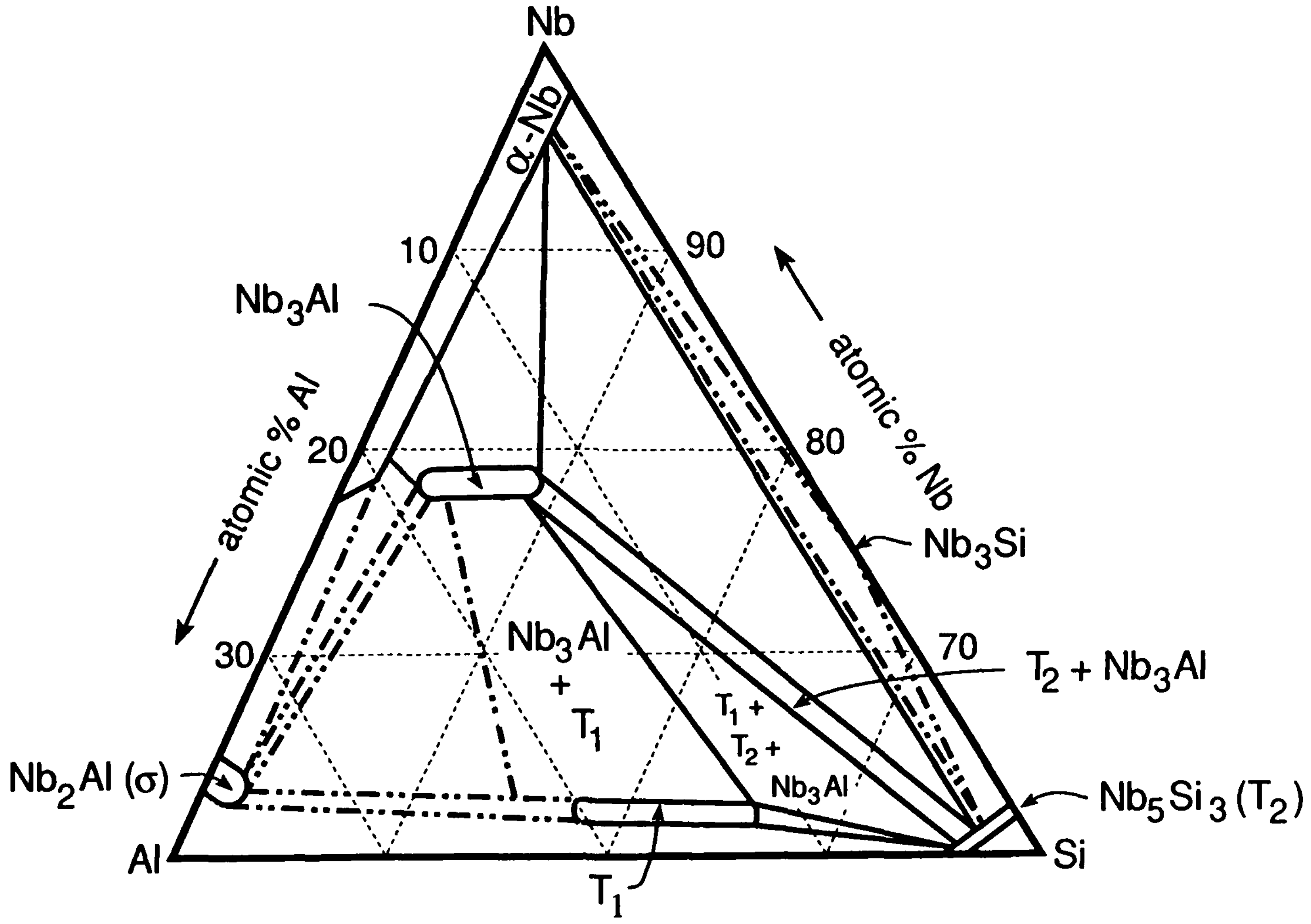
Nb
α-Nb
10
20
30
90
80
70
atomic % Al
atomic % Nb
Nb_3Al
Nb_3Si
$Nb_3Al + T_1$
$T_1 + T_2 + Nb_3Al$
$T_2 + Nb_3Al$
Nb_2Al (σ)
Nb_5Si_3 (T_2)
T_1
Al
Si

Figure 10: 1820°C Isothermal section, from Reference [15].

Figure 13b: Reaction flow chart at lower temperature

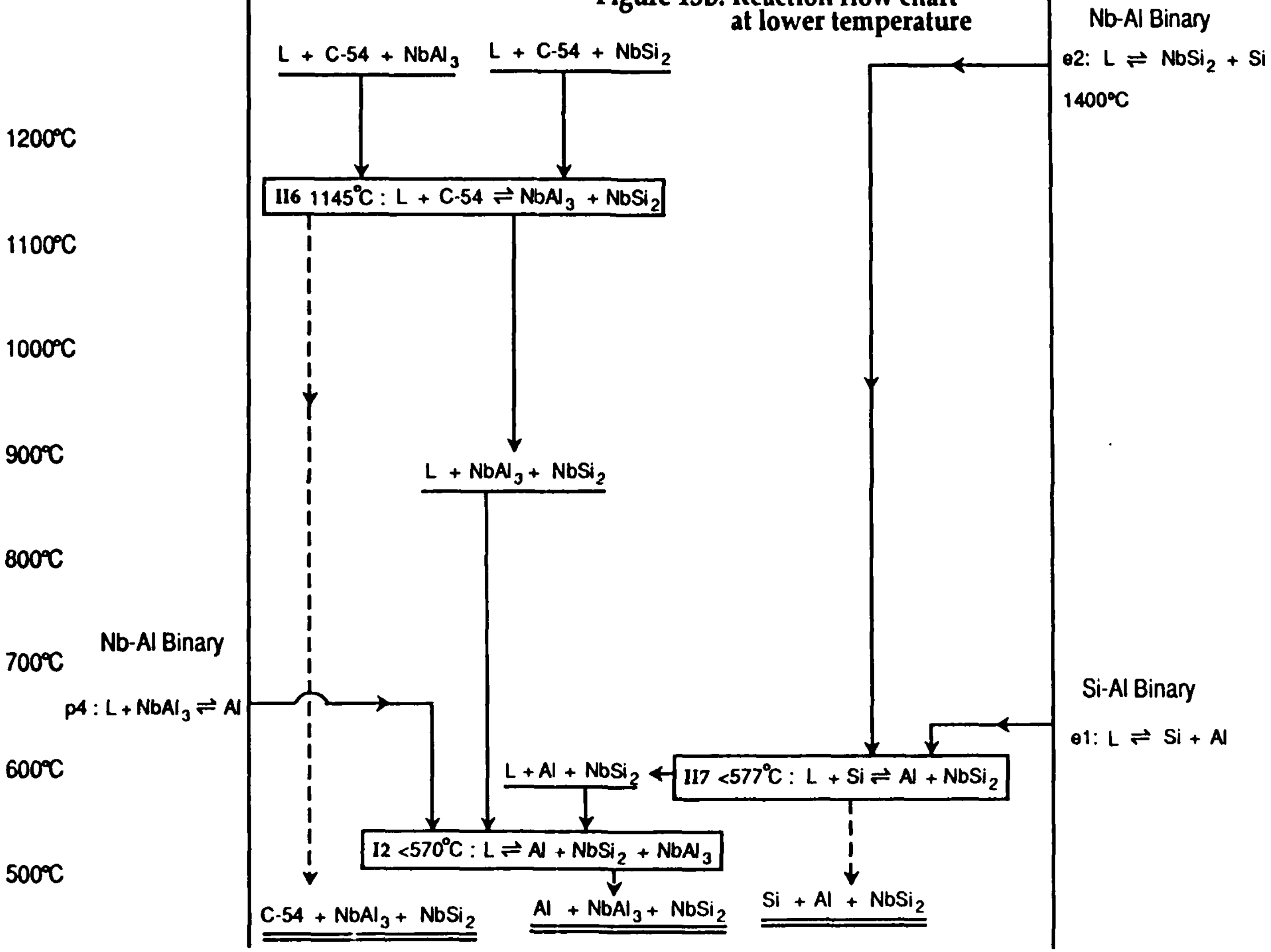
Nb-Al Binary
e2: L ⇌ NbSi2 + Si
1400°C
Si-Al Binary
e1: L ⇌ Si + Al
Nb-Al Binary
p4 : L + NbAl3 ⇌ Al
1200°C
1100°C
1000°C
900°C
800°C
700°C
600°C
500°C
L + C-54 + NbAl3
L + C-54 + NbSi2
II6 1145°C : L + C-54 ⇌ NbAl3 + NbSi2
L + NbAl3 + NbSi2
II7 <577°C : L + Si ⇌ Al + NbSi2
L + Al + NbSi2
I2 <570°C : L ⇌ Al + NbSi2 + NbAl3
C-54 + NbAl3 + NbSi2
Al + NbAl3 + NbSi2
Si + Al + NbSi2

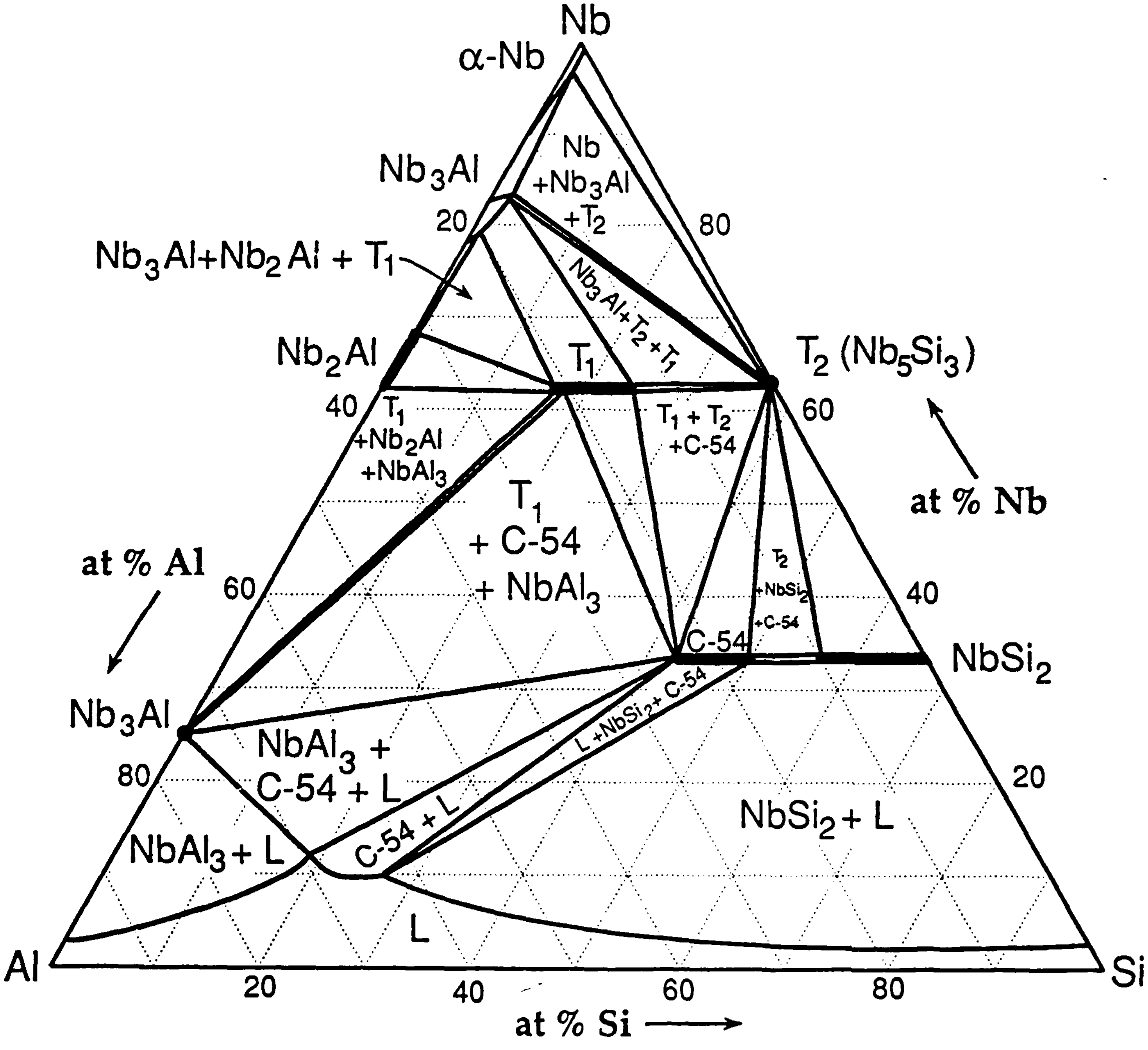
Nb
α-Nb
Nb_3Al
Nb
$+Nb_3Al$
$+T_2$
20
80
$Nb_3Al+Nb_2Al + T_1$
$Nb_3Al+T_2+T_1$
Nb_2Al
T_1
T_2 (Nb_5Si_3)
40
60
T_1
$+Nb_2Al$
$+NbAl_3$
$T_1 + T_2$
+C-54
at % Nb
T_1
+ C-54
$+ NbAl_3$
at % Al
60
T_2
$+NbSi_2$
+C-54
40
C-54
$NbSi_2$
Nb_3Al
$L +NbSi_2+ C\text{-}54$
$NbAl_3$ +
C-54 + L
80
20
C-54 + L
$NbSi_2$+ L
$NbAl_3$+ L
L
Al
Si
20
40
60
80
at % Si

Figure 14. An estimate of the 1400°C Isothermal section

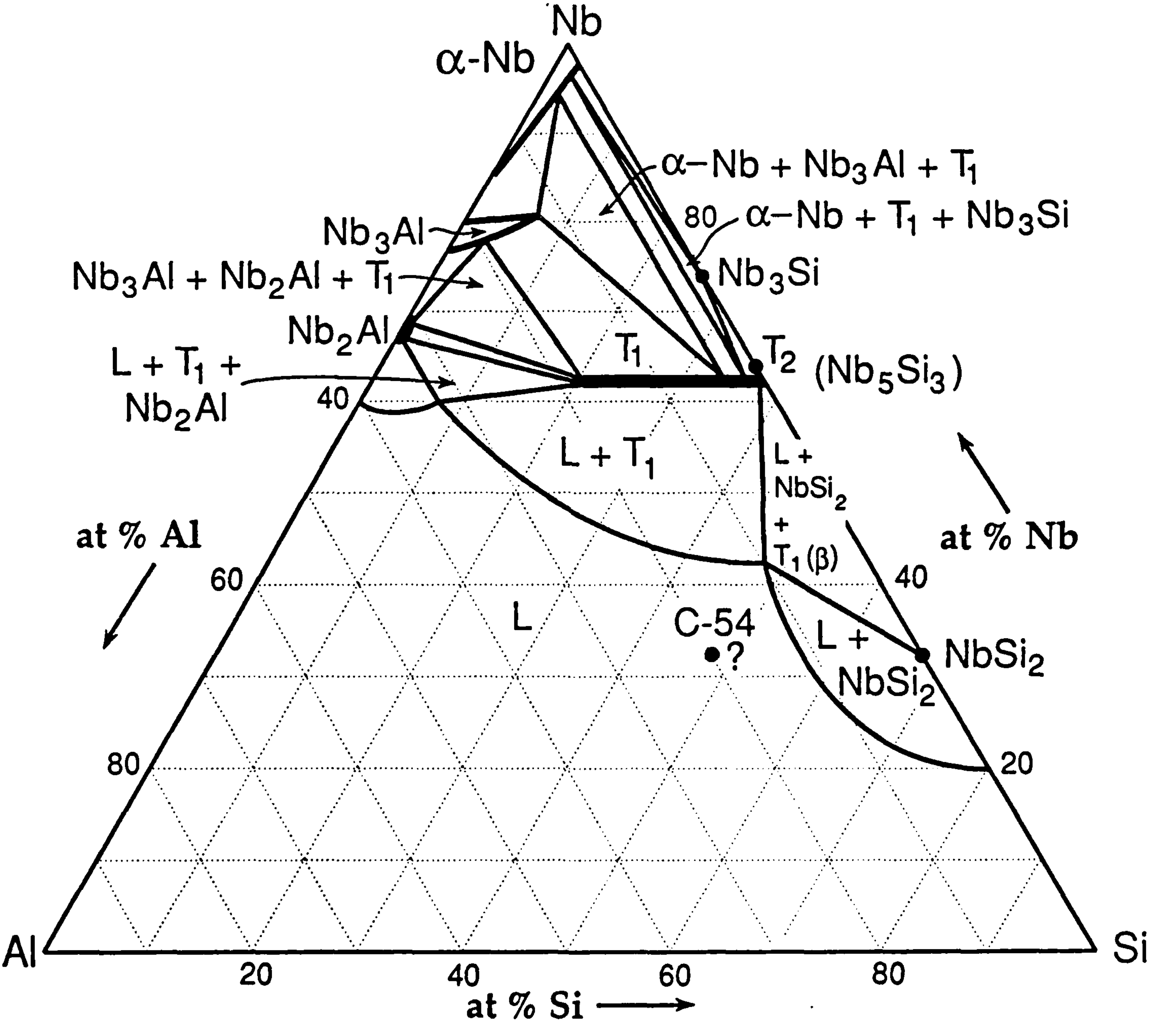

Nb
α-Nb
α–Nb + Nb3Al + T1
80
α–Nb + T1 + Nb3Si
Nb3Al
Nb3Si
Nb3Al + Nb2Al + T1
Nb2Al
T1
T2 (Nb5Si3)
L + T1 +
Nb2Al
40
L + T1
L +
NbSi2
+
T1 (β)
at % Al
at % Nb
60
40
L
C-54
?
L +
NbSi2
NbSi2
80
20
Al
Si
20
40
60
80
at % Si

Figure 15. An estimate of the 1850°C Isothermal section

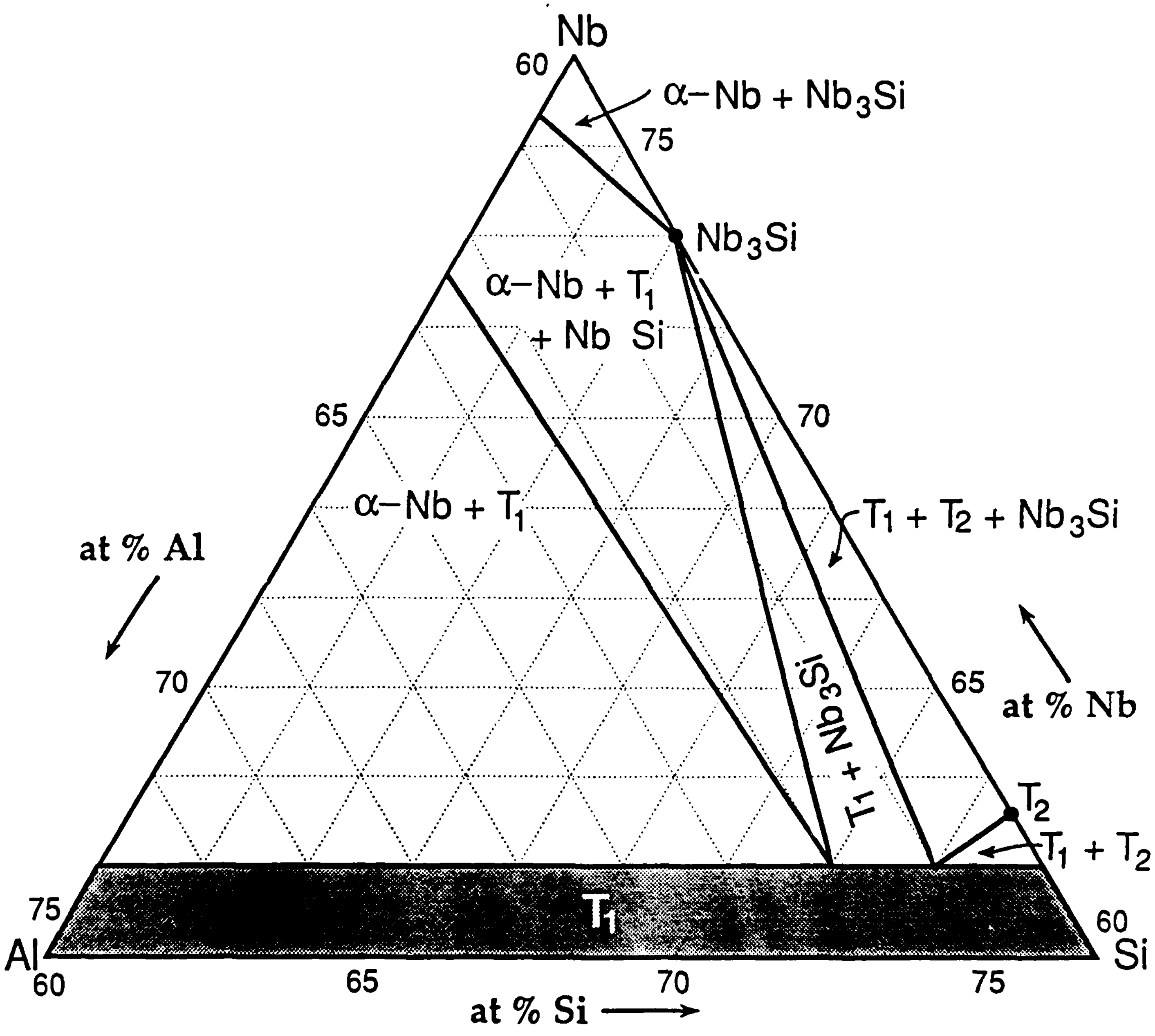
Nb
60
α−Nb + Nb$_3$Si
75
Nb$_3$Si
α−Nb + T$_1$
+ Nb Si
65
70
α−Nb + T$_1$
T$_1$ + T$_2$ + Nb$_3$Si
at % Al
70
T$_1$ + Nb$_3$Si
65
at % Nb
T$_2$
T$_1$ + T$_2$
75
T$_1$
60
Al
Si
60
65
70
75
at % Si

Figure 16. An estimate of the phase fields that may exist in the temperature range 1940°C to ~1820°C.

Figure 17 : Liquidus Projection for Nb-Si-Al System

* All Temperatures in °C

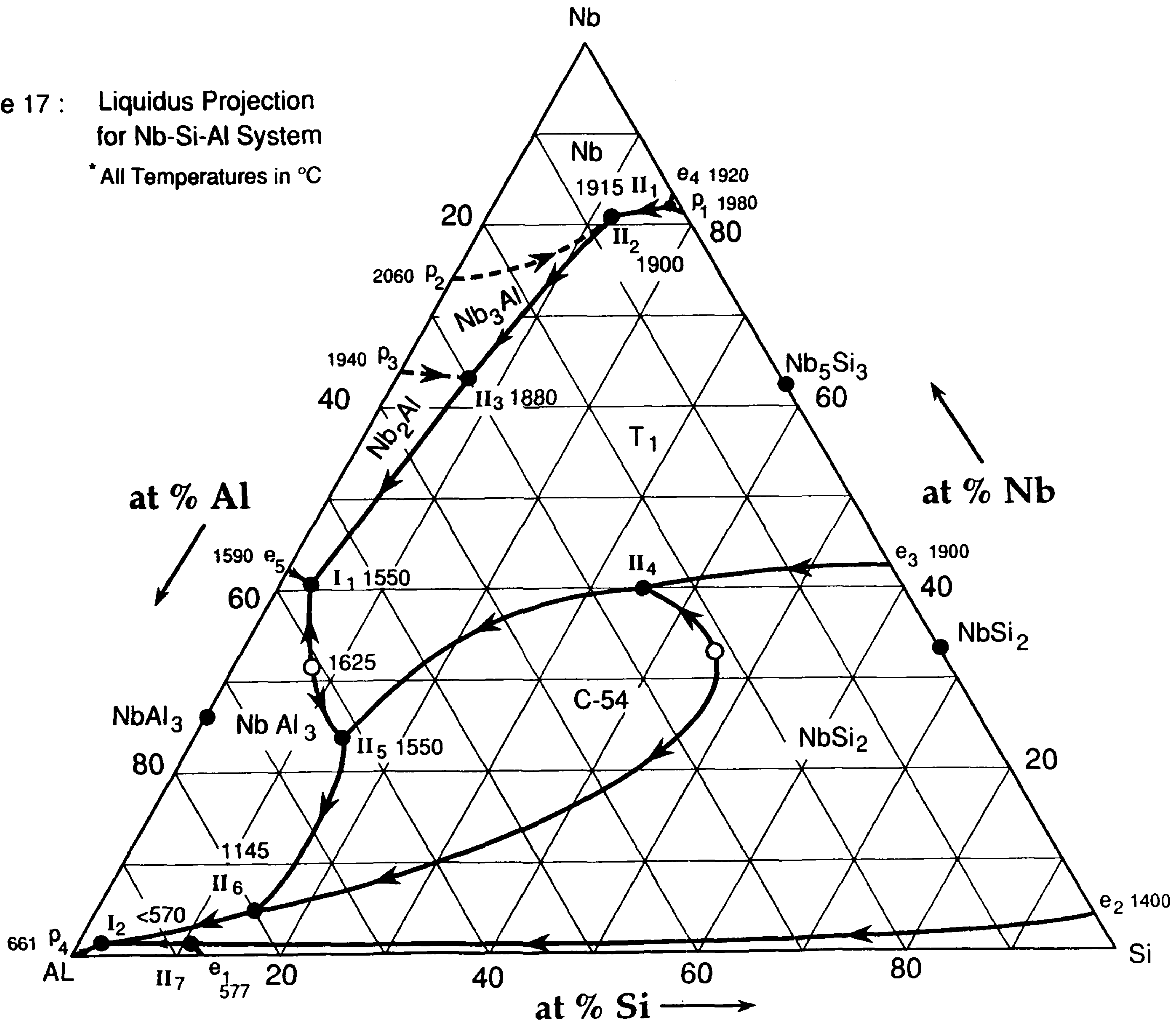
Nb
Nb
1915 II₁
e₄ 1920
p₁ 1980
II₂
1900
2060 p₂
Nb₃Al
1940 p₃
II₃ 1880
Nb₂Al
T₁
Nb₅Si₃
at % Al
at % Nb
1590 e₅
I₁ 1550
II₄
e₃ 1900
1625
NbSi₂
C-54
NbAl₃
Nb Al₃
II₅ 1550
NbSi₂
1145
II₆
I₂
<570
e₂ 1400
661 p₄
AL
II₇
e₁ 577
Si
20
40
60
80
20
40
60
80
20
40
60
80
at % Si

D24 A89-173*9/18b810

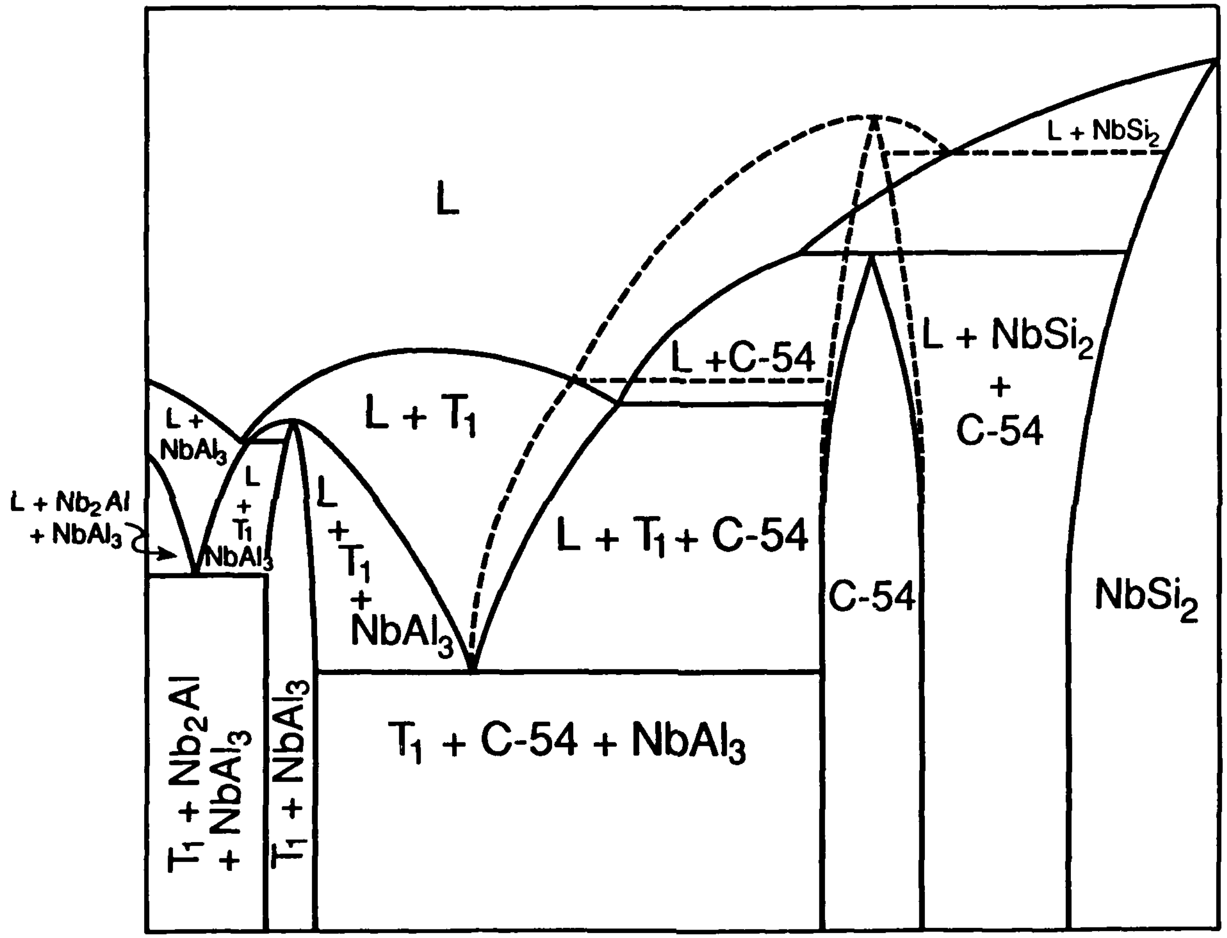
L
L + NbSi$_2$
L +C-54
L + NbSi$_2$ + C-54
L + T$_1$
L + NbAl$_3$
L + Nb$_2$Al + NbAl$_3$
L + T$_1$ NbAl$_3$
L + T$_1$ + NbAl$_3$
L + T$_1$ + C-54
C-54
NbSi$_2$
T$_1$ + Nb$_2$Al + NbAl$_3$
T$_1$ + NbAl$_3$
T$_1$ + C-54 + NbAl$_3$

Figure 18: Isopleth along the 33at%Nb isoconcentration line.

Figure 19 : Group 1 and 2 alloys.

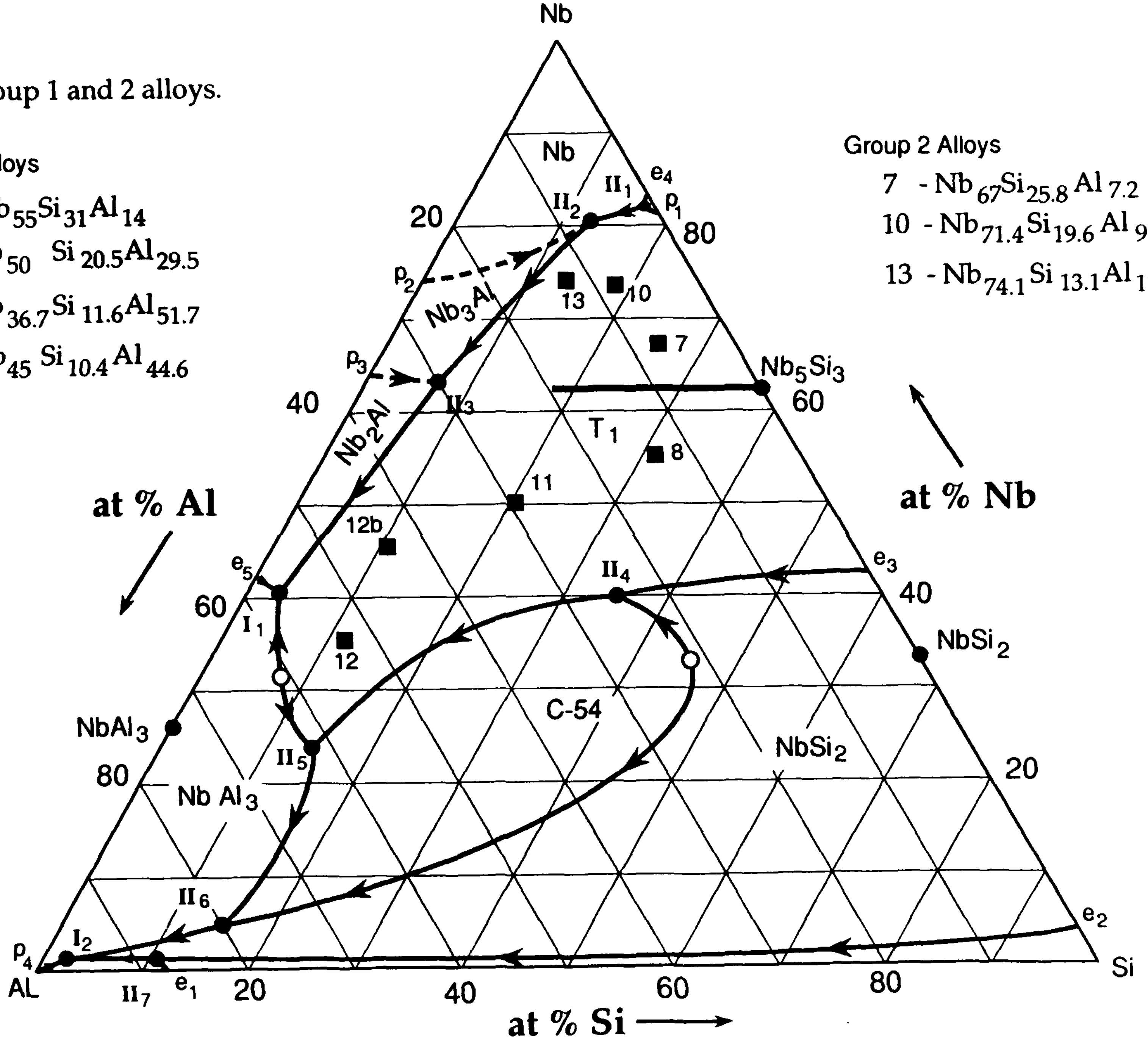
Nb
Nb
II_1
e_4
p_1
II_2
20
80
p_2
13
10
Nb_3Al
7
p_3
Nb_5Si_3
40
II_3
60
T_1
Nb_2Al
8
11
at % Al
at % Nb
12b
e_5
II_4
e_3
60
I_1
40
12
$NbSi_2$
C-54
$NbAl_3$
$NbSi_2$
II_5
80
$Nb Al_3$
20
II_6
e_2
p_4
I_2
Si
AL
II_7
e_1
20
40
60
80
at % Si

Group 1 Alloys

8 - $Nb_{55}Si_{31}Al_{14}$

11 - Nb_{50} $Si_{20.5}Al_{29.5}$

12 - $Nb_{36.7}Si_{11.6}Al_{51.7}$

12b- Nb_{45} $Si_{10.4}Al_{44.6}$

Group 2 Alloys

7 - $Nb_{67}Si_{25.8}Al_{7.2}$

10 - $Nb_{71.4}Si_{19.6}Al_{9}$

13 - $Nb_{74.1}Si_{13.1}Al_{12.8}$

D24 A89-173'9/18b810

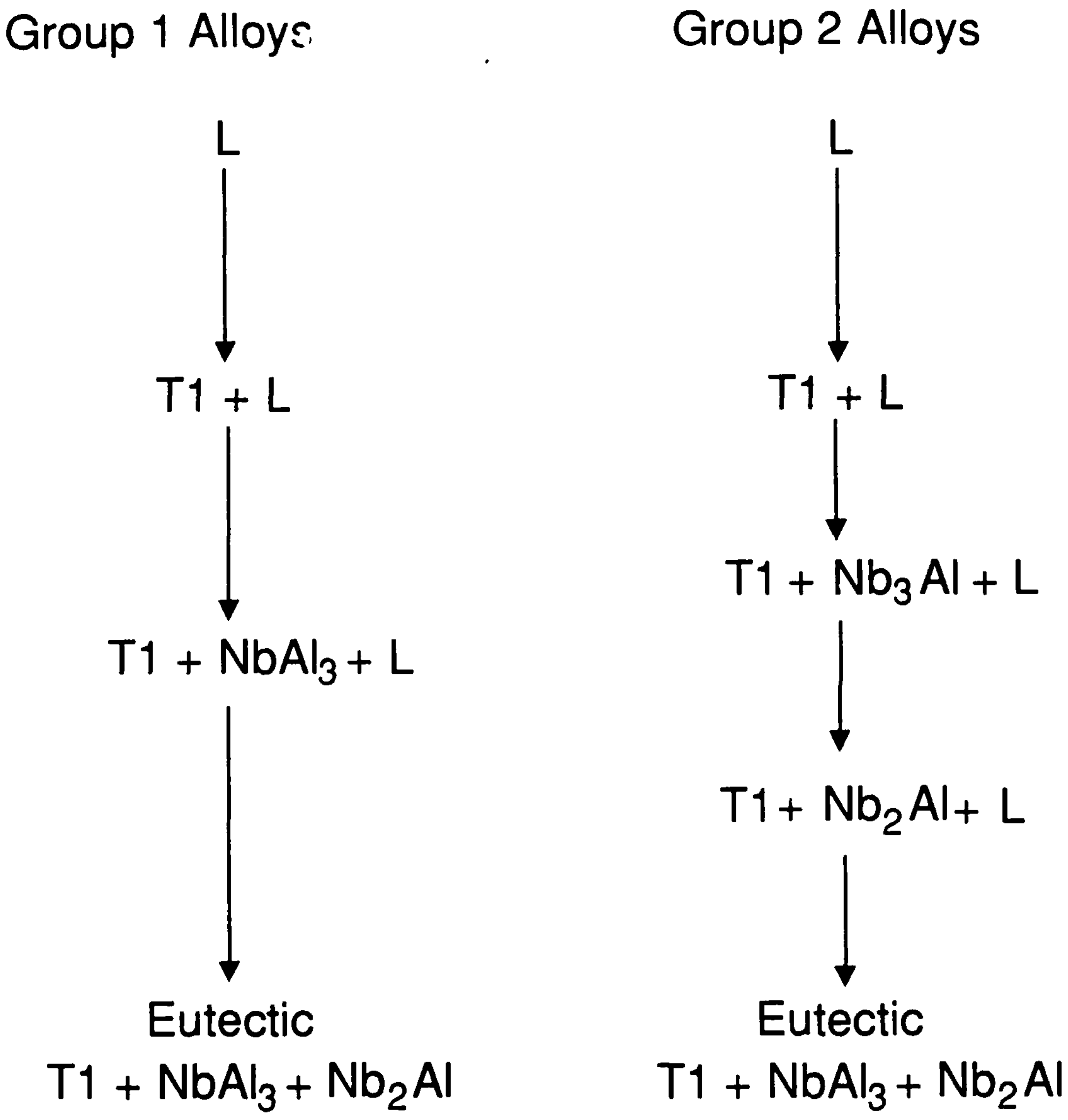
Group 1 Alloys
Group 2 Alloys
L
L
T1 + L
T1 + L
T1 + Nb3Al + L
T1 + NbAl3 + L
T1 + Nb2Al + L
Eutectic
T1 + NbAl3 + Nb2Al
Eutectic
T1 + NbAl3 + Nb2Al

Figure 20 : Solidification phase sequence for alloy groups 1 and 2.

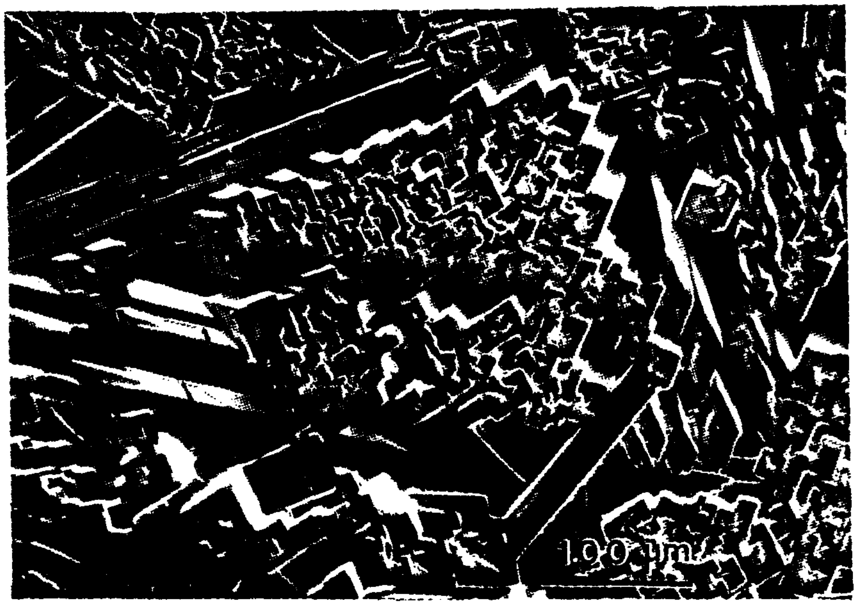

Figure 21:
SEM photomicrograph of a typical primary dendritic structure, taken in a shrinkage cavity of an arc-melted button of alloy 8.

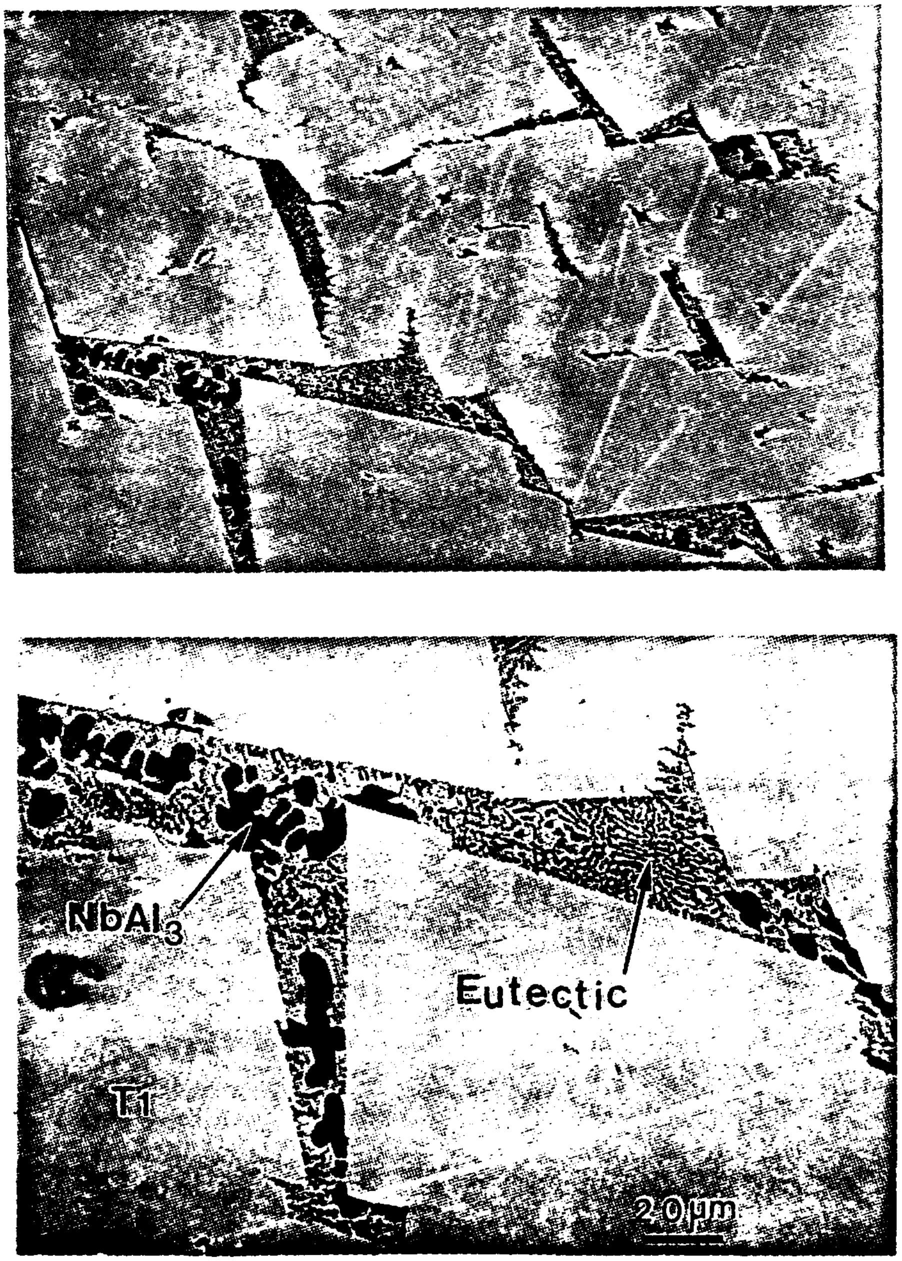
NbAl3
Eutectic
T1
20 µm

Figure 22: Alloy 8, $Nb_{55}Si_{31}Al_{14}$

T1 - $Nb_{60.3}Si_{36.8}Al_{2.9}$
$NbAl_3$ - $Nb_{24.5}Si_{.5}Al_{75}$
Eutectic* - $Nb_{40}Si_2Al_{58}$
*($NbAl_3$ + Nb_2Al + T1)

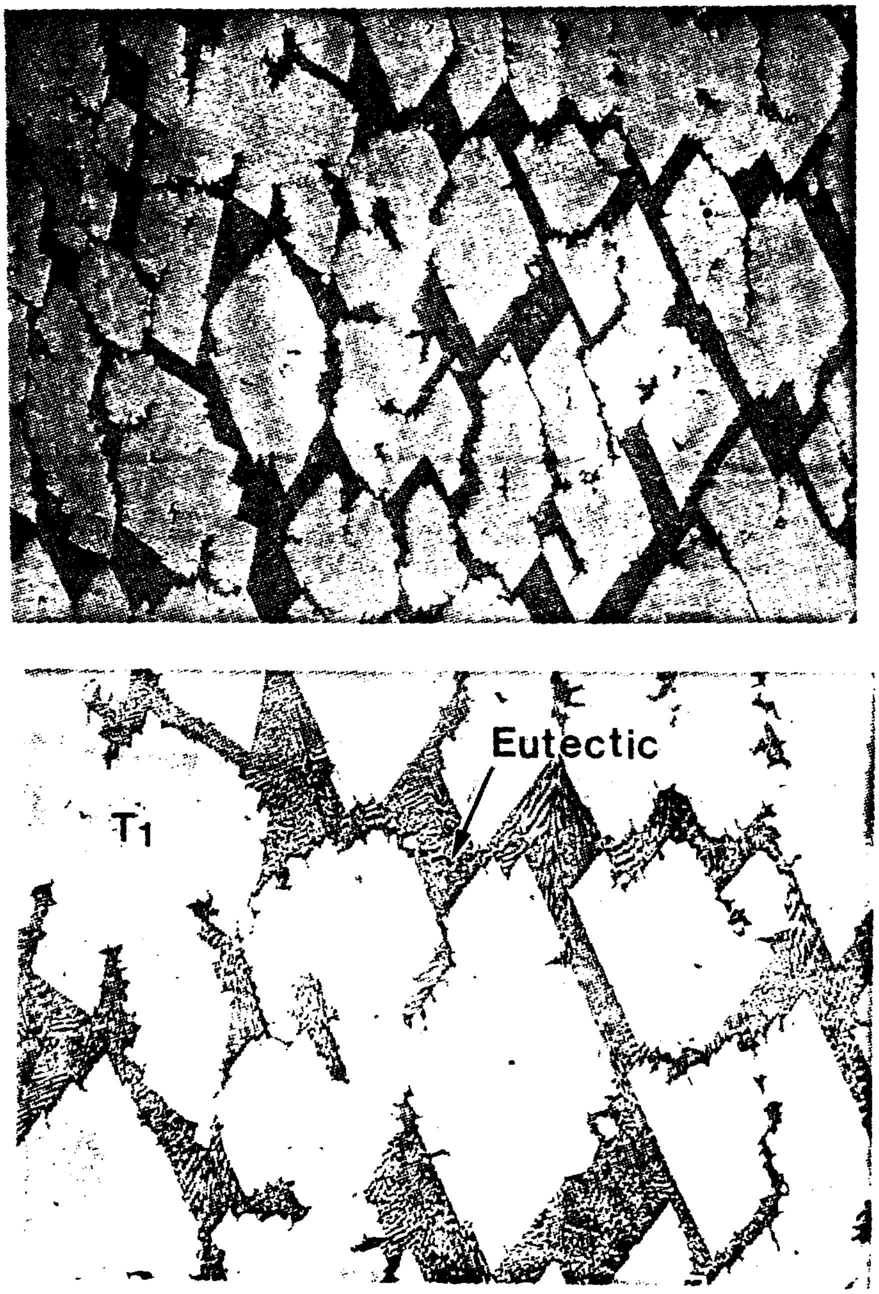
Eutectic
T1

Figure 23: Alloy 11, $Nb_{50}Si_{20.5}Al_{29.5}$

T1 - $Nb_{57.9}Si_{34.6}Al_{7.5}$
Eutectic*- $Nb_{40}Si_2Al_{58}$
*($NbAl_3 + Nb_2Al +$ T1)

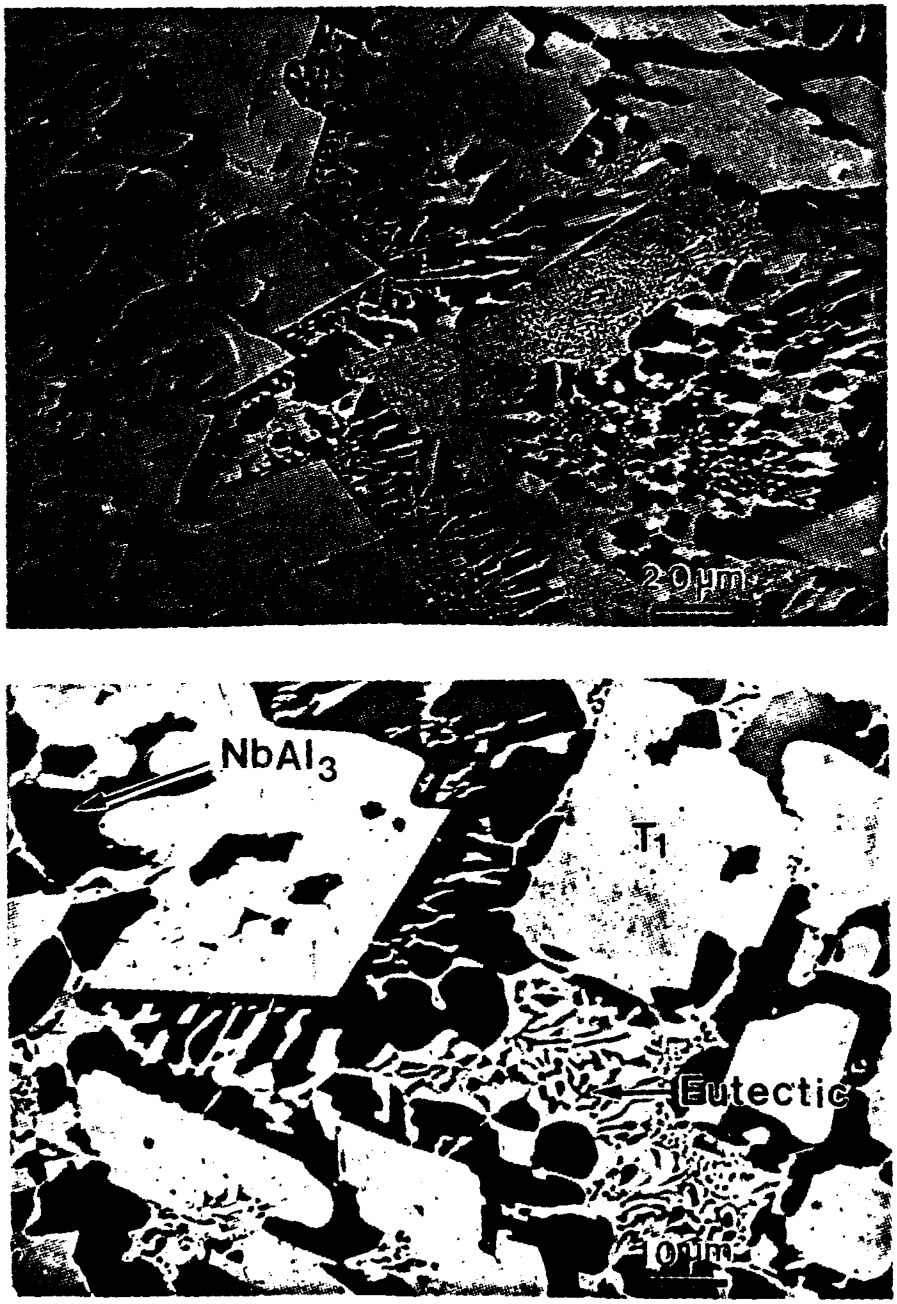
20μm
NbAl3
T1
Eutectic
10μm

Figure 24: Alloy 12, $Nb_{36.7}Si_{11.6}Al_{51.7}$

T1 - $Nb_{57.6}Si_{32.4}Al_{10}$
$NbAl_3$ - $Nb_{22.6}Si_{0.1}Al_{77.3}$
Eutectic* - $Nb_{40.5}Si_{2.2}Al_{57.3}$
*($NbAl_3$ + Nb_2Al + T1)

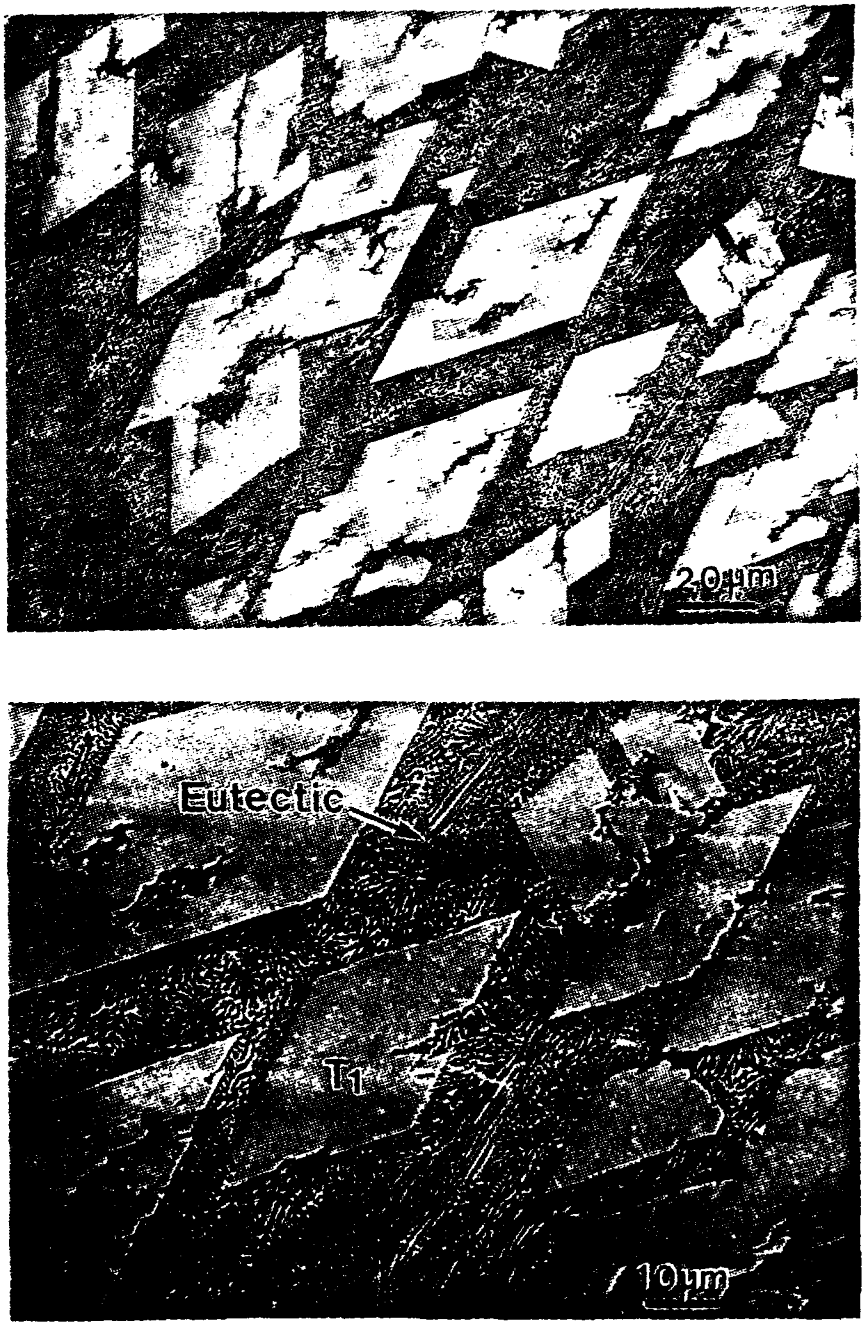
20 µm
Eutectic
T1
10 µm

Figure 25: Alloy 12b, $Nb_{45}Si_{10.4}Al_{44.6}$

T1 - $Nb_{60.43}Si_{24.6}Al_{14.97}$
Eutectic* - $Nb_{40}Si_{2}Al_{58}$
*($NbAl_3 + Nb_2Al$ + T1)

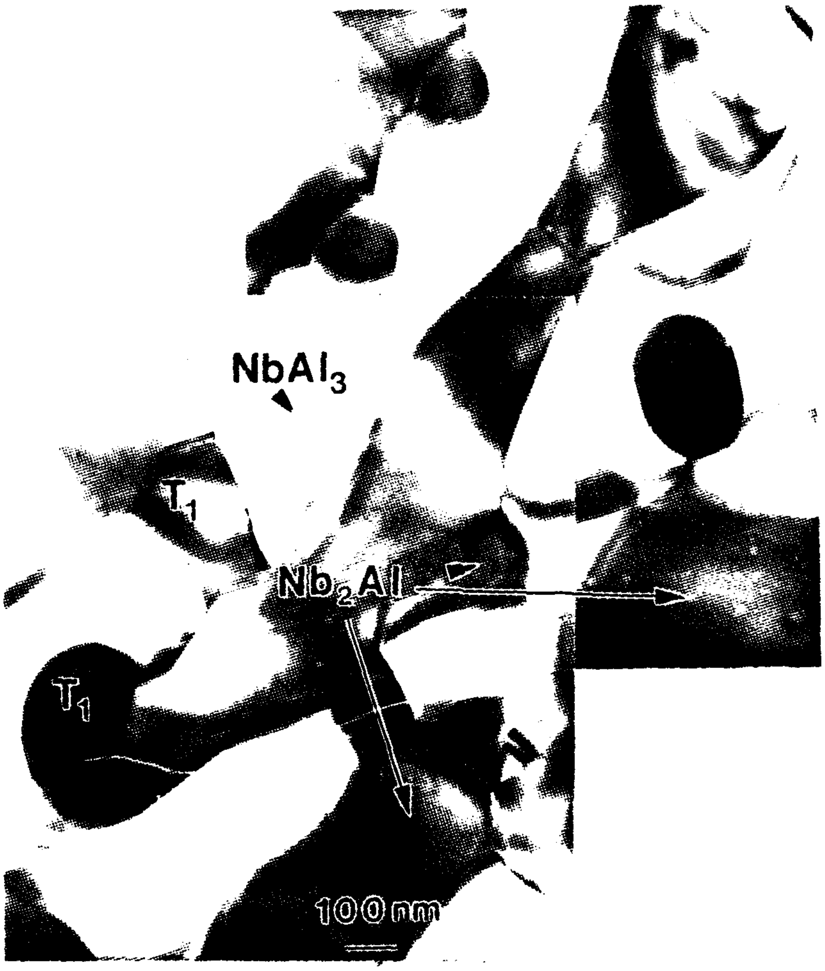

NbAl3
T1
Nb2Al
T1
100 nm

Figure 26: TEM photomicrograph of the eutectic region in Alloy 12b, $Nb_{45}\,Si_{10.4}\,Al_{44.6}$

T1 - $Nb_{60.7}\,Si_{18.8}\,Al_{20.5}$
$NbAl_3$ - $Nb_{25.2}\,Si_{0.3}\,Al_{74.5}$
Nb_2Al- $Nb_{64.2}\,Si_{1.5}\,Al_{34.3}$

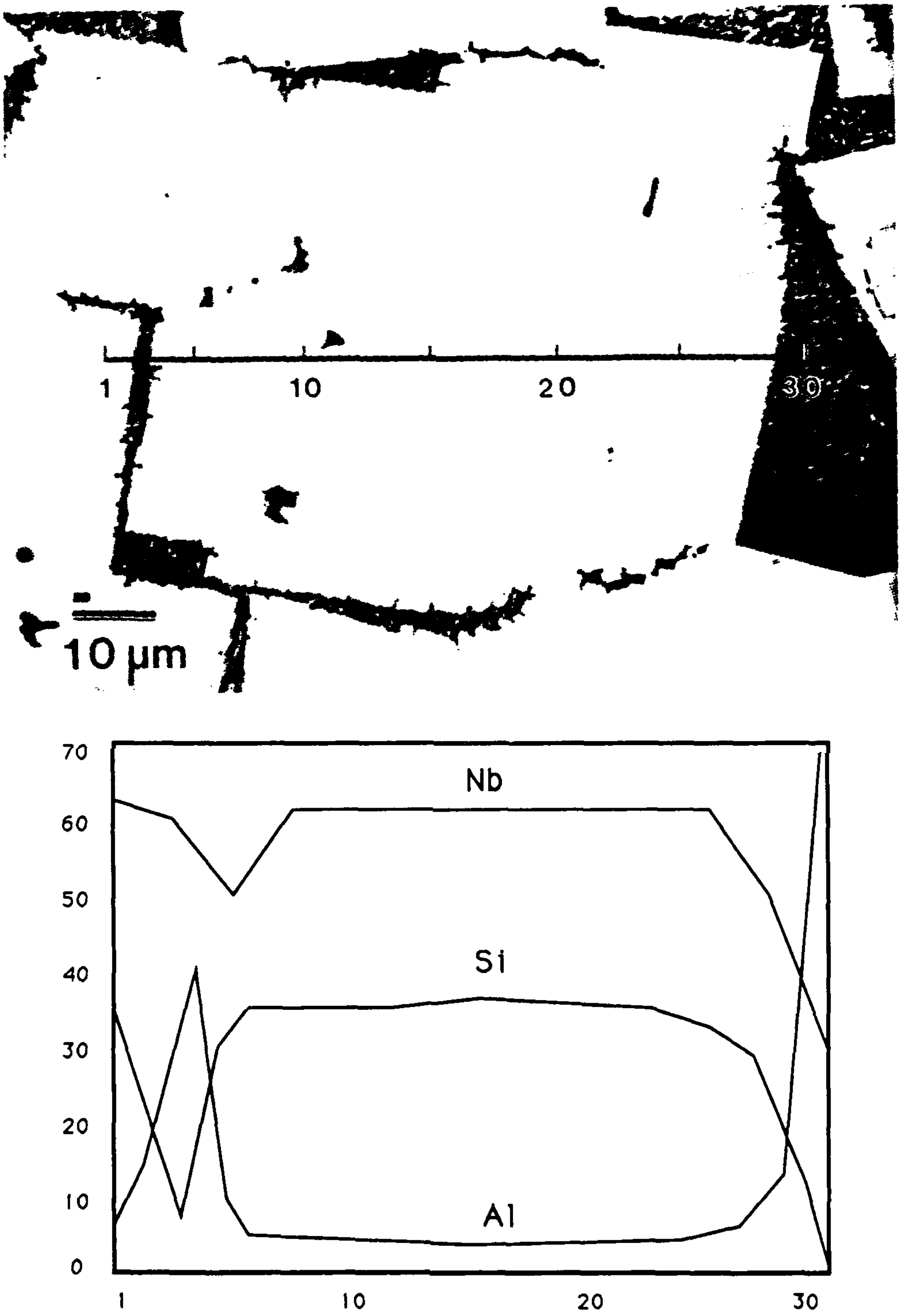

Figure 27: SEM photomicrograph and composition line scan across a dendrite arm in Alloy 8, $Nb_{55}Si_{31}Al_{14}$

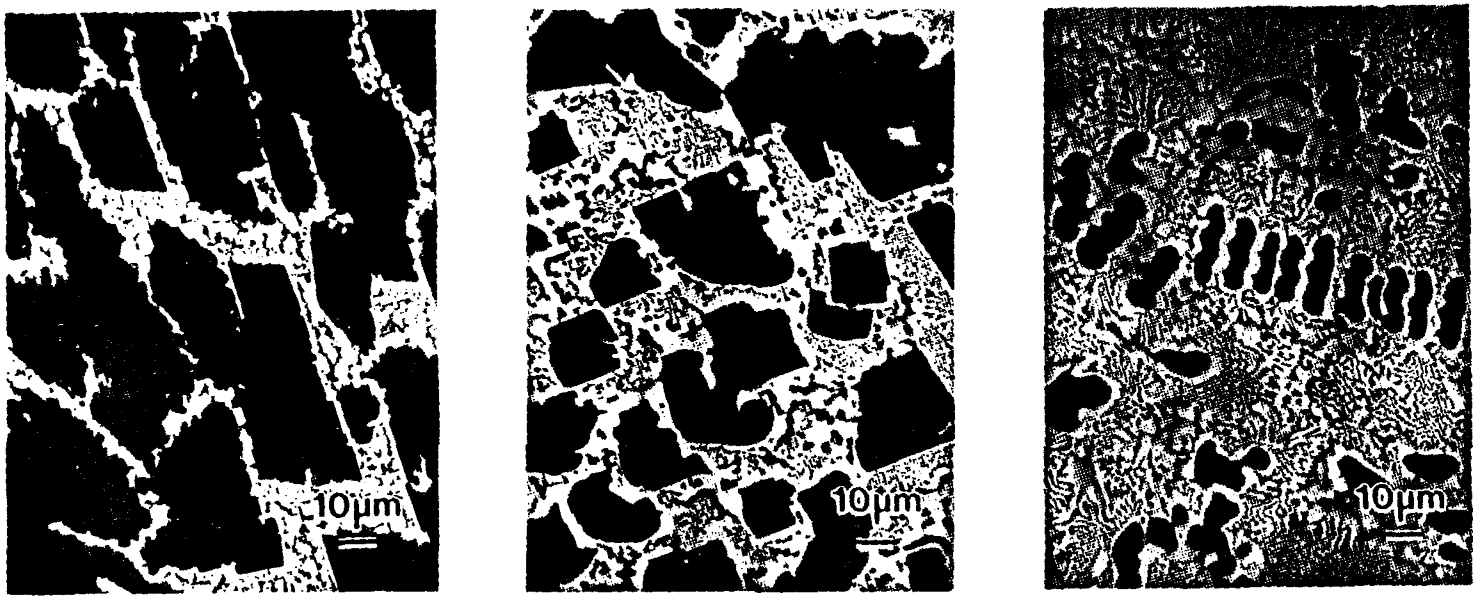
10µm
10µm
10µm

(a) (b) (c)

Figure 28: SEM photomicrograph of alloys,
a) Alloy 7, $Nb_{67}\ Si_{25.8}\ Al_{7.2}$
b) Alloy 10, $Nb_{71.4}\ Si_{19.6}\ Al_{9}$
c) Alloy 13, $Nb_{74.1}\ Si_{13.1}\ Al_{12.8}$

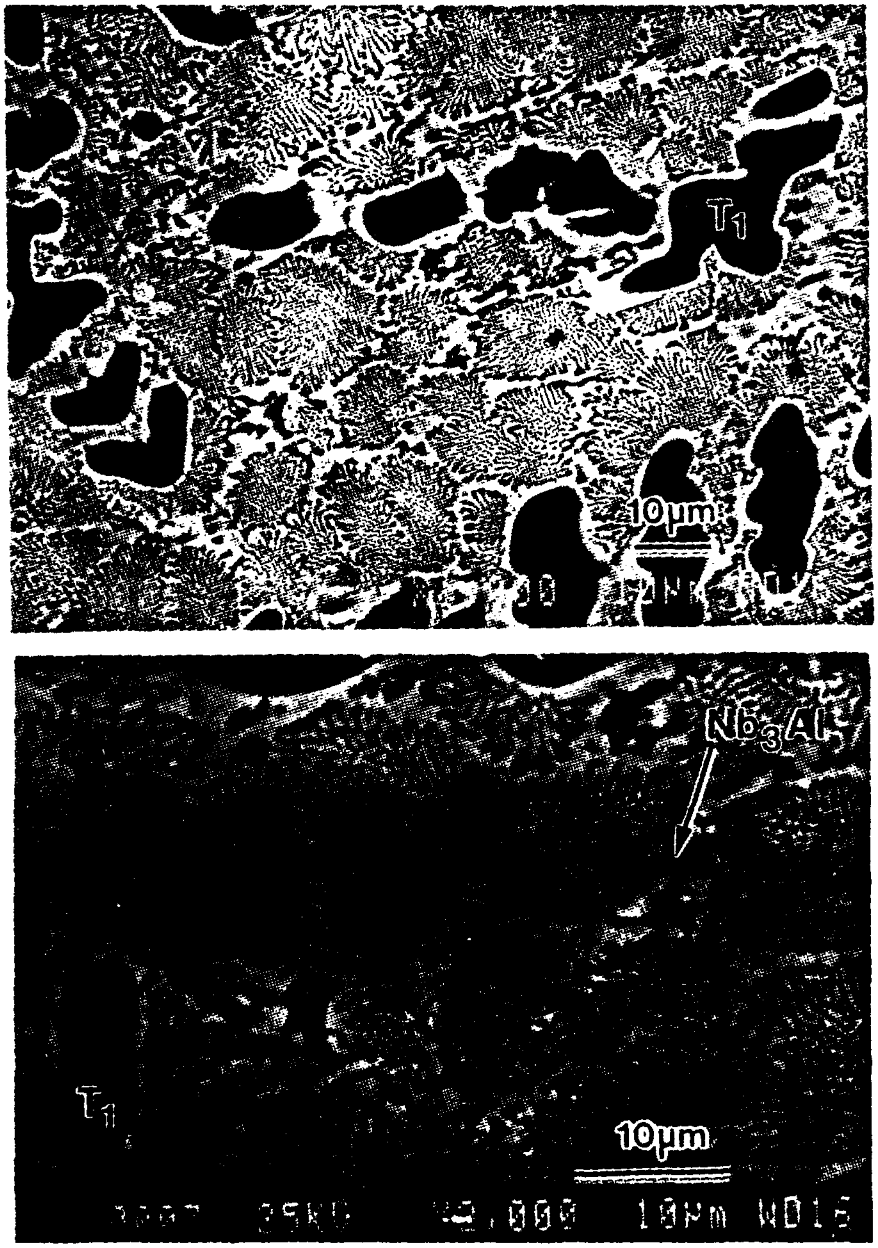
T1
10µm
Nb3Al
T1
10µm
25KV ×2,000 10µm WD16

Figure 29: SEM photomicrograph of primary dendrites (dark phase) and cellular eutectic structure that solidifies along the line of two-fold saturation in alloy 13, $Nb_{74.1}\ Si_{13.1}\ Al_{12.8}$

T1- $Nb_{64.9}\ Si_{27.9}\ Al_{7.2}$
Nb_3Al- $Nb_{77.2}\ Si_{8.4}\ Al_{14.4}$

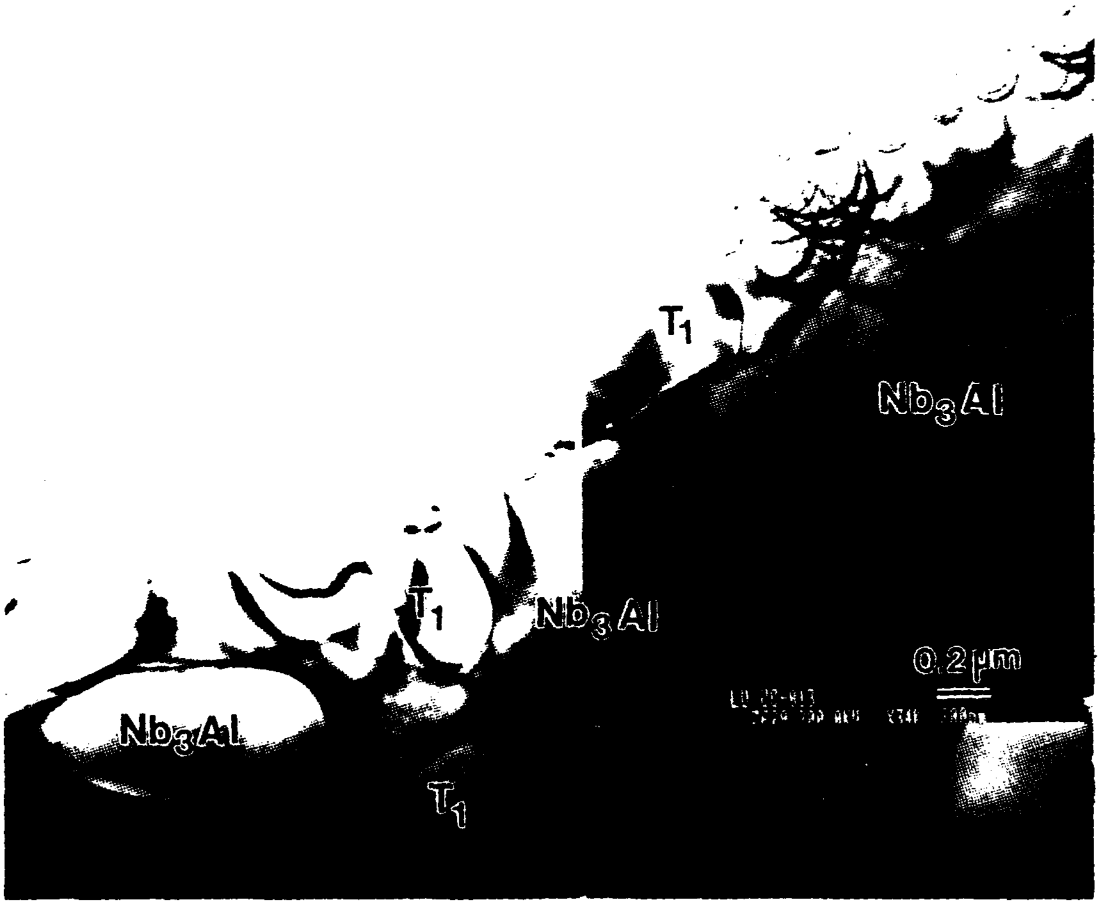
T1
Nb3Al
T1
Nb3Al
0.2 μm
Nb3Al
T1

Figure 30: TEM photomicrograph, showing the T1 and Nb_3Al phases ; Alloy 13, $Nb_{74.1}Si_{13.1}Al_{12.8}$.

T1- $Nb_{64.9}Si_{27.9}Al_{7.2}$
Nb_3Al- $Nb_{77.2}Si_{8.4}Al_{14.4}$

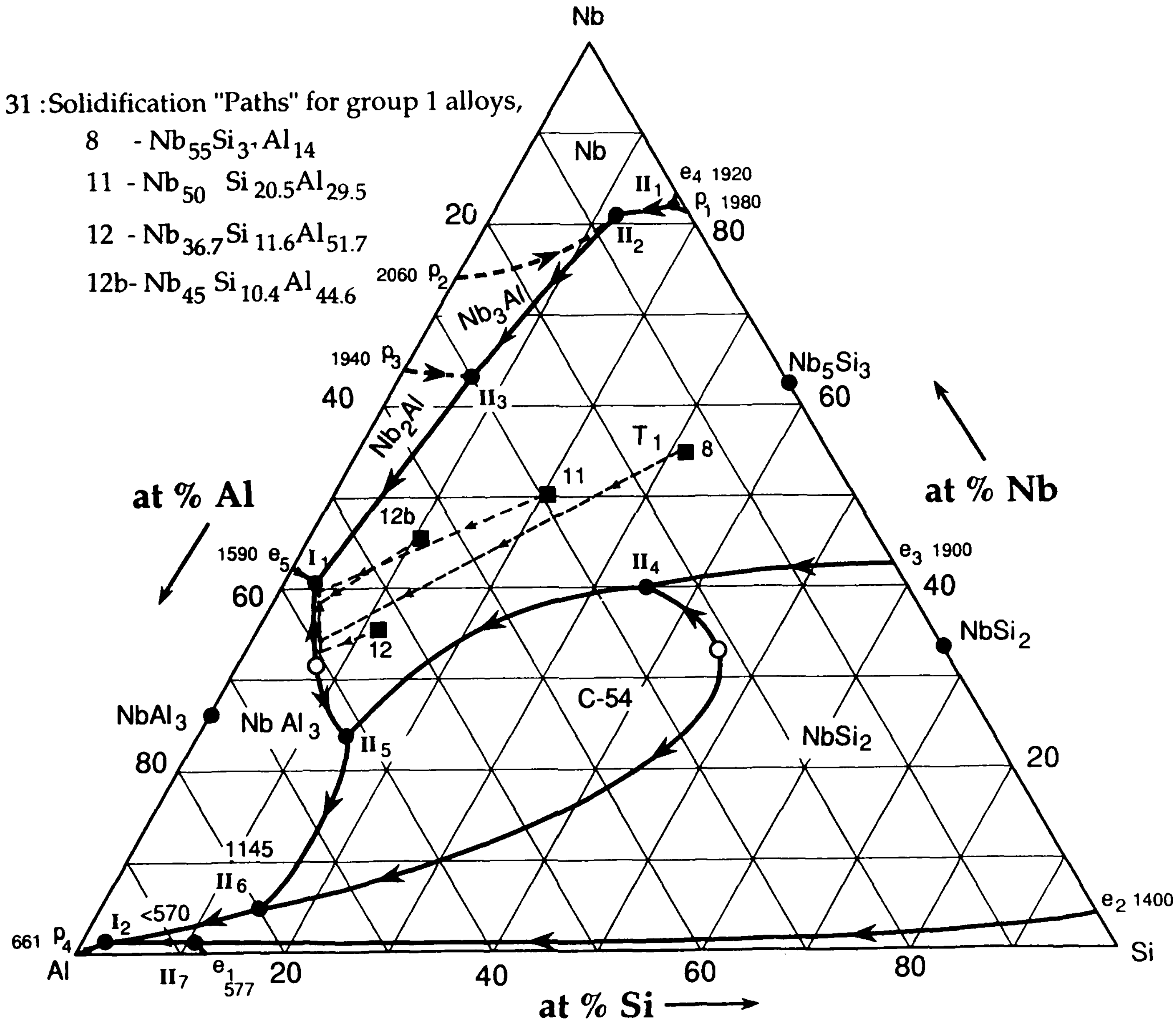
Nb
Nb
20
80
e_4 1920
p_1 1980
II_1
II_2
2060 p_2
Nb_3Al
1940 p_3
II_3
40
Nb_2Al
Nb_5Si_3
60
T_1
8
11
at % Al
at % Nb
12b
1590 e_5
I_1
60
e_3 1900
40
II_4
12
$NbSi_2$
$NbAl_3$
Nb Al_3
C-54
$NbSi_2$
II_5
80
20
1145
II_6
e_2 1400
661 p_4
I_2
<570
Al
II_7
e_1 577
20
40
60
80
Si
at % Si →

Figure 31 :Solidification "Paths" for group 1 alloys,

8 - $Nb_{55}Si_3$, Al_{14}

11 - Nb_{50} $Si_{20.5}Al_{29.5}$

12 - $Nb_{36.7}Si_{11.6}Al_{51.7}$

12b- Nb_{45} $Si_{10.4}Al_{44.6}$

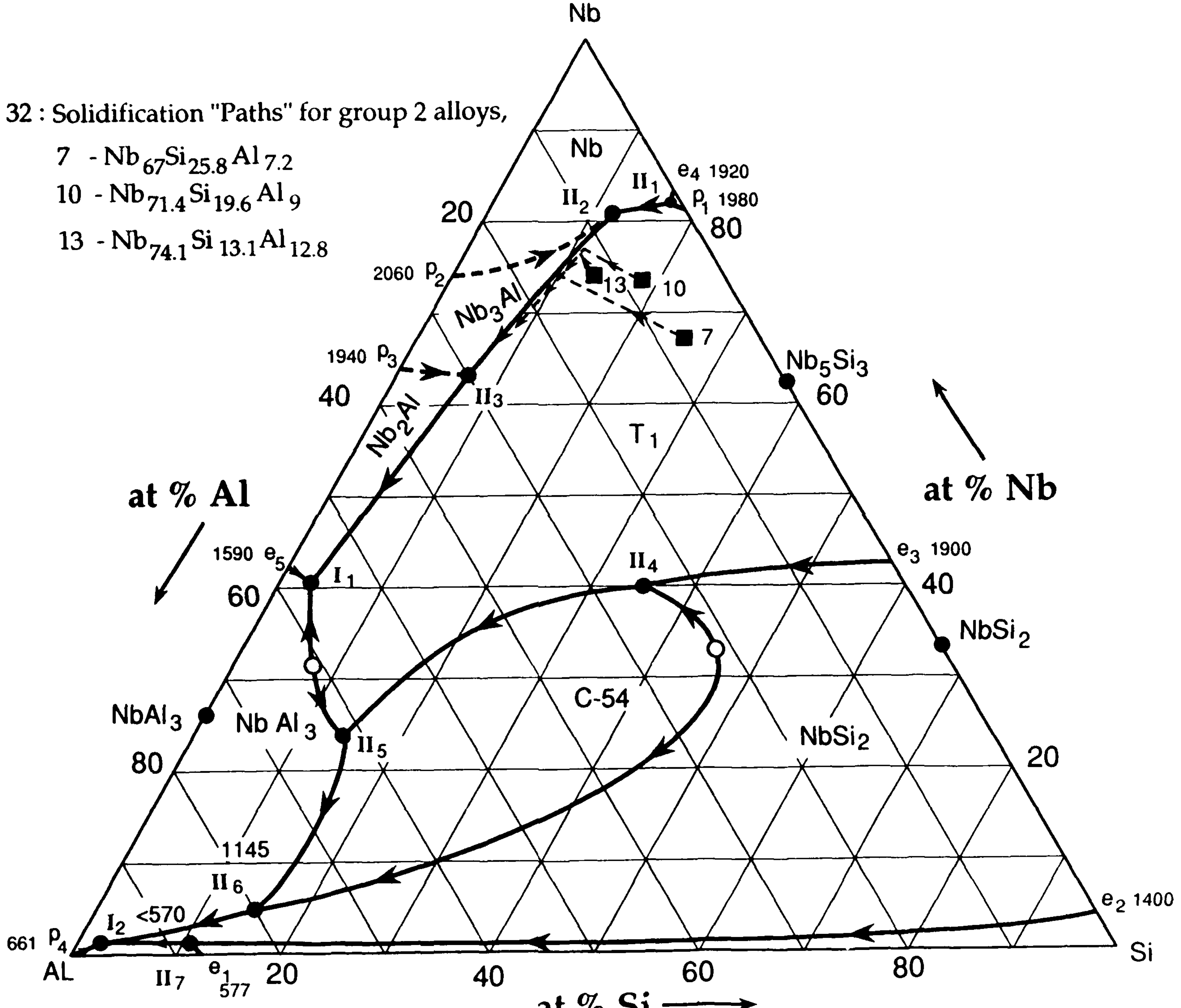
Nb
Nb
II$_1$
e$_4$ 1920
p$_1$ 1980
II$_2$
20
80
2060 p$_2$
13
10
7
Nb$_3$Al
1940 p$_3$
II$_3$
40
60
Nb$_5$Si$_3$
Nb$_2$Al
T$_1$
at % Al
at % Nb
1590 e$_5$
I$_1$
II$_4$
e$_3$ 1900
60
40
NbSi$_2$
NbAl$_3$
Nb Al$_3$
C-54
II$_5$
NbSi$_2$
80
20
1145
II$_6$
e$_2$ 1400
I$_2$
<570
661 p$_4$
AL
II$_7$
e$_1$ 577
20
40
60
80
Si
at % Si

Figure 32 : Solidification "Paths" for group 2 alloys,

7 - $Nb_{67}Si_{25.8}Al_{7.2}$

10 - $Nb_{71.4}Si_{19.6}Al_{9}$

13 - $Nb_{74.1}Si_{13.1}Al_{12.8}$

D24 A89-173'9/18b810

Figure 33 :

Regions where the solidification sequences for group 1 and 2 alloys are valid.

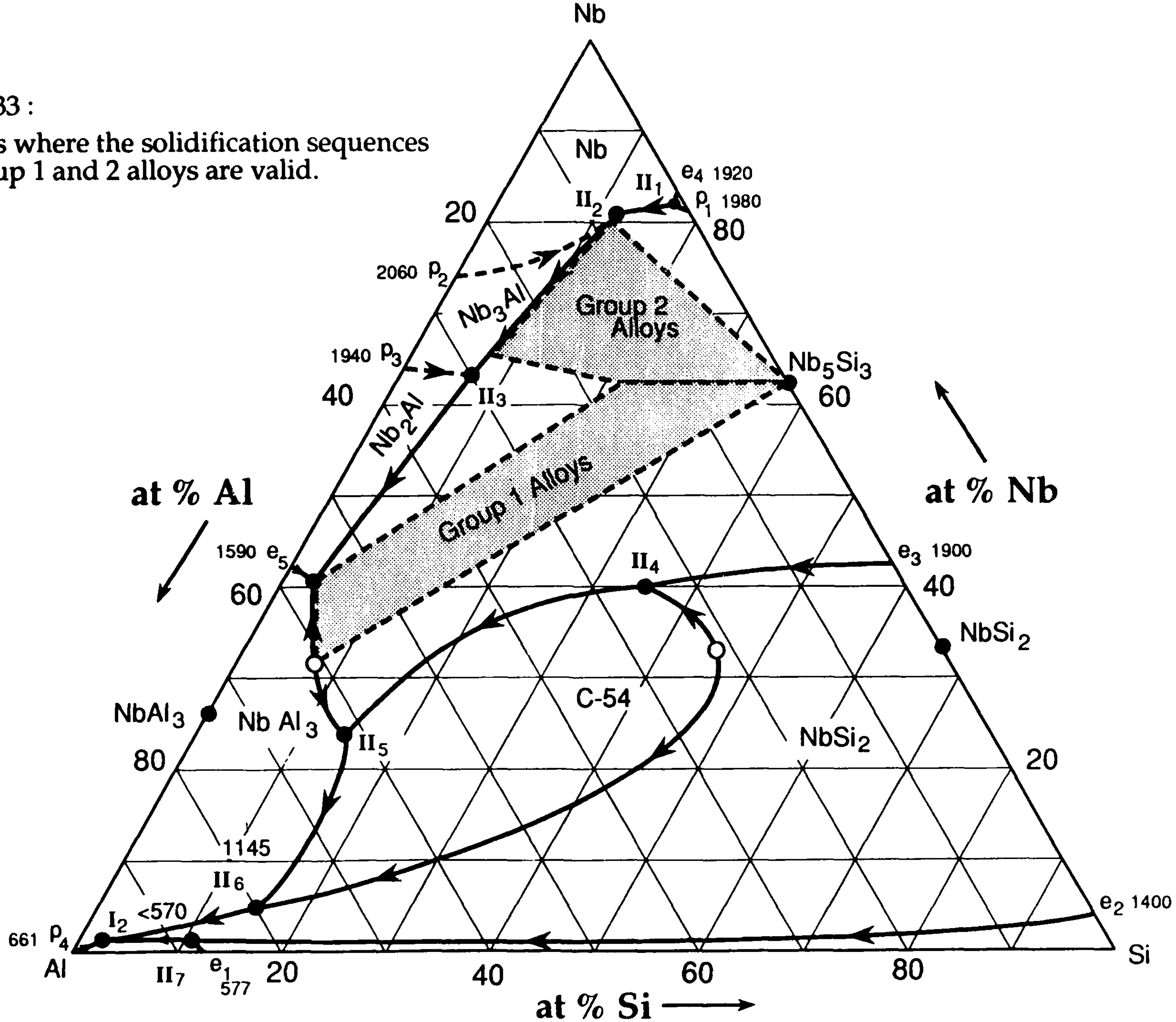
Nb
Nb
II1
e4 1920
p1 1980
II2
20
80
2060 p2
Nb3Al
Group 2 Alloys
1940 p3
Nb5Si3
II3
40
60
Nb2Al
at % Al
at % Nb
Group 1 Alloys
1590 e5
e3 1900
II4
60
40
NbSi2
NbAl3
Nb Al3
C-54
II5
NbSi2
80
20
1145
II6
e2 1400
661 p4
I2
<570
Al
II7
e1 577
20
40
60
80
Si
at % Si